COUPLING POLYMER THERMODYNAMICS AND VISCOELASTICITY TO LIQUID CRYSTALLINE ORDER: SELF-ASSEMBLY AND RELAXATION DYNAMICS OF BLOCK COPOLYMERS IN A NEMATIC SOLVENT

Thesis by

Neal R. Scruggs

In Partial Fulfillment of the Requirements for the

degree of

Doctor of Philosophy

CALIFORNIA INSTITUTE OF TECHNOLOGY

Pasadena, California

2007

(Defended February 15, 2007)

© 2007

Neal R. Scruggs

All Rights Reserved

ACKNOWLEDGEMENTS

"If I have seen further it is by standing on the shoulders of Giants."
-Sir Isaac Newton

Many, many people have helped me in some way, either personally or professionally, to successfully complete this thesis: these are the Giants on whose shoulders I have stood. Beginning with professional acknowledgements, I would like to thank my advisor, Julie Kornfield, first and foremost, for teaching me so much while also allowing me to find my own way. I also owe a debt of gratitude to Mike Kempe for his guidance during my first year. I have worked closely with Rafael Verduzco since day one and I'm thankful we were able to do so much collaboratively. I also thank Anne Hormann for being the glue that holds the Kornfield group together. Peter Palffy-Muhoray and Sam Sprunt at Kent State University have been valued mentors. Jyotsana Lal and Ed Lang at Argonne National Lab, Boualem Hammouda and John Barker at NIST, and Sonjong Hwang at Caltech's Solid-State NMR Facility gave me absolutely invaluable help with my experiments. The inexhaustible David Uhrig at Oak Ridge National Lab provided me with a library of materials that greatly improved by ability to do research, and Mike Vicic gave me excellent advice during two very positive experiences as his teaching assistant. I am grateful to Greg Sotzing for inspiring me to go to graduate school at a time when I was barely even aware such an option existed, and to all of my undergraduate professors who enabled me to get to Caltech in the first place.

I have been privileged to work with a group of extremely talented fellow graduate students, Mike Kempe, Wei Shen, Eric Pape and Derek Thurman (with whom I covered a variety of fascinating conversation topics during the years when we shared an office), Lucia Fernandez-Ballaster, Charles Nickerson, Rafael Verduzco, Mike Mackel, Ameri David, Matthew Mattson, Ryan Turner, Zuli Kurji, Yan Xia, and Diana Smirnova. These are the perfect segue to my personal acknowledgements, since I am proud to call many of them friends.

I am deeply appreciative of my parents' support; they have been both a source of motivation and an understanding outlet for frustration. I am also thankful for the support of my brother (the original Dr. Scruggs), my sister-in-law, and all of my extended family, who all taught me to value education and encouraged me every step of the way. I am sure I could not have succeeded without them or without all of my friends in Los Angeles and elsewhere. In particular I was very fortunate to have known J. J. Feick and will always remember him. Most of all, I am thankful for Scott Carty who's been my biggest fan and a huge source of encouragement and motivation for me in these final months of graduate school.

Caltech is a very special place and I am fortunate to have had the opportunity to study here. I thank every person who somehow shaped my experience into something I will always fondly remember.

ABSTRACT

The discontinuous change in solvent quality of a liquid crystal (LC) solvent, 5CB, at the nematic-isotropic phase transition produces abrupt changes in the phase behavior of solutions of coil and LC-polymers and in the self-assembly of coil-LC block copolymers. Nematic 5CB is strongly selective for a side-group liquid crystal polymer (SGLCP) and isotropic 5CB is a good solvent for both SGLCP and a random coil (polystyrene, PS). In nematic 5CB, unfavorable LC-PS interactions drive phase separation in SGLCP-PS-LC ternary solutions and drive micellization of PS-SGLCP diblocks. In isotropic 5CB, rich phase behavior occurs in both ternary solutions and block copolymer solutions. Despite the fact that isotropic 5CB is a good solvent for both SGLCP and PS, segregation can occur due to the asymmetric solvent effect (i.e., the preference of the solvent for the SGLCP). In concentrated isotropic solutions, unfavorable SGLCP-PS interactions become dominant.

In binary solutions of SGLCP and 5CB, the delicate thermodynamic balance between LC order and polymer entropy manifests itself in a non-monotonic concentration dependence of the solutions' clearing points. The frustration between LC order and polymer entropy in an SGLCP melt is partially relieved by the addition of small molecule LC, greatly increasing the polymer's configurational freedom and stabilizing the nematic phase. In dilute solutions, the polymer adopts an anisotropic conformation because of its coupling to the LC solvent's prevailing director field; the sense and the magnitude of the anisotropy depend on the architecture of the SGLCP (end-on or side-on mesogens).

Coil-SGLCP-coil triblock copolymers self-assemble in 5CB to form liquid crystalline gels in which nematic order is coupled to an associative polymer network. The network's dynamic restructuring couples to fluctuations in the LC's local order to provide an additional relaxation process that is not present in SGLCP solutions or LC elastomers, and the importance of this process is highly dependent on the underlying anisotropy of the SGLCP-based network. The network furthermore provides a memory of the LC orientation state: when the LC is reoriented by electric-magnetic fields or mechanical

shear, the network structure prevents the orientation from relaxing back to a random distribution when the aligning force is removed.

TABLE OF CONTENTS

Acknowledgements iii
Abstract v
Table of Contents vii
List of Tables xi
List of Schemes xiii
List of Figures xiv
Chapter 1: Introduction 1
    1.1 Background 1
    1.2 Motivation 6
    1.3 Thesis Organization 8
    1.4 Figures 9
    1.5 References 17
Chapter 2: Using the "Switchable" Quality of a Liquid Crystal Solvent to Mediate Segregation Between Coil and Liquid Crystalline Homopolymers 22
    2.1 Introduction 22
    2.2 Experimental 24
    2.3 Results 25
    2.4 Discussion 26
    2.5 Conclusions 27
    2.6 Tables 29
    2.7 Figures 30
    2.8 References 34
Chapter 3: Self-Assembly of Coil-Liquid Crystalline Diblock Copolymers in a Solvent of "Switchable" Quality: Structure and Interactions Measured by SANS and Rheometry 35
    3.1 Introduction 36

3.2 Experimental 37
3.3 Results 41
3.4 Discussion 47
3.5 Conclusions 55
3.6 Tables 57
3.7 Figures 59
3.8 References 87
Chapter 4: Synergistic Ordering of Side-Group Liquid Crystal Polymer and Small Molecule Liquid Crystal: Order and Phase Behavior of Nematic Polymer Solutions 90
4.1 Introduction 90
4.2 Experimental 94
4.3 Results 97
4.4 Discussion 100
4.5 Conclusions 105
4.6 Tables 107
4.7 Figures 108
4.8 References 117
Chapter 5: Conformational Anisotropy of Side-Group Liquid Crystal Polymers in Nematic Liquid Crystal Solvent: Small-Angle Neutron Scattering of Semidilute Solutions 122
5.1 Introduction 123
5.2 Experimental 124
5.3 Results 125
5.4 Discussion 130
5.5 Conclusions 132
5.6 Tables 133
5.7 Figures 135
5.8 References 142

Chapter 6: Coupling Liquid Crystal Orienation to an Associating Polymer Network: Mutliple Relaxation Processes in Liquid Crystalline Gels 143
6.1 Introduction 144
6.2 Experimental 146
6.3 Results 148
6.4 Discussion 153
6.5 Conclusions 156
6.6 Tables 158
6.7 Figures 159
6.8 References 175
Chapter 7: Electric-Field Imprinting of Liquid Crystal Gels Self-Assembled from Diblock and Triblock Copolymers in Nematic Solvent 177
7.1 Introduction 177
7.2 Experimental 178
7.3 Results 179
7.4 Discussion 181
7.5 Conclusions 182
7.6 Tables 183
7.7 Figures 184
7.8 References 190
Appendix A: Synthesis and Characterization of Side-Group Liquid Crystal Polymers 191
A.1 Appendix 191
A.2 Tables 197
A.3 Schemes 203
A.4 Figures 205
A.5 References 230
Appendix B: Isotopic Labeling for SANS and NMR 231
B.1 Appendix 231

B.2 Schemes 234
B.3 Figures 235
B.4 References 237
Appendix C: Fitting SANS Data from Coil-Liquid Crystalline Diblock Copolymer Solutions 238
C.1 Appendix 238
C.2 Tables 246
C.3 Figures 247
C.4 References 253
Appendix D: The Spherical Core-Shell Form Factor Applied to Coil-Liquid Crystalline Diblock Copolymer Micelles 255
D.1 Appendix 255
D.2 Tables 260
D.3 Figures 261
D.4 References 263
Appendix E: Dynamic Storage and Loss Moduli of Liquid Crystalline Polymer Solutions 264
E.1 Appendix 264
E.2 Figures 265

LIST OF TABLES

Table 2.1 Molecular weight, conversion, and polydispersity of the side-group liquid crystal homopolymer 29

Table 3.1 Molecular weight, conversion, and polydispersity of end-on side-group liquid crystal diblock copolymers with coil block composed of polystyrene (PS)....................57

Table 3.2 Molecular weight, conversion, and polydispersity of end-on and side-on side-group liquid crystal homopolymers 58

Table 3.3 Molecular weight, conversion, and polydispersity of the side-group liquid crystal diblock copolymer with coil block composed of poly(methyl methacrylate) (PMMA)....................58

Table 4.1 Molecular weight, conversion, and polydispersity of side-group liquid crystal homopolymers....................107

Table 5.1 Molecular weight, conversion, and polydispersity of side-group liquid crystal homopolymers....................133

Table 5.2 Fitting parameters used to model scattering data 134

Table 6.1 Molecular weight, conversion, and polydispersity of side-group liquid crystal polymers....................158

Table 7.1 Molecular weight, conversion, and polydispersity of the side-group liquid crystal block copolymers 183

Table A.1 Molecular weight, composition, and polydispersity of 1,2-polybuatdiene prepolymers used to synthesize side-group liquid crystalline homopolymers in Table A.5....................197

Table A.2 Molecular weight, composition, and polydispersity of poly[styrene-*b*-1,2-butadiene] diblock prepolymers used to synthesize PS-SGLCP diblock copolymers in Table A.6....................198

Table A.3 Molecular weight, composition, and polydispersity of poly[styrene-*b*-1,2-butadiene-*b*-styrene] triblock prepolymer used to synthesize the PS-SGLCP-PS triblock copolymer in Table A.7 199

Table A.4 Molecular weight, composition, and polydispersity of poly[(methyl methacrylate)-*b*-1,2-butadiene] diblock prepolymer used to synthesize the PMMA-SGLCP diblock copolymer in Table A.8 199

Table A.5 Molecular weight, composition, and polydispersity of the side-group liquid crystal homopolymers synthesized from prepolymers in Table A.1 200

Table A.6 Molecular weight, composition, and polydispersity of the side-group liquid crystal diblock copolymers with coil block composed of polystyrene (PS), synthesized from prepolymers in Table A.2 201

Table A.7 Molecular weight, composition, and polydispersity of the side-group liquid crystal triblock copolymer with polystyrene endblocks, synthesized from the prepolymer in Table A.3 202

Table A.8 Molecular weight, composition, and polydispersity of the side-group liquid crystal diblock copolymer with coil block composed of poly(methyl methacrylate) (PMMA), synthesized from the prepolymer in Table A.4 202

Table C.1 Upper bounds on the aggregation number in 5 wt % solutions of diblock copolymers estimated from the size of the core using and from the size of the shell 246

Table D.1 Densities and scattering length densities, ρ, of relevant molecules 260

Table D.2 Densities and scattering length densities, ρ, of polystyrene having various levels of deuteration 260

LIST OF SCHEMES

Scheme A.1 Synthesis of 4-cyano-4′-(3-butenoxy)-biphenyl (CBV4) by Mitsunobu reaction...203

Scheme A.2 Synthesis of 4-cyano-4′-(3-butenoxy)-biphenyl (CBV4) by Williamson ether synthesis...203

Scheme A.3 Synthesis of 4-cyano-4′-(5-(1,1,3,3,-tetramethyldisiloxane)butoxy)biphenyl (SiCB4) by platinum-catalyzed hydrosilylation 204

Scheme A.4 Attachment of SiCB4 to a 1,2-polybutadiene monomer by platinum-catalyzed hydrosilylation 204

Scheme B.1 Synthesis of perdeuterated 4-pentyl-4′-cyanobiphenyl (d_{19}5CB). 234

Scheme B.2 Deuterium labeling of 4-cyano-4′-hydroxybiphenyl (d_2CHB) 234

LIST OF FIGURES

Figure 1.1 Schematic representation of the molecules of a thermotropic liquid crystal in the solid, nematic liquid crystal, and liquid phases 9

Figure 1.2 Schematic representation of the three fundamental distortions of the nematic LC director 10

Figure 1.3 Schematic representation of the three fundamental orientations of the nematic director in relation to the gradient of the velocity in shear flow 10

Figure 1.4 Schematic representation of liquid crystalline polymers 11

Figure 1.5 Chemical structures of the side-on and end-on triblock copolymers that self-assemble in the nematic solvent to form liquid crystalline gels 12

Figure 1.6 Electric field switching of a polydomain end-on triblock copolymer gel. 13

Figure 1.7 Transient electro-optic response of a 5 wt % side-on triblock copolymer gel. .. 14

Figure 1.8 Conoscopic figures demonstrating monodomain alignment of end-on and side-on LC gels induced by shear flow 15

Figure 1.9 Stripe textrure of a 5 wt % end-on LC gel observed at room temperature between crossed polarizers 16

Figure 2.1 Chemical structures of side-group liquid crystal polymer (490HSiCB4), polystyrene (PS), and nematic liquid crystal solvent (5CB) 30

Figure 2.2 Optical micrographs typical of ternary blends of PS, 490HSiCB4, and 5CB 31

Figure 2.3 Partial binary phase diagrams of (a) 490HSiCB4 homopolymer in 5CB and (b) polystyrene homopolymer with 5CB 32

Figure 2.4 Partial ternary phase diagram of PS, 490HSiCB4, and isotropic 5CB determined from optical microscopy 33

Figure 3.1 Chemical structures of end-on side-group liquid crystal diblock copolymers having a coil block composed of polystyrene 59

Figure 3.2 Chemical structures of end-on side-group liquid crystal homopolymers 60

Figure 3.3 Chemical structures of end-on side-group liquid crystal diblock copolymers having a coil block composed of poly(methyl methacrylate) (PMMA) 61

Figure 3.4 Diagram illustrating the relative lengths and compositions of PS-SGLCP diblock copolymers described in Table 3.1 62

Figure 3.5 SANS patterns from solutions of (a) 5 wt % and (b) 10 wt % 320(120)ABSiCB4..63

Figure 3.6 Small-angle neutron scattering patterns from solutions of side-group liquid crystalline diblock copolymers and homopolymers at concentrations of (a) 5 wt % and (b) 10 wt % polymer..64

Figure 3.7 SANS and rheology of 5 wt % 470(40)ABSiCB4 65

Figure 3.8 SANS and rheology of 5 wt % 390(60)ABSiCB4 66

Figure 3.9 SANS and rheology of 5 wt % 420(80)ABSiCB4 67

Figure 3.10 SANS and rheology of 5 wt % 320(120)ABSiCB4 68

Figure 3.11 SANS and rheology of 10 wt % 470(40)ABSiCB4 69

Figure 3.12 SANS and rheology of 10 wt % 390(60)ABSiCB4 70

Figure 3.13 SANS and rheology of 10 wt % 420(80)ABSiCB4 71

Figure 3.14 SANS and rheology of 10 wt % 320(120)ABSiCB4 72

Figure 3.15 SANS and rheology of 5 wt % 210(60)ABSiCB4 73

Figure 3.16 SANS and rheology of 5 wt % 580(190)ABSiCB4 74

Figure 3.17 SANS and rheology of 10 wt % 210(60)ABSiCB4 75

Figure 3.18 SANS and rheology of 10 wt % 580(190)ABSiCB4 76

Figure 3.19 SANS and rheology of 20 wt % 210(60)ABSiCB4 77

Figure 3.20 SANS and rheology of 20 wt % 580(190)ABSiCB4 78

Figure 3.21 Frequency dependence of the magnitude of the complex viscosity of 5 wt % solutions of PS-SGLCP diblock copolymers having similar total molecular weights 79

Figure 3.22 Frequency dependence of the magnitude of the complex viscosity of 10 wt % solutions of PS-SGLCP diblock copolymers having similar total molecular weights 80

Figure 3.23 Frequency dependence of the magnitude of the complex viscosity of solutions of PS-SGLCP diblock copolymer 210(60)ABSiCB4.......................................81

Figure 3.24 Frequency dependence of the magnitude of the complex viscosity of solutions of PS-SGLCP diblock copolymer 580(190)ABSiCB4.....................................82

Figure 3.25 Frequency dependence of the magnitude of the complex viscosity of solutions of PS-SGLCP diblock copolymer 700(70)ABSiCB4.......................................83

Figure 3.26 Frequency dependence of the magnitude of the complex viscosity of solutions of PMMA-SGLCP diblock copolymer 950(70)BdMMASiCB4.......................84

Figure 3.27 The form factor of spheres with radius, *R*, of 400 and 500 Å 85

Figure 3.28 The storage modulus of 5 wt % PS-SGLCP diblock solutions 86

Figure 4.1 Chemical structures of the end-on side-group liquid crystal polymers (350HSiCB4 and $d_2$350HSiCB4) and the nematic liquid crystal solvent (5CB).............108

Figure 4.2 DSC temperature scans from mixtures of 350HSiCB4 and 5CB in proportions ranging from 0 to 100 wt % polymer obtained on heating 109

Figure 4.3 DSC temperature scans from Figure 4.2 plotted individually for clarity......110

Figure 4.4 Latent heat ($|\Delta H|$) and onset temperature (T) of the nematic/isotropic phase transition in mixtures of 350HSiCB4 with 5CB. 111

Figure 4.5 Representative ^{2}H NMR spectra of 5 wt % d_{19}5CB in 5CB 112

Figure 4.6 Microscopic order parameters, S_{zz}, of (a) aromatic deuterium atoms located *para-* to the alkyl chain in d_{19}5CB and (b) aromatic deuterium atoms located *para-* to the oxygen atom in $d_2$350HSiCB4 113

Figure 4.7 Temperature dependence of the ordinary, n_o, and extraordinary, n_e, refractive indices of pure 5CB and solutions of 490HSiCB4 in 5CB...114

Figure 4.8 Temperature dependence of the order parameter of 5CB, and solutions of 490HSiCB4 in 5CB........115

Figure 4.9 (a) Schematic representation of a plausible phase diagram deduced from DSC data (b) Schematic representation of a phase diagram calculated by Chiu and Kyu using Brochard's model........116

Figure 4.10 Schematic representation of mixtures of 350HSiCB4 with 5CB at various concentrations........117

Figure 4.11 (a) Nematic-isotropic transition temperatures predicted by Maier-Saupe theory together with phase transition onset temperatures of 350HSiCB4/5CB measured by DSC on heating. (b) The imposed concentration-dependence of *c* used to generate the phase diagram in (c). (c) Phase boundaries predicted by Brochard's model using a concentration-dependent polymer-solvent nematic interaction parameter........118

Figure 5.1 Chemical structures of end-on (*X*HSiCB4) and side-on (*X*HSiBB) side-group liquid crystal homopolymers and the perdeuterated nematic liquid crystal solvent (d_{19}5CB).........135

Figure 5.2 Two-dimensional small-angle neutron scattering patterns from 5 wt % solutions of (a) oblate end-on and (b) prolate side-on homopolymers in d_{19}5CB........136

Figure 5.3 Sector-averaged small-angle neutron scattering patterns from 5 wt % 500HSiBB in d_{19}5CB........137

Figure 5.4 Sector-averaged small-angle neutron scattering patterns from 5 wt % 990HSiBB in d_{19}5CB........138

Figure 5.5 Sector-averaged small-angle neutron scattering patterns from 5 wt % 350HSiCB4 in d_{19}5CB........139

Figure 5.6 Sector-averaged small-angle neutron scattering patterns from 5 wt % 760HSiCB4 in d_{19}5CB........140

Figure 5.7 Correlation lengths, *L*, in the directions perpendicular and parallel to the nematic director for 5 wt % solutions of (a) end-on and (b) side-on homopolymers......141

Figure 6.1 Schematic diagrams of the splay, twist, and bend distortions in a nematic liquid crystal........159

Figure 6.2 Top-view schematic of the three light scattering geometries used........160

Figure 6.3 Chemical structures of end-on (1100ABASiCB4) and side-on (1400ABASiBB) side-group liquid crystal triblock copolymers with polystyrene endblocks 161

Figure 6.4 Chemical structures of end-on (490HSiCB4) and side-on (710HSiBB) side-group liquid crystal homopolymers 162

Figure 6.5 Normalized time correlation functions at 25 °C and $\theta_s = 30°$ for 5CB, 5 wt % homopolymer solutions, and 5 wt % triblock copolymer gels........163

Figure 6.6 Normalized time correlation functions at 25 °C for end-on and side-on gels164

Figure 6.7 Normalized time correlation functions at 25 °C of end-on polymers at a variety of scattering angles as a function of rescaled delay time........165

Figure 6.8 Normalized time correlation functions at 25 °C of side-on polymers at a variety of scattering angles as a function of rescaled delay time........166

Figure 6.9 Concentration dependence of the normalized time correlation functions at 25 °C and $\theta_s = 30°$ of end-on triblock copolymer gels 167

Figure 6.10 Temperature dependence of the normalized time correlation functions at $\theta_s = 30°$ of 5 wt % end-on homopolymer 168

Figure 6.11 Temperature dependence of the normalized time correlation functions at $\theta_s = 30°$ of 5% side-on homopolymer........169

Figure 6.12 Normalized time correlation functions of side-on homopolymer solution and triblock polymer gel at a variety of scattering angles as a function of rescaled delay time 170

Figure 6.13 Normalized time correlation functions at 25 °C of triblock copolymer gels in the P geometry at a variety of scattering angles as a function of rescaled delay time: (a) 5 wt % end-on triblock (1100ABASiCB4) and (b) 5 wt % side-on triblock (1400ABASiBB)........171

Figure 6.14 Average relaxation rates of (a) end-on and (b) side-on homopolymer solutions at various temperatures in the H and V scattering geometries 172

Figure 6.15 Schematic illustrating the two director relaxation processes in LC physical gels 173

Figure 6.16 Schematic illustrating the effects of bend and splay distortions on an anisotropic network 174

Figure 7.1 Chemical structures of side-group liquid crystal diblock (*X*(*Y*)ABSiCB4) and triblock (1100ABASiCB4) copolymers....184

Figure 7.2 Representative voltage sweep performed on a 10 wt % 390(60)ABSiCB4 gel....185

Figure 7.3 Time-dependence of the percent transmittance of light through a gel composed of 10 wt % 390(60)ABSiCB4 in 5CB after applying a potential difference for 1 min, 10 min, 1 hr, 6, hr, or 1 day....186

Figure 7.4 Time-dependence of the percent transmittance of light through a gel composed of 10 wt % 320(120)ABSiCB4 in 5CB after applying a potential difference for 1 min, 10 min, 1 hr, 6, hr, or 1 day....187

Figure 7.5 Time-dependence of the percent transmittance of light through a gel composed of 5 wt % 1100ABSiCB4 in 5CB after applying a potential difference for 1 min, 10 min, 1 hr, 6, hr, 1 day, or 4 days....188

Figure 7.6 Schematic illustrating the reorientation of liquid crystalline gels before applying an electric field, during field application, and after removing the electric field....189

Figure A.1 300 MHz proton NMR spectrum and GPC chromatograph of 50H....205

Figure A.2 300 MHz proton NMR spectrum and GPC chromatograph of 60H....206

Figure A.3 300 MHz proton NMR spectrum and GPC chromatograph of 100H....207

Figure A.4 300 MHz proton NMR spectrum and GPC chromatograph of 30(60)AB....208

Figure A.5 300 MHz proton NMR spectrum and GPC chromatograph of 100(70)AB....209

Figure A.6 300 MHz proton NMR spectrum and GPC chromatograph of 100(190)AB....210

Figure A.7 300 MHz proton NMR spectrum and GPC chromatograph of 60(40)AB....211

Figure A.8 300 MHz proton NMR spectrum and GPC chromatograph of 60(60)AB...212

Figure A.9 300 MHz proton NMR spectrum and GPC chromatograph of 60(80)AB...213

Figure A.10 300 MHz proton NMR spectrum and GPC chromatograph of 50(120)AB....214

Figure A.11 300 MHz proton NMR spectrum and GPC chromatograph of (60)150(70)ABA......215

Figure A.12 300 MHz proton NMR spectrum and GPC chromatograph of 140(70)BdMMA......216

Figure A.13 300 MHz proton NMR spectrum and GPC chromatograph of 350HSiCB4......217

Figure A.14 300 MHz proton NMR spectrum and GPC chromatograph of $d_2$350HSiCB4......218

Figure A.15 300 MHz proton NMR spectrum and GPC chromatograph of 490HSiCB4......219

Figure A.16 300 MHz proton NMR spectrum and GPC chromatograph of 760HSiCB4......220

Figure A.17 300 MHz proton NMR spectrum and GPC chromatograph of 210(60)ABSiCB4......221

Figure A.18 300 MHz proton NMR spectrum and GPC chromatograph of 700(70)ABSiCB4......222

Figure A.19 300 MHz proton NMR spectrum and GPC chromatograph of 580(190)ABSiCB4......223

Figure A.20 300 MHz proton NMR spectrum and GPC chromatograph of 470(40)ABSiCB4......224

Figure A.21 300 MHz proton NMR spectrum and GPC chromatograph of 390(60)ABSiCB4......225

Figure A.22 300 MHz proton NMR spectrum and GPC chromatograph of 420(80)ABSiCB4......226

Figure A.23 300 MHz proton NMR spectrum and GPC chromatograph of 320(120)ABSiCB4......227

Figure A.24 300 MHz proton NMR spectrum and GPC chromatograph of 1100ABASiCB4......228

Figure A.25 300 MHz proton NMR spectrum and GPC chromatograph of 950(70)BdMMASiCB4......229

Figure B.1 300 MHz proton NMR spectrum of d_{19}5CB and dichloromethane used to calculate the deuterium content 235

Figure B.2 300MHz proton NMR spectrum of d_2CHB 236

Figure C.1 Schematic drawings of examples of structural models that may be used to calculate form factors of block copolymer micelles...247

Figure C.2 Resolution function of the Small-Angle Scattering Instrument (SASI) at Argonne National Laboratory's Intense Pulsed Neutron Source....................................248

Figure C.3 Small-angle neutron scattering data from 5 wt % diblock copolymer solutions with representative fits...249

Figure C.4 Values of the core radius and shell thickness for 5 wt % diblock solutions derived from fitting neutron scattering data to the spherical core-shell model 250

Figure C.5 Values of the core radius and shell thickness for (a) 5 wt % 420(80)ABSiCB4 and (b) 5 wt % 320(120)ABSiCB4 as a function of temperature derived from fitting neutron scattering data to the spherical core-shell model...251

Figure C.6 Small-angle neutron scattering data from 5 wt % 320(120)ABSiCB4 shown together with a representative fit using the spherical core-shell model and the form factor for a cylinder of homogeneous scattering length density 252

Figure D.1 Schematic diagram of a spherical core-shell particle 261

Figure D.2 Achievable neutron scattering length densities of the solvent, side-group liquid crystal polymer (HSiCB4), and polystyrene (PS) by various strategies for changing each component's deuterium content...262

Figure E.1 Frequency dependence of the storage and loss modulus of 2 wt % 210(60)ABSiCB4 in 5CB 265

Figure E.2 Frequency dependence of the storage and loss modulus of 2 wt % 700(70)ABSiCB4 in 5CB 266

Figure E.3 Frequency dependence of the storage and loss modulus of 2 wt % 580(190)ABSiCB4 in 5CB 267

Figure E.4 Frequency dependence of the storage and loss modulus of 5 wt % 210(60)ABSiCB4 in 5CB 268

Figure E.5 Frequency dependence of the storage and loss modulus of 5 wt % 700(70)ABSiCB4 in 5CB 269

Figure E.6 Frequency dependence of the storage and loss modulus of 5 wt % 580(190)ABSiCB4 in 5CB 270

Figure E.7 Frequency dependence of the storage and loss modulus of 5 wt % 470(40)ABSiCB4 in 5CB 271

Figure E.8 Frequency dependence of the storage and loss modulus of 5 wt % 390(60)ABSiCB4 in 5CB 272

Figure E.9 Frequency dependence of the storage and loss modulus of 5 wt % 420(80)ABSiCB4 in 5CB 273

Figure E.10 Frequency dependence of the storage and loss modulus of 5 wt % 320(120)ABSiCB4 in 5CB 274

Figure E.11 Frequency dependence of the storage and loss modulus of 10 wt % 210(60)ABSiCB4 in 5CB 275

Figure E.12 Frequency dependence of the storage and loss modulus of 10 wt % 700(70)ABSiCB4 in 5CB 276

Figure E.13 Frequency dependence of the storage and loss modulus of 10 wt % 580(190)ABSiCB4 in 5CB 277

Figure E.14 Frequency dependence of the storage and loss modulus of 10 wt % 470(40)ABSiCB4 in 5CB 278

Figure E.15 Frequency dependence of the storage and loss modulus of 10 wt % 390(60)ABSiCB4 in 5CB 279

Figure E.16 Frequency dependence of the storage and loss modulus of 10 wt % 420(80)ABSiCB4 in 5CB 280

Figure E.17 Frequency dependence of the storage and loss modulus of 10 wt % 320(120)ABSiCB4 in 5CB 281

Figure E.18 Frequency dependence of the storage and loss modulus of 20 wt % 210(60)ABSiCB4 in 5CB 282

Figure E.19 Frequency dependence of the storage and loss modulus of 20 wt % 700(70)ABSiCB4 in 5CB 283

Figure E.20 Frequency dependence of the storage and loss modulus of 20 wt % 580(190)ABSiCB4 in 5CB 284

Figure E.21 Frequency dependence of the storage and loss modulus of 2 wt % 950BdMMASiCB4 in 5CB 285

Figure E.22 Frequency dependence of the storage and loss modulus 5 wt % 950BdMMASiCB4 in 5CB 286

Figure E.23 Frequency dependence of the storage and loss modulus of 10 wt % 950BdMMASiCB4 in 5CB 287

Figure E.24 Frequency dependence of the storage and loss modulus of 20 wt % 950BdMMASiCB4 in 5CB 288

Figure E.25 Frequency dependence of the storage and loss modulus of 2 wt % 1100ABASiCB4 in 5CB 289

Figure E.26 Frequency dependence of the storage and loss modulus of 5 wt % 1100ABASiCB4 in 5CB 290

Figure E.27 Frequency dependence of the storage and loss modulus of 2 wt % 350HSiCB4 in 5CB....................291

Figure E.28 Frequency dependence of the storage and loss modulus of 2 wt % 760HSiCB4 in 5CB....................292

Figure E.29 Frequency dependence of the storage and loss modulus of 5 wt % 350HSiCB4 in 5CB....................293

Figure E.30 Frequency dependence of the storage and loss modulus of 5 wt % 760HSiCB4 in 5CB 294

Figure E.31 Frequency dependence of the storage and loss modulus of 10 wt % 350HSiCB4 in 5CB....................295

Figure E.32 Frequency dependence of the storage and loss modulus of 10 wt % 760HSiCB4 in 5CB....................296

Figure E.33 Frequency dependence of the storage and loss modulus of 20 wt % 350HSiCB4 in 5CB....................297

Figure E.34 Frequency dependence of the storage and loss modulus of 20 wt % 760HSiCB4 in 5CB....................298

Chapter 1

INTRODUCTION

1.1 Background ... 1
1.2 Motivation ... 6
1.3 Thesis Organization ... 8
1.4 Figures ... 9
1.5 References ... 17

Portions of this chapter are reproduced from Kempe, Scruggs, Verduzco, Lal, and Kornfield, *Nature Materials* **2004,** 3, 177-182 and from Kempe, Verduzco, Scruggs, and Kornfield, *Soft Matter* **2006**, 2, 422-431.

1.1 Background

Crystals and liquids are familiar condensed matter phases in which the relative positions and orientations of the constituent molecules are either well-defined by a rigid lattice or lacking long-range correlation, respectively. In between the crystal and liquid phases lies a progression of partially ordered phases termed “liquid crystalline mesophases,” the simplest of which is termed the “nematic” phase (Figure 1.1).[1, 2] Rod-like molecules typically lend themselves to the formation of a nematic phase in a particular range of temperatures, and such materials are termed “calamitic, thermotropic liquid crystals” (LCs). In the nematic phase, the molecules diffuse about one another randomly, but they tend to retain orientation in a preferred direction called the “director,” ***n***. The director breaks the material’s isotropic symmetry and gives rise to properties such as optical birefringence, dielectric anisotropy, diamagnetic anisotropy, and orientational elasticity. The coupling of order and fluidity makes LCs particularly intriguing materials because their orientation-dependent properties can be influenced by readily accessibly fields.

Nematic LCs are far from perfectly ordered; the LC's molecules have a distribution of orientations with respect to the director. The nematic order parameter, $S = ½ <3 \cos^2 \theta - 1>$, where θ is the angle between a molecule and the director, quantifies the degree of order ranging from $S = 1$ in a perfectly oriented medium to $S = 0$ in an isotropic medium. The intermolecular interactions maintaining the orientational order of a nematic LC are relatively weak: the Maier-Saupe model of nematic ordering estimates their strength to be approximately five times the thermal energy.[2] For this reason, the local director is in a constant state of flux, and these thermally-induced distortions to the director field are responsible for the turbid, milky appearance of nematic LCs. Distortions to a nematic LC can be expressed as the sum of splay, twist, and bend distortions (Figure 1.2), and the elastic free energy per unit volume, F_V, is given by

$$F_V = \tfrac{1}{2}\left[K_1(\nabla \cdot \mathbf{n})^2 + K_2(\mathbf{n} \cdot (\nabla \times \mathbf{n}))^2 + K_3\left|\mathbf{n} \times (\nabla \times \mathbf{n})\right|^2\right], \tag{1.1}$$

where K_1, K_2, and K_3 are the splay, twist, and bend elastic constants, respectively.[2] The dynamics of director fluctuations are governed by the LC's elastic constants and anisotropic viscosity coefficients.[3, 4] One way to express the viscosity of a nematic LC is in reference to the three fundamental orientations of the director in shear flow. The viscosities measured in these geometries, η_a, η_b, and η_c, are known as the Miesowicz viscosities (Figure 1.3).[1, 2]

Macromolecular LCs can be formed when rod-like molecules are either incorporated directly into a polymer chain to form a main-chain liquid crystal polymer (MCLCP) or laterally attached to a polymer chain via a flexible spacer to form a side-group liquid crystal polymer (SGLCP) (Figure 1.4). Macromolecular LCs are frustrated materials because the defining characteristics of polymers and LCs are directly at odds with one another: polymer chains seek random configurations and LC molecules seek long-range order.[5] Bonding LC mesogens to a random-coil polymer forces compromise between the opposing tendencies, compromise that often manifests itself in unique physical phenomena that are not present in either pure LCs or bulk polymers alone.

Nematic order is coupled to the conformation of SGLCPs and MCLCPs in the melt and in solution with small-molecule LCs. The trajectory of an ideal, random-coil polymer is a random walk from one end to the other and the chain's conformation is spherical in solution and in the melt.[6] The conformation of a liquid crystalline polymer deviates from sphericality in order to accommodate the orientational order of its mesogens.[5] Neutron scattering experiments on LC polymers in the melt, reviewed by Cotton and Hardouin,[7] demonstrate that MCLCPs and side-on SGLCPs adopt a highly prolate (aspect ratio > 5) ellipsoidal conformation in the nematic phase.[8, 9] On the other hand, end-on SGLCPs have mild anisotropy (aspect ratio ≈ 1.5) and can be either prolate[10] or oblate[11-15] ellipsoids. Experiments on solutions of liquid crystalline polymers in small-molecule LC solvents, reviewed by Jamieson et al.,[4] reveal that the orientation of the polymer's attached mesogens is coupled to that of the solvent, and that the polymer adapts to the director field similar to the way it does in the melt: MCLCPs and side-on SGLCPs become strongly prolate[16-20] while end-on SGLCPs are mildly anisotropic prolate[21, 22] or oblate[16, 18, 19, 22-27] ellipsoids. A few experiments on solutions of non-LC polymers in LC solvents have demonstrated that these polymers, too, adopt anisotropic conformations in solution, but the strength of the orientational coupling is not as strong as it is when the polymer itself is mesogenic.[28]

The coupling between polymer conformation and liquid crystalline order modifies polymer solution thermodynamics and results in novel phase behavior in mixtures of both LC and non-LC polymers with LC solvents. The phase behavior of LC polymers in LC solvents has been treated theoretically by Brochard[29, 30] and ten Bosch et al.[31] These theories agree with numerous experimental studies demonstrating the coexistence of two nematic phases in these mixtures,[27, 32-37] a phenomenon rarely, if ever, observed in binary mixtures of small-molecule LCs.[36] Nematic-nematic coexistence appears to be a unique consequence of the coupling between LC order and polymer thermodynamics. The phase behavior of non-LC polymers in LC solvents has also been treated theoretically[38, 39] and experimentally.[40-46] In these systems, the solvent's orientational order presents a large entropic penalty to dissolution in the nematic phase, but when the solvent transitions to the isotropic phase the polymer's solubility instantly increases. It is not uncommon to observe a transition from nematic / isotropic coexistence to a single isotropic phase coincident with the solvent's nematic to isotropic phase transition.

When mesogens are grafted to a polymer chain, LC order also becomes coupled to polymer dynamics. Conformational anisotropy of an SGLCP dissolved in small-molecule LC solvent leads to anisotropic modification of the solution's flow properties.[4, 16, 21, 22, 25, 26, 47-50] The hydrodynamics of solutions of LC polymers in LC solvents has been treated by Brochard,[51] whose theory predicts the LC's orientation-dependent viscosity coefficients to be modified differently according to the anisotropy of the dissolved polymer chain: the increase in η_b, for example, is larger when an oblate polymer is dissolved in nematic solvent than when the polymer is prolate. A modification of Brochard's theory[22] has been used with some success to deduce a dissolved polymer's anisotropy from the solution's rheology.[21, 25, 26, 50] Polymer anisotropy also leads to anisotropic modification of the director's fluctuation dynamics.[4, 18, 52, 53] Dynamic light scattering experiments on solutions of SGLCPs in nematic LCs[4, 18, 52, 53] have demonstrated that prolate polymers preferentially slow the relaxation of splay distortions while oblate polymers more strongly affect the relaxation of bend distortions.

The discussion of coupling between LC order and polymer conformation has been thus far limited to homopolymers, but introducing LC order also has a profound effect on the structure and dynamics of block copolymers (BCPs).[54] Two or more different polymers covalently bonded together constitute a BCP, and unfavorable thermodynamic interactions between the blocks usually cause a self-assembled microstructure to form in which the contact between them is minimized. BCPs have been extensively studied in recent decades because they are a versatile system for engineering nanotechnologies, as reviewed by Park, Yoon, and Thomas.[55] Selection of the length, chemical structure, and connectivity of the component blocks gives access to a wide variety of morphologies, having sizes typically on the order of ~10-100 nm, which can be ordered with respect to one another in grains of one micrometer or larger.[55, 56] When one block of a BCP is an LC polymer, the resulting material exhibits order over a variety of length scales from a few nanometers (the cooperative alignment of LC molecules) up to the larger-scale structure of the BCP.[54, 56] In these systems the orientational order of the mesophase couples strongly to the microphase separated BCP morphology, and the LC director often dictates the orientation of the microdomains. In contrast to the alignment tendency of cylindrical microdomains of a triblock copolymer that normally align in the direction of shear, an orientation perpendicular to the shear plane is observed when one block is a LC polymer because of the anchoring of the mesogens to the cylinder walls.[57] Another example of this coupling is the observation that changing LC order can either change the morphology of the microphase separated structure (order-order transition),[58, 59] or trigger the order-disorder transition coincident with the isotropization temperature of the LC block.[60-62]

BCPs in solution are thermodynamically rich systems because the polymer's self-assembled structure depends not only on pairwise interactions between the different polymer blocks, but also on interactions between the blocks and the solvent.[63-70] The polymer concentration and the relative enthalpic interactions between the solvent and the polymer blocks (the solvent's "selectivity") determine the morphology of the BCP in solution. In a strongly selective solvent, the solubility of one block, A, is distinctly greater than the other block, B, and the BCP usually self-assembles into micelles with block B segregated to a core surrounded by a solvent-rich corona containing block A. In the limit of no selectivity, both blocks are soluble and the BCP will not self-assemble in dilute solution where block-block interactions are screened by polymer-solvent interactions. For a fixed BCP at fixed concentration, the choice of solvent determines whether or not micelles form. If they do, the solvent choice also determines their shape, size, and long-range order relative to one another (e.g., BCC or FCC lattice).

Knowing that orientational order is strongly coupled to the thermodynamics of SGLCP homopolymers in LC solvent and to the morphology of LC BCPs in the bulk suggests an additional layer of complexity might be added to the thermodynamics governing self-assembly of BCPs in solution if one block is an SGLCP and the solvent is nematogenic.

From a practical standpoint, swelling an LC BCP with small-molecule solvent could serve to improve their sluggish and weak responses to electro-magnetic stimuli, making them better candidates for use in devices such as liquid crystal displays. Despite these motivations, only one research group[71-73] reported experiments on LC solutions of LC BCPs prior to the Kornfield group's studies of liquid crystalline gels self-assembled from triblock copolymers in nematic solvent.[19, 74, 75] Much of the work described in this thesis was motivated by a desire to better understand the physics of these gels.

1.2 Motivation: Orientational Coupling Phenomena in Self-Assembled Triblock Copolymer Gels

Solutions of coil-SGLCP block copolymers in a nematic solvent combine the thermodynamic phenomena deriving from the coupling of LC order to polymer chains with the rich thermodynamics governing BCP self-assembly in solution. Triblock copolymers were synthesized with polystyrene (PS) endblocks and an SGLCP midblock having mesogens attached either end-on or side-on. Dissolving the triblocks in 4-pentyl-4′-cyanobiphenyl (5CB), a small-molecule nematic LC, causes the random-coil PS endblocks to segregate from the ordered solvent, and a nematic gel is formed when the polymer concentration is 5 wt % or greater (Figure 1.5).[19, 74] The segregated PS-rich domains form the crosslinks of a polymer network spanned by the LC-soluble SGLCP midblocks. The network structure of 5 wt % polymer gels is thermoreversible because the entropic penalty to dissolution of the PS blocks disappears when the solvent is heated to the isotropic phase (> 35 °C), causing the segregated domains to dissolve then re-form when the solution is cooled to the nematic phase again. However, the rheology of gels containing 20 wt % triblock copolymer shows that associations between PS blocks persist beyond the solvent's nematic to isotropic transition,[74] suggesting that polymer concentration plays a non-trivial role in the self-assembly of LC gels, just as it does in the self-assembly of non-mesogenic BCP solutions.

Director reorientation dynamics in nematic gels self-assembled from coil-SGLCP block copolymers are almost as fast as in 5CB itself and are coupled to the underlying polymeric network. The gel's director aligns parallel to electric fields of 1.2 V/μm or greater, allowing for the creation of an optically clear monodomain from an initially opaque, polydomain gel (Figure 1.6). When the electric field is removed, the coupling of the solvent orientation to the topology of the polymer network provides a memory of the original orientation and the gel returns to the polydomain state on time scales as fast as 15 ms,[19] comparable to the relaxation time of pure 5CB in a 5 μm-thick cell (~ 40 ms).[76, 77] In stark contrast to small-molecule LCs, the time required to fully return to the original polydomain state depends strongly on the previously applied field: higher applied fields cause the relaxation time to increase (Figure 1.7). Nevertheless, there appears to be a separate, fast relaxation process present that allows the gel's optical response to track the 1 kHz oscillation of the applied voltage (Figure 1.7).

The gels' responses to mechanical strain also demonstrate the coupling of the LC orientation to the polymer network. The LC director becomes uniformly aligned when the gels are subjected to shear and the orientation of the SGLCP mesogens dictates the orientation of the director relative to the velocity gradient: end-on gels align with the director parallel to the velocity gradient, side-on gels align perpendicular (Figure 1.8). These orientations mirror the behavior of SGLCP homopolymers in nematic solvent.[47] However, in contrast to homopolymer solutions, the gel's network serves to lock in the orientation and the monodomain alignment remains after cessation of shear.

Changing the anisotropy of the SGLCP block by heating or cooling the gel in the nematic phase causes an unusual buckling instability to occur because of the LC director's coupling to the polymer network.[75] When the network initially forms near the nematic / isotropic phase transition, the order parameter of the solvent is low and the induced conformational anisotropy of the SGLCP midblocks is mild. Upon further cooling into the nematic phase, the conformational anisotropy increases, but the SGLCPs are not free to expand in their preferred direction because their PS endblocks lock them into a network that is constrained by anchoring to the gel's contact surface. The compromise between changing conformational anisotropy and the constraints of the polymer network causes a periodic distortion to the director field that generates a striking striped texture when the gel is viewed in a microscope between crossed polarizers (Figure 1.9).

1.3 Thesis Organization

Experimental investigations of the physics underlying the novel phenomenology of self-assembled liquid crystalline gels are the subject of this thesis. In Chapter 2, the phase behavior of SGLCP and random-coil homopolymers in 5CB demonstrates the discontinuous change in random-coil polymer solubility that takes place when the LC solvent is heated from the nematic to isotropic phase. The influence of polymer-polymer interactions on the phase behavior of ternary blends of SGLCP, random-coil polymer, and 5CB is used to understand the self-assembly of coil-SGLCP diblock copolymers, whose temperature-dependent structure and rheology is expounded upon in Chapter 3. The consequences of coupling LC order with the polymer's conformational entropy on orientational order and polymer phase behavior is explored in Chapter 4, and in Chapter 5 the influence of polymer architecture (side-on or end-on) and temperature on conformational anisotropy are demonstrated by small-angle neutron scattering. The coupling of director relaxation dynamics to the underlying polymer network is investigated by dynamic light scattering in Chapter 6. Finally, Chapter 7 looks at the effect of the interconnected triblock copolymer network on the gel's orientational memory and demonstrates that memory is absent in gels composed of non-interconnected diblock copolymer micelles.

1.4 Figures

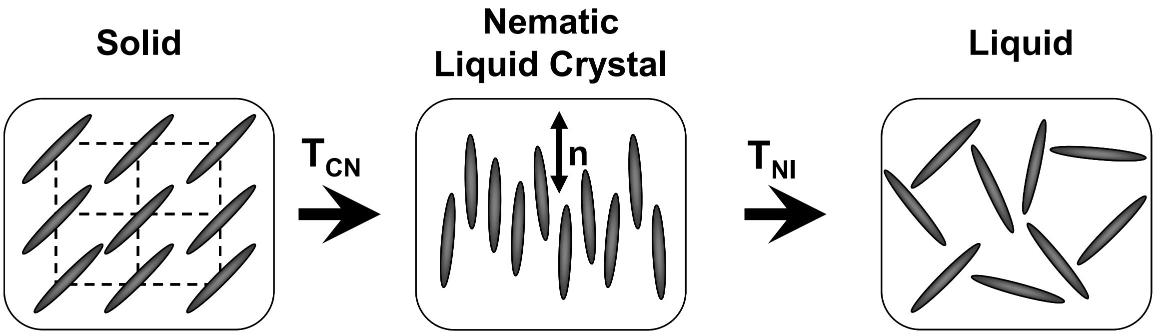

Figure 1.1 Schematic representation of the molecules of a thermotropic liquid crystal, represented by gray ellipses, in the solid, nematic liquid crystal, and liquid phases. In the solid phase, the molecules have regular positions and orientations. When heated above the crystalline to nematic phase transition temperature, T_{CN}, the molecules lose their positional order, but remain oriented in a preferred direction called the "director," $\boldsymbol{n}$. Above the nematic-isotropic transition temperature, T_{NI}, the molecules have no long-range positional or orientational correlations.

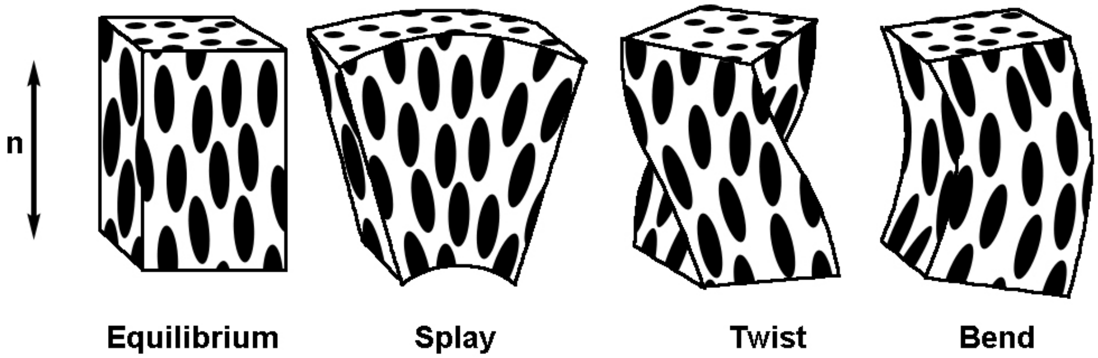

Figure 1.2 Schematic representation of the three fundamental distortions of the nematic LC director. The free energy cost of each distortion is expressed in Equation 1.1 using elastic constants K_1, K_2, and K_3 for splay, twist, and bend, respectively. The spatially varying local director orientation is represented by black ellipses and the equilibrium director is denoted ***n***.

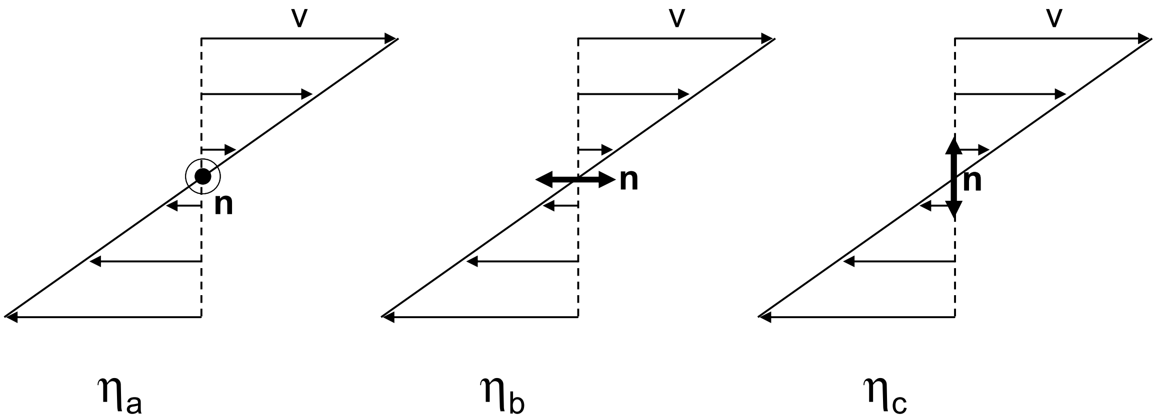

Figure 1.3 Schematic representation of the three fundamental orientations of the nematic director, ***n***, in relation to the gradient of the velocity, *v*, in shear flow. The effective viscosities measured in these geometries, η_a, η_b, and η_c, define the Miesowicz viscosities of a nematic LC.

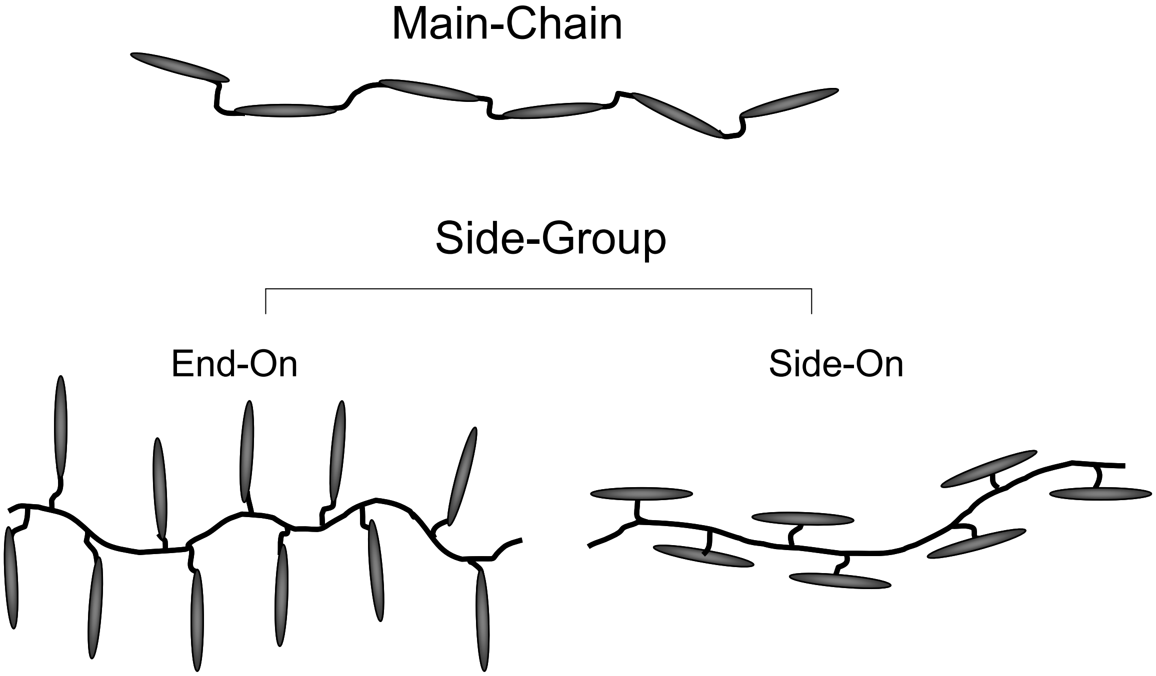

Figure 1.4 Schematic representation of liquid crystalline polymers. Main-chain liquid crystal polymers incorporate the mesogens into the polymer chain, and side-group liquid crystal polymers have mesogens laterally attached to the backbone via a flexible spacer. End-on polymers have the mesogens attached with their long axes perpendicular to the polymer, while side-on polymers have the mesogens attached with their long axes parallel.

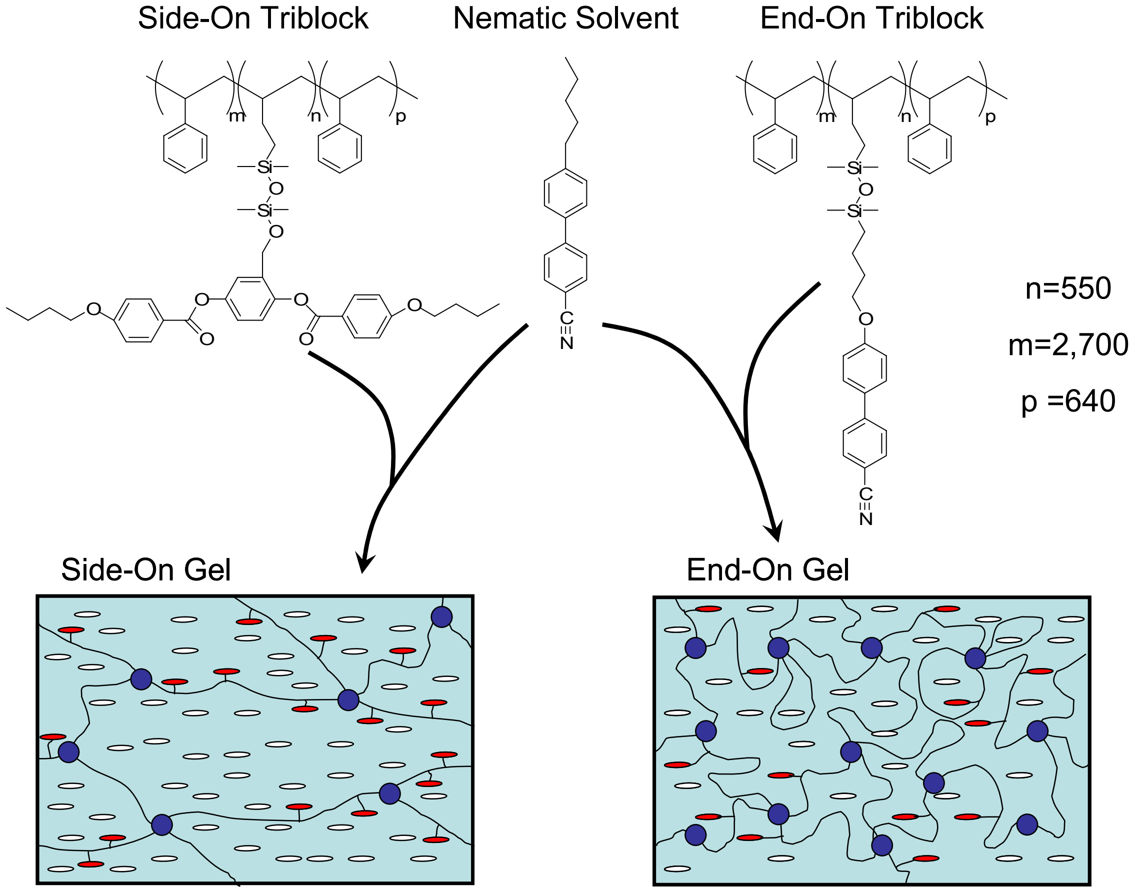

Figure 1.5 Chemical structures of the side-on and end-on triblock copolymers that self-assemble in the nematic solvent (4-pentyl-4′-cyanobiphenyl, 5CB) to form liquid crystalline gels. Schematics of the gels illustrate the segregation of the polystyrene blocks (blue circles) to form physical crosslinks spanned by the LC-soluble SGLCP midblocks (black lines to represent the polymer backbone with red ellipses to represent the attached mesogens). The solvent is represented in the schematics by white ellipses. The relative sizes of the segregated domains, SGLCP midblocks, and solvent molecules are not drawn to scale.

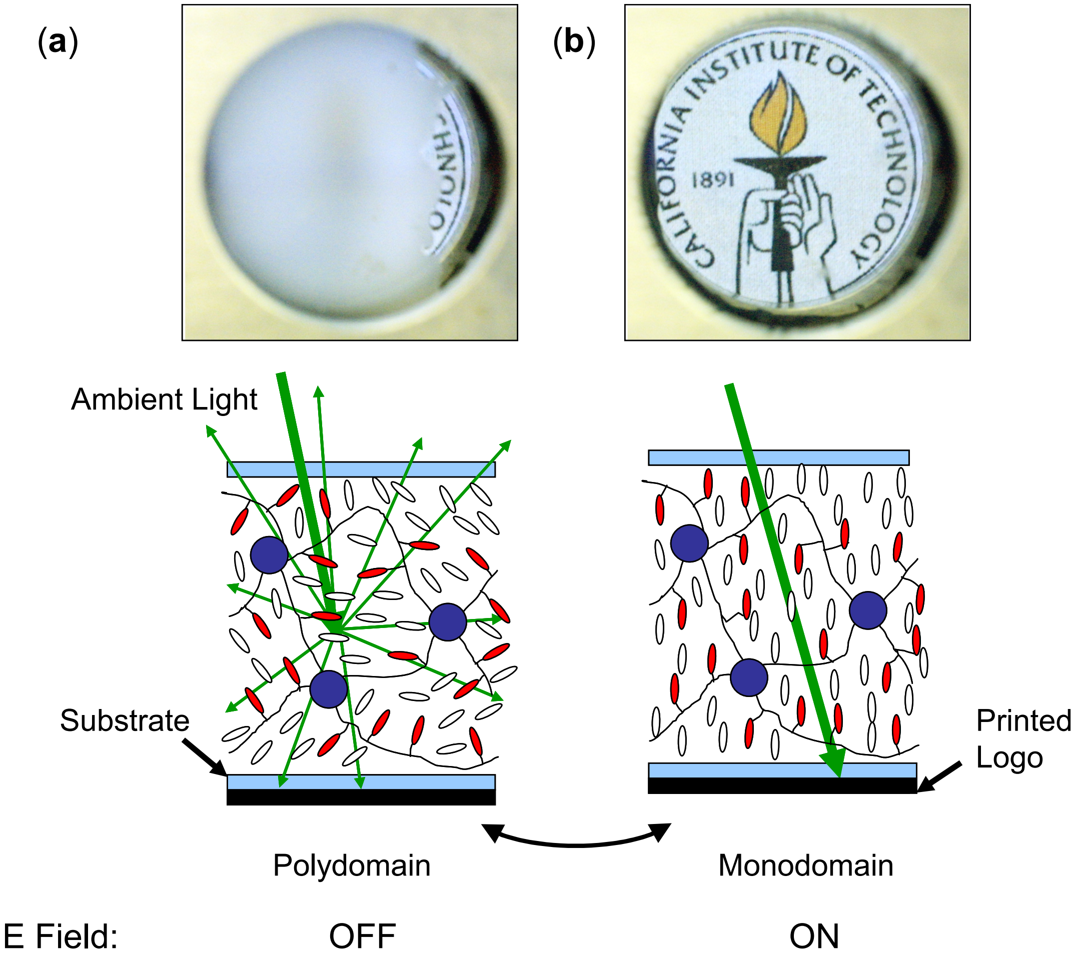

Figure 1.6 (a) A 5 wt % end-on triblock copolymer gel is sandwiched between two transparent indium-tin-oxide electrodes spaced 25 μm apart. The gel is loaded into the cell by capillary action: when heated above 35 °C it transitions to a liquid and flows into the gap, cooling to the nematic phase triggers the polymer's self-assembly. In this case, the gel is only partially filling the field of view, and the printed logo placed behind the cell is clearly visible in the empty portion. (b) Applying an electric field of 1.6 V/μm reoriented the LC director and creates an optically clear monodomain; the empty portion of the cell cannot be distinguished from the portion containing aligned gel and the printed logo behind the cell is clearly visible. The opaque, polydomain state (a) is recovered when the field is removed. The gel's structure is represented schematically according to the same conventions as in Figure 1.5.

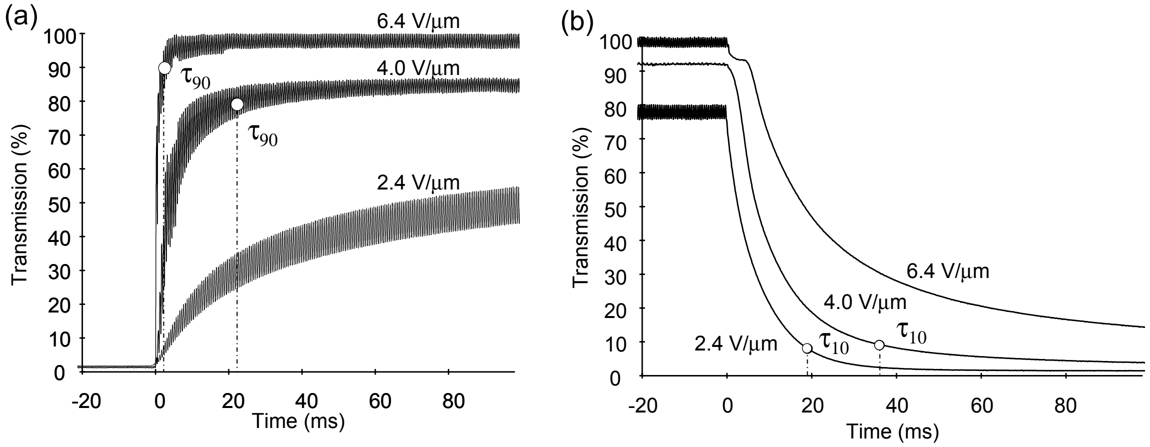

Figure 1.7 Transient electro-optic response of a 5 wt % side-on triblock copolymer gel under application of alternating current electric fields of 2.4, 4.0, and 6.4 V/μm oscillating at 1 kHz. The gel is contained between transparent indium-tin-oxide electrodes and the transmission of a 10 mW, 633 nm laser beam is measured during application of the field. (a) The time required for the transmitted intensity to reach 90% of its maximum when the field is switched on is denoted τ_{90}. (b) The time required for the transmitted intensity to reach 10% of its maximum when the field is switched off is denoted τ_{10}. When not shown, τ_{90} and τ_{10} are beyond the graphs' scales.

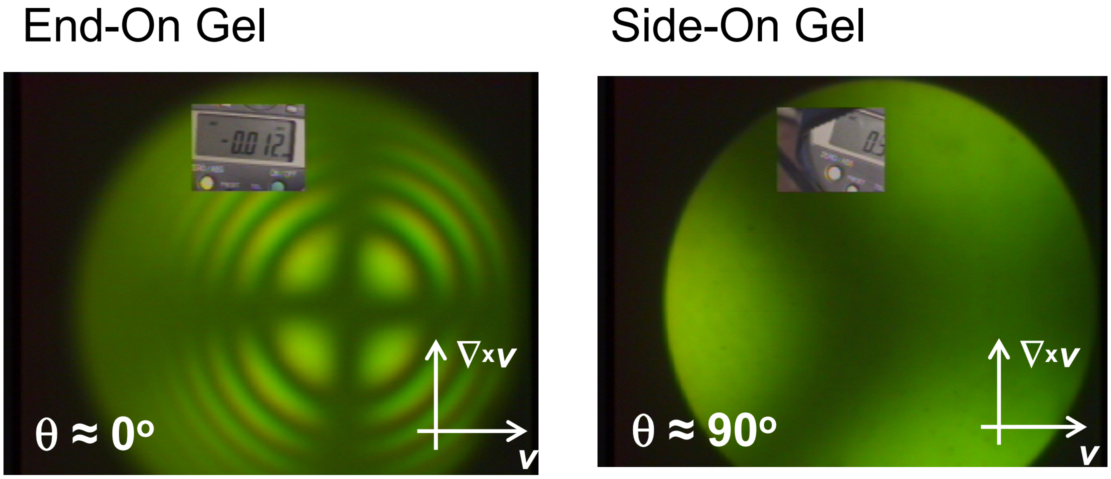

End-On Gel

Side-On Gel

Figure 1.8 Conoscopic figures demonstrating monodomain alignment of end-on and side-on LC gels induced by shear flow. The angle *θ* is the angle between the optic axis and the velocity gradient direction deduced from the type of conoscopic figure observed.[78, 79] The cross pattern observed for end-on gels is characteristic of alignment of the director parallel to the velocity gradient, and the hyperbolic pattern observed for side-on gels is characteristic of alignment perpendicular.

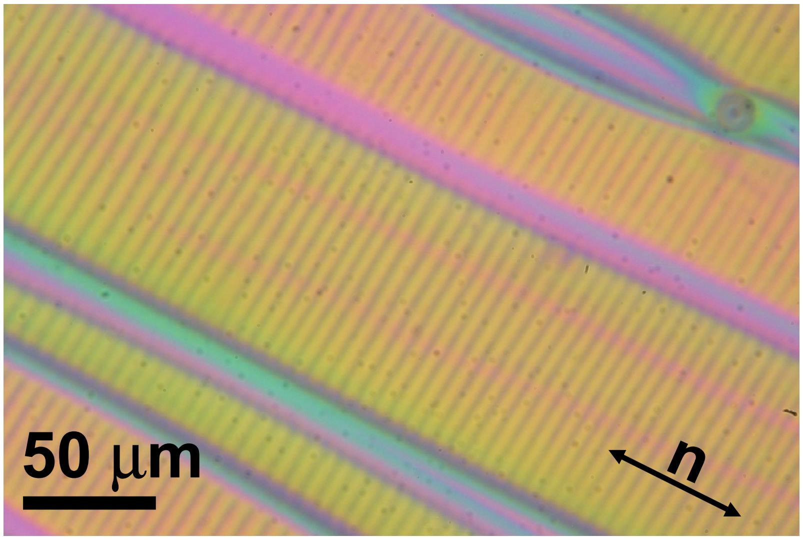

Figure 1.9 Optical micrograph of a 5 wt % end-on LC gel observed at room temperature between crossed polarizers. A periodic stripe pattern is observed because of a buckling instability induced by changes in conformational anisotropy of the gel's SGLCP midblock. The orientation of the director is denoted "***n***".

1.5 References

[1] Collings, P. J.; Hird, M. *Introduction to Liquid Crystals: Chemistry and Physics*, Taylor and Francis: Bristol, PA, 1997.

[2] de Gennes, P.-G. *The Physics of Liquid Crystals*, 2nd ed; Clarendon Press: Oxford, 1993.

[3] Ho, J. T. Light scattering and quasielastic spectroscopy. In *Liquid Crystals*; S. Kumar, Editor; Cambridge University Press: Cambridge, 2001.

[4] Jamieson, A. M.; Gu, D. F.; Chen, F. L.; Smith, S. Viscoelastic behavior of nematic monodomains containing liquid crystal polymers. *Prog. Polym. Sci.* **1996**, *21*, 981-1033.

[5] Wang, X. J.; Warner, M. Theory of nematic comb-like polymers. *J. Phys. A: Math. Gen.* **1987**, *20*, 713-731.

[6] Rubinstein, M.; Colby, R. H. *Polymer Physics*, 1st ed; Oxford University Press: New York, 2003.

[7] Cotton, J. P.; Hardouin, F. Chain Conformation of Liquid-Crystalline Polymers Studied by Small-Angle Neutron Scattering. *Prog. Polym. Sci.* **1997**, *22*, 795-828.

[8] Lecommandoux, S.; Achard, M. F.; Hardouin, F.; Brulet, A.; Cotton, J. P. Are nematic side-on polymers totally extended? A SANS study. *Liq. Cryst.* **1997**, *22*, 549-555.

[9] Leroux, N.; Keller, P.; Achard, M. F.; Noirez, L.; Hardouin, F. Small Angle Neutron Scattering experiments on "side-on fixed" liquid crystal polyacrylates. *J. Phys. II France* **1993**, *3*, 1289-1296.

[10] Davidson, P.; Noirez, L.; Cotton, J. P.; Keller, P. Neutron scattering study and discussion of the backbone conformation in the nematic phase of a side chain polymer. *Liq. Cryst.* **1991**, *10*, 111-118.

[11] Pepy, G.; Cotton, J. P.; Hardouin, F.; Keller, P.; Lambert, M.; Moussa, F.; Noirez, L.; Lapp, A.; Strazielle, C. Liquid Crystal Polymers: Studies of Labelled Parts by Neutron Scattering. *Makromol. Chem. - M. Symp.* **1988**, *15*, 251-258.

[12] Keller, P.; Carvalho, B.; Cotton, J. P.; Lambert, M.; Moussa, F.; Pepy, G. Side chain mesomorphic polymers: studies of labelled backbones by neutron scattering. *J. Physique Lett.* **1985**, *46*, L-1065 - L-1071.

[13] Hardouin, F.; Noirez, L.; Keller, P.; Lambert, M.; Moussa, F.; Pepy, G.; Richard, H. Liquid Crystal Polymers: A Small Angle Neutron Scattering Study. *Mol. Cryst. Liq. Cryst.* **1988**, *155*, 389-397.

[14] Kirste, R. G.; Ohm, H. G. The conformation of liquid-crystalline polymers as revealed by neutron scattering. *Makromol. Chem., Rapid Commun.* **1985**, *6*, 179-185.

[15] Richardson, R. M.; Gray, G. W.; Tajbakhsh, A. R. Neutron scattering studies of terminally attached side chain liquid crystal polymers. *Liq. Cryst.* **1993**, *14*, 871-879.

[16] Gu, D. F.; Jamieson, A. M. Rheological Characterization of Director Dynamics in a Nematic Monodomain Containing Mesogenic Polymers of Differing Architectures. *Macromolecules* **1994**, *27*, 337-347.

[17] Chiang, Y.-C.; Jamieson, A. M. Electrorheological determination of the Leslie viscosity coeffcient (a_2) of a main-chain liquid crystal polymer in a nematic solvent. *Rheol. Acta* **1999**, *38*, 268-273.

[18] Gu, D. F.; Jamieson, A. M.; Kawasumi, M.; Lee, M.; Percec, V. Dynamic Light Scattering from Nematic Monodomains Containing Mesogenic Polymers of Differing Architectures. *Macromolecules* **1992**, *25*, 2151-2155.

[19] Kempe, M. D.; Scruggs, N. R.; Verduzco, R.; Lal, J.; Kornfield, J. A. Self-assembled liquid-crystalline gels designed from the bottom up. *Nat. Mater.* **2004**, *3*, 177-182.

[20] Matoussi, H.; Ober, R.; Veyssie, M.; Finkelmann, H. Conformation of Side Chain Nematic Polymers in Nematic Solutions: a Small-Angle X-Ray Scattering Study: SAXS. *Europhys. Lett.* **1986**, *2*, 233-240.

[21] Chiang, Y.-C.; Jamieson, A. M.; Zhou, Y.; Kasko, A. M.; Pugh, C. Effect of molecular weight on the elctrorheological behavior of side-chain liquid crystal polymers in nematic solvents. *Polymer* **2002**, *43*, 4887-4894.

[22] Yao, N.; Jamieson, A. M. Transient shear flow behavior of dilute solutions of side-chain liquid-crystalline polysiloxanes in 4,4'-(n- pentyloxy)cyanobiphenyl. *Macromolecules* **1998**, *31*, 5399-5406.

[23] Kempe, M. D.; Kornfield, J. A.; Lal, J. Chain Anisotropy Side-Group Liquid Crystalline Polymers in Nematic Solvents. *Macromolecules* **2004**, *37*, 8730-8738.

[24] Mattoussi, H.; Ober, R. Conformation of Comblike Liquid-Crystalline Macromolecules. *Macromolecules* **1990**, *23*, 1809-1816.

[25] Liu, P.-Y.; Jamieson, A. M.; Yao, N. Twist Viscosity of a Side-Chain Liquid-Crsytalline Polysiloxane Dissolved in a Tumbling Nematic Solvent. *Macromolecules* **2000**, *33*, 1692-1697.

[26] Yao, N.; Jamieson, A. M. Rheological behavior of dilute solutions of a side-chain liquid-crystalline polysiloxane in 4,4'-n-octylcyanobiphenyl. *Rheol. Acta* **2000**, *39*, 338-345.

[27] Pereira, F. V.; Borsali, R.; Merlo, A. A.; Pesco da Silveira, N. Small angle X-ray scattering study of chiral side chain liquid crystalline polymers in 5CB and 8CB solvents. *Liq. Cryst.* **2004**, *31*, 655-661.

[28] Dubault, A.; Ober, R.; Veyssie, M.; Cabane, B. Anisotropy of a flexible polymeric chain in a nematic field: neutron scattering versus magnetic resonance. *J. Physique* **1985**, *46*, 1227-1232.

[29] Brochard, F.; Jouffroy, J.; Levinson, P. Phase diagrams of mesomorphic mixtures. *J. Physique* **1984**, *45*, 1125-1136.

[30] Chiu, H.-W.; Kyu, T. Equilibrium phase behavior of nematic mixtures. *J. Chem. Phys.* **1995**, *103*, 7471-7481.

[31] ten Bosch, A.; Maissa, P.; Sixou, P. Molecular model for nematic polymer in liquid crystal solvents. *J. Chem. Phys.* **1983**, *79*, 3462-3466.

[32] Chiu, H.-W.; Zhou, Z. L.; Kyu, T.; Cada, L. G.; Chien, L.-C. Phase Diagrams and Phase Separation Dynamics in Mixtures of Side-Chain Liquid Crystalline Polymers and Low Molar Mass Liquid Crystals. *Macromolecules* **1996**, *29*, 1051-1058.

[33] Kihara, H.; Kishi, R.; Miura, T.; Kato, T.; Ichijo, H. Phase behavior of liquid-crystalline copolymer/ liquid crystal blends. *Polymer* **2001**, *42*, 1177-1182.

[34] Sigaud, G.; Achard, M. F.; Hardouin, F.; Coulon, C.; Richard, H.; Mauzac, M. Flory's Parameters in Solutions of Liquid Crystalline Side-Chain Polymers in Low Molecular Weight Liquid Crystals. *Macromolecules* **1990**, *23*, 5020-5024.

[35] Sigaud, G.; Achard, M. F.; Hardouin, F.; Mauzac, M.; Richard, H.; Gasparoux, H. Relationships between Molecular Structure and Immiscibility of Liquid Crystalline Side-Chain Polymers in Low Molecular Weight Nematic Solvents. *Macromolecules* **1987**, *20*, 578-585.

[36] Casagrande, C.; Veyssie, M.; Finkelmann, H. Phase separations in the mixtures of a mesomorphic polymer with a low molecular mass liquid crystal. *J. Physique* **1982**, *43*, L671 - L675.

[37] Benthack-Thoms, H.; Finkelmann, H. Phase separations in binary mixtures of nematic liquid crystal side chain polymers and low-molar-mass liquid crystals, 1 Influence of the chemical constitution of the low-molar-mass component. *Makromol. Chem.* **1985**, *186*, 1895-1903.

[38] Brochard, F. Solutions of flexible polymers in a nematic liquid. *C. R. Acad. Sc. Paris* **1979**, *289*, 229-232.

[39] Matsuyama, A.; Kato, T. Phase separations and orientational ordering of polymers in liquid crystal solvents. *Phys. Rev. E* **1999**, *59*, 763-770.

[40] Ahn, W.; Kim, C. Y.; Kim, H.; Kim, S. C. Phase Behavior of Polymer/Liquid Crystal Blends. *Macromolecules* **1992**, *25*, 5002-5007.

[41] Hori, H.; Urakawa, O.; Adachi, K. Dielectric Relaxation in Phase-Segregated Mixtures of Polystyrene and Liquid Crystal 5CB. *Macromolecules* **2004**, *37*, 1583-1590.

[42] Benmouna, F.; Daoudi, A.; Roussel, F.; Buisine, J.-M.; Coqueret, X.; Maschke, U. Equilibrium Phase Diagram of Polystyrene and 8CB. *J. Polym. Sci., Part B: Polym. Phys.* **1999**, *37*, 1841-1848.

[43] Benmouna, F.; Daoudi, A.; Roussel, F.; Leclercq, L.; Buisine, J.-M.; Coqueret, X.; Benmouna, M.; Ewen, B.; Maschke, U. Effect of Molecular Weight on the Phase Diagram and Thermal Properties of Poly(styrene)/8CB Mixtures. *Macromolecules* **2000**, *33*, 960-967.

[44] Gogibus, N.; Maschke, U.; Benmouna, F.; Ewen, B.; Coqueret, X.; Benmouna, M. Phase Diagrams of Poly(dimethylsiloxane) and 5CB Blends. *J. Polym. Sci., Part B: Polym. Phys.* **2001**, *39*, 581-588.

[45] Kim, W.-K.; Kyu, T. Phase Separation Dynamics in a Mixture of Polystyrene and Liquid Crystal. *Mol. Cryst. Liq. Cryst.* **1994**, *250*, 131-141.

[46] Kronberg, B.; Bassignana, I.; Patterson, D. Phase Diagrams of Liquid Crystal + Polymer Systems. *J. Phys. Chem.* **1978**, *82*, 1714-1719.

[47] Kempe, M. D.; Kornfield, J. A. Shear alignment behavior of nematic solutions induced by ultralong side-group liquid crystal polymers. *Phys. Rev. Lett.* **2003**, *90*, 115501.

[48] Quijada-Garrido, I.; Siebert, H.; Friedrich, C.; Schmidt, C. Flow Behavior of Two Side-Chain Liquid Crystal Polymers Studied by Transient Rheology. *Macromolecules* **2000**, *33*, 3844-3854.

[49] Yao, N.; Jamieson, A. M. Electrorheological creep response of tumbling nematics. *J. Rheol. (Melville, NY, U. S.)* **1998**, *42*, 603-619.

[50] Weill, C.; Casagrande, C.; Veyssie, M.; Finkelmann, H. Nematic solutions of nematic side chain polymers: twist viscosity effect in the dilute regime. *J. Physique* **1986**, *47*, 887-892.

[51] Brochard, F. Viscosities of Dilute Polymer Solutions in Nematic Liquids. *J. Polym. Sci. Pt. B-Polym. Phys.* **1979**, *17*, 1367-1374.

[52] Gu, D. F.; Jamieson, A. M. Dynamic Light Scattering from a Side-Chain Liquid Crystal in a Nematic Solvent. *Mol. Cryst. Liq. Cryst.* **1991**, *209*, 147-153.

[53] Gu, D. F.; Jamieson, A. M.; Rosenblatt, C.; Tomazos, D.; Lee, M.; Percec, V. Dynamic Light Scattering from a Nematic Monodomain Containing a Side-Chain Liquid Crystal Polymer in a Nematic Solvent. *Macromolecules* **1991**, *24*, 2385-2390.

[54] Mao, G.; Ober, C. K. Block copolymers containing liquid crystalline segments. *Acta Polym.* **1997**, *48*, 405-422.

[55] Park, C.; Yoon, J.; Thomas, E. L. Enabling nanotechnology with self assembled block copolymer patterns. *Polymer* **2003**, *44*, 6725-6760.

[56] Muthukumar, M.; Ober, C. K.; Thomas, E. L. Competing Interactions and Levels of Ordering in Self-Organizing Polymeric Materials. *Science* **1997**, *277*, 1225-1232.

[57] Sanger, J.; Gronski, W.; Leist, H.; Wiesner, U. Preparation of a liquid single-crystal triblock copolymer by shear. *Macromolecules* **1997**, *30*, 7621-7623.

[58] Anthamatten, M.; Wu, J.-S.; Hammond, P. T. Direct Observation of a Smectic Bilayer Microstructure in Side-Chain Liquid Crystalline Diblock Copolymers. *Macromolecules* **2001**, *34*, 8574-8579.

[59] Sanger, J.; Gronski, W.; Maas, S.; Stuhn, B.; Heck, B. Structural transition in a nematic LC block copolymer induced by the transition to the LC phase. *Macromolecules* **1997**, *30*, 6783-6787.

[60] Anthamatten, M.; Zheng, W. Y.; Hammond, P. T. A Morphological Study of Well-Defined Smectic Side-Chain LC Block Copolymers. *Macromolecules* **1999**, *32*, 4838-4848.

[61] Hamley, I. W.; Castelletto, V.; Lu, Z. B.; Imrie, C. T.; Itoh, T.; Al-Hussein, M. Interplay between Smectic Ordering and Microphase Separation in a Series of Side-Group Liquid-Crystal Block Copolymers. *Macromolecules* **2004**, *37*, 4798-4807.

[62] Zheng, W. Y.; Hammond, P. T. Phase Behavior of New Side Chain Smectic C* Liquid Crystalline Block Copolymers. *Macromolecules* **1998**, *31*, 711-721.

[63] Hamley, I. W.; Fairclough, J. P. A.; Ryan, A. J.; Ryu, C. Y.; Lodge, T. P.; Gleeson, A. J.; Pedersen, J. S. Micellar Ordering in Concentrated Solutions of Di- and Triblock Copolymers in a Slightly Selective Solvent. *Macromolecules* **1998**, *31*, 1188-1196.

[64] Hanley, K. J.; Lodge, T. P.; Huang, C.-I. Phase Behavior of a Block Copolymer in Solvents of Varying Selectivity. *Macromolecules* **2000**, *33*, 5918-5931.

[65] Lai, C.; Russel, W. B.; Register, R. A. Phase Behavior of Styrene-Isoprene Diblock Copolymers in Strongly Selective Solvents. *Macromolecules* **2002**, *35*, 841-849.

[66] Lodge, T. P.; Hanley, K. J.; Pudil, B.; Alahapperuma, V. Phase Behavior of Block Copolymers in a Neutral Solvent. *Macromolecules* **2003**, *36*, 816-822.

[67] Lodge, T. P.; Pudil, B.; Hanley, K. J. The Full Phase Behavior for Block Copolymers in Solvents of Varying Selectivity. *Macromolecules* **2002**, *35*, 4707-4717.

[68] Lodge, T. P.; Xu, X.; Ryu, C. Y.; Hamley, I. W.; Fairclough, J. P. A.; Ryan, A. J.; Pedersen, J. S. Structure and Dynamics of Concentrated Solutions of Asymmetric Block Copolymers in Slightly Selective Solvents. *Macromolecules* **1996**, *29*, 5955-5964.

[69] McConnell, G. A.; Gast, A. P. Melting of Ordered Arrays and Shape Transitions in Highly Concentrated Diblock Copolymers Solutions. *Macromolecules* **1997**, *30*, 435-444.

[70] Lodge, T. P.; Blazey, M. A.; Liu, Z. Asymmetric block copolymers in neutral good solvents: self-diffusion through the ordering transition. *Macromol. Chem. Phys.* **1997**, *198*, 983-995.

[71] Walther, M.; Bohnert, R.; Derow, S.; Finkelmann, H. Structure formation of liquid-crystalline isotropic AB block copolymers in nematic solvents. *Macromol. Rapid Commun.* **1995**, *16*, 621-629.

[72] Walther, M.; Faulhammer, H.; Finkelmann, H. On the thread-like morphology of LC/I block copolymers in nematic solvents. *Macromol. Chem. Phys.* **1998**, *199*, 223-237.

[73] Walther, M.; Finkelmann, H. Formation of a transient periodic stripe domain pattern in nematic AB block copolymer solution during photo-induced director reorientation. *Macromol. Rapid Commun.* **1998**, *19*, 145-148.

[74] Kempe, M. D.; Verduzco, R.; Scruggs, N. R.; Kornfield, J. A. Rheological study of structural transitions in triblock copolymers in a liquid crystal solvent. *Soft Matter* **2006**, *2*, 422-431.

[75] Verduzco, R.; Meng, G.; Kornfield, J. A.; Meyer, R. B. Buckling instability in liquid crystalline physical gels. *Phys. Rev. Lett.* **2006**, *96*, 147802.

[76] Khoo, I.-C.; Wu, S. T. *Optics and Nonlinear Optics of Liquid Crystals*, World Scientific: Singapore, 1993.

[77] Skarp, K.; Lagerwall, S. T.; Stebler, B. Measurements of hydrodynamic parameters for nematic 5CB. *Mol. Cryst. Liq. Cryst.* **1980**, *60*, 215-236.

[78] Van Horn, B. L.; Winter, H. H. Analysis of the conoscopic measurement for uniaxial liquid-crystal tilt angles. *Appl. Opt.* **2001**, *40*, 2089-2094.

[79] Bloss, F. D. *Optical Crystallography*, Mineralogical Society of America: Washington, D.C., 1999.

Chapter 2

USING THE "SWITCHABLE" QUALITY OF A LIQUID CRYSTAL SOLVENT TO MEDIATE SEGREGATION BETWEEN COIL AND LIQUID CRYSTALLINE HOMOPOLYMERS

2.1 Introduction..22
2.2 Experimental..24
2.3 Results..25
2.4 Discussion..26
2.5 Conclusions..27
2.6 Tables..29
2.7 Figures..30
2.8 References..34

Reproduced in part with permission from Scruggs, Kornfield, and Lal, *Macromolecules* **2006,** 39, 3921-3926. Copyright 2006 American Chemical Society.

2.1 Introduction

The thermodynamics governing phase behavior in polymer solutions is strikingly different from that of regular, small-molecule solutions. The entropy of mixing that favors miscibility between small-molecule species is substantially reduced by the covalent connectivity of monomers in a polymer chain. The usually unfavorable enthalpy of mixing two species is, therefore, more difficult to overcome when one of them is a polymer. The competition between entropy and enthalpy is summarized by the Flory-Huggins equation[1] which expresses the free energy of mixing, ΔF_{mix}, as a function of the polymer's volume fraction, ϕ, and degree of polymerization, N, as well as an interaction parameter, χ, that quantifies the enthalpy of mixing:

$$\frac{\Delta F_{mix}}{kT} = \frac{\phi}{N}\ln\phi + (1-\phi)\ln(1-\phi) + \chi\phi(1-\phi), \tag{2.1}$$

where k is Boltzmann's constant and T is the temperature. The Flory interaction parameter is usually positive and has been found empirically to depend on temperature according to

$$\chi(T) = A + \frac{B}{T}, \tag{2.2}$$

where A and B are constants.[1]

Small-molecule nematic liquid crystals (LCs) are particularly interesting as solvents for polymers because they can undergo a first-order transition between ordered (nematic) and disordered (isotropic) fluid phases, and the χ parameter changes discontinuously at the nematic-isotropic transition temperature (T_{NI}). Below T_{NI} the entropic penalty of dissolving a random-coil polymer in ordered solvent is lumped into the χ parameter, which grows with the solvent's degree of orientational order, but above T_{NI} this penalty is lost and the LC behaves like a conventional solvent.[2] If, however, the polymer also has liquid crystalline character, χ may switch from being positive to negative when the solvent becomes isotropic. In either case, the miscibility of a polymer with an LC solvent may change drastically in the small temperature window around T_{NI}.

Rich thermodynamics result from dissolving a coil polymer and a side-group liquid crystal polymer (SGLCP) together in an LC solvent. The ternary phase behavior of such a polymer-polymer-solvent system is determined by the entropy of mixing balanced with polymer-solvent interactions (characterized by χ_{AS} and χ_{BS}) as well as polymer-polymer interactions (characterized by χ_{AB}).[3-7] In a nematic solvent, all three χ parameters change discontinuously at T_{NI} and the solution's phase behavior is altered accordingly.

In this chapter, the binary phase behavior of a random-coil polymer (polystyrene, PS) in an LC solvent (4-pentyl-4′-cyanobiphenyl, 5CB) is compared to solutions of an SGLCP in

5CB in order to correlate polymer properties with changes in polymer miscibility that take place at T_{NI}. These results elucidate the physics behind the rich phase behavior of ternary solutions of PS, SGLCP, and 5CB that has consequences for solutions of coil-SGLCP block copolymers discussed in later chapters.

2.2 Experimental

2.2.1 Materials

A side-group liquid crystal homopolymer, 490HSiCB4, was synthesized and characterized according to the methods described in Appendix A (Figure 2.1). A 63 kg/mol 1,2-polybutadiene (PB) prepolymer was synthesized via living anionic polymerization by Steven Smith of Proctor and Gamble, Inc. (see Appendix A for characterization). After attaching the mesogenic side-groups, the polymer's molecular weight (M_n) is 489 kg/mol and 97 mol % of the monomers have SiCB4 mesogens attached. Of the remaining 4 mol %, 1 mol % of the monomers are residual 1,2-butadiene and 3 mol % are unreactive 1,4-butadiene. The polydispersity (PDI = M_w / M_n) is 1.48 (Table 2.1). Monodisperse polystyrene (PS) homopolymer with M_n = 44 kg/mol was purchased and used as received from Aldrich. The nematic LC solvent 4-pentyl-4′-cyanobiphenyl (5CB) was used as received from TCI America.

2.2.2 Methods

Ternary mixtures of 490HSiCB4 homopolymer and PS homopolymer in 5CB were made by combining the three components in controlled quantities for a total mass of approximately 50 mg then dissolving them together in ~100 μL of tetrahydrofuran (THF). Samples were mixed for at least an hour to ensure complete dissolution of all three components. A small drop of the THF solution was placed in the shallow well of an indented microscope slide and the THF was evaporated away at elevated temperature (~100 ^{o}C). Slides were examined using a Zeiss Universal optical microscope equipped with a Mettler FP82 hot stage and removable polarizers. Each sample was first heated from room temperature at a rate of 2 ^{o}C/min to observe the nematic to isotropic phase transition; the temperature at which the colorful, birefringent texture viewed between crossed polarizers (Figure 2.2a) disappeared was recorded as the isotropization point (T_{NI}). Next, the polarizers were removed and the sample was heated further until droplets characteristic of two-phase, isotropic/isotropic coexistence (Figure 2.2b) were no longer observed (Figure 2.2c). Then, the sample was cooled at a rate of 10 ^{o}C/min and the temperature at which droplets reappeared was recorded as a nominal upper critical solution temperature (UCST). This measurement was repeated five times, examining a different area on the slide each time, and the results averaged. To set a bound on the subcooling required for observable drops to form on cooling, several samples were raised to 5 °C above the nominal UCST. Consistently, a single phase formed over time. Therefore, the true UCST lies within 5 °C of the nominal one. Since the changes in UCST with solution composition were very large, this uncertainty did not affect the conclusions of this study.

2.3 Results

Binary solutions of 490HSiCB4 with 5CB were observed to be single phase both above and below T_{NI} (Figure 2.3a). Binary solutions of PS with 5CB exhibit a small biphasic window in the isotropic phase of 7.4 ^{o}C or less (Figure 2.3b) and are single-phase above an upper critical solution temperature (UCST). This result is consistent with previously established phase diagrams of PS with 5CB,[8, 9] which found the two to be miscible above 40 ^{o}C, provided the concentration of PS is less than 50 wt %.

Ternary mixtures of PS, 490HSiCB4, and 5CB were observed to phase separate below T_{NI} into coexisting nematic and isotropic phases at all compositions tested (up to 20 wt %). The measured isotropization points in ternary mixtures (i.e., transition from N + I to I + I biphase or N + I to I) were found to be within 3.5 ^{o}C of the bulk T_{NI} of 5CB (35 ^{o}C), indicating that the nematic phase contains little or no isotropic diluent and partitioning of the polymers into an SGLCP-rich, nematic phase and a PS-rich, isotropic phase must therefore be nearly complete. Above T_{NI} wide miscibility gaps were observed up to the UCST.

The UCST of ternary mixtures of PS, 490HSiCB4, and isotropic 5CB was found to be highly sensitive to the concentrations of the two polymers and an effective solubility limit was quickly reached with increasing concentrations (Figure 2.4). For example, holding the concentration of 490HSiCB4 fixed at 4.5 wt %, the addition of 0.5 wt % PS opens up a 14 ^{o}C miscibility gap (UCST = 49 ^{o}C) which expands to 97 ^{o}C (UCST = 132 ^{o}C) when the concentration of PS is 6 wt %. When the overall concentration of polymer, PS and 490HSiCB4 combined, exceeds approximately 10 wt %, the UCST cannot be reached before the sample thermally degrades, representing an effective solubility limit. This steep increase in UCST with increasing polymer concentration is surprising because each of the two polymers dissolves in all proportions tested in isotropic 5CB alone.

2.4 Discussion

Binary and ternary mixtures of 490HSiCB4 and PS dissolved in 5CB show that nematic 5CB is strongly selective solvent for the SGLCP. As previously reported by Hori et al.,[9] PS is insoluble in nematic 5CB; mixtures phase separate into an isotropic, PS-rich phase and a nematic phase nearly devoid of PS altogether. On the other hand, 490HSiCB4 is soluble in nematic 5CB at all concentrations tested (up to 20 wt %). The liquid crystalline order of the nematic solvent imposes a large entropic penalty to solvation of a random coil polymer (e.g. PS),[9-11] but the chemically similar side-groups and liquid crystalline nature of the SGLCP facilitate miscibility with the nematic solvent.[2]

The observation of large miscibility gaps in ternary mixtures of PS, 490HSiCB4, and 5CB was surprising because single-phase solutions are easily achieved in binary mixtures of 5CB with either polymer alone. One reason for the polymers' poor solubility in ternary solutions is that unfavorable interactions between the polymers themselves (a large contribution of χ_{AB}) increase the free energy of mixing.[7] However, this effect is weak in dilute solutions where polymer-polymer interactions are effectively screened by solvent. Small-angle neutron scattering experiments presented in Chapter 5 demonstrate that 5 wt % solutions of similar SGLCPs (310HSiCB4 and 780HSiCB4) are in the semidilute regime, but when the concentration of 490HSiCB4 is substantially lower the polymer chains should be dilute and non-interacting. The overlap concentration of PS is calculated[12] to be approximately 7 wt % at 35 °C in cyclohexane[13] which represents a lower bound on the dilute regime since 5CB is not as good a solvent for PS as cyclohexane. A portion of the measured phase diagram is, therefore, well within a regime where the free energy contribution of inter-polymer interaction (χ_{AB}) should be small.

Besides polymer-polymer interactions, polymer-solvent interactions also contribute to the system's thermodynamics, as described by the Patterson[6]-Prausnitz[3] treatment of the Scott[4]-Tompa[5] theory for ternary polymer-polymer solutions. Patterson and Prausnitz found that any differential preference of the solvent for one polymer over the other ($\chi_{AS} \neq \chi_{BS}$), even if that preference is small, can induce phase separation. Furthermore, the effect is exacerbated when the molecular weight difference between the polymers is large. The asymmetric solvent effect is, therefore, predicted to play a substantial role in the thermodynamics governing phase separation of solutions of PS and 490HSiCB4 in 5CB: the chemical structure of the two polymers is sufficiently different to cause an appreciable difference in polymer-solvent interactions between the two, and the molecular weight ratio of PS to HSiCB4 is approximately 1:10. Isotropic 5CB is, therefore, not a neutral solvent ($\chi_{AS} = \chi_{BS}$), but is better classified as "slightly selective" ($|\chi_{AS} - \chi_{BS}| << \chi_{AS} \approx \chi_{BS}$).

Compared to conventional solvents, 5CB is unique in its ability to undergo a discontinuous, thermally-induced change in its miscibility with polymers. Solvent quality is typically a monotonic function of temperature,[1] but the first-order nematic-isotropic phase transition results in an abrupt change so that increasing temperature less than 1 °C can cause an initially insoluble polymer to become miscible with 5CB. This phenomenon is termed "switchable solvent quality."

2.5 Conclusions

The "switchable" solvent quality of an LC solvent results in rich ternary solution thermodynamics. Unfavorable polymer-polymer interactions work together with strong solvent selectivity to drive macroscopic phase separation in the nematic phase. In the isotropic phase, favorable interactions between the solvent and both polymers are balanced against polymer-polymer incompatibility and the asymmetric solvent effect, resulting in phase behavior that is strikingly sensitive to changes in the solution's composition. Modulation between the two regimes is achieved with temperature changes of less than 1 °C.

The unique phase behavior of homopolymer solutions in an LC solvent suggests that the driving force for self-assembly of a coil-SGLCP block copolymer could also be modulated by the solvent's transition between the nematic and isotropic phases. Below T_{NI} the solvent's orientational order would drive the block copolymer to self-assemble into a structure that segregates the coil-block from the LC host. Above T_{NI} this driving force would be lost, but self-assembly could still occur as a result of the same thermodynamic interactions that drive phase separation in the isotropic homopolymer solutions. This topic is explored in detail in Chapter 3.

2.6 Tables

Table 2.1 Molecular weight, conversion, and polydispersity of the side-group liquid crystal homopolymer. Details of characterization are presented in Appendix A.

Name	M_n [kg/mol]	Mole Fraction 1,2 PB	Mole Fraction 1,4 PB	Mole Fraction LC	PDI[a]
490HSiCB4	489	0.01	0.03	0.96	1.48

[a] PDI = Polydispersity Index (M_w/M_n)

2.7 Figures

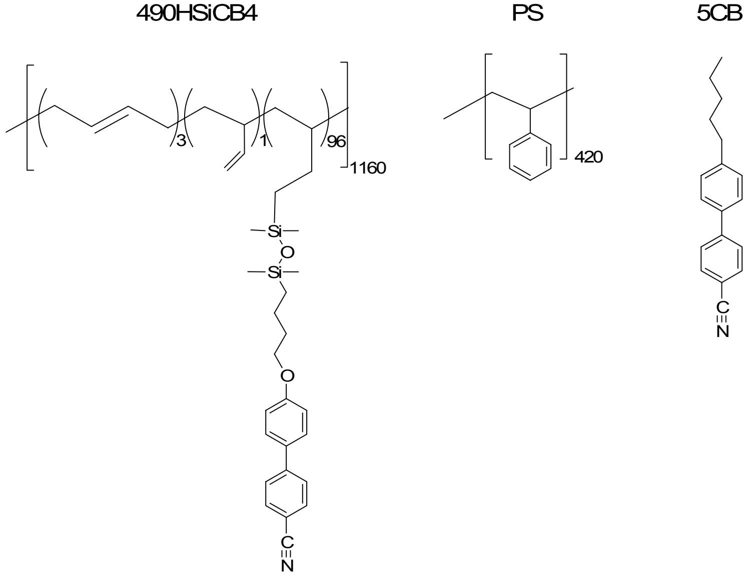

Figure 2.1 Chemical structures of side-group liquid crystal polymer (490HSiCB4), polystyrene (PS), and nematic liquid crystal solvent (5CB). The SGLCP's name is derived from its molecular weight (489 kg/mol), the letter "H" to indicate a homopolymer, and "SiCB4" to indicate end-on attachment of the mesogens. In addition to monomers having an attached mesogen, the polymer also contains ~ 1 mol % each of residual 1,2- and 1,4-butadiene monomers. Its properties are summarized in Table 2.1 and the details of its synthesis and characterization are presented in Appendix A.

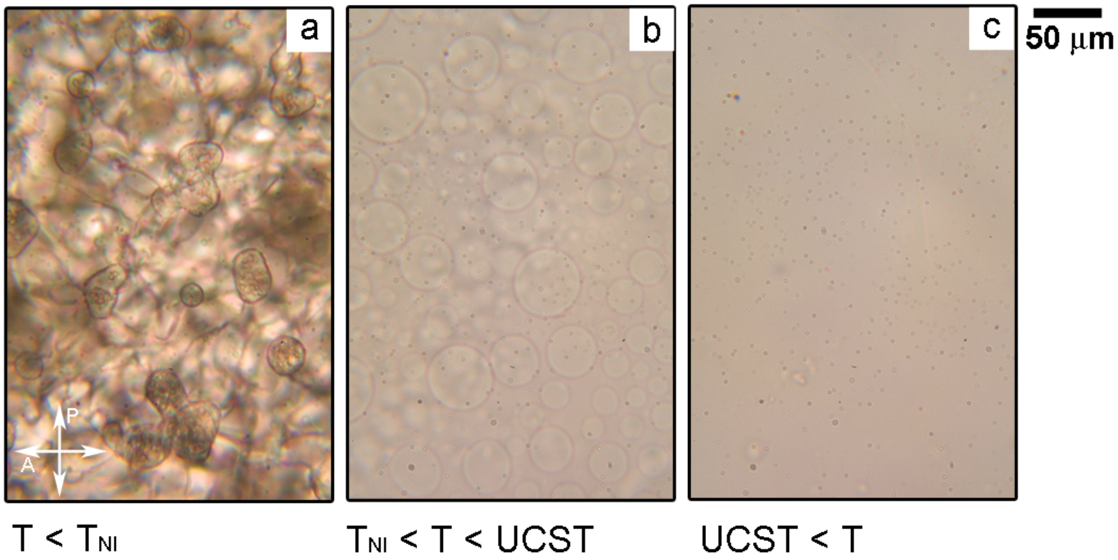

Figure 2.2 Optical micrographs typical of ternary blends of PS, 490HSiCB4, and 5CB at temperatures (a) below T_{NI}, (b) between T_{NI} and the UCST, and (c) above UCST. The sample is imaged between crossed polarizers in the nematic phase ($T < T_{NI}$). These particular micrographs are of 2.25 wt % PS and 4.57 wt % 490HSiCB4 in 5CB at (a) 34 °C, (b) 70 °C, and (c) 90 °C.

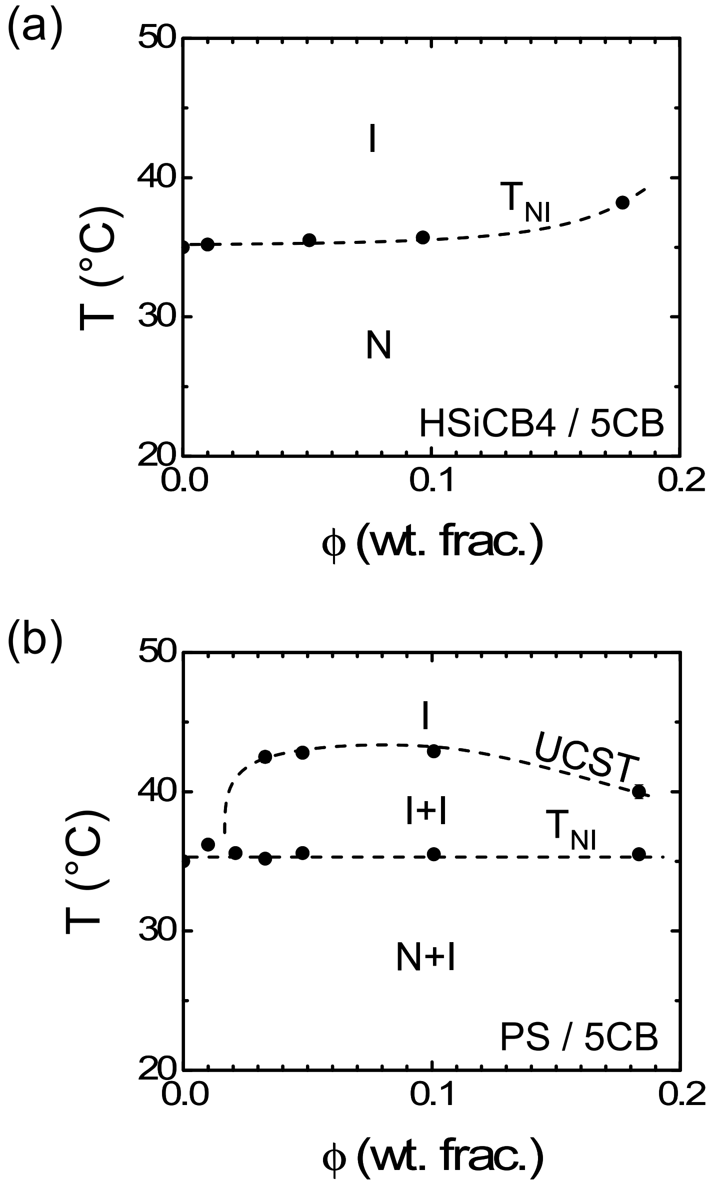

Figure 2.3 Partial binary phase diagrams of (a) 490HSiCB4 homopolymer in 5CB and (b) polystyrene homopolymer with 5CB. Dashed lines are drawn to guide the eye toward plausible phase boundaries. The letters "N" and "I" indicate a single nematic or isotropic phase, respectively. "I+I" indicates two coexisting isotropic phases and "N+I" indicates coexisting nematic and isotropic phases.

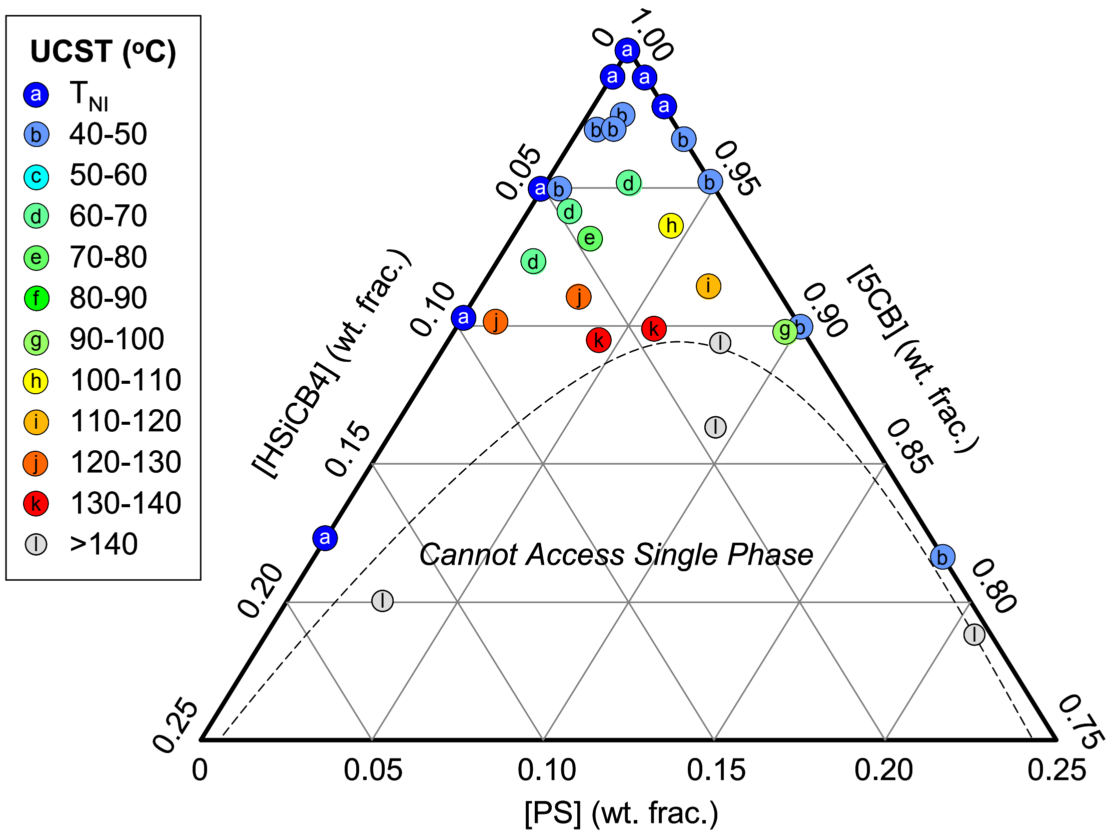

Figure 2.4 Partial ternary phase diagram of PS (44 kg/mol), 490HSiCB4, and isotropic 5CB determined from optical microscopy. The shading and letter of each point expresses the upper critical solution temperature (UCST) at which a single-phase solution is obtained. A UCST equal to T_{NI} means the solution became single-phase immediately upon transitioning to the isotropic phase. A UCST > 140 °C means a single phase was inaccessible because the mixture began to decompose. The dashed line is drawn to guide the eye to the region where a single-phase solution cannot be reached.

2.8 References

[1] Rubinstein, M.; Colby, R. H. *Polymer Physics*, 1st ed; Oxford University Press: New York, 2003.

[2] Brochard, F. Solutions of flexible polymers in a nematic liquid. *C. R. Acad. Sc. Paris* **1979**, *289*, 229-232.

[3] Hsu, C. C.; Prausnitz, J. M. Thermodynamics of Polymer Compatibility in Ternary Systems. *Macromolecules* **1974**, *7*, 320-324.

[4] Scott, R. L. The Thermodynamics of High Polymer Solutions. V. Phase Equilibria in the Ternary System: Polymer 1- Polymer 2- Solvent. *J. Chem. Phys.* **1949**, *17*, 279-284.

[5] Tompa, H. Phase Relationships in Polymer Solutions. *Trans. Faraday Soc.* **1949**, *45*, 1142-1152.

[6] Zeman, L.; Patterson, D. Effect of the Solvent on Polymer Incompatibility in Solution. *Macromolecules* **1972**, *5*, 513-516.

[7] Olabisi, O.; Robeson, L. M.; Shaw, M. T. *Polymer-Polymer Miscibility*, Academic Press, Inc.: San Diego, 1979.

[8] Hakemi, H. Elastic constants in dilute poly(styrene)/nematic liquid crystal solutions - effects of concentration and molecular weight. *Polymer* **1999**, *40*, 4099-4103.

[9] Hori, H.; Urakawa, O.; Adachi, K. Dielectric Relaxation in Phase-Segregated Mixtures of Polystyrene and Liquid Crystal 5CB. *Macromolecules* **2004**, *37*, 1583-1590.

[10] Benmouna, F.; Daoudi, A.; Roussel, F.; Buisine, J.-M.; Coqueret, X.; Maschke, U. Equilibrium Phase Diagram of Polystyrene and 8CB. *J. Polym. Sci., Part B: Polym. Phys.* **1999**, *37*, 1841-1848.

[11] Gogibus, N.; Maschke, U.; Benmouna, F.; Ewen, B.; Coqueret, X.; Benmouna, M. Phase Diagrams of Poly(dimethylsiloxane) and 5CB Blends. *J. Polym. Sci., Part B: Polym. Phys.* **2001**, *39*, 581-588.

[12] Noda, I.; Kato, N.; Kitano, T.; Nagasaw, M. Thermodynamics of Moderately Concentrated Solutions of Linear Polymers. *Macromolecules* **1981**, *14*, 668-676.

[13] Brandup, J.; Immergut, E. H.; Grulke, E. A., eds. *Polymer Handbook*. 4th ed. 1999, Wiley: New York.

Chapter 3

SELF-ASSEMBLY OF COIL-LIQUID CRYSTALLINE DIBLOCK COPOLYMERS IN A SOLVENT OF “SWITCHABLE” QUALITY: STRUCTURE AND INTERACTIONS MEASURED BY SANS AND RHEOMETRY

3.1 Introduction..36

3.2 Experimental..37

3.3 Results..41

3.4 Discussion..47

3.5 Conclusions..55

3.6 Tables..57

3.7 Figures..59

3.8 References..87

Reproduced in part with permission from Scruggs, Kornfield, and Lal, *Macromolecules* **2006,** 39, 3921-3926. Copyright 2006 American Chemical Society.

Rafael Verduzco contributed to the experiments discussed in this chapter. He synthesized and characterized the side-on polymers (names ending with “BB”). He and I traveled together to Argonne National Lab where we shared the responsibility of performing the neutron scattering experiments. He also performed rheometry on solutions of side-on polymers. Zuleikha Kurji assisted us in performing neutron scattering experiments. We

are grateful to the Macromolecular Complex Systems group at Oak Ridge National Laboratory's Center for Nanophase Material Sciences (CNMS), especially David Uhrig, for synthesizing some of our diblock prepolymers. We also thank Jyotsana Lal and Ed Lang at Argonne's Intense Pulsed Neutron Source for their help with neutron scattering experiments.

3.1 Introduction

Microphase separation in diblock copolymer melts is a well-understood phenomenon that allows access to a wide range of morphologies that find application in nanotechnologies, as reviewed by Park, Yoon, and Thomas.[1] The symmetry and length scale of the ordered state are controlled by selection of the chemical structure, connectivity, and relative lengths of the component blocks.[2] Binary thermodynamic interactions between the polymer blocks ultimately determine the block copolymer's nanostructure in the melt. In solution, thermodynamic interactions with a third component modulate the self-assembled structure: a fixed block copolymer at a fixed concentration can adopt various morphologies depending on the solvent.[3-10] Block copolymers in selective solvents are used as rheology modifiers and drug delivery systems, for example, and are also of fundamental interest because of the rich thermodynamics governing their self-assembly.

The choice of solvent heavily influences the equilibrium microstructure of AB diblock copolymer micelles.[3, 5-8] Partitioning of the solvent between the microdomains rich in block A and those rich in block B is referred to as the solvent's "selectivity" and is determined by thermodynamic interaction parameters between the solvent (S) and each polymer, χ_{AS} and χ_{BS}.[11-15] In the limit of strong selectivity towards A ($\chi_{BS} >> \chi_{AS}$), diblock copolymers form micelles with cores composed of B almost completely devoid of solvent. In contrast, a neutral, or non-selective, solvent partitions between core and corona. In the former case, dense-core micelles are formed having stronger inter-micelle interaction potentials than the highly swollen, soft micelles afforded in the latter case.[16, 17]

When the solvent is a small-molecule thermotropic liquid crystal (LC) the phase behavior of a dissolved block copolymer is enriched by the discontinuous change in quality at the LC phase transitions. The simplest example is the transition from the nematic to the isotropic phase. The orientational order of the LC in the nematic phase presents a large entropic penalty to solvation of a random coil polymer, but in the isotropic phase the solvent's spherical symmetry imposes no such solubility constraints.[18, 19] In contrast to a random coil polymer, a side-group liquid crystalline polymer (SGLCP) can undergo the change in orientational order with the LC solvent, making it soluble in both the nematic and isotropic phases. A coil-SGLCP block copolymer in a LC solvent can switch from being dissolved in a strongly selective solvent to being dissolved in a good solvent for both blocks when the first-order transition from the nematic to isotropic phase takes place. Such abrupt changes in solvent quality do not occur in non-LC solvents, and we term the phenomenon "switchable solvent quality." We demonstrate that the jump in solvent quality indeed produces an abrupt change in the self-assembly of block copolymers, specifically a change in micelle structure of coil-SGLCP diblocks in solution. We infer the driving force for block copolymer self-assembly from the phase behavior of ternary homopolymer solutions and further demonstrate that exceptional sensitivity to temperature and concentration allows the dominant driving force for block copolymer self-assembly to be modulated with small changes to these parameters.

3.2 Experimental

3.2.1 Materials

A series of diblock copolymers was synthesized having a random coil polymer block (polystyrene, PS) and a side-group liquid crystal polymer (SGLCP) block (Figure 3.1). Starting with poly[styrene-*b*-1,2-butadiene], the reactive 1,2-butadiene monomers were functionalized with cyanobiphenyl-based mesogenic side groups by methods described in Appendix A. These polymers are referred to as "end-on" SGLCPs because the mesogenic group is attached along its long axis, perpendicular to the polymer backbone. Their properties are summarized in Table 3.1 and details of their characterization are given in

Appendix A. Using the same set of PS-PB prepolymers (Appendix A), a series of SGLCPs bearing “side-on” mesogens, attached with the long axis parallel to the polymer backbone, was synthesized by Rafael Verduzco.[20]

Prepolymers were obtained from two different sources; the details of characterization are given in Appendix A. A series of four PS-PB diblock copolymers having approximately equally sized PB blocks and variably sized PS blocks were synthesized via living anionic polymerization by David Uhrig at Oak Ridge National Laboratory’s Center for Nanophase Material Sciences (CNMS). The molecular weight (M_n) of the PB block is approximately 55 kg/mol and the molecular weight of the PS block ranges from 40 to 120 kg/mol. The PB block contains greater than 95 mol % 1,2-butadiene monomers, the remainder being unreactive 1,4-butadiene. These prepolymers were used to synthesize the first four polymers listed in Table 3.1. Other PS-PB prepolymers were purchased from Polymer Source (Montreal, Quebec) and used to synthesize the remaining three polymers listed in Table 3.1. These diblocks are also synthesized by living anionic polymerization and the PB block is composed of 10 - 20 mol % 1,4-butadiene monomers.

The sizes of the PS and PB blocks were chosen to yield a series of PS-SGLCP diblock copolymers that would access a variety of polymer compositions and overall molecular weights, changing only one variable at a time (Figure 3.4). The four polymers synthesized at the CNMS give a series of variable composition, but approximately equal molecular weight. Two of the polymers purchased from Polymer Source closely match the composition of the largest CNMS polymer, giving a series of different molecular weights.

In addition to PS-SGLCP diblock copolymers, end-on and side-on SGLCP homopolymers (Figure 3.2) were synthesized from an anionically polymerized PB prepolymer purchased from Polymer Source. The prepolymer has M_n = 47.5 kg/mol and the properties of the resulting SGLCPs are summarized in Table 3.2. Finally, a coil-SGLCP diblock copolymer with a poly(methyl methacrylate) (PMMA) coil block (Figure 3.3) was synthesized, starting from a poly[(methyl methacrylate)-*b*-1,2-butadiene] prepolymer. This prepolymer was also purchased from Polymer Source and the properties of the PMMA-SGLCP diblock are summarized in Table 3.3. A PS-SGLCP diblock with similar coil block content and total molecular weight was synthesized from a PS-PB prepolymer also purchased from Polymer Source. The details of the characterization of all these polymers and their precursors are given in Appendix A.

Solutions of SGLCP homopolymers and diblock copolymers in liquid crystal solvent were prepared by dissolving a polymer together with the nematic LC 4-pentyl-4′-cyanobiphenyl (5CB) in dichloromethane, then evaporating the dichloromethane under a stream of air followed by drying in vacuum for at least 18 hours.

3.2.2 Methods

Small-angle neutron scattering (SANS) experiments were performed on the Small-Angle Scattering Instrument (SASI) at Argonne National Laboratory's Intense Pulsed Neutron Source (IPNS). The instrument records the intensity of neutrons scattered from a sample at various scattering vectors, $q = 4\pi/\lambda \sin(\theta/2)$, between approximately 0.007 and 2 $Å^{-1}$. Neutrons at the IPNS are generated by spallation and are therefore polychromatic. The wavelength, λ, is calculated from a neutron's time of flight to a detector at an angle, θ, to the sample. The raw intensity scattered onto a two-dimensional array of detectors is converted to the two-dimensional scattered intensity in *q*-space by computers at the IPNS. An advantage of time-of-flight SANS at a spallation source is that the instrument's entire *q* range is accessed in a single experiment without having to change the sample-detector distance.

Samples were prepared by dissolving diblock copolymers in a perdeuterated liquid crystal solvent. Since the coherent neutron scattering length of hydrogen ($b_H = -3.74 \times 10^{-5}$ Å) is very different from that of deuterium ($b_D = 6.67 \times 10^{-5}$ Å), the perdeuterated solvent provides scattering contrast without significantly altering the solvent's other physical properties. Perdeuterated 4-penyl-4'-cyanobiphenyl (d_{19}5CB) was synthesized according to methods described in Appendix B. The nematic-isotropic transition temperature (T_{NI}) of d_{19}5CB is approximately 3 °C lower than that of hydrogenated 5CB.[21]

Diblock copolymer solutions were contained in cells consisting of circular quartz windows spaced apart by a metal or quartz ring either 0.5 or 1.0 mm thick. In most cases the samples were simply loaded in the polydomain state; no effort was made to achieve uniform alignment of the liquid crystal director. During the scattering experiments the cells were held in a heated aluminum block where the temperature was stable within approximately 0.1 °C. At least fifteen minutes of temperature equilibration was allowed prior to collecting data. Samples were typically irradiated for one hour and the two-dimensional scattering pattern was circularly averaged to yield data in the form of intensity versus q.

Rheometry was performed on solutions of diblock copolymers dissolved in 5CB using a TA Instruments ARES-RFS fluids rheometer with a dynamic range of 0.001 to 200 rad/s. Approximately 200 mg of solution was held in a titanium cone-and-plate tool 25 mm in diameter. The temperature was controlled with the rheometer's built-in Peltier plate and was stable to within 0.1 °C. Frequency sweeps were performed in the linear regime at temperatures ranging from 25 °C to at least 60 °C, traversing small temperature increments near the isotropization point. Temperature ramps between 25 and 60 °C were performed in the linear regime at heating/cooling rates of 1, 5, and 10 °C/min. Prior to beginning each experiment, the sample's thermal history was erased by heating it to 60 °C for at least 5 minutes, then annealing at the desired temperature for at least 5 minutes.

The transition temperatures of diblock copolymer solutions were measured by polarized optical microscopy (POM). A drop of solution was placed on a microscope slide and observed between crossed polarizers in a Zeiss Universal stereomicroscope with temperature controlled by a Mettler FP82 hot stage. The temperature at which the colorful, birefringence texture began to disappear was recorded as the isotropization point (T_{NI}). Two temperatures were recorded for samples that became biphasic during the transition: the temperature at which the first black spots appear marks the beginning of the biphasic region and the temperature at which the last colorful spots disappear marks the end.

3.3 Results

3.3.1 Neutron Scattering at High *q*

The scattering patterns from diblock copolymer solutions all have a few basic features in common (Figure 3.5 and Figure 3.6). The scattered intensity is highest at low q and drops precipitously as q increases, until it merges with $I(q)$ of the equivalent SGLCP homopolymer for $q > \sim 0.06$ Å^{-1}. At large q, q-independent, incoherent background scattering becomes dominant beyond $q \approx 0.3 - 0.5$ Å^{-1}. The magnitude of the scattered intensity at low q is highly sensitive to changes in temperature (Figure 3.5). For example, the maximum intensity, I_{max}, for a 5 wt % 320(120)ABSiCB4 solution drops an order of magnitude as the temperature is raised from 25 °C to 40 °C (Figure 3.5a). A similar decrease of I_{max} is observed as 10 wt % 320(120)ABSiCB4 is heated from 25 °C to 50 °C and then drops down to the level seen for the equivalent SGLCP homopolymer as T increases to 60 °C (Figure 3.5b). At high q ($q > \sim 0.06$ Å^{-1}), however, $I(q)$ is insensitive to temperature (Figure 3.5). The high-q scattering is also unaffected by changing the size of the polystyrene block (Figure 3.6). Scattering patterns from diblocks having approximately matched SGLCP blocks and PS blocks varying in size from 40 to 120 kg/mol all overlap at q greater than approximately 0.06 Å^{-1} (Figure 3.6).

Since the high-q scattering is completely described by the scattering of SGLCP homopolymers (Figure 3.5 and Figure 3.6), this portion of the SANS patterns is attributed to the monomer-level structure of SGLCP chains. At low values of q the self-assembled structure dominates the scattering and from here on the presentation of SANS patterns will be limited to this regime.

3.3.2 Effects of PS Block Size on Structure: Temperature Dependence of SANS and Rheometry

The diblock copolymers 470(40)ABSiCB4, 390(60)ABSiCB4, 420(80)ABSiCB4, and 320(120)ABSiCB4 comprise a series with approximately constant total molecular weight (440 – 510 kg/mol) having increasing PS content from 8 and 23 wt % (Figure 3.4). The changes in the SANS patterns from these diblock solutions with temperature (Figure 3.7a-

Figure 3.14a) are correlated with the temperature dependence of the storage modulus, G' (Figure 3.7b-Figure 3.14b). The SANS patterns from 5 wt % solutions of all four polymers change shape within a small temperature window near T_{NI}, and three out of the four polymers have a large change in the maximum scattered intensity, I_{max}, near T_{NI} (Figure 3.7a-Figure 3.10a, inset). The storage modulus of each of these solutions drops from $G' \sim O(10^0 \text{ Pa})$ to $G' \sim O(10^{-2} \text{ Pa})$ within, at most, 5 °C of T_{NI} (Figure 3.7b-Figure 3.10b). The correlated changes in SANS and G' are similar to those observed at the order-disorder or order-order transition temperatures of non-LC diblock copolymers in isotropic solvents[3, 8].

The temperature at which the low q scattering decreases to the level seen in an analogous homopolymer solution increases with increasing PS block length, M_{PS}. In the case of the smallest PS block (M_{PS} = 40 kg/mol) this temperature is below T_{NI} (Figure 3.7a); for the next in the series (M_{PS} = 60 kg/mol), it is above T_{NI} (at 40 °C, $I(q)$ is similar to that of a homopolymer solution) (Figure 3.8a). Block copolymer segregation persists up to 40 °C for the case of PS block lengths greater than 60 kg/mol and the resulting scattering that remains at 40 °C is of higher intensity for the polymer with M_{PS} = 120 kg/mol (Figure 3.10a) than for the polymer with M_{PS} = 80 kg/mol (Figure 3.9a).

Similarly, the temperature at which G' drops below 1 Pa increases with increasing PS block length. For the diblock with M_{PS} = 40 kg/mol, G' falls to 1 Pa at T_{NI} – 0.4 °C (the subsequent rise and fall of G' results from the narrow biphasic temperature range of 5 wt % 470(40)ABSiCB4) (Figure 3.7b). When M_{PS} = 60 or 80 kg/mol, G' falls to 1 Pa at the end of the nematic-isotropic phase transition (35.4 and 36.6 °C, respectively) (Figure 3.8b and Figure 3.9b). For the longest PS block in the series (M_{PS} = 120 kg/mol), the decrease in G' with increasing temperature beyond T_{NI} is relatively gradual, reaching 1 Pa at a temperature distinctly greater than T_{NI} (Figure 3.10b). Within the nematic phase, increasing PS block length causes the temperature dependence of G' to change from softening (M_{PS} = 40 kg/mol) to stiffening (M_{PS} = 60, 80, and 120 kg/mol), and the steepness of stiffening with increasing temperature increases as the size of the PS block increases from 60 to 120 kg/mol (Figure 3.7b-Figure 3.10b).

Solutions of 10 wt % diblock copolymer (Figure 3.11-Figure 3.14) exhibit similar trends in SANS and rheology as the 5 wt % solutions. At high q, the scattered intensity is approximately two times greater in the 10 wt % as in their 5 wt % counterparts, as it should be for scattering arising from approximately the monomer-level structure. Interestingly, at small q, the 10 wt % solutions with $M_{PS} \leq 60$ kg/mol do *not* have greater intensity; indeed, when normalized by concentration, I_{max} / c is greater for the 5 wt % solutions in each pair. When $M_{PS} \geq 80$ kg/mol, I_{max} / c is approximately the same for 5 and 10 wt % solutions, as expected. The storage modulus of a 10 wt % solution is approximately ten times greater than its 5 wt % counterpart. Similar to 5 wt % solutions, G' increases with temperature in the nematic phase (except for the diblock with M_{PS} = 40 kg/mol) and decreases with temperature above T_{NI}. However, for $M_{PS} \geq 60$ kg/mol the decay of G' in the isotropic phase is much more gradual for 10 wt % solutions. Whereas G' of 5 wt % solutions fell approximately tenfold at T_{NI} for diblocks with M_{PS} = 60 or 80 kg/mol, the corresponding drop requires T > T_{NI} for the 10 wt % solutions (Figure 3.12b and Figure 3.13b). The largest PS block delays a comparable drop in G' to T_{NI} + 10 °C (Figure 3.14b).

3.3.3 Effects of Total Molecular Weight on Structure: Temperature Dependence of SANS and Rheometry

Together with 320(120)ABSiCB4, the diblock copolymers 210(60)ABSiCB4 and 580(190)ABSiCB4, synthesized from prepolymers purchased from Polymer Source, comprise a series with approximately constant PS content (~24 wt %) having total molecular weights of 270, 440, and 780 kg/mol (Figure 3.4). Similar to 5 wt % 320(120)ABSiCB4 (Figure 3.10a), scattering patterns from 5 wt % 210(60)ABSiCB4 (Figure 3.15a) change shape at T_{NI}; however, unlike 5 wt % 320(120)ABSiCB4 and solutions of other polymers derived from prepolymers provided by the CNMS, their maximum scattered intensities are insensitive to temperature. For the longest polymer in this series, neither the shape nor intensity change across T_{NI}. The magnitude of the storage modulus in the nematic phase increases with increasing molecular weight from $G' \sim O(10^0$ Pa) (Figure 3.10b and Figure 3.15b) to $G' \sim O(10^2$ Pa) (Figure 3.16b). The decay of G' above T_{NI} becomes increasingly gradual as the polymer molecular weight is increased. For the smallest polymer, 210(60)ABSiCB4, G' decays tenfold at T_{NI} (Figure 3.15b).

Increasing the molecular weight causes the tenfold decay of G' to shift to T_{NI} + 2.5 °C (Figure 3.10b), and for the largest polymer, 580(190)ABSiCB4, G' does not decay tenfold until T_{NI} + 16 °C (Figure 3.16b).

The same trends are observed in 10 wt % solutions (Figure 3.17, Figure 3.14, and Figure 3.18). The effect of increasing concentration on G' is similar to what was observed for diblocks with a series of different PS contents; doubling the concentration increases G' approximately tenfold and the decay of G' in the isotropic phase becomes more gradual. In the case of the largest polymer, G' decays so slowly that it changes less than four-fold over the entire temperature range (Figure 3.18b). When the concentration of 210(60)ABSiCB4 or 580(190)ABSiCB4 is increased to 20 wt % (Figure 3.19 and Figure 3.20), the storage modulus remains relatively constant throughout the entire temperature range studied (Figure 3.19b and Figure 3.20b). The value of I_{max} / c in 20 wt % solutions (Figure 3.19a and Figure 3.20a, inset) is lower than that of their 5 or 10 wt % counterparts. The shapes of the scattering patterns from 20 wt % 210(60)ABSiCB4 (Figure 3.19a) are also qualitatively different than those of its 5 and 10 wt % counterparts.

3.3.4 Effects of PS Block Size on Dynamics: Frequency Dependent Rheology

Frequency dependent rheology of diblock solutions exposes their dynamics as a function of temperature. The magnitude of the complex viscosity, $|\eta^*|$, is normalized by the bulk viscosity of 5CB, η_{5CB}, at the same temperature to remove the solvent's temperature dependence. Solutions of 5 wt % diblock copolymers having varied PS block sizes are viscoelastic fluids in the nematic phase: the reduced viscosity slopes upward at low frequency (Figure 3.21). In the isotropic phase, the three diblocks with $M_{PS} < 120$ kg/mol remain viscoelastic fluids right after T_{NI} and at T ≥ 40 °C the reduced viscosity becomes frequency-independent, characteristic of a viscous fluid (Figure 3.21a,b,c). The polymer with the largest PS block remains a viscoelastic fluid for temperatures less than 50 °C and is a viscous fluid at T ≥ 50 °C (Figure 3.21d).

When the polymer concentration is increased to 10 wt % the solutions become room-temperature gels: $|\eta^*| / \eta_{5CB} \sim \omega^{-1}$ at 25 °C, corresponding to nearly constant storage modulus, $G'(\omega)$, and $G'(\omega) >> G''(\omega)$ (Figure 3.22)[†]. When these solutions are heated above T_{NI} they immediately cease to be gels. When M_{PS} = 40 kg/mol the solution transitions directly to a viscous fluid at T_{NI} (Figure 3.22a), but when $M_{PS} \geq 60$ kg/mol the solutions are viscous fluids only at T ≥ 50 °C (Figure 3.22b,c,d). Within the nematic phase, the size of the PS block is correlated to deviations from $|\eta^*| / \eta_{5CB} \sim \omega^{-1}$. Solutions of diblocks with $M_{PS} \geq 80$ kg/mol retain this scaling throughout the dynamic range at all temperatures in the nematic phase (Figure 3.22c and d). When the PS block is decreased to M_{PS} = 60 kg/mol, deviations are observed at 35 °C (Figure 3.22b). The viscosity of 10 wt % 470(40)ABSiCB4 begins to deviate from $|\eta^*| / \eta_{5CB} \sim \omega^{-1}$ at T = 32 °C, and the frequency range over which the scaling is valid shrinks as temperature is increased (Figure 3.22a).

3.3.5 Effects of Total Molecular Weight on Dynamics: Frequency Dependent Rheology

The frequency dependent rheology of solutions of 210(60)ABSiCB4 and 580(190)ABSiCB4 was measured at concentrations of 2, 5, 10, and 20 wt %. Solutions of 210(60)ABSiCB4 are room-temperature gels only at concentrations of 10 and 20 wt %; lower concentration solutions are fluids. At 2 wt % the solution is a viscous fluid both above and below T_{NI} (Figure 3.23a). Increasing the concentration to 5 wt % results in a solution that is a viscoelastic fluid in the nematic phase and a viscous fluid at T ≥ 40 °C (Figure 3.23b). The 10 wt % solution is a gel in the nematic phase and the viscosity deviates from $|\eta^*| / \eta_{5CB} \sim \omega^{-1}$ when T = 35 °C. At T ≥ 50 °C the solution is a viscous fluid (Figure 3.23c). When the polymer concentration is 20 wt % the solution is a gel throughout the entire temperature range (Figure 3.23d).

Increasing the molecular weight of the diblock results in solutions that are nematic gels at all four concentrations (Figure 3.24). The most dilute solution, 2 wt % 580(190)ABSiCB4, transitions to a viscoelastic fluid at T_{NI} and becomes a viscous fluid at T ≥ 50 °C (Figure 3.24a). The other three solutions remain gels after the nematic-isotropic transition (Figure

---

[†] Detailed plots of $G'(\omega)$ and $G''(\omega)$ are located in Appendix E.

3.24b,c,d). The 5 and 10 wt % solutions become viscoelastic fluids at 50 and 60 °C, respectively (Figure 3.24b,c). The 5 wt % solution becomes a viscous fluid at 60 °C (Figure 3.24b), but the 10 wt % solution remains a viscoelastic fluid over the entire temperature range (Figure 3.24c). The 20 wt % solution remains a gel up to at least 100 °C (Figure 3.24d).

3.3.6 Frequency Dependent Rheology: Changing the Identity of the Coil Block

Comparing solutions of 700(70)ABSiCB4 and 950(70)BdMMASiCB4 allows the effects of changing the identity of the coil block to be investigated in polymers having similar composition (~9 and 7 wt % coil block, respectively) and molecular weight (770 and 1,050 kg/mol, respectively). At low concentration (2 wt % polymer) solutions of both PS- and PMMA-containing diblocks are viscoelastic fluids in the nematic phase and transition to viscous fluids above T_{NI} (Figure 3.25a and Figure 3.26a). Data are not available for 5 wt % 700(70)ABSiCB4, but a 10 wt % solution is a gel in the nematic phase, transitioning to a viscoelastic fluid at T_{NI} and at T ≥ 50 °C the solution is a viscous fluid (Figure 3.25b). Deviation from $|\eta^*| / \eta_{5CB} \sim \omega^{-1}$ is never seen in 10 wt % 700(70)ABSiCB4. The 10 wt % solution of PMMA-based polymer behaves similarly in that it is a gel in the nematic phase, transitioning to a viscoelastic fluid in the temperature range between T_{NI} and 40 °C (Figure 3.26c). However, in contrast to its PS-based counterpart, the reduced viscosity shows strong low-frequency deviations $|\eta^*| / \eta_{5CB} \sim \omega^{-1}$ at temperatures between 30 °C and T_{NI}. The frequency range over which deviations from this scaling occur expands as temperature is increased. When the concentration is increased to 20 wt % polymer, both 700(70)ABSiCB4 and 950(70)ABSiCB4 behave similarly (Figure 3.25c and Figure 3.26d); the reduced viscosity scales with ω^{-1} throughout the nematic phase and at temperatures just above T_{NI}. In the isotropic phase the solutions are viscoelastic fluids with the PS-based diblock transitioning to a viscous fluid at 80 °C.

3.4 Discussion

3.4.1 Background: Connecting SANS and Rheology to Self-Assembled Particle Structure

Dissolving a coil-SGLCP diblock copolymer in a small-molecule LC solvent causes the polymer to self-assemble into a core-shell type structure where the LC-phobic coil block is segregated into the core and surrounded by a corona rich in the SGLCP block. SANS and rheometry provide complimentary means to understand both the structure of self-assembled micelles and the interactions between them.

Within a given polymer solution, changes in I_{max} that occur with changing temperature can be related to changes in the number of polymer chains participating in one micelle (the aggregation number, N_{agg}). Regardless of whether any self-assembled structure exists, the monomer-level scattering (at large q) of solutions of diblock copolymers resembles that of homopolymer solutions (Figure 3.5 and Figure 3.6). Excess scattering at low q, however, is from the structure of the self-assembled micelles. The differential scattering cross-section for a solution of N_p particles (here, micelles) of volume V_P and overall neutron scattering contrast $(\Delta\rho)^2$ is

$$\frac{\partial\Sigma}{\partial\Omega}(q) = N_p V_P^2 (\Delta\rho)^2 P(q) S(q), \tag{3.1}$$

where $P(q)$ is the form factor describing the shape of the particle and $S(q)$ is the structure factor describing interparticle correlations.[22] In the limit of vanishing q, $P(q) = 1$ and in the absence of long-range correlations, $S(q) = 1$. The differential scattering cross-section of uncorrelated particles at $q = 0$ is, therefore

$$\frac{\partial\Sigma}{\partial\Omega}(q = 0) = N_p V_P^2 (\Delta\rho)^2 . \tag{3.2}$$

Equation 3.2 is valid for any solution of uncorrelated particles; it assumes nothing about the shape or constitution of the scatterers. The scattering length density (ρ_p) of a micellar particle swollen with solvent, such that the overall volume fraction of polymer in the particle is ϕ_A, may be calculated from the scattering length densities of the polymer (ρ_A) and solvent (ρ_B):

$$\rho_p = \phi_A \rho_A + (1-\phi_A)\rho_B\,, \tag{3.3}$$

so that the contrast between the micelle and a pure solvent background is

$$(\Delta\rho)^2 = \phi_A^2(\rho_A - \rho_B)^2\,. \tag{3.4}$$

The volume of a solvent-swollen micelle is

$$V_p = \frac{N_{agg} v}{\phi_A}\,, \tag{3.5}$$

where v is the volume of a single polymer chain, and the number of particles in a volume of solution, V_S, is

$$N_p = \frac{V_S c}{V_p \phi_A}\,, \tag{3.6}$$

where c is the volume fraction of "dry" polymer. Combining Equations 3.2, 3.4, 3.5, and 3.6 gives the differential scattering cross-section in terms of fixed solution properties (V_S, c, v, ρ_A, ρ_B) and only one structural property, N_{agg}:

$$\frac{\partial\Sigma}{\partial\Omega}(q=0) = V_S c v (\rho_A - \rho_B)^2 N_{agg}\,. \tag{3.7}$$

Equation 3.7 is valid for any solution of arbitrarily shaped, uncorrelated micelles, provided every polymer chain participates in a micelle and the matrix surrounding the micelles is composed of pure solvent. In the case of overlapping micelles, the scattering length density of the surrounding matrix, ρ_M, is unknown and the contrast becomes

$$(\Delta\rho)^2 = [\phi_A(\rho_A - \rho_B) + \rho_B - \rho_M]^2\,. \tag{3.8}$$

The differential scattering cross-section will depend on both N_{agg} and ϕ_A, but Equation 3.7 may still be a valid approximation if the matrix is composed of a dilute polymer solution ($\rho_M \approx \rho_B$).

Zero-angle scattering is not accessible in these experiments, but the relative changes in I_{max} for a given polymer solution at different temperatures still reflect changes in N_{agg} according to Equation 3.7, provided the form factor is not drastically different from one temperature to the next. For example, if the size of the particles increases, the form factor may shift within the window of observation to decrease the maximum measured intensity (Figure 3.27). Nevertheless, in many data sets (e.g., 10 wt % 390(60)ABSiCB4, Figure

3.14a) the shape of $I(q)$ is virtually unchanged over several temperatures (in this case, 25 - 32 °C) indicating that $P(q)$ is not responsible for the observed drop in I_{max}.

Micellar dispersions studied here are all within the "liquid-like" or "gas-like" concentration regime. In both cases, micelles lack long-range order, but micelles in a liquid-like dispersion remain correlated with one another, while in a gas-like dispersion they are non-interacting.[3] The "solid-like" regime is ruled out because SANS patterns do not exhibit structure factor peaks resulting from inter-micelle interference,[3, 8] nor do they exhibit diffraction peaks characteristic of well-ordered micellar lattices.[23, 24] Inter-micellar correlations are, however, clearly demonstrated by rheology, and result in viscoelasticity or gelation. In general, the more strongly the micelles interact with one another, the higher G' becomes. The most likely mechanism for inter-micellar interactions is the overlap of adjacent coronas or, equivalently, correlation of chain conformations in neighboring coronas in order to satisfy the osmotic requirement of minimum concentration variation in the matrix surrounding the micellar cores.[24-26] SANS on SGLCP homopolymer solutions demonstrated that 5 wt % solutions are in the semidilute regime (Chapter 2), suggesting that diblock solutions of equal or greater concentration must also have corona chains that overlap one another, if only at the outermost edge of the micelle.

The time-scale for relaxation in a micellar solution, indicated by the transition to frequency-independent viscosity, indicates the strength of the coil block's segregation and may be qualitatively linked to how "hard" or "soft" are the micelle cores. When the reduced viscosity deviates from $|\eta^*| / \eta_{5CB} \sim \omega^{-1}$ it indicates that the micelle-micelle interactions have dissipated on the time-scale where the viscosity is frequency-independent, and this time-scale may be attributed to the lifetime of a micelle (the time required for all the participating polymer chains to disengage from the core). Micelles have longer lifetimes as the free energy cost of chain dissociation (the strength of segregation) increases.[27, 28] Micelles with short lifetimes have "soft" cores; mechanical interactions are weak because stress is relieved by the dissociation of the polymer chains.

3.4.2 Implications of "Switchable" Solvent Quality

The thermodynamic driving forces for self-assembly of coil-SGLCP diblock copolymers may be inferred from the phase behavior of PS and SGLCP homopolymers in 5CB discussed in Chapter 3. In the nematic phase, the entropic cost of dissolving PS in an ordered solvent makes it insoluble in 5CB. When the entropic penalty disappears in the isotropic phase, 5CB and PS become miscible. On the other hand, the covalent attachment of chemically similar, mesogenic units to the polymer backbone makes the SGLCP miscible with 5CB both above and below T_{NI}. Self-assembly of coil-SGLCP diblock copolymers below T_{NI} is intuitively understood as being driven by the solvent's strong selectivity for the SGLCP block. In the isotropic phase, where the solvent is reasonably good for both blocks, self-assembly is driven by a combination of unfavorable interactions between the polymer blocks and by the asymmetric solvent effect; the solvent's slight thermodynamic preference for the SGLCP block can drive self-assembly of a diblock copolymer in the same way that macroscopic phase separation is driven in ternary PS-SGLCP-5CB blends. At low polymer concentration, polymer-polymer interactions are screened by solvent, but as concentration is increased they dominate the system's thermodynamics.

Heating samples through the nematic-isotropic phase transition often has a profound and sudden effect on micellar structure and micelle-micelle interactions as a result of the discontinuous change in solvent quality that takes place at T_{NI}. In contrast to conventional solvents, whose quality changes continuously with temperature, the unique ability of the LC solvent to undergo a first-order phase transition between two distinct fluid phases allows the regimes of strong selectivity[5, 7, 9] and slight selectivity[3, 6, 8] to be accessed with small changes in temperature. Depending on the copolymer's composition and molecular weight, the temperature at which the micelles disassemble to become free chains (the microphase separation temperature, MST) can be below, above, or coincident with T_{NI}.

3.4.3 Influence of PS Content on the Driving Force for Self-Assembly

Just as the upper critical solution temperature of ternary homopolymer solutions is highly sensitive to changes in the relative concentrations of the two polymers, the MST of diblock solutions gets progressively higher as the copolymers' PS content is increased. At fixed total polymer concentration and molecular weight, increasing M_{PS} serves to increase the total volume fraction of PS and decrease the volume fraction of SGLCP. Interestingly, at low PS content, the covalent bonding between PS and SGLCP serves to draw the PS block into solution even when the solvent quality for PS is poor; the MST of these solutions (both 5 and 10 wt %) is less than T_{NI}. When M_{PS} is small, the free energy cost of mixing PS with a blend of nematic 5CB and SGLCP is not large enough to outweigh the entropic penalty of organizing the SGLCP into micelles. Increasing the size of the PS block to M_{PS} = 120 kg/mol shifts the MST of diblock solutions to be greater than T_{NI}, indicating that the asymmetric solvent effect together with unfavorable polymer-polymer interactions is sufficiently strong to overcome the favorable free energy of mixing the individual blocks with isotropic 5CB.

The aggregation number appears to increase with the size of the PS block, as predicted for solutions of associating polymers.[27, 29, 30] Comparing the data from 5 or 10 wt % solutions at 25 °C, the increase in G' that takes place with increasing PS content indicates greater overlap between micelle coronas or, equivalently, an increase in the size of the micelle. The thickness of the micelle corona should be much larger than the radius of the core (a "hairy" micelle) by virtue of the SGLCP block's substantially larger volume fraction in the bulk polymer ($V_{SGLCP} / V_{PS} \geq 3$ for all polymers studied). At fixed N_{agg}, the size of a hairy micelle is insensitive to changes in the size of the core block because the dimensions of the corona chains dictate those of the micelle. Increasing N_{agg}, however, causes increased stretching of the corona chains due to greater crowding at the core-corona interface,[30] and results in larger micelles with a greater degree of corona-corona overlap. In accord with the rheological data, I_{max} / c at 25 °C also increases with PS content in both 5 and 10 wt % solutions, implying an increase in N_{agg}. However, I_{max} / c cannot necessarily be compared from sample to sample because of possible differences in the form factor.

In a given diblock copolymer solution the temperature dependence of G' in the nematic phase is primarily due to changes in the aggregation number. In solutions of all but the diblock with M_{PS} = 40 kg/mol, G' increases with temperature in the nematic phase and is accompanied by a decrease in N_{agg} indicated by the decrease in I_{max} / c (except in 5 wt % 320(120)ABSiCB4 where I_{max} / c increases slightly between 25 and 32 °C). The order parameter of 5CB gets smaller with temperature, lessening the entropic penalty to dissolution of PS and allowing the solvent to penetrate the core. This decreases the energy per unit area of the core-corona interface and results in a decrease in N_{agg}. Consequently, the solution contains more micelles, each with fewer polymer chains. Swelling increases the volume fraction of micelles, pushes them closer together, and causes them to interact more strongly. The temperature-dependence of G' is stronger in diblocks with higher PS content because the swelling of the cores affects a larger volume fraction of the overall sample.

For samples that have a substantial G' above T_{NI} (Figure 3.10b, Figure 3.12b, Figure 3.13b, and Figure 3.14b), the temperature-dependence falls into two categories: G' rapidly decreases at T_{NI} (Figure 3.10b, Figure 3.12b, and Figure 3.13b), or G' decreases gradually at first, then rapidly decays after some $T > T_{NI}$ (Figure 3.14b). The former is characteristic of composition fluctuations that decay above the MST in conventional micellar solutions,[3, 8] and the latter indicates that distinct micelles continue to exist in a range of $T_{NI} < T <$ MST, then decay with similar composition fluctuations. These observations are in accord with the scattering patterns that clearly demonstrate the existence of micelles in the temperature range where G' is gradually decreasing (Figure 3.14), but only show diffuse excess scattering in the range where G' is falling rapidly (Figure 3.10, Figure 3.12, Figure 3.13, Figure 3.14). The aggregation number of the isotropic micelles decreases with temperature, but the inter-micellar interactions decrease because the cores become very soft; frequency-dependent rheology shows that the fluid's relaxation time is fast (~ O(10^2 s) or greater) in this temperature range (Figure 3.22d).

3.4.4 Influence of Molecular Weight on the Driving Force for Self-Assembly

At fixed PS content, increasing the molecular weight of a coil-SGLCP diblock copolymer increases the driving force for self-assembly in 5CB; the MST of both 5 and 10 wt % solutions increases from being coincident with T_{NI} at low molecular weight (Figure 3.15 and Figure 3.17) to being much higher than T_{NI} at high molecular weight (Figure 3.16 and

Figure 3.18). Decreasing the degree of polymerization increases the polymer's entropy of mixing because shorter chains benefit from greater positional entropy in solution.

Similar to what was observed as a function of PS content in the previous series of diblocks, increasing the total molecular weight causes the temperature dependence of G' in the isotropic phase to shift from being a steep decay reflecting composition fluctuations above the MST (Figure 3.10b and Figure 3.17b) to a gradual decay between T_{NI} and the MST characteristic of persisting micellization (Figure 3.14b, Figure 3.16b, and Figure 3.18b). However, the corroborating evidence from SANS is unclear in solutions of 210(60)ABSiCB4 and 580(190)ABSiCB4. Scattering patterns at high temperature do not resemble the diffuse excess scattering observed in solutions of 320(120)ABSiCB4; a high-intensity upturn at low q is observed at all temperatures. The explanation for these anomalous scattering patterns is unclear, but may be related to the high content of 1,4-butadiene in the SGLCP block. Perhaps there is some clustering among short domains of 1,4-polybutadiene driven by poor solubility in the strongly dipolar solvent that gives rise to low-q scattering, similar to clustering between hydrocarbon end-groups and polymer backbones in solutions of poly(ethylene oxide) in water.[31] The ambiguity in interpreting the high-temperature SANS patterns makes it impossible to draw conclusions about changes in N_{agg} that take place with increasing temperature; I_{max} / c is virtually constant in these samples.

As predicted by theory,[27, 28, 30] both the strength of coil-block associations and N_{agg} increase with molecular weight. Comparing samples at the same concentration, increase in segregation strength is evidenced by the slowing of the solution's relaxation time (Figure 3.22b, Figure 3.23c, and Figure 3.24c). The increase in N_{agg} with increasing molecular weight results in a transition from viscoelastic fluid to gel in 5 wt % solutions below T_{NI}. At higher concentration, the increased N_{agg} causes isotropic solutions of high molecular weight polymer to be gels (Figure 3.24c) while their low molecular counterparts form viscous liquid solutions (Figure 3.22b, Figure 3.23c).

3.4.5 Influence of Polymer Concentration on the Driving Force for Self-Assembly

In dilute solution, the relatively weak asymmetric solvent effect is the dominant thermodynamic driving force for self-assembly. The unfavorable interactions between the polymer blocks become increasingly important with concentration as they are less effectively screened by solvent. As a result, the segregation strength and, consequently, the MST increase with concentration. This is demonstrated most clearly in solutions of 210(60)ABSiCB4 and 580(190)ABSiCB4 because frequency-dependent rheometry was performed over the concentration range of 2 to 20 wt % polymer (Figure 3.23 and Figure 3.24). The increase in segregation strength is best illustrated by comparing 10 and 20 wt % solutions. The micelle lifetime in 10 wt % solutions of both polymers lies within the dynamic range at a few temperatures, but at 20 wt % deviations from $|\eta^*| / \eta_{5CB} \sim \omega^{-1}$ are never observed. The increase in the MST is also evident because the temperature required to achieve viscous liquid behavior increases with concentration. Similarly, SANS and rheology of the most concentrated samples (Figure 3.19 and Figure 3.20) show that polymers remain self-assembled throughout the entire temperature range of 25 to 60 °C, which is not the case in 5 wt % solutions (Figure 3.15 and Figure 3.16).

Similar trends are also observed in solutions of diblocks from the variable PS content series, though these were only studied at two concentrations (5 and 10 wt %). The observation that I_{max} / c decreased as the concentration of 470(40)ABSiCB4 or 390(60)ABSiCB4 was increased from 5 to 10 wt % is probably the result of a change in what constitutes the matrix surrounding the micelles. If the background matrix is pure solvent, the micelle's scattering contrast is maximized (Equation 3.4), but if the volume fraction of micelles increases to the point they are space-filling, the effective matrix becomes a solution of SGLCP chains in 5CB and the scattering contrast is lowered (Equation 3.8). The perceived scattering may then be from an effective corona composed of a dense layer of SGLCP adjacent to the core surface.[32]

3.4.6 Influence of the Coil Block Identity on the Driving Force for Self-Assembly

Though the entropy of mixing is probably comparable, the enthalpy of mixing PMMA with 5CB is greater than that of PS with 5CB and the PMMA-SGLCP diblock is, therefore, less strongly associated. Studies of the phase behavior of polyacrylates with cyanobiphenyl LCs shows them to be slightly more miscible with one another than PS and 5CB.[33-36] The improved miscibility decreases the segregation strength so that the lifetime of a PMMA-based micelle is evident within the dynamic range of rheometry (Figure 3.26), while that of an equivalent PS-based micelle is not (Figure 3.25). Otherwise, solutions of the PMMA-based behave very similarly to their PS-based counterparts; the MST is comparable for solutions having the same polymer concentration.

3.5 Conclusions

Solutions of coil-SGLCP diblock copolymers in small-molecule LC solvent are unique in that two distinct regimes of solvent selectivity can be accessed in a single solution, simply by heating the solution through its nematic-to-isotropic phase transition. In the nematic phase, the solvent is strongly selective for the SGLCP block, but in the isotropic phase it is a reasonably good solvent for both blocks. The change in solvent quality often triggers the transition from self-assembled micelles to a solution of free chains, but by tailoring the composition and molecular weight of the block copolymer, the MST can be adjusted to be above or below the T_{NI}. These conclusions are summarized in Figure 3.28, where the structure and interactions between diblock copolymer micelles in 5 wt % PS-SGLCP solutions are superimposed over the phase diagram of PS content versus total molecular weight over a temperature range from well below to well above T_{NI}.

In the context of the literature on block copolymers in isotropic solvents, the results presented here imply that new juxtapositions of ordered phases can be introduced into their phase diagrams. The progression of ordered phases that would conventionally be observed in two separate solvents of different quality (strongly selective[5, 7, 9] versus slightly selective [3, 6, 8]) can now be combined into the single phase diagram of a given block copolymer in a single LC solvent. Small temperature changes could switch the system between the two regimes of ordered phases. The present systems switch from a disordered micelle phase that is relatively rigid and has a low volume fraction of the PS-rich domains to a different disordered micelle phase that is much softer and has a substantial volume fraction of the PS-rich domains. This suggests that for other relative block lengths and concentrations, the system could jump between ordered phases (e.g., FCC and BCC) very abruptly with temperature.

3.6 Tables

Table 3.1 Molecular weight, conversion, and polydispersity of the end-on side-group liquid crystal diblock copolymers with coil block composed of polystyrene (PS). Details of characterization are presented in Appendix A.

Name	PS Block M_n [kg/mol]	SGLCP Block M_n [kg/mol]	SGLCP Block Mole Fraction 1,2 PB	SGLCP Block Mole Fraction 1,4 PB	SGLCP Block Mole Fraction LC	PDI[a]
470(40)ABSiCB4	43	472	0	0.01	0.99	1.19
390(60)ABSiCB4	59	388	0.15	0.03	0.85	1.11
420(80)ABSiCB4	83	422	0.05	0.05	0.90	1.07
320(120)ABSiCB4	121	323	0.22	0.01	0.77	1.05
700(70)ABSiCB4	70	700	0	0.11	0.89	1.50
210(60)ABSiCB4	63.5	205	0.13	0.15	0.72	1.22
580(190)ABSiCB4	191	577	0.09	0.23	0.68	1.56

[a] PDI = Polydispersity Index (M_w/M_n)

Table 3.2 Molecular weight, conversion, and polydispersity of end-on and side-on side-group liquid crystal homopolymers. Details of characterization are presented in Appendix A.

Name	M_n [kg/mol]	Mole Fraction 1,2 PB	Mole Fraction 1,4 PB	Mole Fraction LC	PDI[a]
350HSiCB4	347	0	0.11	0.89	1.27

[a] PDI = Polydispersity Index (M_w/M_n)

Table 3.3 Molecular weight, conversion, and polydispersity of the side-group liquid crystal diblock copolymer with coil block composed of poly(methyl methacrylate) (PMMA). Details of characterization are presented in Appendix A.

Name	PMMA Block	SGLCP Block				PDI[a]
	M_n [kg/mol]	M_n [kg/mol]	Mole Fraction 1,2 PB	Mole Fraction 1,4 PB	Mole Fraction LC	
950(70)BdMMASiCB4	68	954	0.07	0.13	0.80	1.11

[a] PDI = Polydispersity Index (M_w/M_n)

3.7 Figures

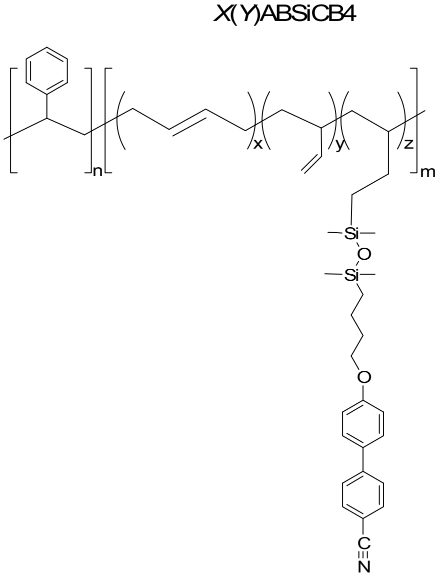

Figure 3.1 Chemical structures of end-on side-group liquid crystal diblock copolymers having a coil block composed of polystyrene. The polymers' names are derived from the molecular weights of the liquid crystal polymer block (*X*) and the coil block (*Y*) in units of kg/mol, the letters "AB" to indicate a diblock copolymer, and "SiCB4" to indicate end-on, cyanobiphenyl-based mesogens. In addition to monomers having an attached mesogen, the polymer also contains some residual 1,2- and 1,4-butadiene monomers. Compositions, expressed as the mole fractions *x*,*y*, and *z*, are given in Table 3.1 and details of characterization are given in Appendix A.

XHSiCB4

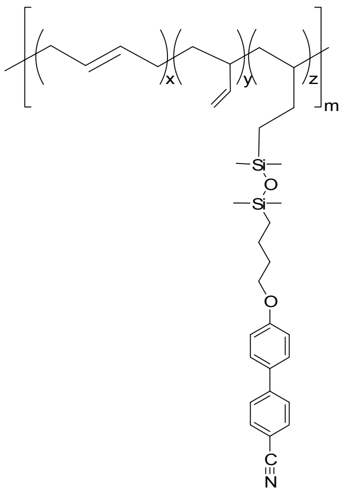

Figure 3.2 Chemical structures of end-on side-group liquid crystal homopolymers. The polymers' names are derived from the polymer's molecular weight in units of kg/mol, the letter "H" to indicate a homopolymer, and "SiCB4" to indicate end-on, cyanobiphenyl-based mesogens. In addition to monomers having an attached mesogen, the polymer also contains some residual 1,2- and 1,4-butadiene monomers. Compositions, expressed as the mole fractions *x*,*y*, and *z*, are given in Table 3.2 and details of characterization are given in Appendix A.

X(*Y*)BdMMASiCB4

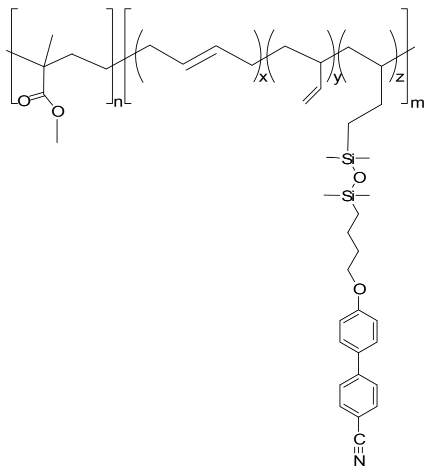

Figure 3.3 Chemical structures of end-on side-group liquid crystal diblock copolymers having a coil block composed of poly(methyl methacrylate) (PMMA). The polymer's name is derived from the molecular weights of the liquid crystal polymer block (*X*) and the coil block (*Y*) in units of kg/mol, the letters "BdMMA" to indicate a diblock copolymer with PMMA coil block, and "SiCB4" to indicate end-on, cyanobiphenyl-based mesogens. In addition to monomers having an attached mesogen, the polymer also contains some residual 1,2- and 1,4-butadiene monomers. Compositions, expressed as the mole fractions *x*,*y*, and *z*, are given in Table 3.3 and details of characterization are given in Appendix A.

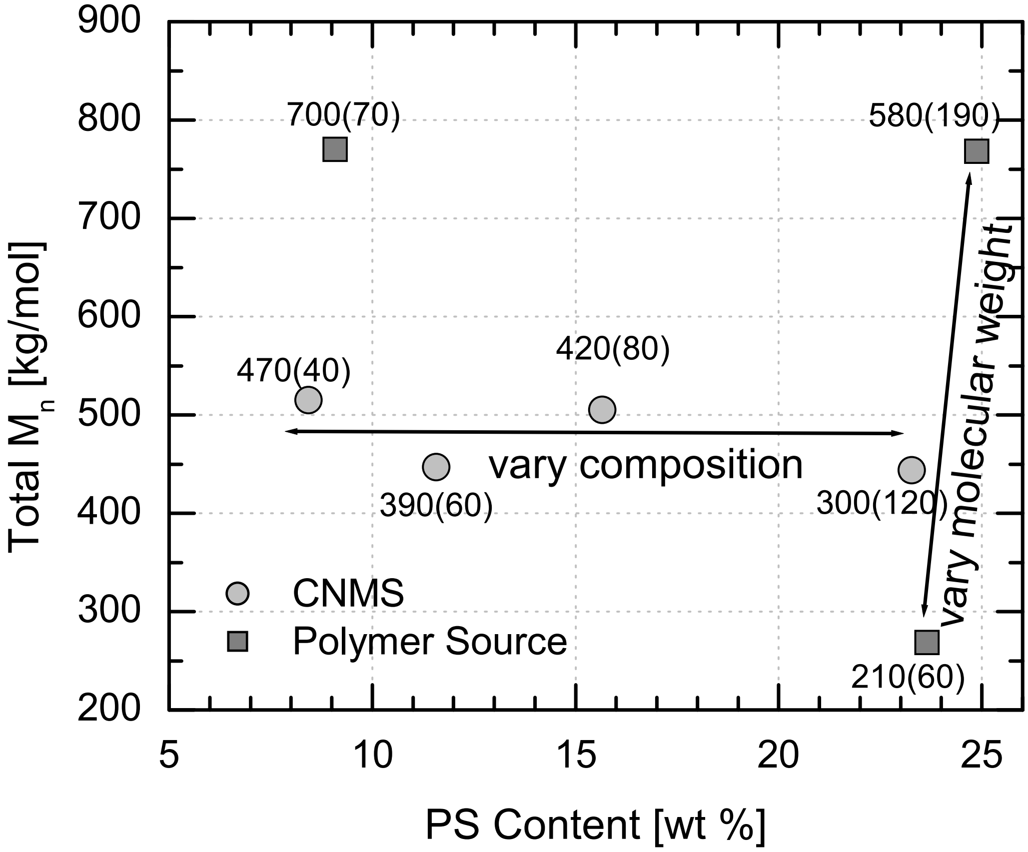

Figure 3.4 Diagram illustrating the relative lengths and compositions of PS-SGLCP diblock copolymers described in Table 3.1. The polymers derived from prepolymers synthesized at the Center for Nanophase Material Sciences (CNMS) comprise a series of almost equal total molecular weight (440 - 510 kg/mol) having PS block lengths between 40 and 120 kg/mol. Diblocks derived from prepolymers purchased from Polymer Source, together with the CNMS polymer having the largest PS block, comprise a series in which the PS content is almost constant (~ 24 wt %), but the total molecular weight varies between 270 and 770 kg/mol.

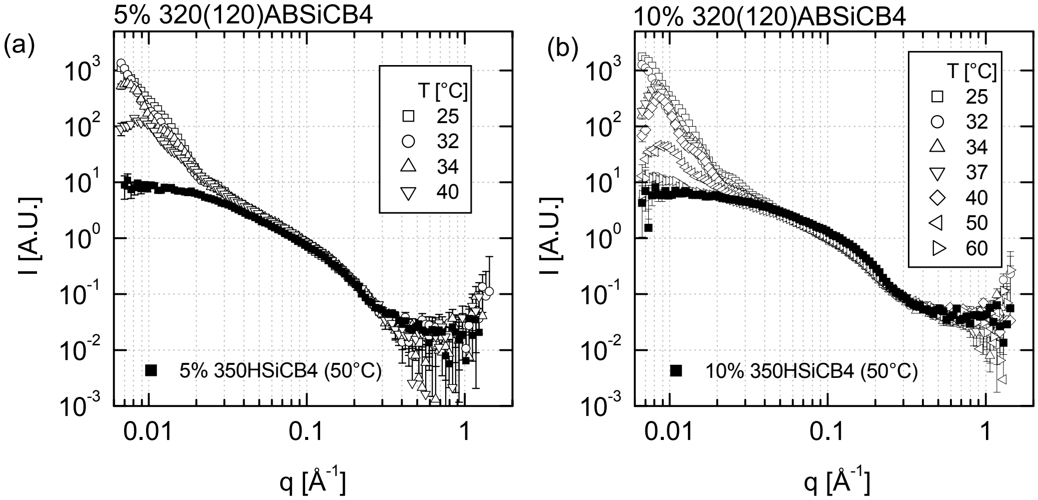

Figure 3.5 SANS patterns from solutions of (a) 5 wt % and (b) 10 wt % 320(120)ABSiCB4 at a variety of temperatures as compared to patterns from homopolymer solutions collected at 50 °C. The low *q* scattering of the diblock solutions is shown in detail in Figure 3.10a and Figure 3.14a.

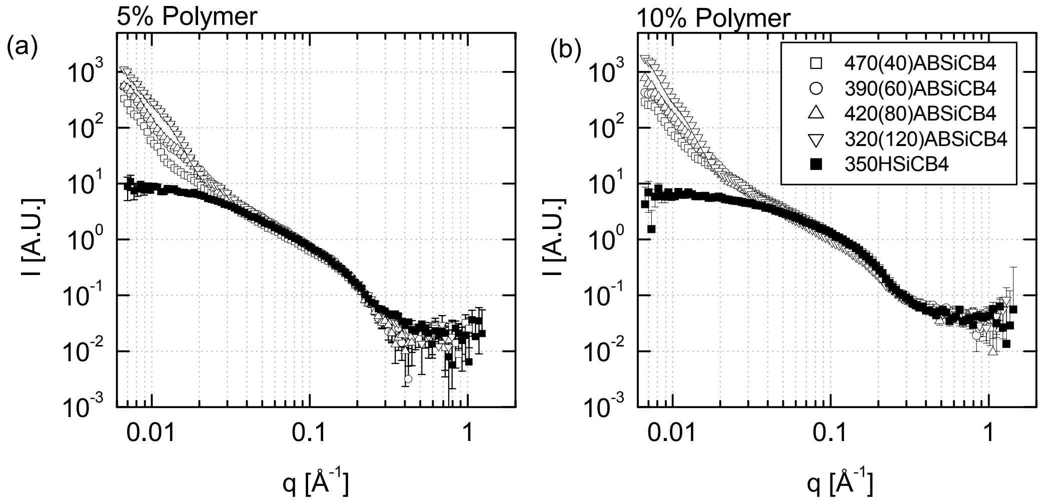

Figure 3.6 Small-angle neutron scattering patterns from solutions of side-group liquid crystalline diblock copolymers and homopolymers at concentrations of (a) 5 wt % and (b) 10 wt % polymer. The scattering patterns from diblock solutions were collected at 25 °C and the patterns from homopolymer solutions were collected at 50 °C. The low *q* scattering of the diblock solutions is shown in detail in Figure 3.7a-Figure 3.14a.

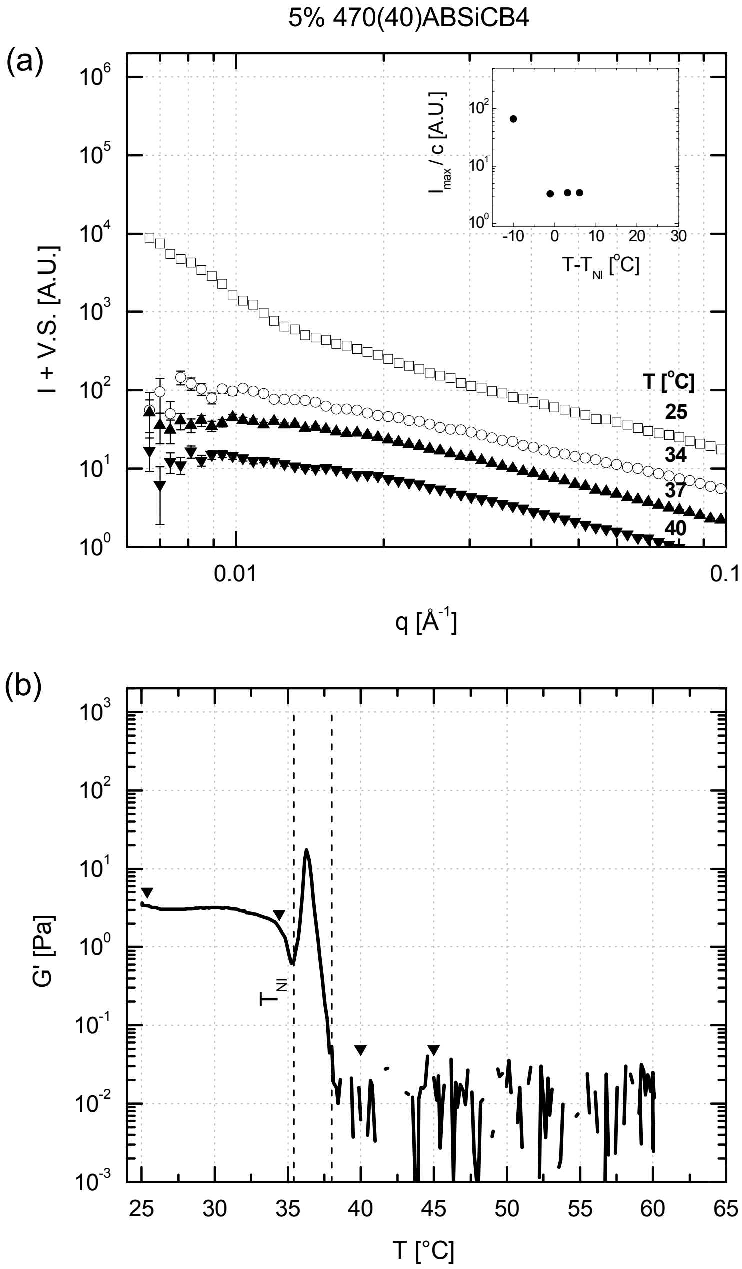

Figure 3.7 SANS and rheology of 5 wt % 470(40)ABSiCB4. (a) The low *q* portions of SANS patterns collected at different temperatures in the nematic phase (open symbols) and in the isotropic phase (filled symbols). The intensities at temperatures less than 40 °C are successively shifted upwards by powers of three for clarity. The inset shows the maximum scattered intensity normalized by the solution concentration (I_{max} / c) as a function of reduced temperature (T - T_{NI}). (b) The storage modulus (G') at ω = 10 rad/s as a function of temperature. Triangles are positioned at the same reduced temperatures where SANS patterns were collected. The solution is biphasic between 35.4 and 38.0 °C.

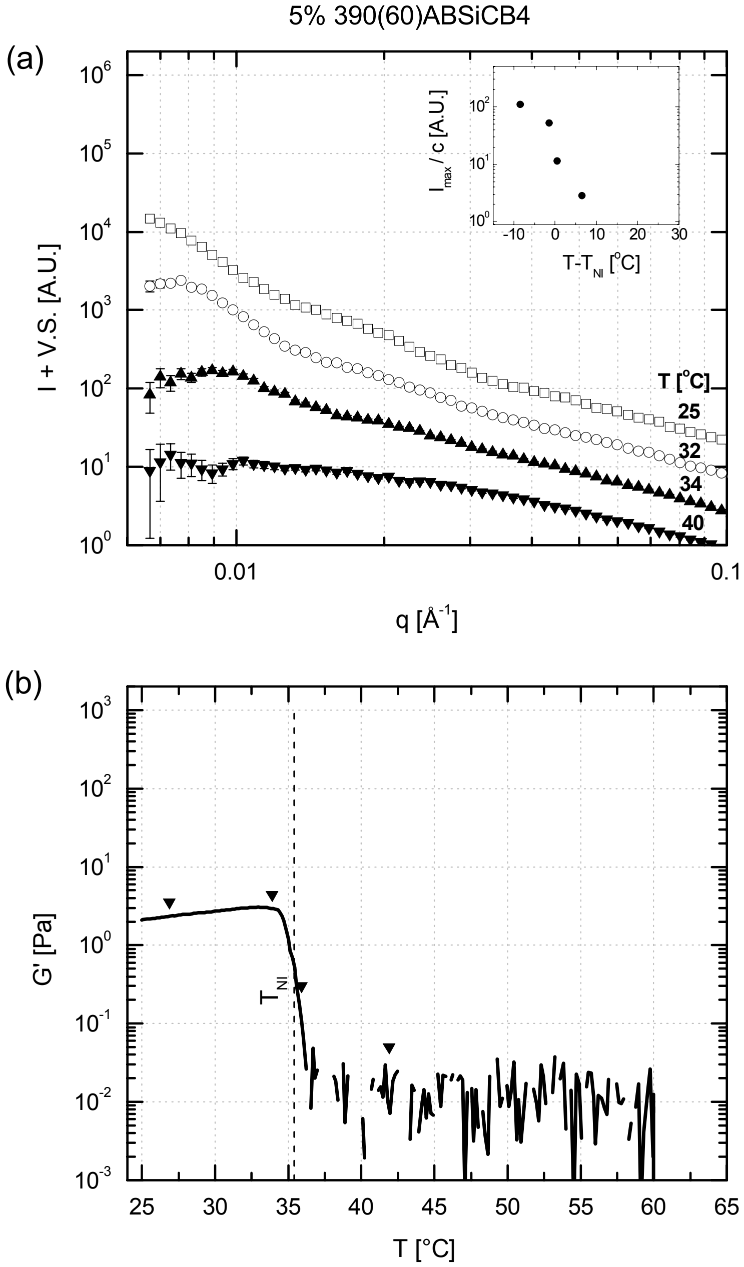

Figure 3.8 SANS and rheology of 5 wt % 390(60)ABSiCB4. (a) The low *q* portions of SANS patterns collected at different temperatures in the nematic phase (open symbols) and in the isotropic phase (filled symbols). The intensities at temperatures less than 40 °C are successively shifted upwards by powers of three for clarity. The inset shows the maximum scattered intensity normalized by the solution concentration (I_{max} / c) as a function of reduced temperature (T - T_{NI}). (b) The storage modulus (G') at $\omega = 10$ rad/s as a function of temperature. Triangles are positioned at the same reduced temperatures where SANS patterns were collected.

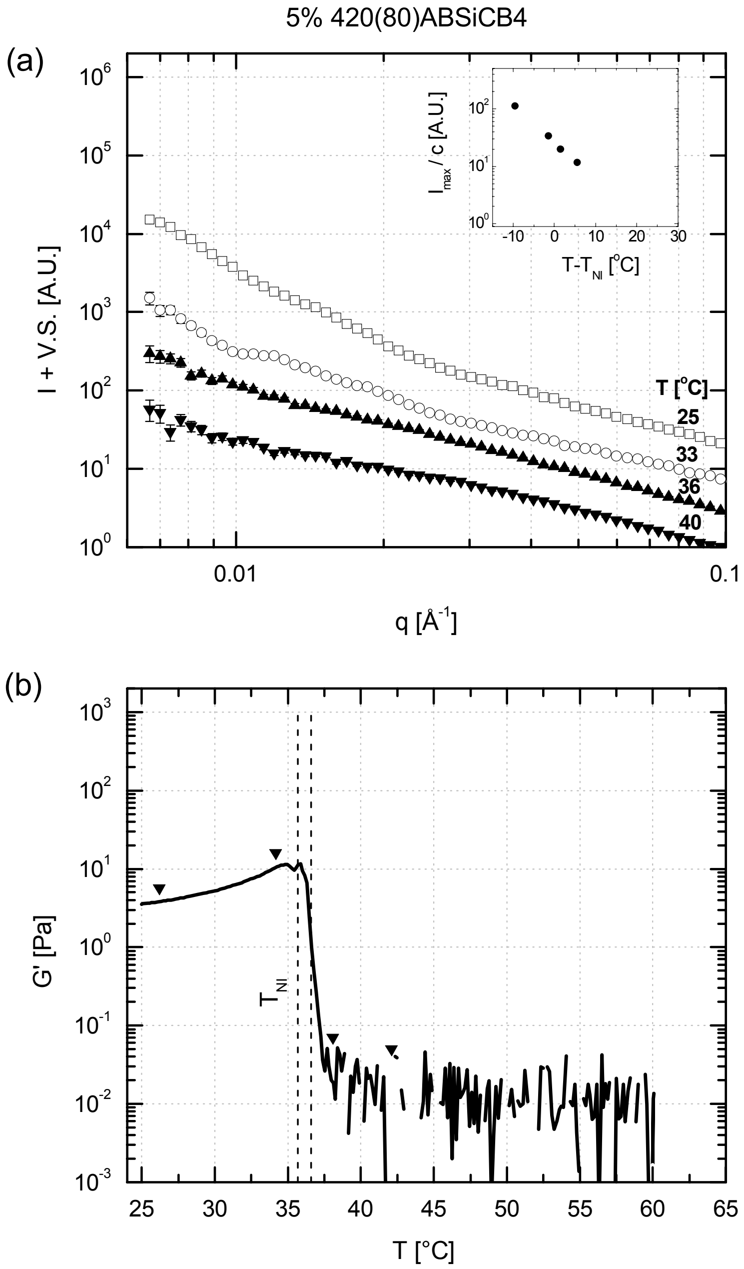

Figure 3.9 SANS and rheology of 5 wt % 420(80)ABSiCB4. (a) The low *q* portions of SANS patterns collected at different temperatures in the nematic phase (open symbols) and in the isotropic phase (filled symbols). The intensities at temperatures less than 40 °C are successively shifted upwards by powers of three for clarity. The inset shows the maximum scattered intensity normalized by the solution concentration (I_{max} / c) as a function of reduced temperature (T - T_{NI}). (b) The storage modulus (G') at ω = 10 rad/s as a function of temperature. Triangles are positioned at the same reduced temperatures where SANS patterns were collected. The solution is biphasic between 35.4 and 38.0 °C.

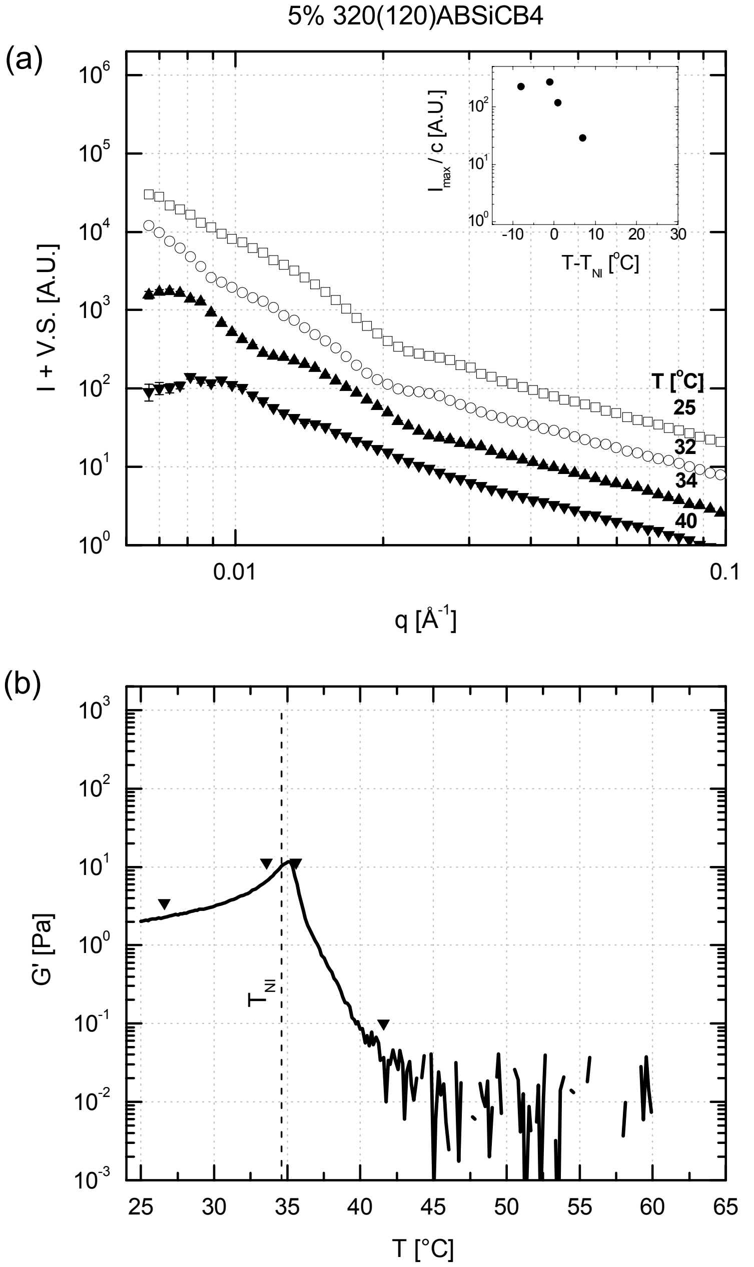

Figure 3.10 SANS and rheology of 5 wt % 320(120)ABSiCB4. (a) The low *q* portions of SANS patterns collected at different temperatures in the nematic phase (open symbols) and in the isotropic phase (filled symbols). The intensities at temperatures less than 40 °C are successively shifted upwards by powers of three for clarity. The inset shows the maximum scattered intensity normalized by the solution concentration (I_{max} / c) as a function of reduced temperature (T - T_{NI}). (b) The storage modulus (G') at ω = 10 rad/s as a function of temperature. Triangles are positioned at the same reduced temperatures where SANS patterns were collected.

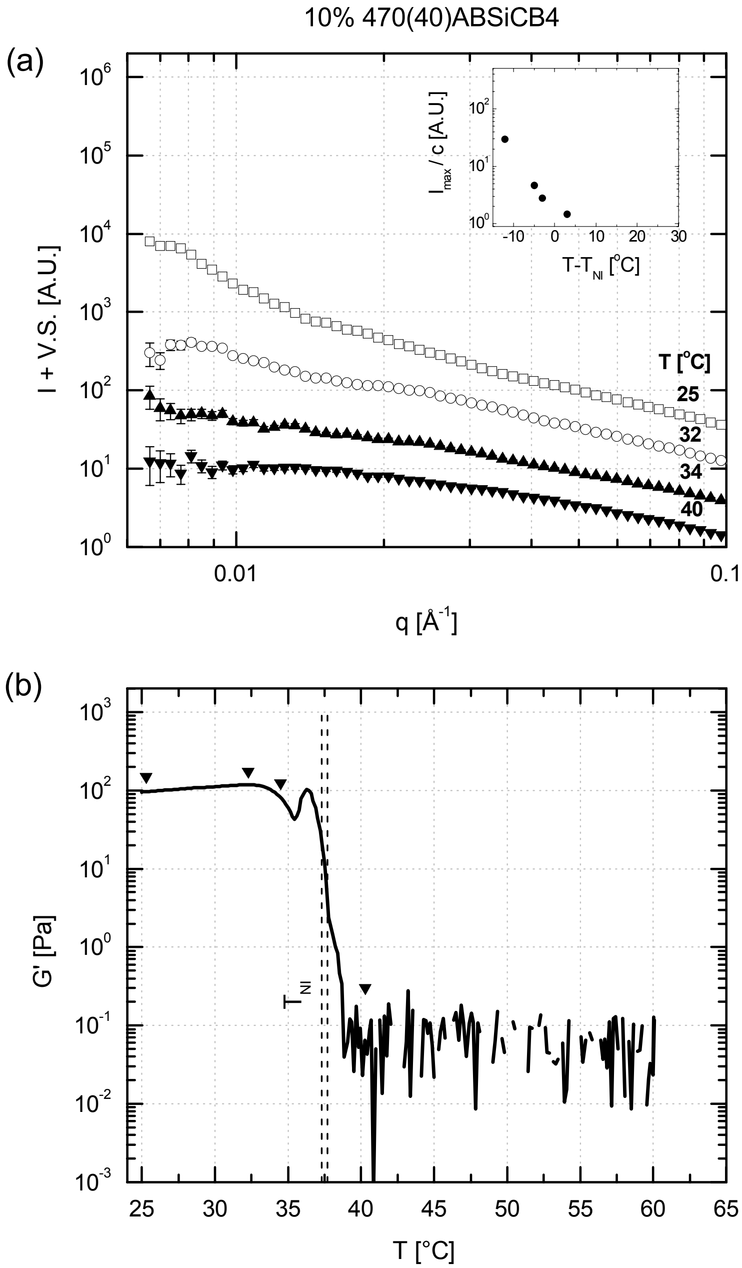

Figure 3.11 SANS and rheology of 10 wt % 470(40)ABSiCB4. (a) The low *q* portions of SANS patterns collected at different temperatures in the nematic phase (open symbols) and in the isotropic phase (filled symbols). The intensities at temperatures less than 40 °C are successively shifted upwards by powers of three for clarity. The inset shows the maximum scattered intensity normalized by the solution concentration (I_{max} / c) as a function of reduced temperature (T - T_{NI}). (b) The storage modulus (G') at ω = 10 rad/s as a function of temperature. Triangles are positioned at the same reduced temperatures where SANS patterns were collected. The solution is biphasic between 37.3 and 37.7 °C.

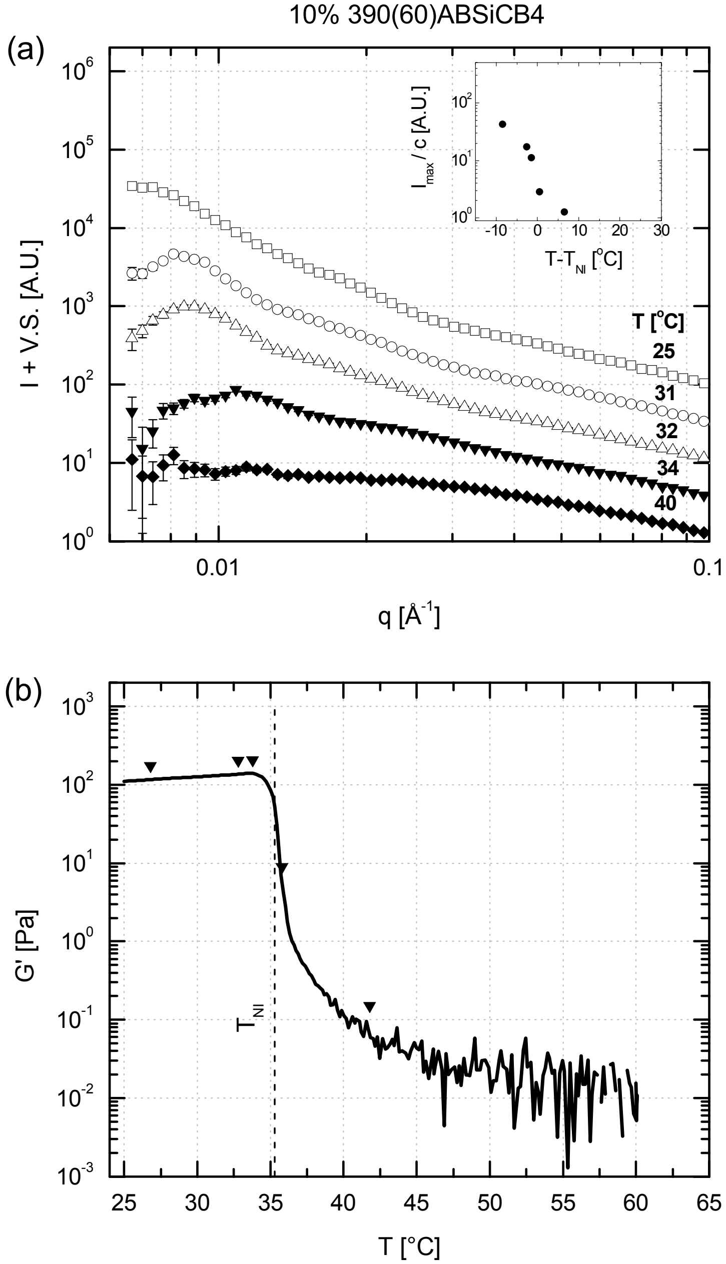

Figure 3.12 SANS and rheology of 10 wt % 390(60)ABSiCB4. (a) The low *q* portions of SANS patterns collected at different temperatures in the nematic phase (open symbols) and in the isotropic phase (filled symbols). The intensities at temperatures less than 40 °C are successively shifted upwards by powers of three for clarity. The inset shows the maximum scattered intensity normalized by the solution concentration (I_{max} / c) as a function of reduced temperature (T - T_{NI}). (b) The storage modulus (G') at ω = 10 rad/s as a function of temperature. Triangles are positioned at the same reduced temperatures where SANS patterns were collected.

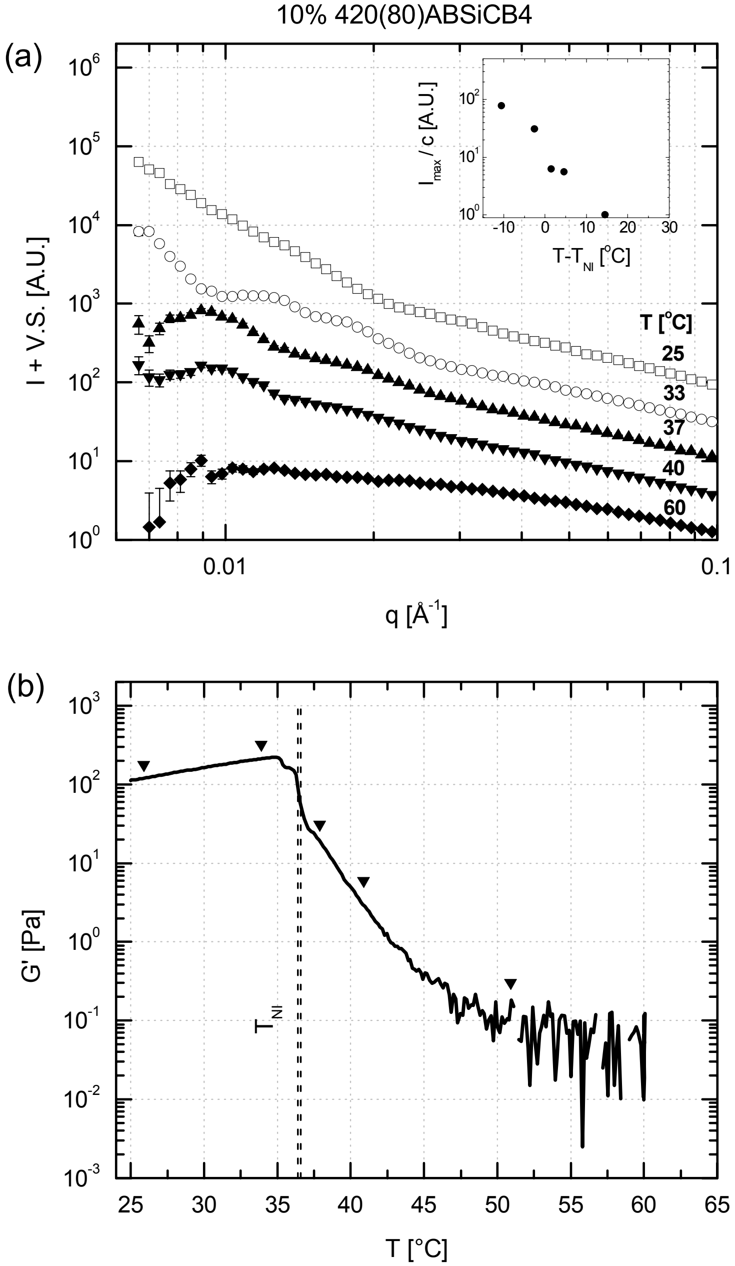

Figure 3.13 SANS and rheology of 10 wt % 420(80)ABSiCB4. (a) The low *q* portions of SANS patterns collected at different temperatures in the nematic phase (open symbols) and in the isotropic phase (filled symbols). The intensities at temperatures less than 40 °C are successively shifted upwards by powers of three for clarity. The inset shows the maximum scattered intensity normalized by the solution concentration (I_{max} / c) as a function of reduced temperature (T - T_{NI}). (b) The storage modulus (G') at ω = 10 rad/s as a function of temperature. Triangles are positioned at the same reduced temperatures where SANS patterns were collected. The solution is biphasic between 36.4 and 36.6 °C.

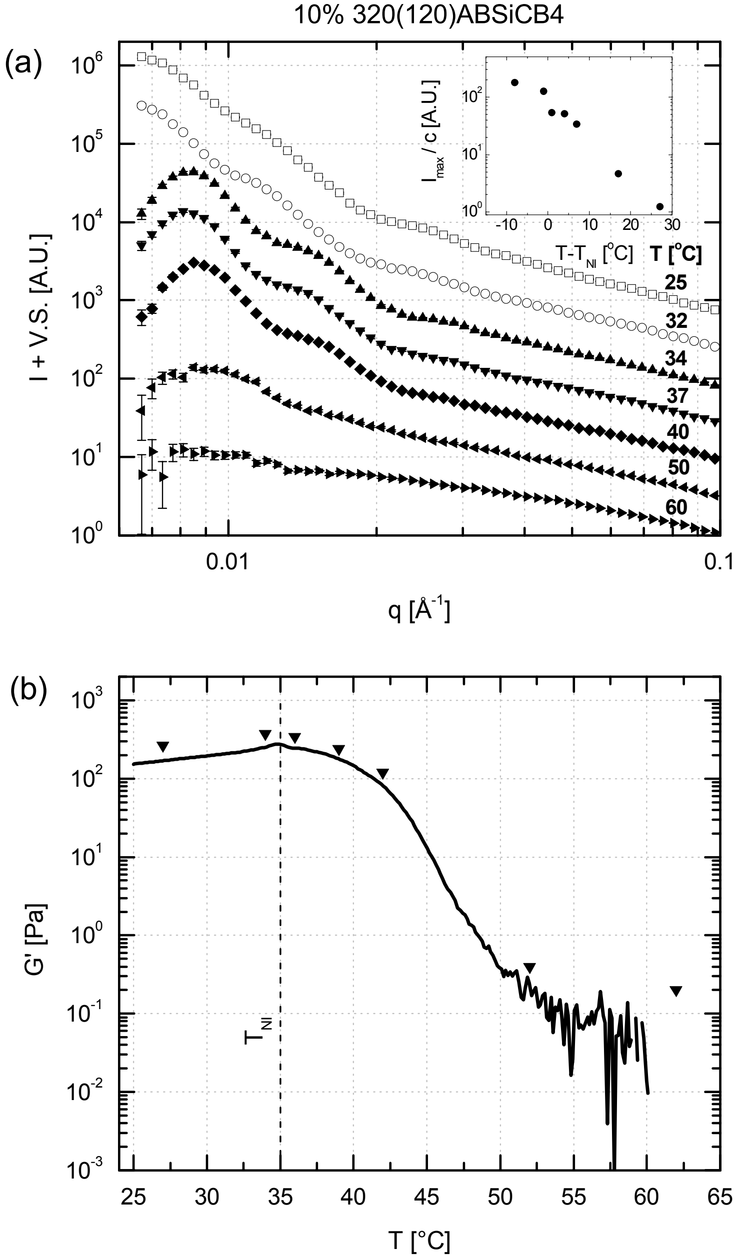

Figure 3.14 SANS and rheology of 10 wt % 320(120)ABSiCB4. (a) The low q portions of SANS patterns collected at different temperatures in the nematic phase (open symbols) and in the isotropic phase (filled symbols). The intensities at temperatures less than 40 °C are successively shifted upwards by powers of three for clarity. The inset shows the maximum scattered intensity normalized by the solution concentration (I_{max} / c) as a function of reduced temperature (T - T_{NI}). (b) The storage modulus (G') at ω = 10 rad/s as a function of temperature. Triangles are positioned at the same reduced temperatures where SANS patterns were collected.

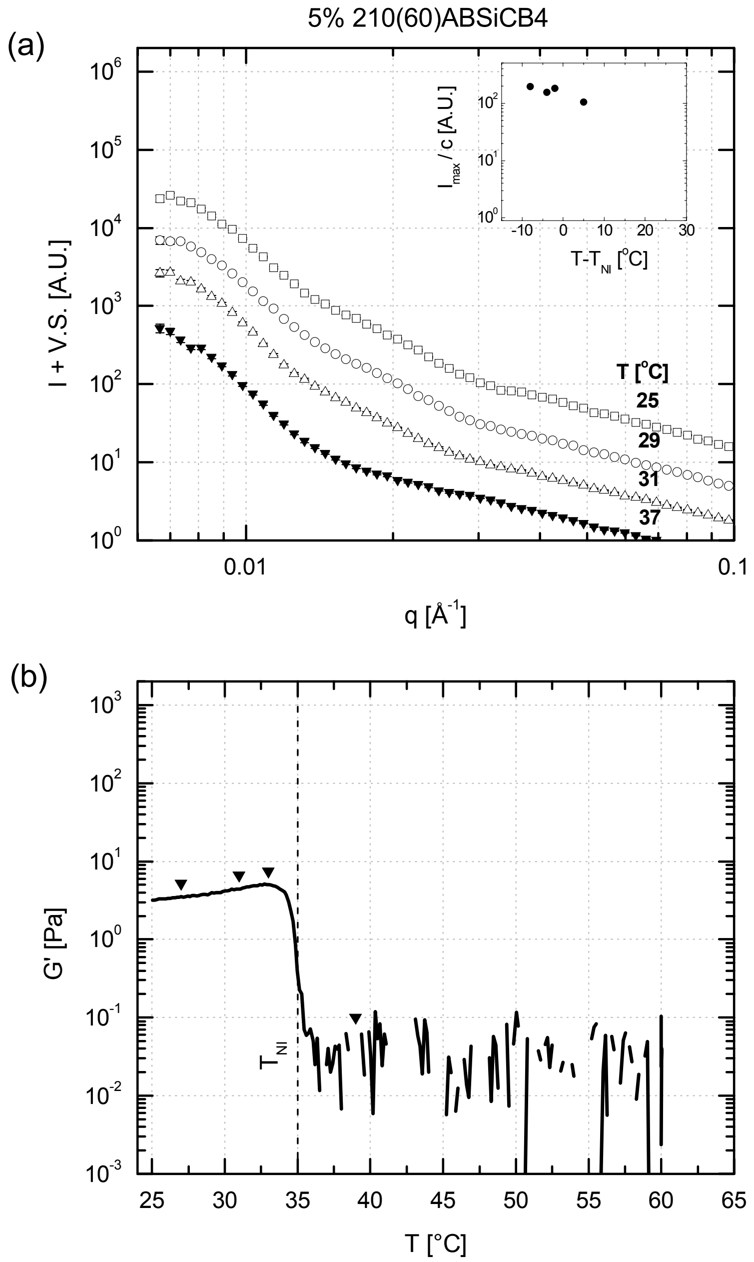

Figure 3.15 SANS and rheology of 5 wt % 210(60)ABSiCB4. (a) The low *q* portions of SANS patterns collected at different temperatures in the nematic phase (open symbols) and in the isotropic phase (filled symbols). The intensities at temperatures less than 40 °C are successively shifted upwards by powers of three for clarity. The inset shows the maximum scattered intensity normalized by the solution concentration (I_{max} / c) as a function of reduced temperature (T - T_{NI}). (b) The storage modulus (G') at ω = 10 rad/s as a function of temperature. Triangles are positioned at the same reduced temperatures where SANS patterns were collected.

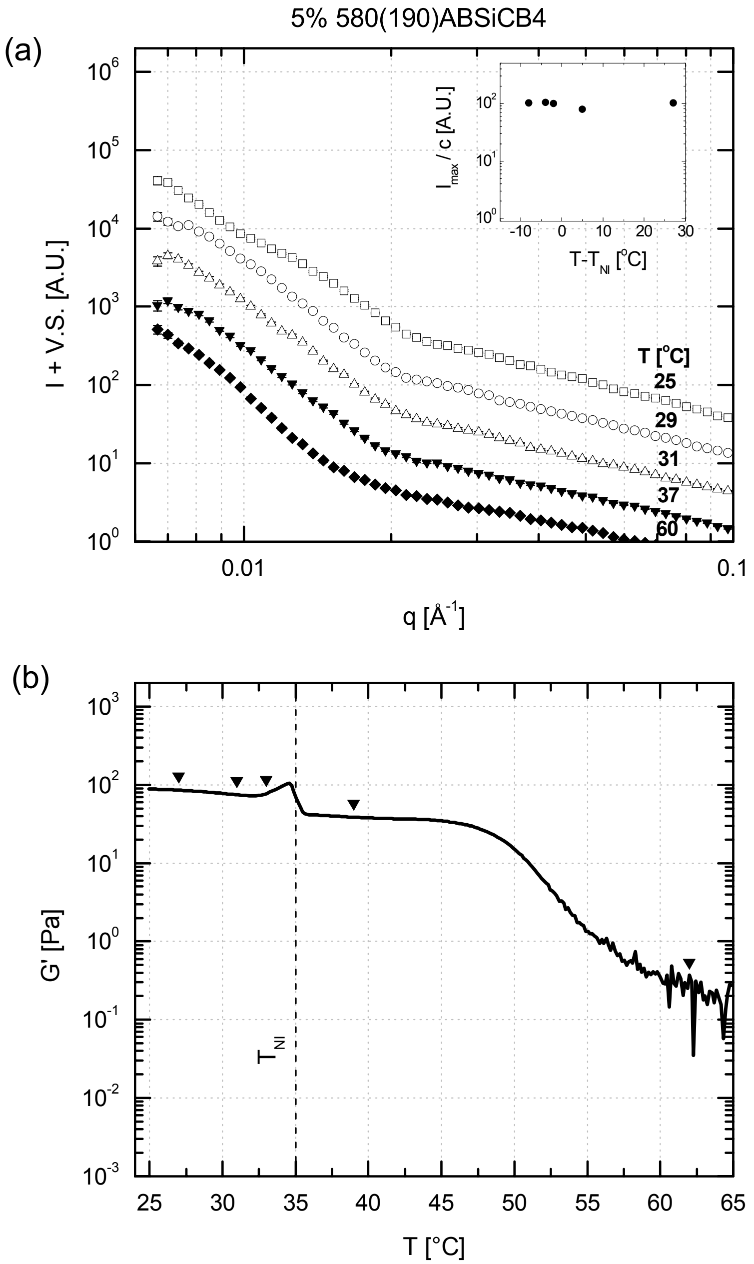

Figure 3.16 SANS and rheology of 5 wt % 580(190)ABSiCB4. (a) The low q portions of SANS patterns collected at different temperatures in the nematic phase (open symbols) and in the isotropic phase (filled symbols). The intensities at temperatures less than 40 °C are successively shifted upwards by powers of three for clarity. The inset shows the maximum scattered intensity normalized by the solution concentration (I_{max} / c) as a function of reduced temperature (T - T_{NI}). (b) The storage modulus (G') at ω = 10 rad/s as a function of temperature. Triangles are positioned at the same reduced temperatures where SANS patterns were collected.

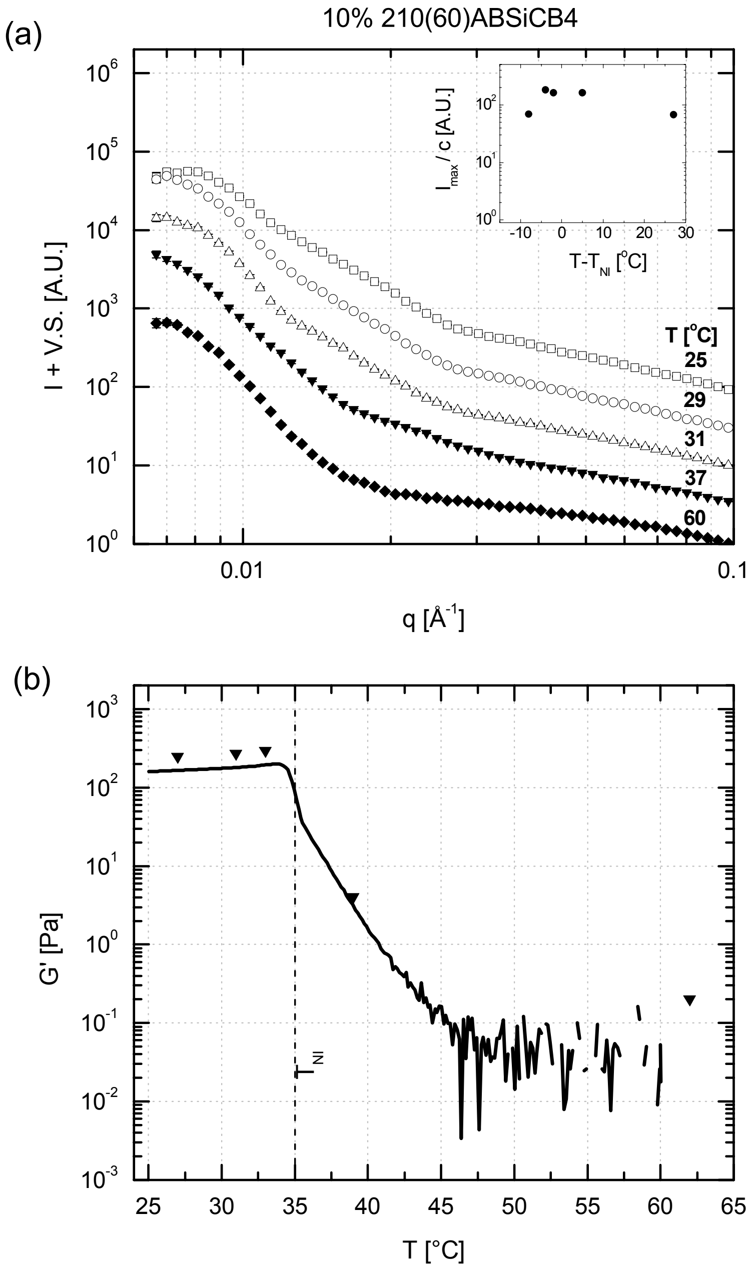

Figure 3.17 SANS and rheology of 10 wt % 210(60)ABSiCB4. (a) The low *q* portions of SANS patterns collected at different temperatures in the nematic phase (open symbols) and in the isotropic phase (filled symbols). The intensities at temperatures less than 40 °C are successively shifted upwards by powers of three for clarity. The inset shows the maximum scattered intensity normalized by the solution concentration (I_{max} / c) as a function of reduced temperature (T - T_{NI}). (b) The storage modulus (G') at ω = 10 rad/s as a function of temperature. Triangles are positioned at the same reduced temperatures where SANS patterns were collected.

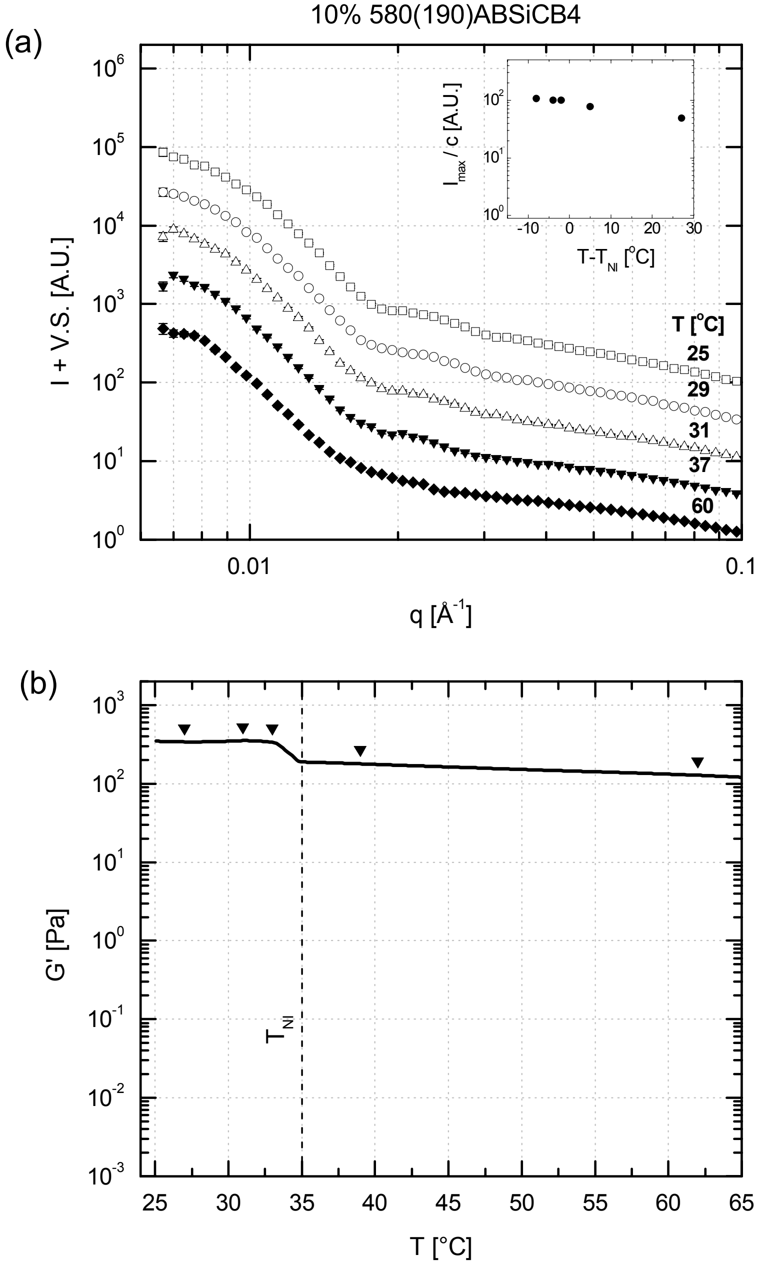

Figure 3.18 SANS and rheology of 10 wt % 580(190)ABSiCB4. (a) The low *q* portions of SANS patterns collected at different temperatures in the nematic phase (open symbols) and in the isotropic phase (filled symbols). The intensities at temperatures less than 40 °C are successively shifted upwards by powers of three for clarity. The inset shows the maximum scattered intensity normalized by the solution concentration (I_{max} / c) as a function of reduced temperature (T - T_{NI}). (b) The storage modulus (G') at ω = 10 rad/s as a function of temperature. Triangles are positioned at the same reduced temperatures where SANS patterns were collected.

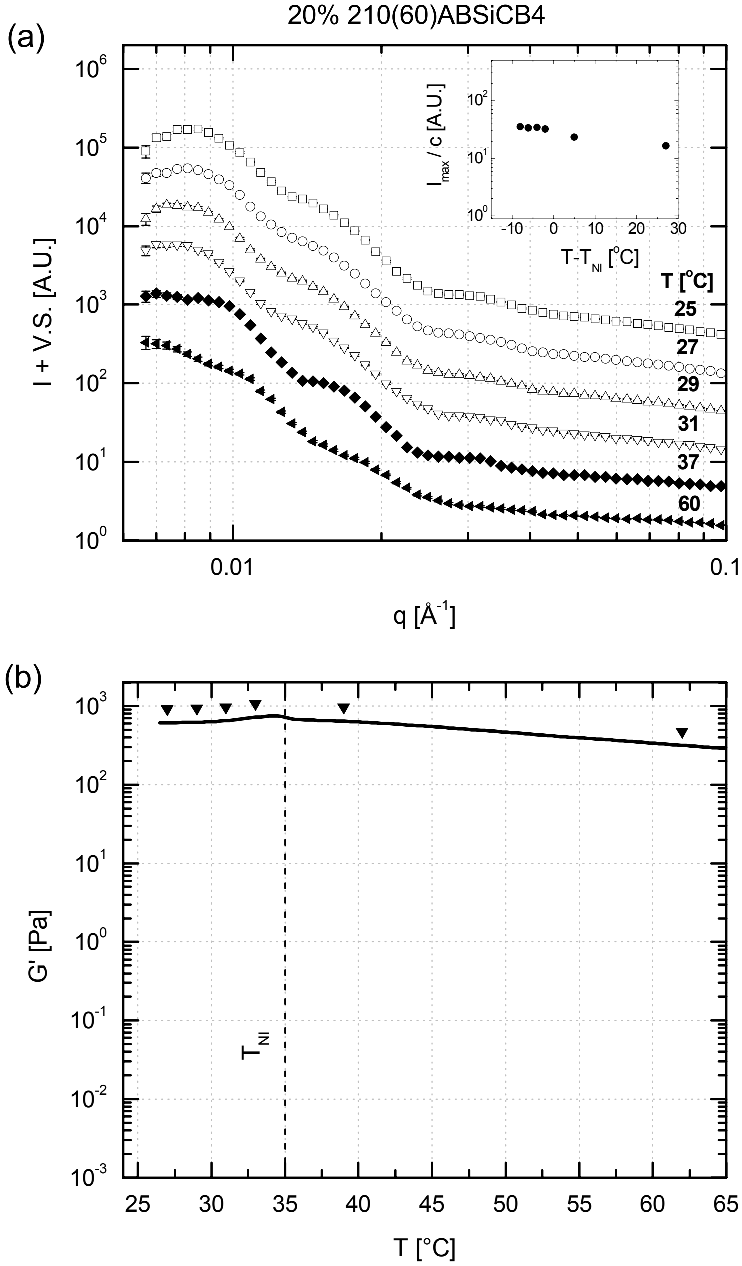

Figure 3.19 SANS and rheology of 20 wt % 210(60)ABSiCB4. (a) The low q portions of SANS patterns collected at different temperatures in the nematic phase (open symbols) and in the isotropic phase (filled symbols). The intensities at temperatures less than 40 °C are successively shifted upwards by powers of three for clarity. The inset shows the maximum scattered intensity normalized by the solution concentration (I_{max} / c) as a function of reduced temperature (T - T_{NI}). (b) The storage modulus (G') at $\omega = 10$ rad/s as a function of temperature. Triangles are positioned at the same reduced temperatures where SANS patterns were collected.

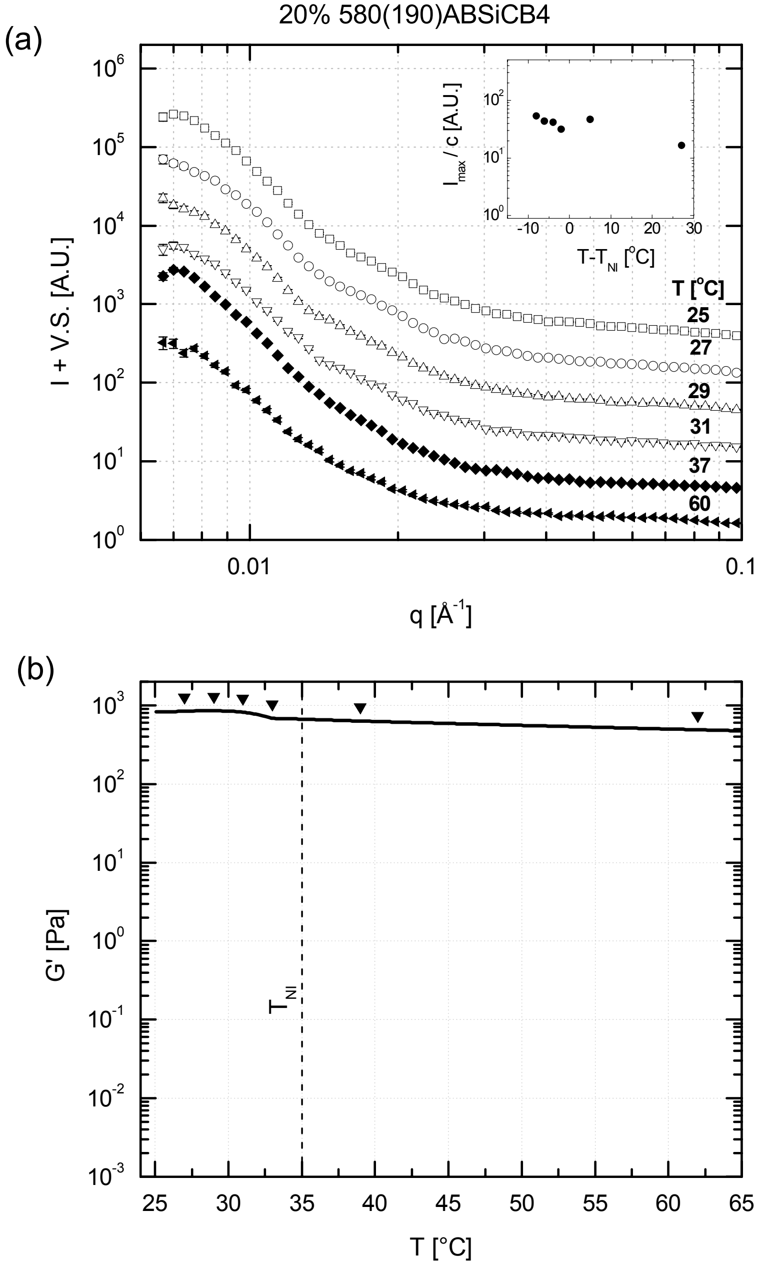

Figure 3.20 SANS and rheology of 20 wt % 580(190)ABSiCB4. (a) The low *q* portions of SANS patterns collected at different temperatures in the nematic phase (open symbols) and in the isotropic phase (filled symbols). The intensities at temperatures less than 40 °C are successively shifted upwards by powers of three for clarity. The inset shows the maximum scattered intensity normalized by the solution concentration (I_{max} / c) as a function of reduced temperature (T - T_{NI}). (b) The storage modulus (G') at ω = 10 rad/s as a function of temperature. Triangles are positioned at the same reduced temperatures where SANS patterns were collected.

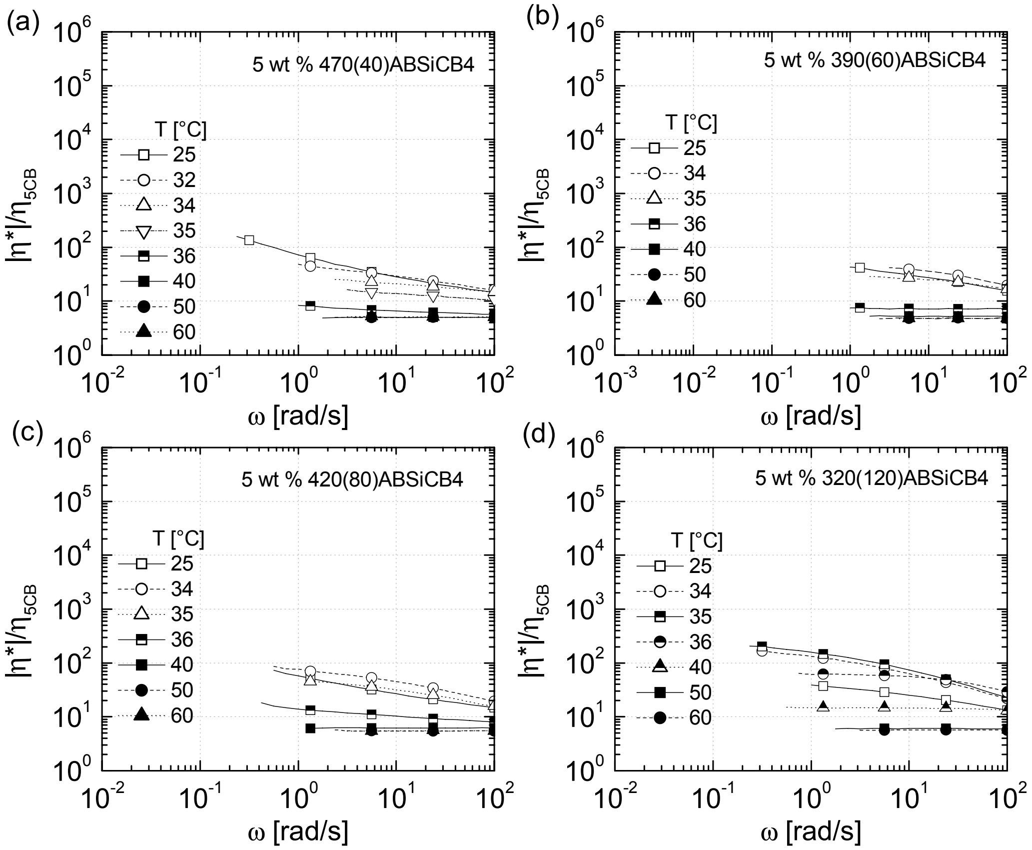

Figure 3.21 Frequency (ω) dependence of the magnitude of the complex viscosity ($|\eta^*|$) of 5 wt % solutions of PS-SGLCP diblock copolymers having similar total molecular weights (440 - 510 kg/mol) and PS block sizes of (a) 40 kg/mol, (b) 60 kg/mol, (c) 80 kg/mol, and (d) 120 kg/mol. The complex viscosity is reduced by the bulk viscosity of 5CB (η_{5CB}) at the same temperature. In the nematic phase, data are represented by open symbols. In the isotropic phase, half-filled symbols indicate a viscoelastic solution and filled symbols are used in the terminal regime where solutions behave as viscous fluids.

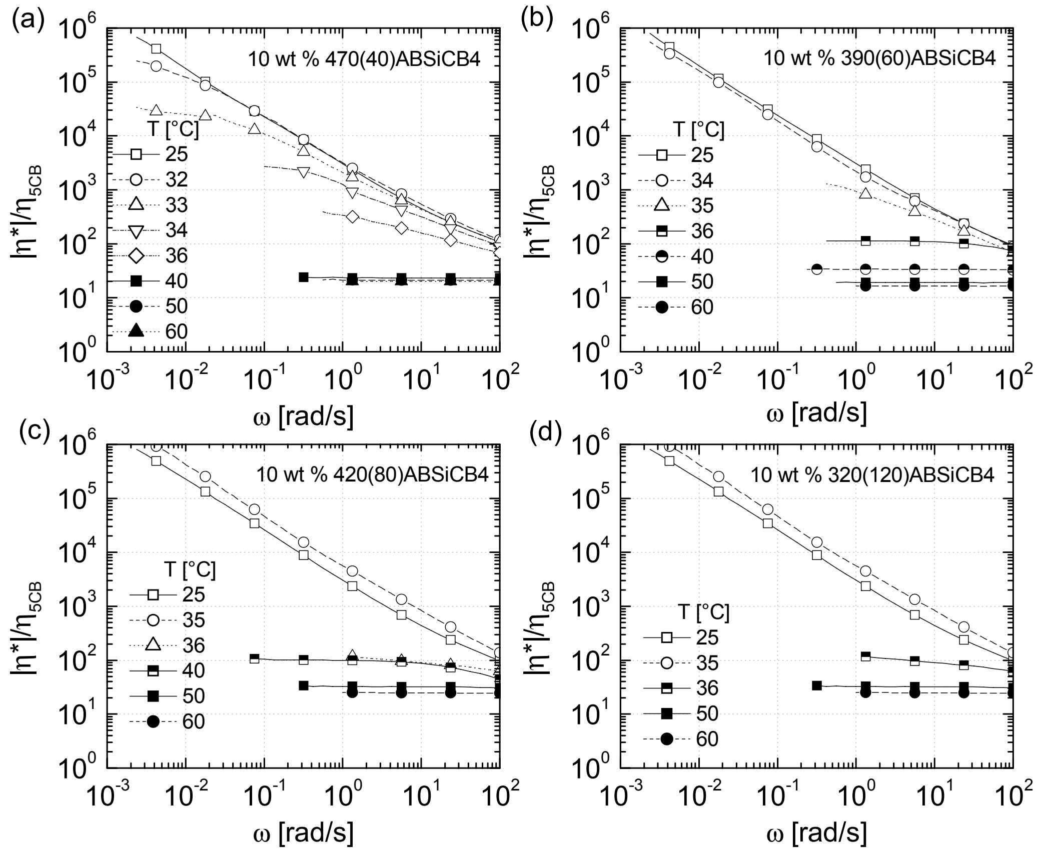

Figure 3.22 Frequency (ω) dependence of the magnitude of the complex viscosity ($|\eta^*|$) of 10 wt % solutions of PS-SGLCP diblock copolymers having similar total molecular weights (440 - 510 kg/mol) and PS block sizes of (a) 40 kg/mol, (b) 60 kg/mol, (c) 80 kg/mol, and (d) 120 kg/mol. The complex viscosity is reduced by the bulk viscosity of 5CB (η_{5CB}) at the same temperature. In the nematic phase, data are represented by open symbols. In the isotropic phase, half-filled symbols indicate a viscoelastic solution and filled symbols are used in the terminal regime where solutions behave as viscous fluids.

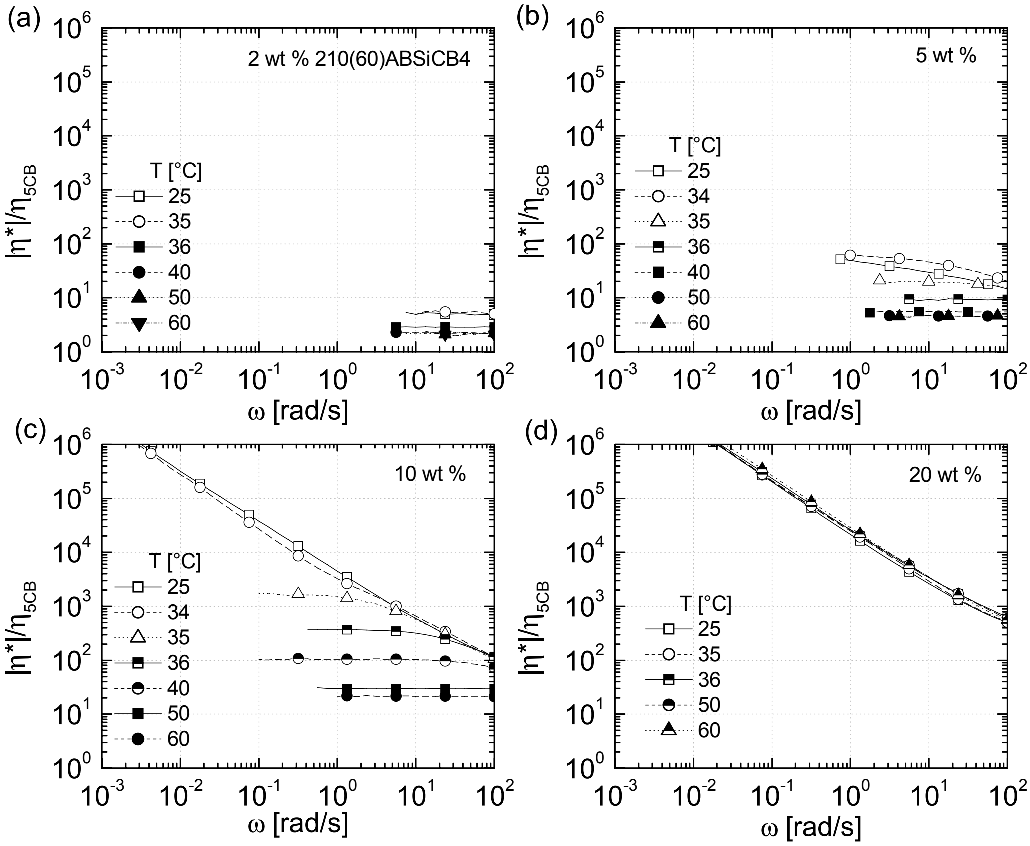

Figure 3.23 Frequency (ω) dependence of the magnitude of the complex viscosity ($|\eta^*|$) of solutions of PS-SGLCP diblock copolymer 210(60)ABSiCB4 at concentrations of (a) 2 wt %, (b) 5 wt %, (c) 10 wt %, and (d) 20 wt %. The complex viscosity is reduced by the bulk viscosity of 5CB (η_{5CB}) at the same temperature. In the nematic phase, data are represented by open symbols. In the isotropic phase, half-filled symbols indicate a viscoelastic solution and filled symbols are used in the terminal regime where solutions behave as viscous fluids.

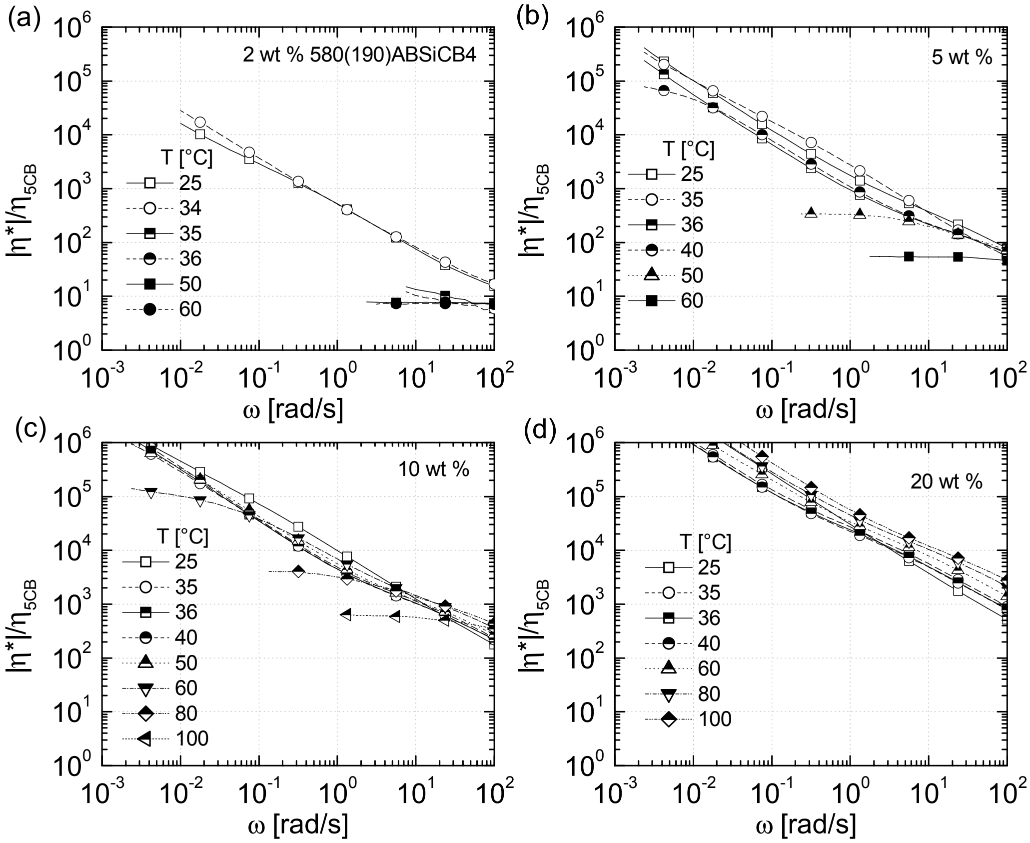

Figure 3.24 Frequency (ω) dependence of the magnitude of the complex viscosity ($|\eta^*|$) of solutions of PS-SGLCP diblock copolymer 580(190)ABSiCB4 at concentrations of (a) 2 wt %, (b) 5 wt %, (c) 10 wt %, and (d) 20 wt %. The complex viscosity is reduced by the bulk viscosity of 5CB (η_{5CB}) at the same temperature. In the nematic phase, data are represented by open symbols. In the isotropic phase, half-filled symbols indicate a viscoelastic solution and filled symbols are used in the terminal regime where solutions behave as viscous fluids.

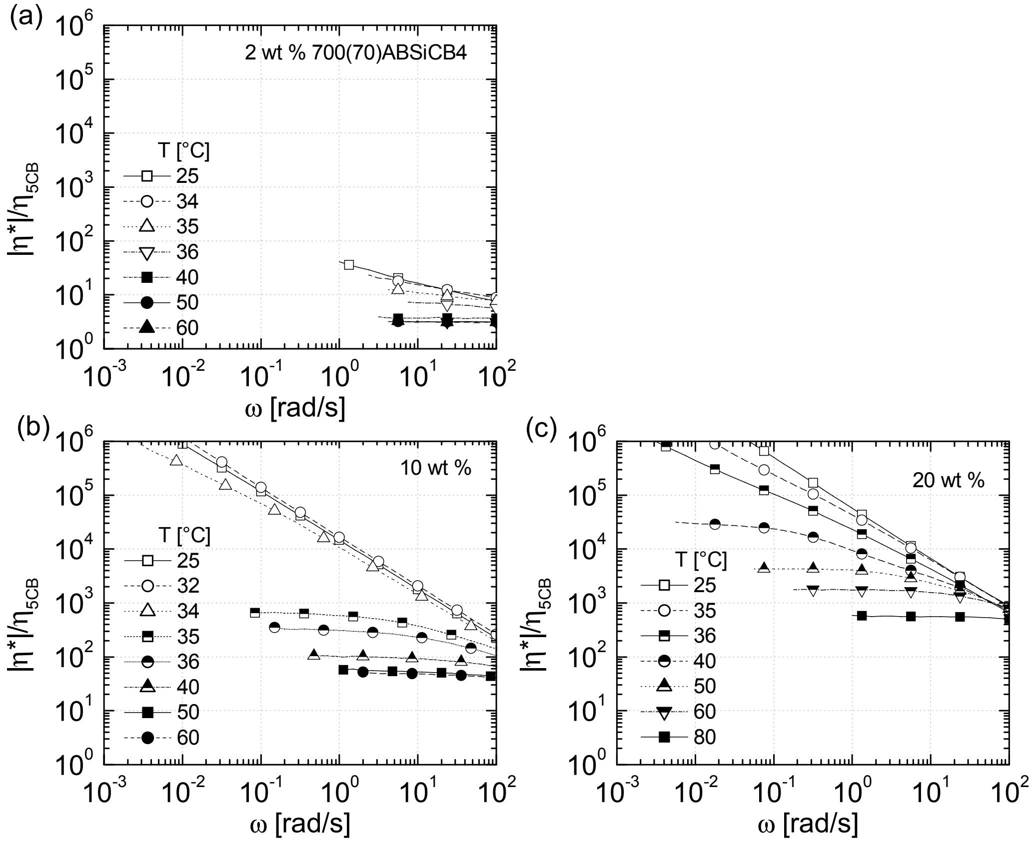

Figure 3.25 Frequency (ω) dependence of the magnitude of the complex viscosity ($|\eta^*|$) of solutions of PS-SGLCP diblock copolymer 700(70)ABSiCB4 at concentrations of (a) 2 wt %, (b) 10 wt %, and (c) 20 wt %. The complex viscosity is reduced by the bulk viscosity of 5CB (η_{5CB}) at the same temperature. In the nematic phase, data are represented by open symbols. In the isotropic phase, half-filled symbols indicate a viscoelastic solution and filled symbols are used in the terminal regime where solutions behave as viscous fluids.

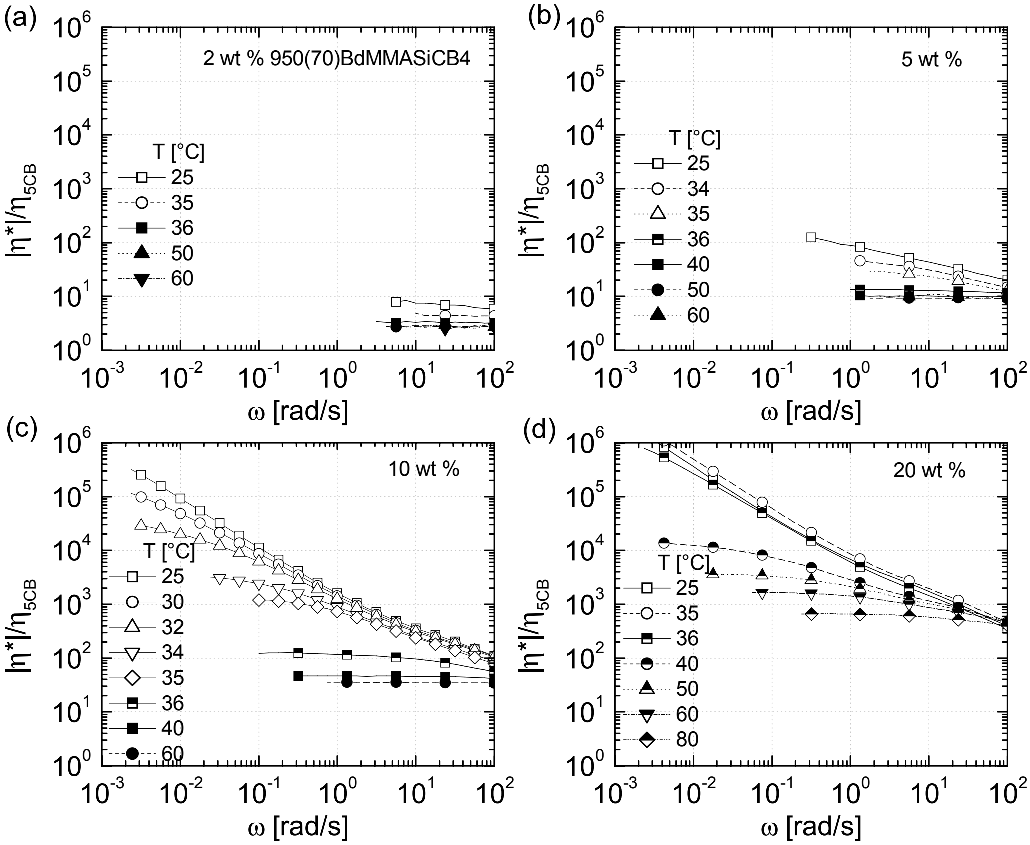

Figure 3.26 Frequency (ω) dependence of the magnitude of the complex viscosity ($|\eta^*|$) of solutions of PMMA-SGLCP diblock copolymer 950(70)BdMMASiCB4 at concentrations of (a) 2 wt %, (b) 5 wt %, (c) 10 wt %, and (d) 20 wt %. The complex viscosity is reduced by the bulk viscosity of 5CB (η_{5CB}) at the same temperature. In the nematic phase, data are represented by open symbols. In the isotropic phase, half-filled symbols indicate a viscoelastic solution and filled symbols are used in the terminal regime where solutions behave as viscous fluids.

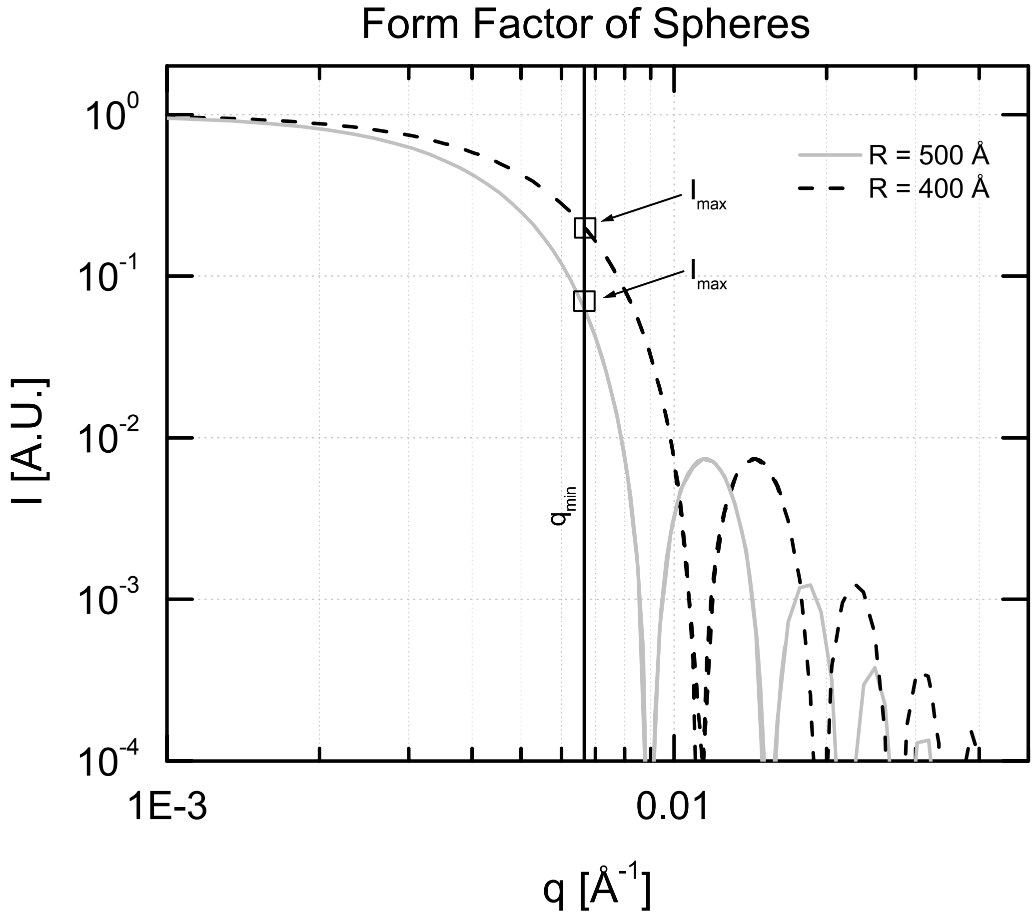

Figure 3.27 The form factor of spheres with radius, *R*, of 400 and 500 Å. In the low *q* limit, both form factors are equal ($P(q) = 1$), but the maximum scattered intensity is measured at the minimum accessible *q* ($q_{min} = 0.00666$ Å^{-1}). Thus, changing the size of the particles can result in changes to the measured I_{max}.

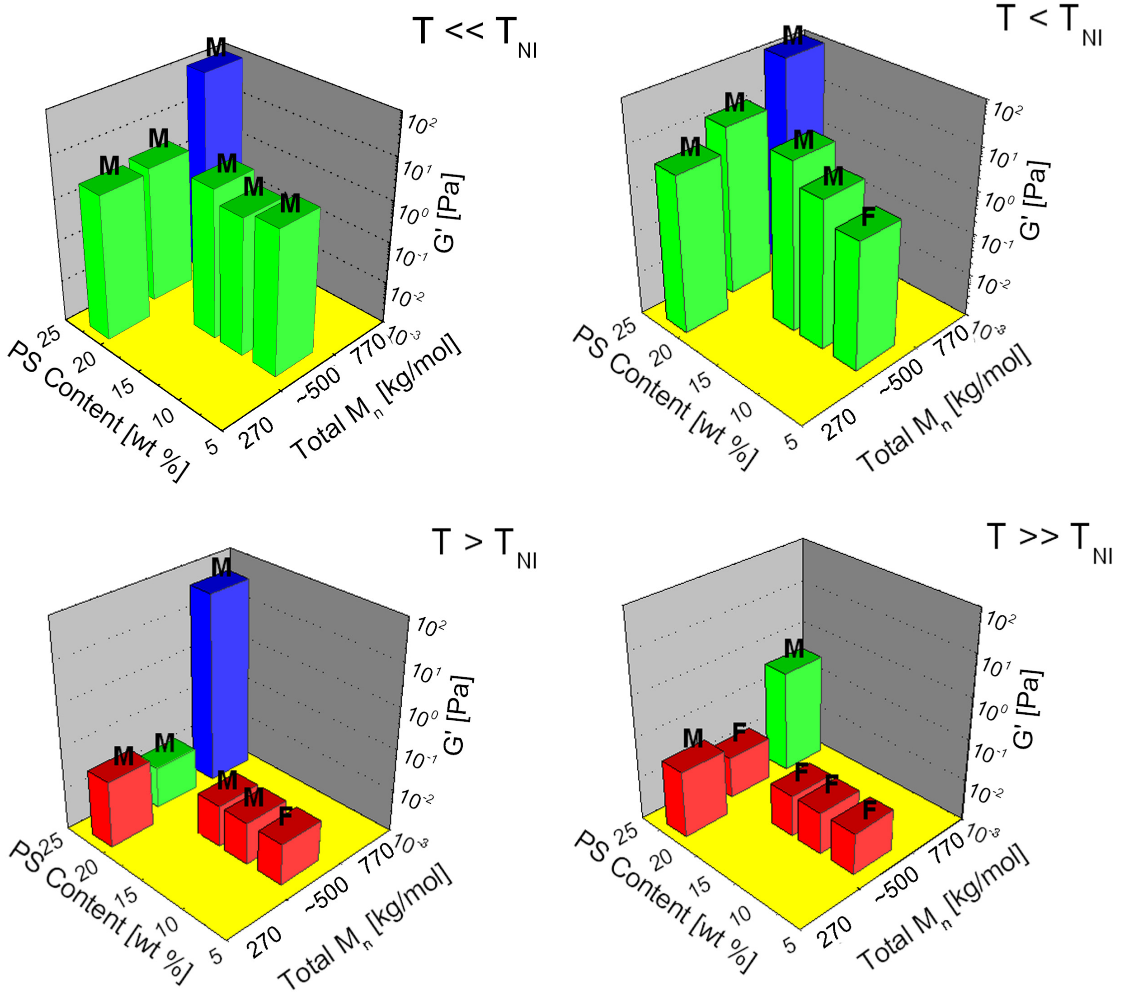

Figure 3.28 The storage modulus (*G'*) of 5 wt % PS-SGLCP diblock solutions at $\omega = 10$ rad/s and temperatures of 25 °C ($T << T_{NI}$), 32-34 °C ($T < T_{NI}$), 40 °C ($T > T_{NI}$), and 60 °C ($T >> T_{NI}$). Blue bars indicate the solution is a gel, green bars indicate a viscoelastic fluid, and red bars indicate a viscous fluid. The letters "M" and "F" indicate that the diblock exists as micelles or free chains, respectively.

3.8 References

[1] Park, C.; Yoon, J.; Thomas, E. L. Enabling nanotechnology with self assembled block copolymer patterns. *Polymer* **2003**, *44*, 6725-6760.

[2] Hamley, I. W. *The Physics of Block Copolymers*, Oxford University Press: Oxford, 1998.

[3] Hamley, I. W.; Fairclough, J. P. A.; Ryan, A. J.; Ryu, C. Y.; Lodge, T. P.; Gleeson, A. J.; Pedersen, J. S. Micellar Ordering in Concentrated Solutions of Di- and Triblock Copolymers in a Slightly Selective Solvent. *Macromolecules* **1998**, *31*, 1188-1196.

[4] Hanley, K. J.; Lodge, T. P.; Huang, C.-I. Phase Behavior of a Block Copolymer in Solvents of Varying Selectivity. *Macromolecules* **2000**, *33*, 5918-5931.

[5] Lai, C.; Russel, W. B.; Register, R. A. Phase Behavior of Styrene-Isoprene Diblock Copolymers in Strongly Selective Solvents. *Macromolecules* **2002**, *35*, 841-849.

[6] Lodge, T. P.; Hanley, K. J.; Pudil, B.; Alahapperuma, V. Phase Behavior of Block Copolymers in a Neutral Solvent. *Macromolecules* **2003**, *36*, 816-822.

[7] Lodge, T. P.; Pudil, B.; Hanley, K. J. The Full Phase Behavior for Block Copolymers in Solvents of Varying Selectivity. *Macromolecules* **2002**, *35*, 4707-4717.

[8] Lodge, T. P.; Xu, X.; Ryu, C. Y.; Hamley, I. W.; Fairclough, J. P. A.; Ryan, A. J.; Pedersen, J. S. Structure and Dynamics of Concentrated Solutions of Asymmetric Block Copolymers in Slightly Selective Solvents. *Macromolecules* **1996**, *29*, 5955-5964.

[9] McConnell, G. A.; Gast, A. P. Melting of Ordered Arrays and Shape Transitions in Highly Concentrated Diblock Copolymers Solutions. *Macromolecules* **1997**, *30*, 435-444.

[10] Lodge, T. P.; Blazey, M. A.; Liu, Z. Asymmetric block copolymers in neutral good solvents: self-diffusion through the ordering transition. *Macromol. Chem. Phys.* **1997**, *198*, 983-995.

[11] Hsu, C. C.; Prausnitz, J. M. Thermodynamics of Polymer Compatibility in Ternary Systems. *Macromolecules* **1974**, *7*, 320-324.

[12] Olabisi, O.; Robeson, L. M.; Shaw, M. T. *Polymer-Polymer Miscibility*, Academic Press, Inc.: San Diego, 1979.

[13] Scott, R. L. The Thermodynamics of High Polymer Solutions. V. Phase Equilibria in the Ternary System: Polymer 1- Polymer 2- Solvent. *J. Chem. Phys.* **1949**, *17*, 279-284.

[14] Tompa, H. Phase Relationships in Polymer Solutions. *Trans. Faraday Soc.* **1949**, *45*, 1142-1152.

[15] Zeman, L.; Patterson, D. Effect of the Solvent on Polymer Incompatibility in Solution. *Macromolecules* **1972**, *5*, 513-516.

[16] Bang, J.; Viswanathan, K.; Lodge, T. P.; Park, M. J.; Char, K. Temperature-dependent micellar structures in poly(styrene-b-isoprene) diblock copolymer solutions near the critical micelle temperature. *J. Chem. Phys.* **2004**, *121*, 11489-11500.

[17] Lodge, T. P.; Bang, J.; Park, M. J.; Char, K. Origin of the Thermoreversible fcc-bcc Transition in Block Copolymer Solutions. *Phys. Rev. Lett.* **2004**, *92*, 145501.

[18] Benmouna, F.; Daoudi, A.; Roussel, F.; Buisine, J.-M.; Coqueret, X.; Maschke, U. Equilibrium Phase Diagram of Polystyrene and 8CB. *J. Polym. Sci., Part B: Polym. Phys.* **1999**, *37*, 1841-1848.

[19] Gogibus, N.; Maschke, U.; Benmouna, F.; Ewen, B.; Coqueret, X.; Benmouna, M. Phase Diagrams of Poly(dimethylsiloxane) and 5CB Blends. *J. Polym. Sci., Part B: Polym. Phys.* **2001**, *39*, 581-588.

[20] Verduzco, R. Texture Transitions, Electro-Optics, and Dynamics of Liquid Crystal Gels with Novel Network Architectures. Ph.D. Thesis, California Institute of Technology, Pasadena, CA, February 5, 2007.

[21] Wu, S. T.; Wang, Q. H.; Kempe, M. D.; Kornfield, J. A. Perdeuterated cyanobiphenyl liquid crystals for infrared applications. *J. Appl. Phys.* **2002**, *92*, 7146-7148.

[22] King, S. M.; Griffiths, P. C.; Cosgrove, T. Using SANS to Study Adsorbed Layers in Colloidal Dispersions. In *Applications of Neutron Scattering to Soft Condensed Matter*; B.J. Gabrys, Editor; Gordon and Breach Science Publishers: Amsterdam, 2000.

[23] McConnell, G. A.; Gast, A. P.; Huang, J. S.; Smith, S. D. Disorder-Order Transitions in Soft Sphere Polymer Micelles. *Physical Review Letters* **1993**, *71*, 2102-2105.

[24] Watanabe, H.; Kotaka, T. Rheology of Ternary Mixtures of Styrene - Butadiene Diblock Copolymer, Homopolymer, and n-Tetradecane. *Journal of Rheology* **1983**, *27*, 223-240.

[25] Watanabe, H. Rheology of diblock copolymer micellar systems. *Acta Polymerica* **1997**, *48*, 215-233.

[26] Watanabe, H.; Kanaya, T.; Takahashi, Y. Equilibrium Elasticity of Diblock Copolymer Micellar Lattice. *Macromolecules* **2001**, *34*, 662-665.

[27] Tanaka, F. Theoretical Study of Molecular Association and Thermoreversible Gelation in Polymers. *Polym. J. (Tokyo, Jpn.)* **2002**, *34*, 479-509.

[28] Tanaka, F. Flows in Polymer Networks. *JSME Int J B-Fluid T* **2002**, *45*, 123-128.

[29] Fredrickson, G. H.; Leibler, L. Theory of Block Copolymer Solutions: Nonselective Good Solvents. *Macromolecules* **1989**, *22*, 1238-1250.

[30] Halperin, A.; Tirrell, M.; Lodge, T. P. Tethered Chains in Polymer Microstructures. *Advances in Polymer Science* **1992**, *100*, 31-71.

[31] Hammouda, B.; Ho, D. L.; Kline, S. Insight into Clustering in Poly(ethylene oxide) Solutions. *Macromolecules* **2004**, *37*, 6932-6937.

[32] Mortensen, K.; Pedersen, J. S. Structural Study of the Micelle Formation of Poly(ethylene oxide)-Poly(propylene oxide)-Poly(ethylene oxide) Triblock Copolymer in Aqueous Solution. *Macromolecules* **1993**, *26*, 805-812.

[33] Bouchaour, T.; Benmouna, F.; Leclercq, L.; Ewen, B.; Coqueret, X.; Benmouna, M.; Maschke, U. Phase equilibrium of poly (n-butyl acrylate) and E7. *Liq. Cryst.* **2000**, *27*, 413-420.

[34] Ahn, W.; Kim, C. Y.; Kim, H.; Kim, S. C. Phase Behavior of Polymer/Liquid Crystal Blends. *Macromolecules* **1992**, *25*, 5002-5007.

[35] Hori, H.; Urakawa, O.; Adachi, K. Dielectric Relaxation in Phase-Segregated Mixtures of Polystyrene and Liquid Crystal 5CB. *Macromolecules* **2004**, *37*, 1583-1590.

[36] Hakemi, H. Elastic constants in dilute poly(styrene)/nematic liquid crystal solutions - effects of concentration and molecular weight. *Polymer* **1999**, *40*, 4099-4103.

Chapter 4

SYNERGISTIC ORDERING OF SIDE-GROUP LIQUID CRYSTAL POLYMER AND SMALL MOLECULE LIQUID CRYSTAL: ORDER AND PHASE BEHAVIOR OF NEMATIC POLYMER SOLUTIONS

4.1 Introduction..90

4.2 Experimental...94

4.3 Results..97

4.4 Discussion..100

4.5 Conclusions...105

4.6 Tables..107

4.7 Figures...108

4.8 References...117

I am grateful to Sonjong Hwang (Caltech Solid-State NMR Facility) for his assistance with setting up the deuterium NMR experiments reported in this chapter.

4.1 Introduction

4.1.1 Background

Random-coil polymers are rarely soluble in small-molecule nematic liquid crystals (LCs) because the solvent's orientational order presents a large entropic penalty to dissolution.[1, 2] Decorating the polymer backbone with liquid crystalline moieties yields a side-group liquid crystal polymer (SGLCP) with orientational order of its own. Nematic interactions with the polymer side-groups make it possible to dissolve an SGLCP in an LC solvent, and rich phase behavior results from the thermodynamic balance between liquid crystalline order and the consequently anisotropic conformation of the polymer backbone. [3-16]

Mixtures of SGLCPs and small-molecule LCs usually have a transition to the isotropic phase that occurs at temperatures near or below the isotropization temperatures of the pure components;[3-14] in rare instances the mixture's isotropization point may lie slightly above that of the pure components.[16] Mixtures of SGLCP and LC also often exhibit isotropic-nematic or nematic-nematic coexistence between fully nematic and fully isotropic states.[3, 4, 7-14, 16] Phase diagrams similar to observed behavior (and a host of others yet to be observed) can be derived from Brochard's mean-field theory[12, 15] combining the Flory-Huggins theory of mixing with the Maier-Saupe theory for nematic order. Within the Brochard model, the nematic order parameters predicted by the Maier-Saupe theory strongly influence the free energy of an SGLCP/LC mixture; however, there have been surprisingly few studies in which the component order parameters were measured in conjunction with the mixture's phase behavior. The few that exist examine main-chain liquid crystal polymers,[17, 18] for which Brochard's theory breaks down because of the strong coupling of liquid crystalline order to polymer conformation.

Here we examine the phase behavior and the order parameter of each component in an SGLCP/LC mixture. Calorimetry shows that nematic order can be strongly stabilized in the mixtures relative to the pure components: there exist compositions that have isotropization points more than 15 °C greater than that of either component and have latent heats of transition much greater than either pure component. This cooperative ordering at high polymer concentration (~80 wt %) occurs despite the opposite tendency at low polymer concentration, leading to strikingly non-monotonic effects of concentration. The underlying molecular order of each component in the solutions is characterized using deuterium labeling and ^{2}H NMR spectroscopy; the solutions' overall order parameters are assessed using birefringence measurements. The results demonstrate a strong coupling between liquid crystalline order and polymer conformational entropy that is unique in comparison to the prior literature on mixtures of SGLCPs with small-molecule nematic LCs.

4.1.2 Theory

Brochard's model for predicting the phase behavior of SGLCPs and small-molecule LCs assumes complete decoupling between the polymer backbone and the orientational order of the attached mesogens. The molar free energy, G, is calculated from the sum of an isotropic contribution, G_{iso}, and a nematic contribution, G_{nem}. The isotropic free energy is given by the Flory-Huggins theory for dissolving a polymer, B, with degree of polymerization N_B in a small-molecule solvent, A:

$$G_{iso} = kT\left[\phi_A \ln \phi_A + \frac{(1-\phi_A)}{N_B}\ln(1-\phi_A) + \chi\phi_A(1-\phi_A)\right], \tag{4.1}$$

where χ is the Flory interaction parameter, ϕ_A is the volume fraction of species A, T is the temperature and k is Boltzmann's constant. The nematic free energy is given by the Maier-Saupe model:

$$G_{nem} = -\tfrac{1}{2}U_{AA}S_A^2\phi_A{}^2 - \tfrac{1}{2}U_{BB}S_B^2(1-\phi_A)^2 - U_{AB}S_AS_B\phi_A(1-\phi_A) - T\Sigma(S_A)\phi_A - T\Sigma(S_B)(1-\phi_A), \tag{4.2}$$

where S_A and S_B are the nematic order parameters of the solvent and polymer, respectively, and U_{AA}, U_{BB}, and U_{AB} are the pairwise nematic interaction parameters of two solvent mesogens, two polymer mesogens, and a solvent mesogen with a polymer mesogen, respectively. These nematic interactions are assumed to arise from van der Waals interactions between the molecules. The final two terms express the loss of entropy due to LC order that is described below.

The order parameters in G_{nem} are functions of temperature, composition, and the nematic interaction parameters and are evaluated numerically as a function of temperature and composition. Brochard uses the usual approximation of U_{ij} independent of temperature and the familiar relationship between the pure-component isotropization temperature, T_A or T_B, and its self-interaction:

$$\frac{kT_A}{U_{AA}} = \frac{kT_B}{U_{BB}} = \frac{1}{\alpha_c}, \quad \alpha_c = 4.54.^{[19]} \tag{4.3}$$

The cross interaction parameter, U_{AB}, is assumed to be related to U_{AA} and U_{BB} by

$$U_{AB} = c\sqrt{U_{AA}U_{BB}}\,, \tag{4.4}$$

where c is an unknown proportionality constant.[12, 13] If $c < 1$, nematic interactions between the polymer and solvent are unfavorable and the nematic phase is destabilized by mixing. If $c > 1$, nematic interactions between the polymer and solvent are stronger than in either pure component. At fixed T and ϕ_A, the individual species adopt individual order parameters that minimize the free energy of nematic interactions, completely decoupled from the conformational entropy of the polymer. The penalty for deviation of the orientation of species i from the director is coupled to that of the other species. The severity of the penalty for misalignment is captured by the field parameters, m_i, of the Maier-Saupe theory adapted for mixtures:

$$\begin{aligned} m_A &= \frac{\tfrac{3}{2}U_{AA}}{kT} S_A\phi_A + \frac{\tfrac{3}{2}U_{AB}}{kT} S_B(1-\phi_A) \\ m_B &= \frac{\tfrac{3}{2}U_{BB}}{kT} S_B(1-\phi_A) + \frac{\tfrac{3}{2}U_{AB}}{kT} S_A\phi_A \end{aligned} .^{[12, 15, 19]} \tag{4.5}$$

The greater m_i, the sharper the orientation distribution of species i ($m_i \to \infty$ gives a δ-function and $m_i \to 0$ gives a perfectly isotropic distribution). Therefore, the S_i's in Equation 4.5 must simultaneously satisfy

$$S_i = -\frac{1}{2} + \frac{3}{2Z_i}\int_0^1 x^2 \exp\left(m_i x^2\right)dx\,, \tag{4.6}$$

where the partition function, Z_i, is given by

$$Z_i = \int_0^1 \exp\left(m_i x^2\right)dx\,. \tag{4.7}$$

At fixed values of T and ϕ_A, S_A is solved as a function of S_B, and vice versa, and the intersection of the two curves gives the solution.

With the order parameters known, G_{nem} is calculated from Equation 4.2 with the entropy terms given by

$$\Sigma(S_i) = -k\left(\log\frac{4\pi}{Z_i} + m_i S_i\right).^{[15]} \tag{4.8}$$

When both order parameters fall below the critical value of $S_i = 0.429$ the nematic phase is unstable and G_{nem} is set to zero. The total free energy is calculated from $G = G_{nem} + G_{iso}$ assuming the Flory interaction parameter is proportional to the reciprocal of temperature

($\chi = A / T$) and two-phase coexistence is indicated when a single tangent line connects two points on $G(\phi_A)$ curve with fixed T.[12, 15]

4.2 Experimental

4.2.1 Materials

Two side-group liquid crystal homopolymers, 350HSiCB4 and 490HSiCB4, were synthesized according to the methods described in Appendix A. Isotopic labeling of the side-group was performed according to the method described in Appendix B and the labeled side-group was used to synthesize $d_2$350HSiCB4, the deuterium-labeled analog of 350HSiCB4 (Figure 4.1). These polymers' properties are summarized in Table 4.1 and the details of their characterization may be found in Appendix A.

Solutions of these polymers in the nematic LC 4-pentyl-4′-cyanobiphenyl (5CB, used as received from TCI America) were prepared by dissolving the two together in dichloromethane (DCM) then evaporating the DCM under a stream of air followed by drying in vacuum overnight.

4.2.2 Differential Scanning Calorimetry (DSC)

Differential scanning calorimetry (DSC) was performed using a Perkin-Elmer DSC 7 calorimeter. Each sample consisted of between 10 and 20 mg of solution contained in an aluminum pan and loosely covered with an aluminum lid. The pans were not sealed so as to avoid squeezing the solution out during the crimping process. Prior to loading a sample, the calorimeter's empty sample chamber was heated to 200 °C for a few minutes to drive off any residual moisture then cooled to 20 °C. Temperature scans were performed at a rate of 10 °C/min in a maximum range of 20 to 100 °C; the actual range used for a given sample was chosen to encompass the nematic-isotropic transition. The data from at least the first three full cycles of heating and cooling were discarded: data were retained when six consecutive cycles gave virtually indistinguishable results.

The onset temperature and latent heat of the nematic-isotropic phase transition were calculated from DSC data using Perkin-Elmer's Pyris® software (version 3.04). Since the heat flow versus time data has a sloping baseline, the data was numerically differentiated and ranges where the second derivative was non-zero were used to select the beginning and end points for integration. The results from six separate scans were averaged to arrive at the onset temperatures of the phase transitions on heating and on cooling. Random errors in the data sets are primarily associated with choosing the limits of integration.

A baseline subtraction and normalization procedure was applied to DSC temperature scans to aid in visualizing qualitative differences in the nematic-isotropic transition endotherms. The magnitude and the temperature-dependence of the heat capacity differs between the nematic and isotropic phase. Therefore, a quadratic fit of the baseline was performed in regions well below and well above the phase transition. To estimate a baseline underlying the phase transition itself, the two fits were extrapolated inside the transition and spliced together at the temperature that minimized the difference between the two polynomials (they would ideally be equal). The piecewise fit was subtracted from the data, which was then divided by the sample mass to give the normalized, subtracted heat flow, Q, due to the phase transition. Note that the discontinuity in the spliced baseline gives rise to a discontinuity in $Q(T)$.

4.2.3 Polarized Optical Microscopy (POM)

Polarized optical microscopy (POM) was performed using a Zeiss Universal stereomicroscope with temperature controlled by a Mettler FP82 hot stage. A small amount of polymer was placed on a microscope slide and the colorful, birefringent texture was observed between crossed polarizers while the temperature was ramped at a rate of 10 °C/min.

4.2.4 Deuterium Nuclear Magnetic Resonance Spectroscopy (^{2}H NMR)

Deuterium NMR spectra were recorded at a variety of temperatures using a Bruker Avance 200 MHz solid-state NMR spectrometer tuned to 30.73 MHz. Approximately 250 mg of polymer solution was loaded into a zirconium NMR rotor 7 mm in diameter and cooled from the isotropic phase inside the magnet to ensure alignment of the LC director parallel to the magnetic field. The sample was equilibrated at the desired temperature for 15 minutes prior to beginning data acquisition. Spectra were acquired statically using a solid-echo pulse sequence with proton decoupling and averaging between 32 and 512 scans, depending on the signal strength.

The NMR spectrometer's thermocouple was brought into registration with that of the microscope hot stage and the DSC using the liquid crystal itself: the transition temperature (T_{NI}) of each sample determined by POM (the temperature at which a sample's colored, birefringent texture disappeared) or from DSC (onset temperature upon heating) was compared to the temperature at which a single peak characteristic of an isotropic sample was first observed by ^{2}H NMR. The spectrometer's temperature controller only permits control to the nearest degree. For the purposes of these experiments, the T_{NI} was taken as the first temperature at which an isotropic ^{2}H NMR spectrum was recorded when successively increasing temperature in increments of 1 °C. The thermocouple of the spectrometer was systematically 3 °C below that of the hot stage or the DSC.

Deuterium was incorporated into the SGLCP ($d_2$350HSiCB4) or into the LC solvent by mixing d_{19}5CB with 5CB. Since the T_{NI} of d_{19}5CB (~32 °C) is substantially lower than that of 5CB (35 °C) its concentration was kept below 5 wt % in order to keep each sample's transition temperature within 1 °C of an equivalent hydrogenous sample.

4.2.5 Refractive Index Measurement

The ordinary and extraordinary refractive indices (n_o and n_e) of mixtures of 490HSiCB4 and 5CB were measured in an Atago 4T Abbe refractometer illuminated by LEDs having a peak wavelength of 630 nm and with temperature control of ± 0.1 ^{o}C achieved using circulated water from a Fisher Scientific Isotemp Refrigerated Circulator Model 900. The refractometer was calibrated with liquid standards to read the index of refraction for light with 633 nm wavelength. Monodomain samples having a uniformly aligned LC director are required to measure both n_o and n_e.[20] Alignment was achieved by coating the prisms of the refractometer with a solution of 1 % lecithin in chloroform. When the lecithin alignment layer alone was inadequate, monodomain alignment was achieved by wiggling the top prism to create shear stresses large enough to induce some macroscopic order. Prior literature on a similar polymer[21] dissolved in 5CB at similar concentration showed that shear causes the director to align near the velocity gradient direction, here normal to the prism surfaces. The birefringence of an LC monodomain causes light with different polarizations to refract at different angles; instead of the single line separating a light and dark area observed in isotropic fluids, a polarizer is used to visualize the two indices. In one orientation, a change from a bright to a dimmer region is seen at n_e and when rotated 90^o a second line corresponding to n_o is observed.

4.3 Results

4.3.1 Differential Scanning Calorimetry (DSC)

All mixtures of 350HSiCB4 and 5CB with polymer concentrations ranging from 0 to 100 wt % are nematic at room temperature and undergo a transition to the isotropic phase, indicated by an endothermic peak in the DSC trace, somewhere in the temperature range of 30 to 90 °C. The onset temperature of the transition shows a strikingly non-monotonic dependence on polymer concentration: at low polymer concentration (0 to 20 wt %) the position of the peak changes very little with concentration, it shifts to higher T in the range of 20 to 78 wt %, and shifts to lower T as concentration is further increased. In two ranges of polymer concentration, approximately 20 to 70 wt % and 85 to 95 wt %, the nematic to isotropic phase transition takes place over a broad temperature range and a shoulder is often observed in the phase transition endotherm (Figure 4.3). Although POM shows no evidence of two-phase coexistence in either the nematic or isotropic phase, the broad transitions are attributed to a biphasic region near the phase transition. We suspect that two-phase coexistence is difficult to detect by POM because the coarsening of phase separation to observable length scales is very slow, particularly for polymer concentrations of 20 wt % or more.

The qualitative trends observed in the DSC traces are reflected in the concentration dependence of the nematic to isotropic phase transition's onset temperature, T, and latent heat, $|\Delta H|$ (Figure 4.4). At concentrations less than 20 wt % polymer the onset temperature during heating is relatively constant, but in the range of 20 to 78 wt % polymer it increases sharply (Figure 4.4a), eclipsing the onset temperature of either of the pure components by a wide margin (it reaches a maximum of 80.5 °C, much greater than 36.2 °C and 63.0 °C for pure 5CB and bulk polymer, respectively). The onset temperature decreases with further increase in concentration beyond 80 wt %, and the transition becomes remarkably broad. The peculiarly broad transition observed at 91 wt % polymer (spanning > 20 °C range) is not inherent to the polymer itself, which has a single peak with a full width at half-maximum less than 3 °C. Small differences between the onset temperatures on heating versus cooling are attributed to the subcooling regularly observed in LC phase transitions. Corresponding features are evident in the transition enthalpies (Figure 4.4b). The measured value of $|\Delta H|$ on heating for pure 5CB is 2.01 ± 0.07 J/g, in good agreement with values reported in the literature[22, 23] (2.00 J/g or 1.56 J/g). For the bulk polymer $|\Delta H|$ on heating is 4.23 ± 0.03 J/g, which is much greater than values reported for other SGLCPs (0.53 and 1.9 J/g).[5, 24] In the range of 0 to 20 wt % polymer, $|\Delta H|$ decreases slightly with increasing concentration. Above 20 wt % the latent heat increases sharply with concentration, reaching a maximum (6.34 ± 0.05 J/g) at 83 wt % polymer that is substantially greater than either pure component. Between 83 and 91 wt %, $|\Delta H|$ again decreases with concentration. The concentration-dependence of $|\Delta H|$ is in stark contrast to the linear dependence reported by Finkelmann, Kock, and Rehage.[5]

4.3.2 Deuterium Nuclear Magnetic Resonance Spectroscopy (^{2}H NMR)

^{2}H NMR spectra were collected from samples containing between 0 and 10 wt % SGLCP with deuterium incorporated into either the solvent or the polymer's side groups. In the nematic phase, the spectra from d_{19}5CB consist of pairs of peaks symmetric about a frequency, ν, of 0 kHz with splittings, $\Delta\nu$, that depend on temperature (Figure 4.5a). The spectra from $d_2$350HSiCB4 consist of one pair of symmetric peaks centered about $\nu = 0$ kHz, also split by a temperature-dependent magnitude, $\Delta\nu$. The splitting derives from the deuterons' quadrupolar interactions with the local electric field gradient and when the director is parallel to the magnetic field, as is the case in these experiments, its magnitude is directly proportional to the microscopic order parameter, S_{ZZ}, of the C-D bond of interest:[25]

$$\Delta\nu = \tfrac{3}{2} Q_{CD}^{Ar} \frac{3\cos^2\theta - 1}{2} S_{ZZ}, \tag{4.9}$$

Where S_{zz} accounts for the orientation distribution of the molecule's long axis, $\boldsymbol{u}$, with respect to the magnetic field, $\boldsymbol{H}$, ½ (3 $\cos^2\theta$-1) accounts for the orientation angle of the C-D bond with respect to the molecular axis, $\boldsymbol{u}$, and $Q_{CD}{}^{Ar}$ is the quadrupolar coupling constant equal to 185 kHz for aromatic deuterons.[26] For the purposes of making comparisons between the orientational order of the solvent and the polymer side groups, the measurement of $\Delta\nu$ from d_{19}5CB is restricted to deuterons located *para-* to the alkyl chain (site "d" in Figure 4.5) since they are geometrically equivalent to the deuterons of $d_2$350HSiCB4. Emsley, Luckhurst, and Stockley have found $\theta = 60.6°$ for these deuterons in d_{19}5CB,[27] and previous measurements of the quadrupolar splittings of 4-hexyloxy-4′-cyanobiphenyl (6OCB) have demonstrated that the geometry of the aromatic deuterons located *para-* to the oxygen atom is not significantly different.[26, 28] When the polymer concentration exceeds 10 wt % the peaks in the nematic phase become broad and difficult to distinguish, possibly due to poor alignment of the LC molecules with the magnetic field.

In the isotropic phase the spectra from both d_{19}5CB and $d_2$350HSiCB4 consist of a single peak centered at $\nu = 0$ kHz (Figure 4.5b). At temperatures 1 or 2 °C below the nominal T_{NI}, ^{2}H NMR spectra from d_{19}5CB and $d_2$350HSiCB4 have both an isotropic peak at $\nu = 0$ kHz and nematic peaks split by $\Delta\nu$. The presence of both nematic and isotropic character in the spectra near T_{NI} is attributed to pretransitional orientation fluctuations induced by the strong magnetic field,[29] and should not be taken as a sign of two-phase nematic/isotropic coexistence.

The measured values of $\Delta\nu$ for the distinguishable deuterons in d_{19}5CB in the absence of polymer are within 5% of those reported by Auger et al.[30] All of these splittings decrease when polymer is added. Thus, the order parameter of the LC solvent decreases when polymer is dissolved in it (inset in Figure 4.6a). At each concentration, the order parameter of the polymer is consistently lower than that of the LC solvent (Figure 4.6): for example, at 5 wt % polymer and $T = T_{NI}$ - 9 °C, $S_{ZZ}^{5CB} = 0.31$ and $S_{ZZ}^{350HSiCB4} = 0.25$. As the concentration of polymer increases, S_{ZZ} of d_{19}5CB decreases (Figure 4.6a). On the other hand, S_{ZZ} of $d_2$350HSiCB4 is relatively insensitive to polymer concentration (Figure 4.6b).

4.3.3 Refractive Indices

The temperature-dependent ordinary and extraordinary refractive indices (n_o and n_e, respectively) measured for pure 5CB (Figure 4.7) are within 0.5% of the values reported by Karat and Madhusudana.[31] The effect of polymer on both n_o and n_e could be measured up to 10 wt %; however, n_e could not be measured for 20 wt % 490HSiCB4 because the sample alignment was poor and at concentrations > 20 wt %, neither n_o nor n_e could be measured accurately. Addition of polymer distinctly reduces n_e, over the range of accessible concentrations. The ordinary refractive index is relatively insensitive to polymer concentration, showing a slight increase with increasing concentration. The refractive index in the isotropic phase, n_{iso} is also insensitive to added polymer, showing a slight decrease with addition of polymer.

The nematic order parameter, S, is calculated from the ordinary and extraordinary refractive indices using the method described by Haller et al.[32] The order parameter is related to n_o and n_e by

$$S = \frac{n_e^2 - n_o^2}{n_{avg}^2 - 1}\frac{\langle\alpha\rangle}{\Delta\alpha}, \tag{4.10}$$

where $n_{avg}^2 = ⅓n_e^2 + ⅔n_o^2$, $\Delta\alpha$ is the anisotropy of the polarizability, and $<\alpha>$ is the average polarizability.[31-33] The Haller analysis aims to estimate the ratio $<\alpha>/\Delta\alpha$ from the temperature dependence of n_o and n_e, using the empirical observation that $\log[S\Delta\alpha]$ is proportional to $\log[(T_{NI} - T)/T_{NI}]$. The average polarizability is related to the refractive indices by

$$\frac{4\pi\rho N_A}{M}\langle\alpha\rangle = \frac{n_e^2 + 2n_o^2 - 3}{3n_{avg}^2 + 6}, \tag{4.11}$$

where ρ and M are the LC's density and the molar mass, respectively, and N_A is Avogadro's number.[32] Combining Equations 4.10 and 4.11 gives $S\Delta\alpha$ in terms of the known quantities n_o, n_e, ρ, and M. Plotting log[$S\Delta\alpha$] versus log[(T_{NI} - T)/T_{NI}] and extrapolating to T = 0 K, where S = 1, gives $\Delta\alpha$. Combined with $<\alpha>$ calculated from Equation 4.11, the order parameter is calculated from the estimate of $<\alpha>/\Delta\alpha$ (Figure 4.8).

The calculated order parameters for 5CB are less than 13% different from those estimated by Karat and Madhusudana.[31] The order parameter of 1 wt % 490HSiCB4 is unchanged from that of 5CB throughout the entire temperature range studied. As polymer concentration is increased to 5 or 10 wt %, the order parameter curve is shifted to progressively lower values (Figure 4.8).

4.4 Discussion

Although we do not have sufficient information to produce the phase diagram of 350HSiCB4 and 5CB, we can deduce its character from the calorimetry results on heating (Figure 4.9a). In particular, the narrow single peak in the endotherm of 78 wt % 350HSiCB4 solution indicates that the phase diagram has a direct transition from the nematic to isotropic phase at that composition, with T_{NI} of approximately 80 °C. At concentrations immediately above and below 78 wt %, two-phase coexistence is indicated by broad endotherms. The biphasic temperature range can be estimated from the measured onset temperature and the temperature at which the transformation to the isotropic phase is complete (the endotherm's intensity final decrease). The DSC traces from solutions with high polymer concentration indicate wide biphasic regions; for example, in 91 wt % 350HSiCB4 the biphasic region may be as wide as 25 °C. On the solvent-rich side, the biphasic region, if it exists, appears to be less than 10 °C wide. Our data do not allow for identification of the coexisting phases (e.g. N + N or N + I).

The Brochard model commonly used to describe the phase behavior of SGLCPs with small molecule LCs can capture some of the characteristics of the 350HSiCB4/5CB phase diagram; however it does not accord with the underlying molecular order. A phase diagram calculated by Chiu and Kyu[12] using the theory for an SGLCP/LC mixture with strong interactions between the different polymer and solvent mesogens ($c = U_{AB}/(U_{AA}U_{BB})^{1/2} = 1.2$) is somewhat similar to the phase diagram inferred from the

DSC data (Figure 4.9b). The model captures the presence of a stabilized, single nematic phase that transitions to a single isotropic phase at a high temperature relative to the pure components. It also has biphasic windows at compositions above and below the composition having the maximum clearing point. However, owing to the Flory-Huggins treatment of the polymer-solvent interaction in Brochard's model, the theoretical phase diagram predicts the biphasic window to be wider on the solvent-rich side of the phase diagram ($\phi < 0.5$). In contrast, the behavior of 350HSiCB4/5CB suggests a wider biphasic window in polymer-rich solutions. Furthermore, the temperature at which the solution becomes completely isotropic in the model has a concentration dependence that is strictly concave down, whereas the observed isotropization transition changes from concave up to concave down as concentration is increased.

Brochard's theory has been used to model the experimental phase diagrams of SGLCP/LC mixtures,[11-13] and its apparent success cited as evidence that conformational entropy and LC order are decoupled. However, there appears to be no prior verification that the component order parameters are adequately modeled, so it is not known whether the theory's assumptions are substantiated or whether its agreement with observed phase behavior is coincidental. The Brochard model is founded on the Maier-Saupe theory for nematic interactions. Flory-Huggins interactions are included, which can add biphasic windows to the phase diagram, but cannot change the underlying composition dependence of the order parameters. Maier-Saupe theory predicts the species with the lower pure-component T_{NI} always has the lower order parameter in a mixture. In the present system that would imply that the order parameter of 350HSiCB4 (T_{NI} = 63 °C) would always be greater than that of 5CB (T_{NI} = 35 °C). This is clearly not the case over the range of concentration in which we can measure the component order parameters (polymer concentrations up to 10 wt %). ^{2}H NMR data from these solutions are in clear opposition to the mixing rule based on the Maier-Saupe model, showing that the order parameter of 350HSiCB4 is less than that of 5CB despite its higher clearing point in the bulk. The Brochard model gives phase diagrams with elevated T_{NI} at intermediate ϕ by allowing the nematic potential between the two species, U_{AB}, to be greater than those for the individual species, $c = U_{AB} /(U_{AA}U_{BB})^{1/2} > 1$. In this case, the Maier-Saupe mixing rule predicts that addition of the high T_{NI} species to the low T_{NI} species will increase the order parameter of the latter. In the present system that would imply that the order parameter of 5CB would increase upon addition of polymer, which is clearly not the case: both ^{2}H NMR and refractive index data show that S of 5CB decreases as polymer concentration increases from 0 to 10 wt %.

Maier-Saupe theory assumes that mesogens interact with one another entirely through van der Waals forces, and the theory's failure to describe the measured component order parameters suggests that additional thermodynamic interactions are of importance in mixtures of 350HSiCB4 and 5CB. Indeed, it has been suggested by other authors that backbone flexibility and steric effects may have a strong influence on SGLCP/LC phase behavior.[4, 7, 8, 14] Compared to the systems modeled by Chiu and Kyu, et al.[11-13] using Brochard's theory, 350HSiCB4/5CB is similar with respect the structural details of the polymer and solvent. Fits were performed to experimental data from systems employing both phenyl benzoate-based and cyanobiphenyl-based mesogens, some with polymer mesogens that are chemically similar to the solvent[4, 5, 13] and some where the mesogens are mismatched.[11, 16] They furthermore modeled SGLCPs having different types of backbones, including polysiloxane[4, 5, 16], polyacrylate[11], and poly(ethylene glycol)[13] derivatives. Their fitting to the Brochard model is equally successful for this diverse group of SGLCP/LC systems, indicating that its failure to describe data from 350HSiCB4/5CB is not simply a consequence of the species' chemical structures. The one noteworthy difference between the present SGLCP and prior systems is its extremely high molecular weight. Data fit to the Brochard model previously were from polymers having molecular weights of approximately 50 kg/mol (degree of polymerization of approximately 100), but 350HSiCB4 is almost ten times as large. The influence of polymer length in the Brochard model enters via the Flory-Huggins interaction. Therefore, increasing the chain length can open biphasic windows in the phase diagram (or increase their width). However, Brochard's model has no coupling between the polymer backbone and the nematic order of the pendant mesogens, so changing SGLCP length has no effect on the order parameter of either species.

There must be an important thermodynamic contribution from the polymer that is unaccounted for in Brochard's model, which assumes the mesogens of an SGLCP are completely decoupled from the backbone. The coupling of the polymer backbone's conformational entropy to the nematic orientation field is neglected by Brochard's theory, but likely makes an important contribution to the thermodynamics of mixtures of 350HSiCB4 and 5CB. Indeed, such an effect could also play a major role in the thermodynamics of previously studied SGLCP/LC systems. In the bulk polymer, the tendency of the mesogenic side groups to align with one another competes with the polymer's conformational entropy and the system is highly frustrated (Figure 4.10d). It appears that at compositions intermediate between bulk polymer and dilute solution the solvent serves to increase the polymer's configurational freedom, allowing it to relax some of the frustration present in the melt. The strong, non-monotonic dependence of $|\Delta H|$ and onset T on polymer concentration, especially at compositions near bulk polymer, suggests the effect is related to the two components' relative proportions. We envision that the peak in $|\Delta H|$ arises from maximizing the mesogens' orientational order while minimizing the polymer's perturbation from a random-walk conformation (Figure 4.10c). If we consider the opposite extreme, starting from pure LC and adding SGLCP to it, we introduce a population of mesogens that are constrained by attachment to the polymer. In this regime we envision that the compromise between LC orientation and conformational entropy causes the order parameters of both polymer and solvent drop as a result of the orientational frustration between the two (Figure 4.10b).

It might be possible to rigorously account for the coupling between polymer entropy and LC order by including effects of chain flexibility, similar to the theory of ten Bosch, Maissa, and Sixou for main-chain polymers.[34] In the absence of such a theory, the coupling can be empirically accounted for by introducing concentration dependence to the polymer-solvent nematic interaction parameter, U_{AB}. By doing so, the concentration dependence of the nematic-isotropic transition temperatures can be correctly captured, but the relative magnitudes of the component order parameters still cannot. The theoretical T_{NI}'s of 350HSiCB4/5CB mixtures were calculated from Equation 4.2 at fixed values of c between 0.8 and 1.2 (Figure 4.11a). The c values necessary to describe the data were used to generate a continuous function $c(\phi_B)$ using a B-spline (Figure 4.11b). The empirical $c(\phi_B)$ was then used to calculate a theoretical diagram using Brochard's model with the Flory interaction parameter arbitrarily set to $\chi = 350 / T$ (Figure 4.11c). The theoretical phase diagram resembles that inferred from the DSC data (Figure 4.9a); however, there is no physical basis for choosing a concentration dependence of U_{AB}. This exercise does serve to emphasize the idea that the interplay between polymer entropy and LC orientation depends strongly on the relative proportions of the two components and plays an important role in the system's thermodynamics that is not accounted for in Brochard's model.

4.5 Conclusions

4.5.1 Conclusions Based on the Present Work

The delicate thermodynamic balance between liquid crystalline order and polymer conformational entropy serves to stabilize the nematic phase in mixtures of 350HSiCB4 and 5CB. In dilute solutions, the tradeoff between the two causes the order parameter of the polymer side-groups to be less than that of the solvent. As concentration is increased, the orientational frustration between the two decreases the solvent order parameter as well. When the polymer concentration is increased to the range of 70 to 85 wt.-%, the minority fraction of small-molecule solvent affords the SGLCP freedom to optimize LC order subject ot the connectivity between the polymer backbone and its pendant side-groups, raising the nematic-isotropic transition temperature almost 20 °C above that of the bulk polymer and almost 45 °C higher than that of the LC solvent alone. Thus, the SGLCP must also provide a favorable host for 5CB.

The results presented here are in stark contrast to the body of literature on solutions of SGLCPs in nematic solvent. Stabilization of the nematic phase is rarely[16] observed in these systems and the LC orientation is usually concluded to be decoupled from the conformational entropy of an SGLCP. Our results suggest an avenue for future theoretical work that accounts for the interplay between the polymer's conformational entropy and liquid crystalline order in a regime intermediate between strong coupling (e.g. main-chain polymers, as considered by ten Bosch et al.[38]) and complete decoupling (Brochard's theory for side-chain polymers).

4.5.2 Suggestions for Future Experiments

^{2}H NMR spectroscopy and refractive index measurements are limited to the dilute regime because of the difficulty in aligning the samples. However, these results beg the question: what is the relative orientation order of the polymer and solvent at higher concentration? Small-angle neutron scattering experiments on selectively labeled polymer solutions might reveal a strong concentration dependence of the polymer's conformational anisotropy and provide evidence of orientational coupling, or wide-angle x-ray scattering experiments could be used to measure the nematic order parameter in the concentrated regime. It would, furthermore, be of interest to study the molecular weight dependence of the polymer's phase behavior, perhaps using smaller polymers to compare with previous studies more directly.

4.6 Tables

Table 4.1 Molecular weight, conversion, and polydispersity of the side-group liquid crystal homopolymers. Details of characterization may be found in Appendix A.

Name	M_n (kg/mol)	Mole Fraction 1,2 PB	Mole Fraction 1,4 PB	Mole Fraction LC	PDI[a]
350HSiCB4	347	0	0.11	0.89	1.27
$d_2$350HSiCB4	348	0	0.11	0.89	1.27
490HSiCB4	489	0.01	0.03	0.96	1.48

[a] PDI = Polydispersity Index (M_w/M_n)

4.7 Figures

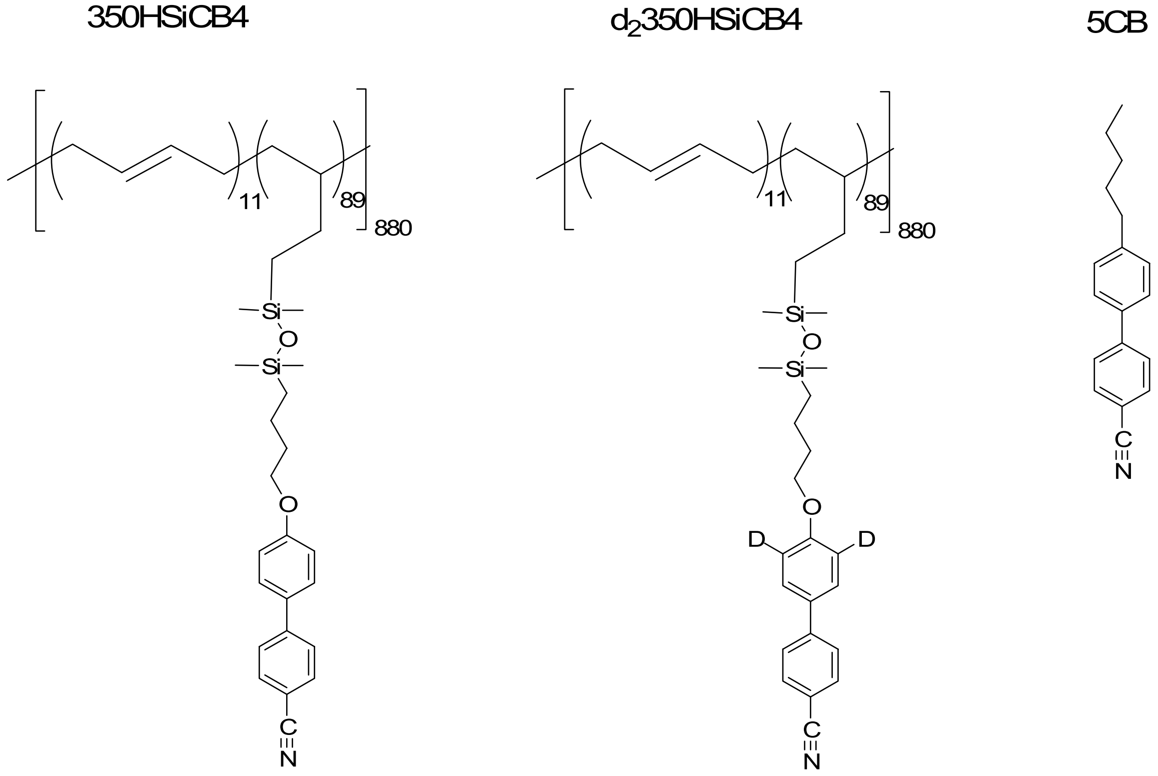

Figure 4.1 Chemical structures of the end-on side-group liquid crystal polymers (350HSiCB4 and d$_2$350HSiCB4) and the nematic liquid crystal solvent (5CB). The polymer's name is derived from its molecular weight (350 kg/mol), the letter "H" to indicate a homopolymer, and "SiCB4" to indicate end-on mesogens. In addition to monomers having an attached mesogen, the polymer also contains some residual 1,2- and 1,4-butadiene monomers. The polymers' properties are summarized in Table 4.1. Full details of polymer characterization are given in Appendix A.

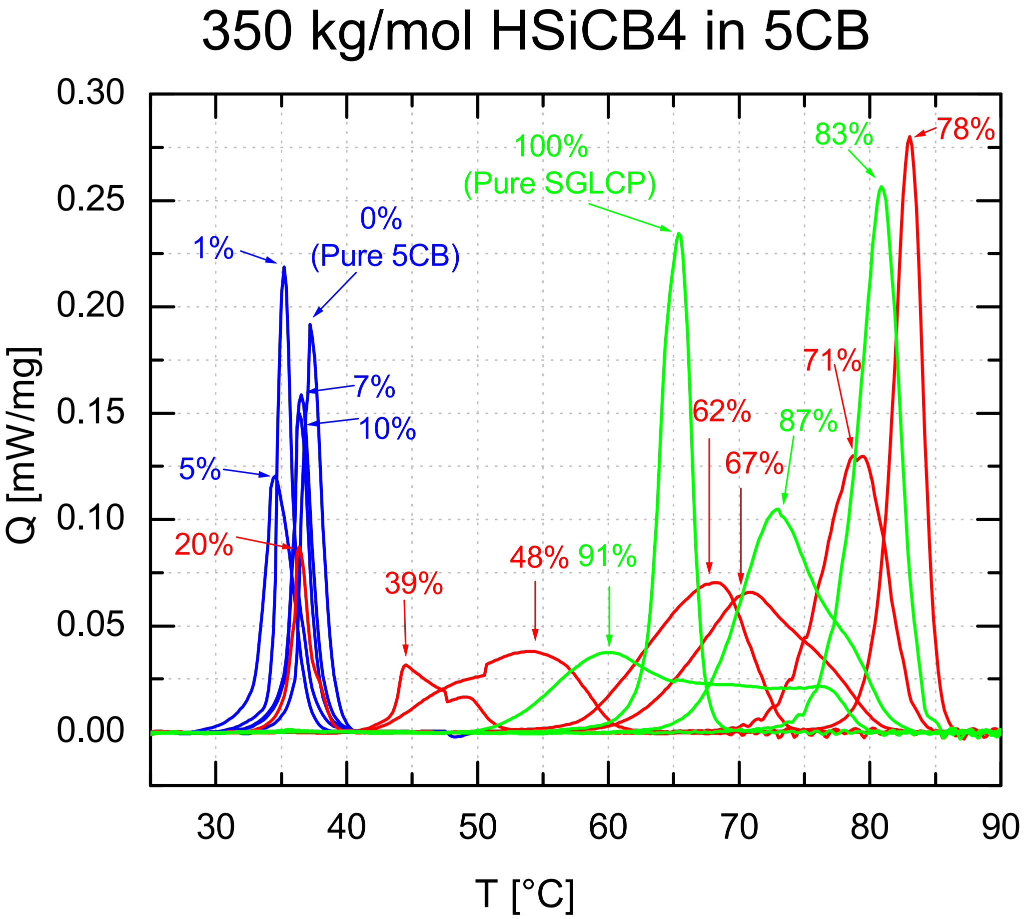

Figure 4.2 DSC temperature scans from mixtures of 350HSiCB4 and 5CB in proportions ranging from 0 to 100 wt % polymer obtained on heating. The peak position changes very little as concentration is increased from 0 to 20 wt % polymer (blue curves), then shifts to higher temperature as concentration is increased from 39 to 78 wt % polymer (red curves). Above 78 wt % polymer the peak position shifts to lower *T* with increasing concentration (green curves). Baselines were subtracted from the DSC scans as described in the text; in some cases the procedure produced a small discontinuity in the baseline, leading to the discontinuities evident in some of the baseline subtracted curves.

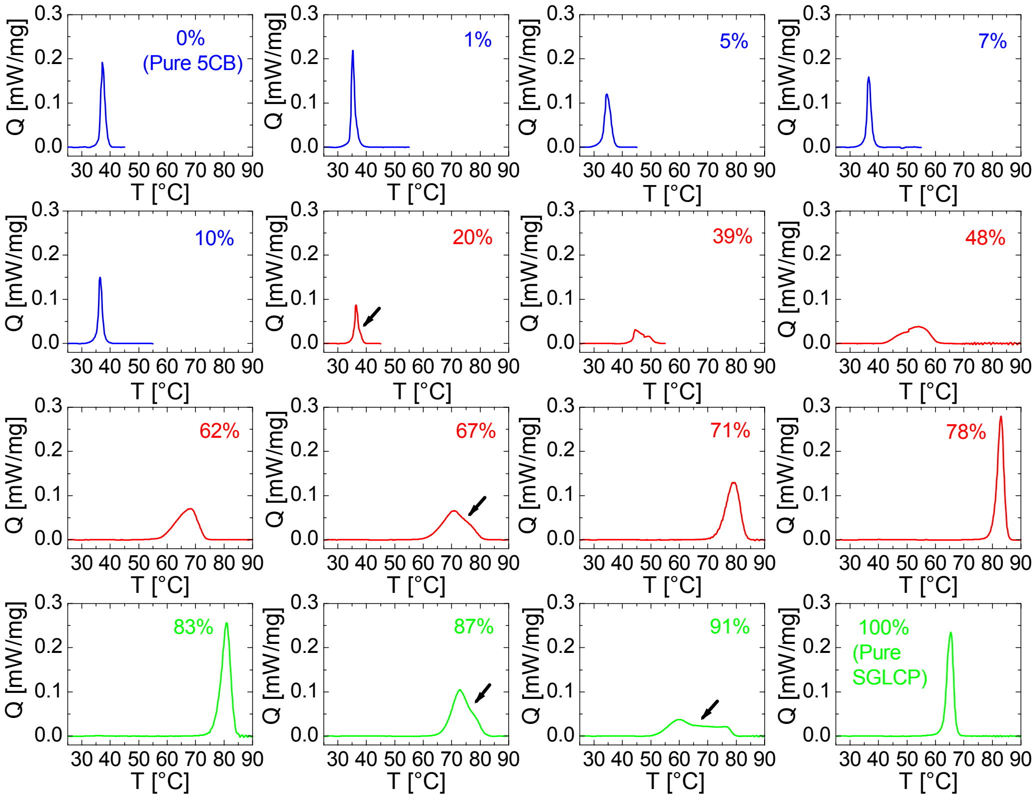

Figure 4.3 DSC temperature scans from Figure 4.2 plotted individually for clarity. The peak position changes very little as concentration is increased from 0 to 20 wt % polymer (blue curves), then shifts to higher temperature as concentration is increased from 39 to 78 wt % polymer (red curves). Above 78 wt % polymer the peak position shifts to lower *T* with increasing concentration (green curves). Arrows are used to indicate shoulders in the phase transition endotherms. Baselines were subtracted from the DSC scans by fitting to second degree piecewise polynomials and data were normalized by the sample weight to give normalized, subtracted heat flow, *Q*.

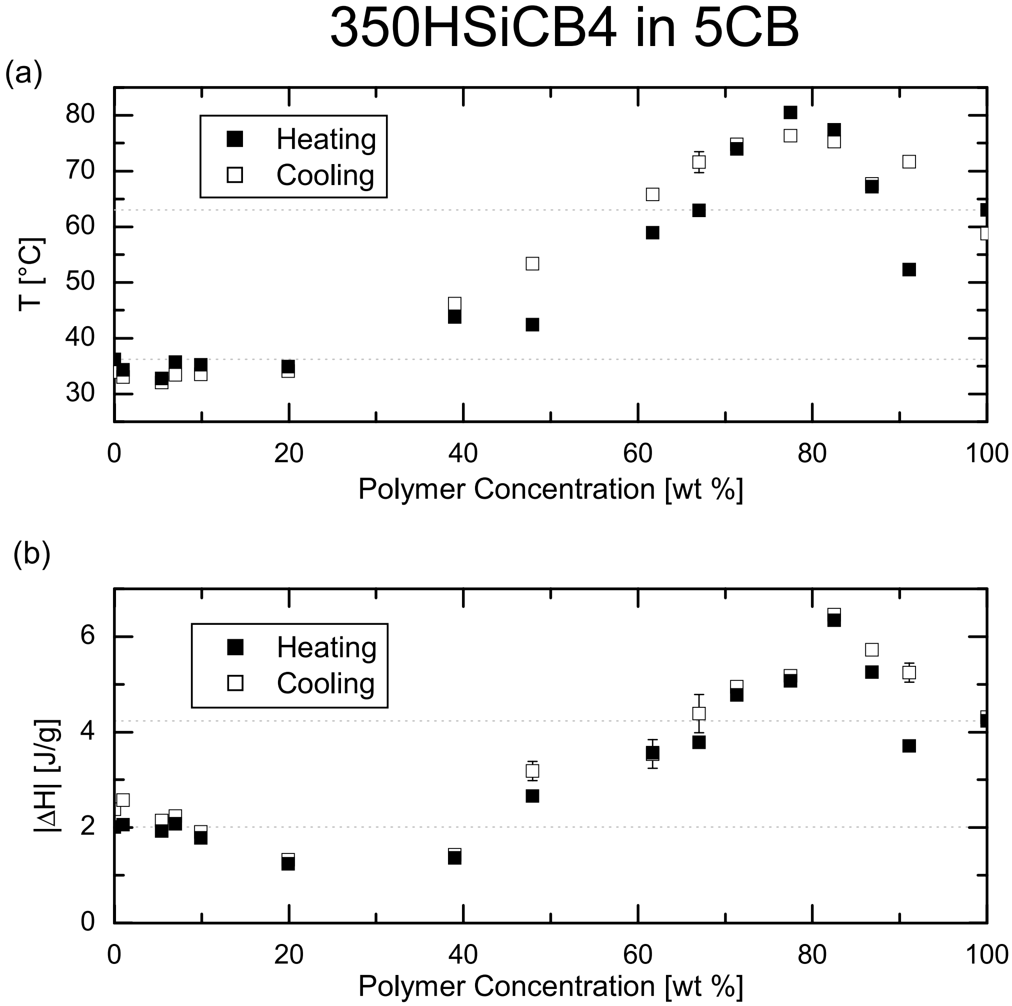

Figure 4.4 Latent heat (|Δ*H*|) and onset temperature (*T*) of the nematic/isotropic phase transition measured from DSC scans on heating and cooling in mixtures of 350HSiCB4 with 5CB as a function of polymer concentration. Data points are the average of six consecutive temperature scans and error bars indicate the standard deviation. Dotted lines indicate the onset temperatures for pure 5CB and SGLCP.

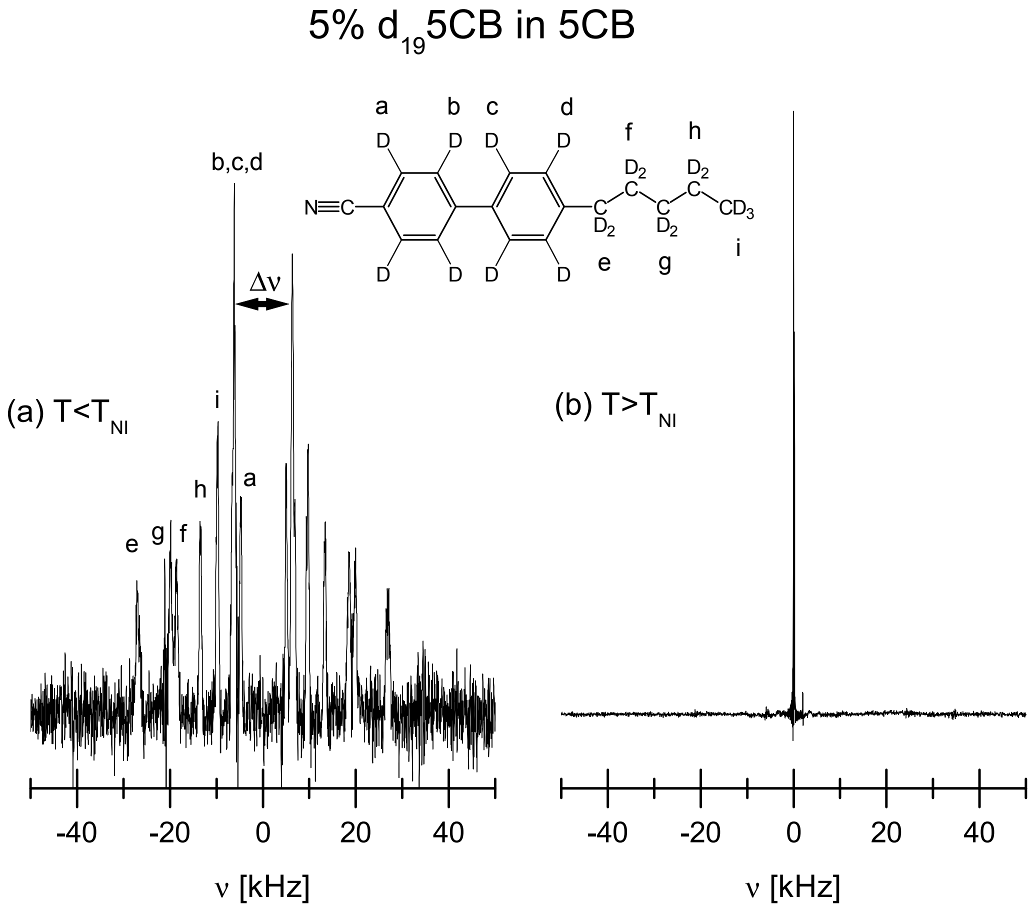

Figure 4.5 Representative ^{2}H NMR spectrum of 5 wt % d$_{19}$5CB in 5CB taken at (a) $T = T_{NI} - 8$ °C and (b) $T = T_{NI} + 2$ °C (b) (a) Orienational order in the nematic phase ($T < T_{NI}$) gives rise to a symmetric spectrum where the quadrupolar splitting, $\Delta\nu$, for each set of equivalent deuterons depends on the microscopic order parameter and the angle between the director and the magnetic field. Peak assignments have been made according to Auger et al.[30] (b) In the isotropic phase ($T > T_{NI}$) the quadrupolar interactions are averaged to yield a single peak centered at $\nu = 0$.

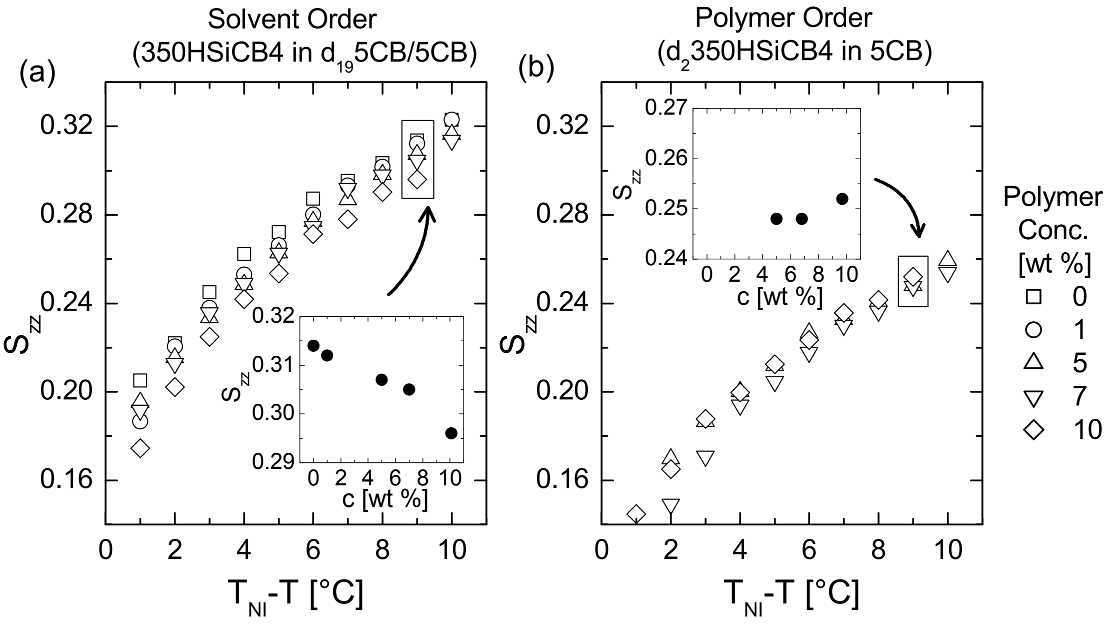

Figure 4.6 Microscopic order parameters, S_{zz}, measured from quadrupolar splittings, $\Delta\nu$, of (a) aromatic deuterium atoms located *para-* to the alkyl chain in d_{19}5CB and (b) aromatic deuterium atoms located *para-* to the oxygen atom in $d_2$350HSiCB4 as a function of reduced temperature, T_{NI} - T, containing various polymer concentrations, c, (legend to the right applies to both graphs). The dependence of $\Delta\nu$ on polymer concentration (c) at $T = T_{NI}$ - 9 °C is expanded in the inset plot.

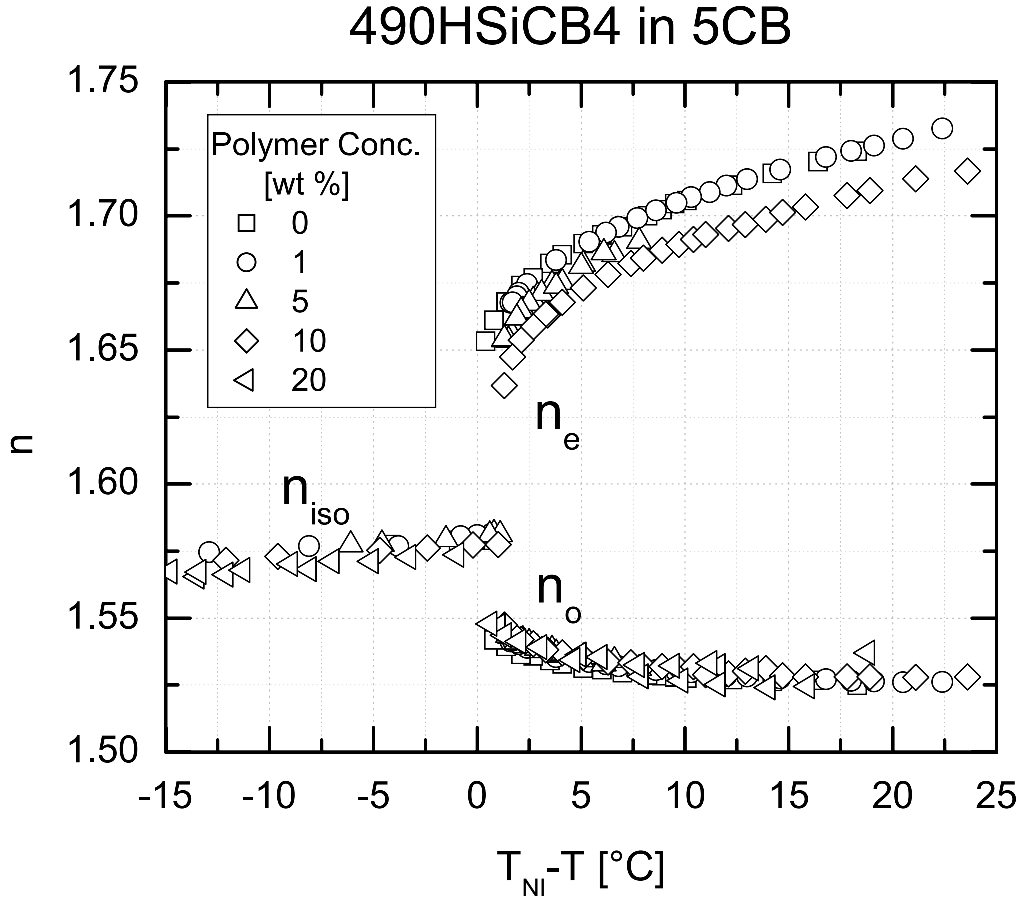

Figure 4.7 Temperature dependence of the ordinary, n_o, and extraordinary, n_e, refractive indices of pure 5CB and solutions of 490HSiCB4 in 5CB in the nematic phase and in the isotropic phase, n_{iso}.

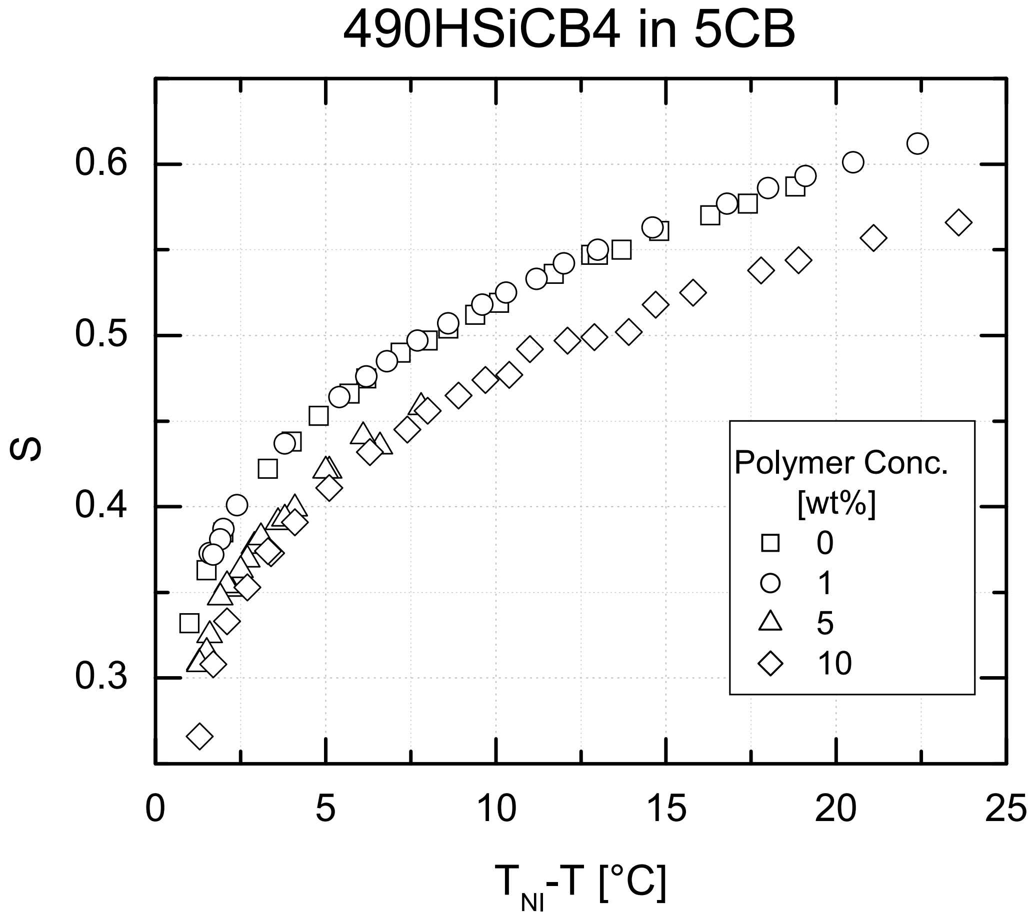

Figure 4.8 Temperature dependence of the order parameter (*S*) of 5CB, and solutions of 490HSiCB4 in 5CB, determined from refractive index measurements. In performing the Haller analysis[32], the density and molar mass for polymer solutions were assumed equal to those of 5CB[31] ($\rho = 1$ g/cm^3, $M = 249$ g/mol).

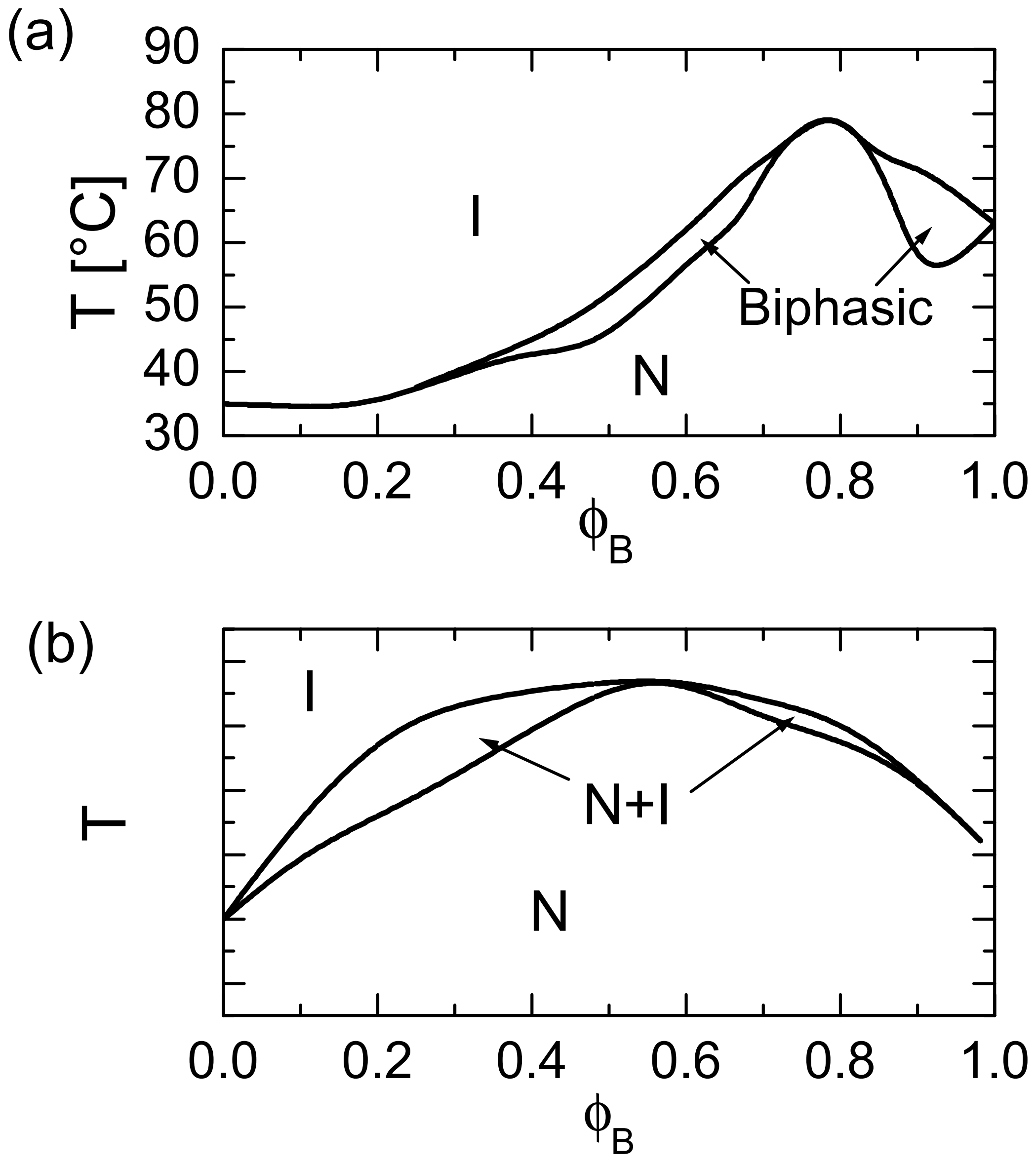

Figure 4.9 (a) Schematic representation of a plausible phase diagram deduced from DSC data. The letter "*N*" represents a single nematic phase and the letter "*I*" represents a single isotropic phase. (b) Schematic representation of a phase diagram calculated by Chiu and Kyu[12] using Brochard's model[15] for an SGLCP polymer and a small-molecule LC with strong nematic interactions between the two ($c = U_{AB}/(U_{AA}U_{BB})^{1/2} = 1.2$).

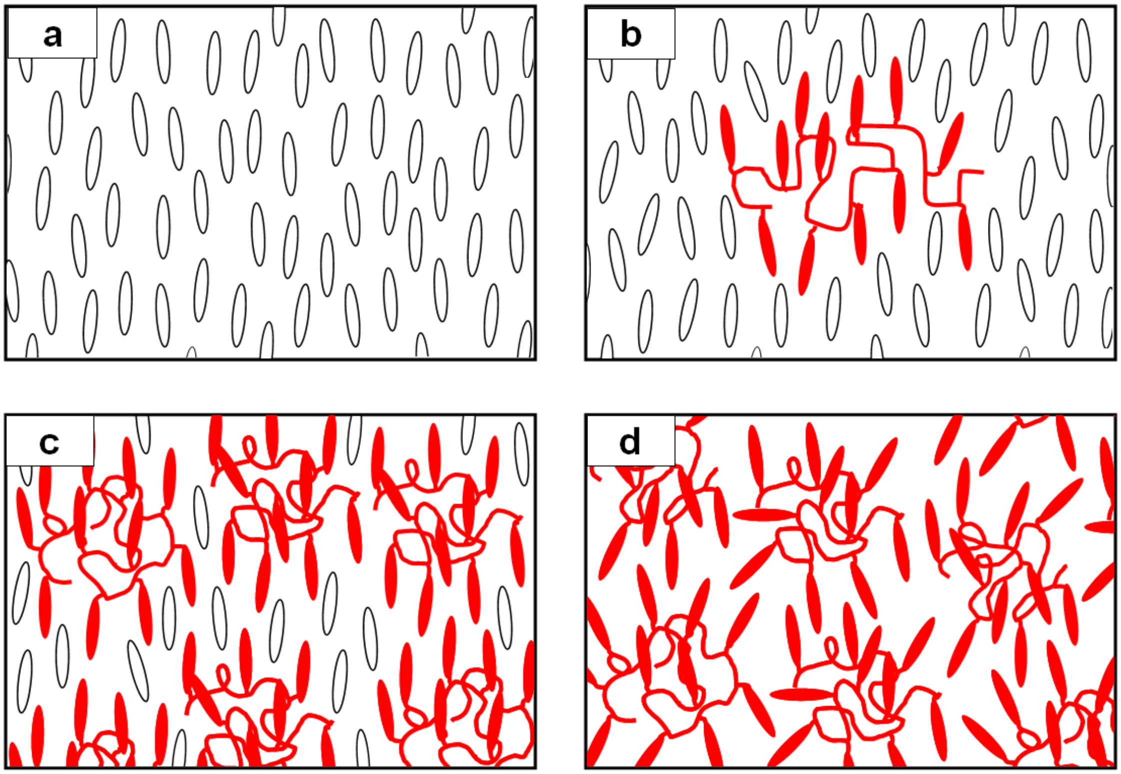

Figure 4.10 Schematic representation of mixtures of 350HSiCB4 with 5CB at various concentrations. Mesogens are represented by white (5CB) and red (350HSiCB4) ellipses. (a) 5CB without any dissolved polymer. (b) A dilute solution of polymer in 5CB. The polymer adopts an anisotropic conformation because of its coupling to the solvent's director field. (c) Polymer with a small amount of 5CB, corresponding to the stabilized nematic phase at approximately 80 wt.-% 350HSiCB4. The solvent serves to increase the polymer's configurational freedom, allowing it to relax some of the frustration present in the melt. (d) Bulk polymer without any small-molecule solvent. The polymer's mesogens are strongly coupled to the backbone conformation.

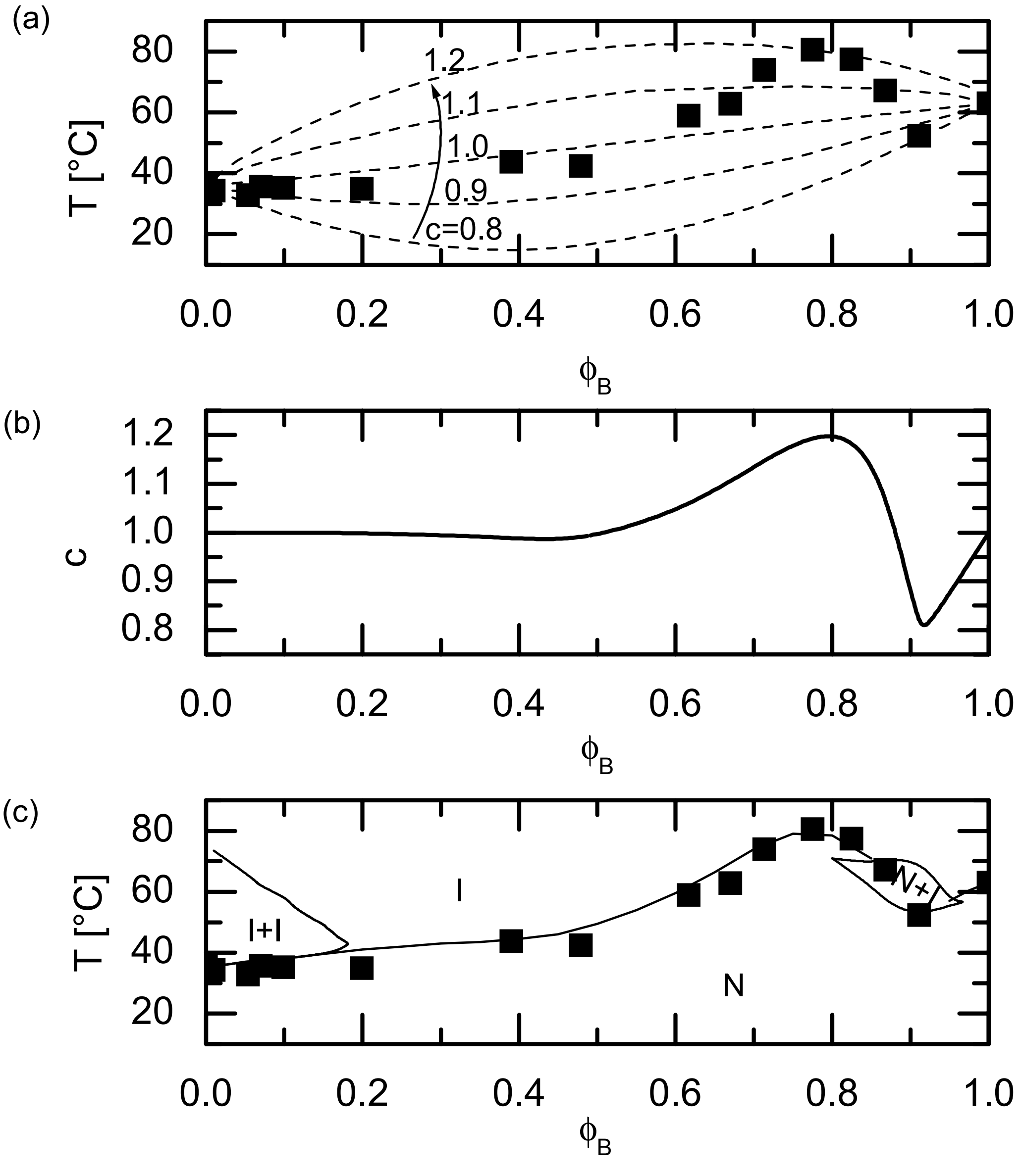

Figure 4.11 (a) Nematic-isotropic transition temperatures predicted by Maier-Saupe theory using values of $c = U_{AB} / (U_{AA}U_{BB})^{1/2}$ between 0.8 and 1.2 (dotted lines) together with phase transition onset temperatures of 350HSiCB4/5CB measured by DSC on heating (solid squares). (b) The imposed concentration-dependence of *c* used to generate the phase diagram in (c). (c) Phase boundaries (solid lines) predicted by Brochard's model using a concentration-dependent polymer-solvent nematic interaction parameter, U_{AB}, together with phase transition onset temperatures of 350HSiCB4/5CB measured by DSC on heating (solid squares). "*N*" and "*I*" indicate single nematic and isotropic phases, respectively. "*I+I*" indicates two coexisting isotropic phases and "*N+I*" indicates coexistence of a nematic and an isotropic phase. The Flory interaction parameter was arbitrarily set to $\chi = 350 / T$. In (a), (b), and (c), ϕ_B is the volume fraction of polymer.

4.8 References

[1] Benmouna, F.; Daoudi, A.; Roussel, F.; Buisine, J.-M.; Coqueret, X.; Maschke, U. Equilibrium Phase Diagram of Polystyrene and 8CB. *J. Polym. Sci., Part B: Polym. Phys.* **1999**, *37*, 1841-1848.

[2] Gogibus, N.; Maschke, U.; Benmouna, F.; Ewen, B.; Coqueret, X.; Benmouna, M. Phase Diagrams of Poly(dimethylsiloxane) and 5CB Blends. *J. Polym. Sci., Part B: Polym. Phys.* **2001**, *39*, 581-588.

[3] Kihara, H.; Kishi, R.; Miura, T.; Kato, T.; Ichijo, H. Phase behavior of liquid-crystalline copolymer/ liquid crystal blends. *Polymer* **2001**, *42*, 1177-1182.

[4] Casagrande, C.; Veyssie, M.; Finkelmann, H. Phase separations in the mixtures of a mesomorphic polymer with a low molecular mass liquid crystal. *J. Physique* **1982**, *43*, L671 - L675.

[5] Finkelmann, H.; Kock, H.-J.; Rehage, G. Phase Studies of Liquid Crystalline Side Chain Polymers Mixed with Low Molar Mass Liquid Crystals of Similar Structure. *Mol. Cryst. Liq. Cryst.* **1982**, *89*, 23-36.

[6] Ringsdorf, H.; Schmidt, H.-W.; Schneller, A. Miscibility Studies of Polymeric and Low Molecular Weight Liquid Crystals and Their Behaviour in an Electric Field. *Makromol. Chem., Rapid Commun.* **1982**, *3*, 745-751.

[7] Benthack-Thoms, H.; Finkelmann, H. Phase separations in binary mixtures of nematic liquid crystal side chain polymers and low-molar-mass liquid crystals, 1 Influence of the chemical constitution of the low-molar-mass component. *Makromol. Chem.* **1985**, *186*, 1895-1903.

[8] Gilli, J. M.; C., F.; Sixou, P.; Robert, P.; Villenave, J. J.; Fontanille, M. New Thermotropic Polymers with Flexible Backbone and Mesogenic Side Chains: Blends with Small Molecule Liquid Crystals. *Mol. Cryst. Liq. Cryst.* **1989**, *167*, 73-87.

[9] Sigaud, G.; Achard, M. F.; Hardouin, F.; Coulon, C.; Richard, H.; Mauzac, M. Flory's Parameters in Solutions of Liquid Crystalline Side-Chain Polymers in Low Molecular Weight Liquid Crystals. *Macromolecules* **1990**, *23*, 5020-5024.

[10] Sigaud, G.; Achard, M. F.; Hardouin, F.; Mauzac, M.; Richard, H.; Gasparoux, H. Relationships between Molecular Structure and Immiscibility of Liquid Crystalline Side-Chain Polymers in Low Molecular Weight Nematic Solvents. *Macromolecules* **1987**, *20*, 578-585.

[11] Chang, M. C.; Chiu, H. W.; Wang, X. Y.; Kyu, T.; Leroux, N.; Campbell, S.; Chien, L. C. Phase transitions in mixtures of a side-on-side chain liquid crystalline polymer and low molar mass nematic liquid crystals. *Liq. Cryst.* **1998**, *25*, 733-744.

[12] Chiu, H.-W.; Kyu, T. Equilibrium phase behavior of nematic mixtures. *J. Chem. Phys.* **1995**, *103*, 7471-7481.

[13] Chiu, H.-W.; Zhou, Z. L.; Kyu, T.; Cada, L. G.; Chien, L.-C. Phase Diagrams and Phase Separation Dynamics in Mixtures of Side-Chain Liquid Crystalline Polymers and Low Molar Mass Liquid Crystals. *Macromolecules* **1996**, *29*, 1051-1058.

[14] Attard, G. S.; Karasz, F. E. Phase studies of blends of polystyrene-based liquid-crystalline side-chain polymers with low-molar-mass mesogens. *Makromol. Chem., Rapid Commun.* **1990**, *11*, 145-150.

[15] Brochard, F.; Jouffroy, J.; Levinson, P. Phase diagrams of mesomorphic mixtures. *J. Physique* **1984**, *45*, 1125-1136.

[16] Hwang, J. C.; Kikuchi, K.; Kajiyama, T. Aggregation states and electro-optical properties of the induced smectic phase by mixing a nematic liquid crystalline polymer and a low molecular weight liquid crystal. *Polymer* **1992**, *33*, 1822-1825.

[17] Ratto, J. A.; Volino, F.; Blumstein, R. B. Phase Behavior and Order in Mixtures of Main-Chain Nematic Polyesters with Small Molecules: A Combined Proton and Deuterium NMR Study. *Macromolecules* **1991**, *24*, 2862-2867.

[18] Volino, F.; Gauthier, M. M.; Giroud-Godquin, A. M. NMR Study of Dilute Solutions of Main-Chain Nematic Polyesters in *p*-Azoxyanisole. *Macromolecules* **1985**, *18*, 2620-2623.

[19] de Gennes, P.-G. *The Physics of Liquid Crystals*, 2nd ed; Clarendon Press: Oxford, 1993.

[20] Haller, I.; Huggins, H. A.; Freiser, M. J. Measurement of Indices of Refraction of Nematic Liquids. *Mol. Cryst. Liq. Cryst.* **1972**, *16*, 53-59.

[21] Kempe, M. D.; Kornfield, J. A. Shear alignment behavior of nematic solutions induced by ultralong side-group liquid crystal polymers. *Phys. Rev. Lett.* **2003**, *90*, 115501.

[22] Mansare, T.; Decressain, R.; Gors, C.; Dolganov, V. K. Phase Transformations and Dynamics of 4-Cyano-4'-Pentylbiphenyl (5CB) by Nuclear Magnetic Resonance, Analysis Differential Scanning Calorimetry, and Wideangle X-Ray Diffraction Analysis. *Mol. Cryst. Liq. Cryst.* **2002**, *382*, 97-111.

[23] Van Roie, B.; Leys, J.; Denolf, K.; Glorieux, C.; Pitsi, G.; Thoen, J. Weakly first-order character of the nematic-isotropic phase transition in liquid crystals. *Phys. Rev. E* **2005**, *72*, 041702.

[24] Finkelmann, H.; Kock, H.-J.; Rehage, G. Investigations on liquid crystalline polysiloxanes 3. Liquid crystalline elastomers -- a new type of liquid crystalline material. *Makromol. Chem., Rapid Commun.* **1981**, *2*, 317-322.

[25] Dong, R. R. *Nuclear Magnetic Resonance of Liquid Crystals*, 2nd ed; Partially Ordered Systems, ed. L. Lam; D. Langevin; Springer: New York, 1997.

[26] Tabayashi, K.; Akasaka, K. Natural Abundance ^{2}H NMR for Liquid Crystal Studies. Application to 4'-(Hexyloxy)-4-cyanobiphenyl. *J. Phys. Chem. B* **1997**, *101*, 5108-5111.

[27] Emsley, J. W.; Luckhurst, G. R.; Stockley, C. P. The deuterium and proton-{deuterium} N.M.R. spectra of the partially deuteriated nematic liquid crystal 4-n-penyl-4'-cyanobiphenyl. *Mol. Phys.* **1981**, *44*, 565-580.

[28] Emsley, J. W.; Foord, E. K.; Gandy, P. J. F.; Turner, D. L. Assignment of the quadrupolar splittings in fully deuteriated alkyl chains of liquid crystalline compounds The case of 4-n-hexyloxy-4'-cyanobiphenyl. *Liq. Cryst.* **1994**, *17*, 303-309.

[29] Luckhurst, G. R. Pretransitional Behaviour in Liquid Crystals. *J. Chem. Soc., Faraday Trans. 2* **1988**, *84*, 961-986.

[30] Auger, C.; Lesage, A.; Caldarelli, S.; Hodgkinson, P.; Emsley, L. Assignment and Measurement of Deuterium Quadrupolar Couplings in Liquid Crystals by

Deuterium-Carbon NMR Correlation Spectroscopy. *J. Phys. Chem. B* **1998**, *102*, 3718-3723.

[31] Karat, P. P.; Madhusudana, N. V. Elastic and Optical Properties of Some 4'-n-Alkyl-4-Cyanobiphenyls. *Mol. Cryst. Liq. Cryst.* **1976**, *36*, 51-64.

[32] Haller, I.; Huggins, H. A.; Lilienthal, H. R.; McGuire, T. R. Order-Related Properties of Some Nematic Liquids. *J. Phys. Chem.* **1973**, *77*, 950-954.

[33] Woo, I.-C.; Wu, S.-T. *Optics and Nonlinear Optics of Liquid Crystals*, World Scientific: River Edge, NJ, 1993.

[34] ten Bosch, A.; Maissa, P.; Sixou, P. Molecular model for nematic polymer in liquid crystal solvents. *J. Chem. Phys.* **1983**, *79*, 3462-3466.

Chapter 5

CONFORMATIONAL ANISOTROPY OF SIDE-GROUP LIQUID CRYSTAL POLYMERS IN NEMATIC LIQUID CRYSTAL SOLVENT: SMALL-ANGLE NEUTRON SCATTERING OF SEMIDILUTE SOLUTIONS

5.1 Introduction 123
5.2 Experimental 124
5.3 Results 125
5.4 Discussion 130
5.5 Conclusions 132
5.6 Tables 133
5.7 Figures 135
5.8 References 142

Rafael Verduzco contributed to the experiments discussed in this chapter. He synthesized and characterized the side-on polymers (names ending with “BB”). He and I traveled together to the NIST Center for Neutron Research (NCNR) where we shared the responsibility of performing the neutron scattering experiments. Zuleikha Kurji also assisted us with those experiments. We thank Boualem Hammouda and John Barker at the NCNR for their help with experimental design and interpretation of data.

5.1 Introduction

The molecules of a liquid crystal (LC) tend to align with one another in a preferred direction called the "director," yielding a fluid material with anisotropic optical, electro-magnetic, and mechanical properties. Random coil polymers are typically insoluble in LCs because of the entropic penalty to dissolution in an ordered solvent, but a side-group liquid crystal polymer (SGLCP) with mesogens covalently bonded to the polymer backbone can be dissolved in a small-molecule LC, where it adopts an anisotropic conformation as a result of its coupling to the orientational order of the host. [1-3] The shape of the polymer in solution depends on the thermodynamic balance between maximizing its conformational entropy and alignment of its side groups with the solvent's nematic orientation field.

The coupling between the LC solvent and the polymer backbone is strongly influenced by the polymer architecture, the flexibility of the spacer connecting the side groups to the polymer backbone, and the strength of nematic interactions between the solvent and the side groups.[4] Attaching the side groups with their long axis perpendicular to the polymer backbone ("end-on") usually causes the polymer to extend its conformation perpendicular to the director, but when side groups are attached with their long axis parallel to the backbone ("side-on") the polymer tends to extend parallel to the director. The magnitude of the anisotropy is dependent on the flexibility of the spacer: when the side groups are connected by a rigid spacer their orientation is translated more efficiently to the polymer, but a flexible spacer provides partial screening of the orientational order. The anisotropy also depends on the strength of nematic interactions between the solvent and the side groups. When the pairwise interactions between the solvent and the side-groups are strong, the dissolved polymer strengthens the nematic order and when they are weak the solute polymer destabilizes the nematic phase.[5]

Small-angle neutron scattering (SANS) is an ideal tool for measuring the conformational anisotropy of SGLCPs. Anisotropic scattering patterns from samples with the nematic director aligned into a uniform, homogeneous monodomain allow the polymer's dimensions to be probed in the directions parallel and perpendicular to the director. SANS experiments are usually performed on dilute solutions of polymers to extract the dimensions of individual polymer chains. The experiments presented here are on solutions in the semidilute regime where the scattering from individual chains cannot be isolated. Although the polymers' sizes cannot be measured, their conformational anisotropy is readily accessible through measurement of the correlation length, the length beyond which a monomer's local environment contains monomers from other chains.

SANS experiments are performed on semidilute solutions of SGLCPs in a nematic solvent. The conformational anisotropy of closely matched end-on and side-on polymers is examined as a function of temperature and molecular weight, and comparisons between the polymers give insight into the coupling between configurational entropy and orientational order.

5.2 Experimental

5.2.1 Materials

Polybutadiene prepolymers were purchased from Polymer Source (Montreal, Quebec) and functionalized with end-on (SiCB4) and side-on (SiBB) mesogens to make side-group liquid crystal polymers (SGLCPs) (Figure 5.1). End-on polymers were synthesized according to the methods described in Appendix A and side-on polymers were synthesized by Rafael Verduzco.[6] The prepolymers had molecular weights of 48 kg/mol and 104 kg/mol and the characteristics of the converted SGLCPs are summarized in Table 5.1. The details of end-on polymer characterization may be found in Appendix A.

Perdeuterated 4-pentyl-4′-cyanobiphenyl (d_{19}5CB, Figure 5.1) was synthesized according to methods described in Appendix B and had a nematic-to-isotropic transition temperature (T_{NI}) of 32.3 °C. Solutions of 5 wt % SGLCP in d_{19}5CB were prepared by dissolving the two components together in dichloromethane (DCM) then evaporating the DCM under an air stream followed by drying in vacuum overnight. The T_{NI}s of SGLCP solutions were within 1 °C of pure d_{19}5CB's T_{NI}.

5.2.2 Small-Angle Neutron Scattering (SANS)

Cells were prepared by coating quartz plates with a rubbed polyimide alignment layer, then using epoxy to glue the plates together separated by an 813 μm thick aluminum spacer ring. SGLCP solutions were loaded into the cells with a syringe. Cells were then placed in a room-temperature vacuum oven to remove small air bubbles and allowed to sit undisturbed for at least 18 hours prior to starting an experiment. This allowed enough time for the sample to align into a uniform monodomain under the influence of the alignment layers with the LC director parallel to the cell surfaces.

Small-angle neutron scattering (SANS) experiments were performed on the NG7 beamline at the National Institute of Standards and Technology Center for Neutron Research (NCNR). Cells containing homogeneously aligned SGLCP solutions were mounted in the beam contained in a temperature-regulated aluminum block held between the pole pieces of a 1.3 T electromagnet. The magnetic field served to reinforce the planar alignment induced by the rubbed polyimide layers and the neutron beam was incident perpendicular to the LC director. Samples were annealed at the desired temperature for fifteen minutes prior to collecting data. Experiments were performed at two temperatures in the nematic phase, 25 and 30 °C, and one temperature in the isotropic phase, 50 °C.

Two-dimensional scattering patterns were sector-averaged for easier visualization. Data having the same magnitude of the scattering vector, $|\boldsymbol{q}| = q = 4\pi/\lambda \sin(\theta/2)$, within ± 15° of the horizontal direction were averaged to give the scattering parallel to the director, I_{par}, and data in a sector of ± 15° from the vertical direction were averaged to give the scattering perpendicular to the director, I_{perp}.

5.3 Results

5.3.1 Conformational Anisotropy: Effects of Polymer Architecture, Temperature, and Molecular Weight

The scattering patterns from SGLCP solutions are anisotropic below the nematic-isotropic transition temperature (T_{NI}) (Figure 5.2a,b) indicating that SGLCPs adopt ellipsoidal conformations in LC solvent. These patterns are similar to other scattering patterns of SGLCPs in LC solvents reported in the literature[1-3] and similar to SANS patterns collected at Argonne National Laboratory's Intense Pulsed Neutron Source from polymers of identical structure, but different molecular weight.[7] Since the nematic director must be an axis of symmetry for the ellipsoid, it is deduced that end-on polymers adopt an oblate conformation while side-on polymers adopt a prolate conformation. A rough measure of the conformational anisotropy may be obtained from contours of equal scattered intensity on the two-dimensional patterns; the ratio of the major axis to the minor axis gives an aspect ratio. Thus calculated, the aspect ratios at 25 °C of side-on polymers 500HSiBB and 990HSiBB are 4.5 and 4.1, respectively, while end-on polymers 350HSiCB4 and 760HSiCB4 have aspect ratios at 25 °C of 1.6 and 1.7, respectively. In isotropic solvent, the scattering patterns from both end-on and side-on polymers are circularly symmetric (aspect ratio equal to one), indicating that polymer conformations are spherical (Figure 5.2c).

Conformational anisotropy is also evident in the polymers' sector-averaged scattering patterns (Figure 5.3-Figure 5.6). In the highest decade of q, side-on polymers scatter more strongly in the direction perpendicular to the nematic director (Figure 5.3 and Figure 5.4), while end-on polymers scatter more strongly in the direction parallel to the director (Figure 5.5 and Figure 5.6). Another rough measure of the anisotropy can be obtained from the ratio of the scattered intensity in the two orientations, I_{par} and I_{perp}, in the high q regime where I_{par} and I_{perp} are almost parallel. Measured this way at 25 °C, the side-on polymers, 500HSiBB and 990HSiBB, both have anisotropies $I_{perp} / I_{par} \approx 10$ and the end-on polymers, 350HSiCB4 and 760HSiCB4, both have $I_{par} / I_{perp} \approx 2$.

Changing the molecular weight has very little effect on scattering patterns from 5 wt % solutions of side-on or end-on SGLCPs, suggesting that the polymer solutions are in the semidilute concentration regime.[8] End-on polymers are particularly insensitive to molecular weight; the scattering patterns from 350HSiCB4 and 760HSiCB4 are virtually superimposable on one another (Figure 5.5 and Figure 5.6). The scattering patterns from side-on polymers, 500HSiBB and 990HSiBB, also overlap one another at 25 °C, but when the temperature is increased to 30 °C, I_{par} from 5 wt % 500HSiBB increases, indicating a decrease in the polymer's anisotropy (Figure 5.3). The anisotropy of 990HSiBB also decreases when the temperature is raised, but to a much lesser extent (Figure 5.4).

Scattering from all four polymer solutions is anomalously high at low q. Theoretically, the scattering from a solution of Gaussian polymer chains is described by the Debye equation,[9] which predicts the scattered intensity to become virtually independent of q as q approaches zero. The SGLCP solutions closely resemble the $I \sim q^{-2}$ scaling predicted by the Debye equation at high q, and in an intermediate range all but I_{par} from side-on polymers begin to flatten out as predicted. However, strong deviations from the Debye prediction are observed at low q where the intensity takes a sharp upturn. Similar excess scattering at low q has been previously observed in semidilute solutions of poly(ethylene oxide) and attributed to associations between polymer chains.[10, 11] Supramolecular polymer aggregates have been observed in solutions of SGLCPs in isotropic solvents, such as tetrahydrofuran or chloroform, by light scattering[12-15] and rheology[16] and are attributed to specific interactions between the side groups of different polymer chains. The observation of inter-polymer associations confirms that solutions are in the semidilute regime.

In all four polymer solutions, the scattering patterns from isotropic solutions at $T = 50$ °C have high-q intensities intermediate between I_{par} and I_{perp} in the nematic phase (Figure 5.3-Figure 5.6). Otherwise, the patterns' qualitative shapes are not very different from nematic solutions.

5.3.2 Quantitative Analysis of Conformational Anisotropy: Fitting Data to Models

Models for dilute solutions of non-interacting polymer chains, such as the Debye equation, cannot be applied to the data from SGLCP solutions. Instead, the data are fit to the form

$$I(q) = \frac{C_1}{q^n} + \frac{C_2}{1 + (qL)^m} + C_3 \, . \tag{5.1}$$

This equation has been used to model SANS from clusters of poly(ethylene oxide) in water.[10] The first term describes Porod scattering from the surface of the cluster. The exponent n is predicted to be between 3 and 4 for an object with a fractal surface and will be exactly 4 if the surface is smooth.[9] The second term is a Lorentzian describing the scattering from the polymer chains. The length L is the polymer's correlation length and the exponent m is predicted to be 2 when the polymer is in a theta solvent and 1.7 for an expanded polymer in good solvent.[9] C_1 and C_2 are weighting factors for the two terms and C_3 accounts for a constant, incoherent background. C_3 was set to zero when fitting data from SGLCP solutions since incoherent background makes no apparent contribution to the scattering.

Preliminary data fitting was performed allowing all the parameters to float freely. The results gave similar values of n and m for a given polymer type (end-on or side-on) and direction (parallel or perpendicular to the director), regardless of molecular weight or temperature. A second round of data fitting was performed fixing the exponent m at its average value. The average value of n was between 2.5 and 3.2 and was therefore fixed at its theoretical minimum of 3, in agreement with the experimentally observed exponent for isotropic solutions of SGLCPs.[12, 15] The results are summarized in Table 5.2. The value of L that results when the exponents are fixed is less than 10% different from that obtained when all the parameters are floating.

I_{par} from side-on polymers could not be fit with Equation 5.1 because the correlation length, L, is too large. In order to determine L from data fitting, the scattering pattern must crossover from an $I \sim q^{-m}$ power law ($qL >> 1$) to a region approaching $I \sim q^0$ ($qL << 1$). When L is much larger than q^{-1} throughout the entire q range, the intensity becomes

$$I(q) = \frac{C_1}{q^n} + \frac{C_2}{L^m} q^{-m} , \tag{5.2}$$

and the value of L is absorbed into the fitting parameter C_2. Nevertheless, the fact that a crossover is not observed can be used to establish a lower bound on L. Assuming the crossover regime needs to span at least from q_{min} = 1.4 x 10^{-3} Å^{-1} to q = 3 x 10^{-3} Å^{-1} to be observable, the maximum value of L that can be measured with this experiment is calculated from qL = 3 x 10^{-3} Å^{-1} to be 330 Å. Indeed, fixing m = 2 and C_1 =0, tabulating $I(q)$ from Equation 5.1 at varying values of L demonstrates that an $I \sim q^{-2}$ power law spans the entire q range when L is larger than approximately 350 Å. The minimum value of L for side-on polymers in the direction parallel to the director is, therefore, ≈ 350 Å.

The correlation length in the direction perpendicular to the director, L_{perp}, is larger than L parallel to the director, L_{par}, in end-on polymer solutions (Figure 5.7a). The reverse is true for side-on polymers, where $L_{par} > L_{perp}$ (Figure 5.7b). The conformational anisotropy, measured as the ratio of correlation lengths parallel and perpendicular to the director, is $1.8 < L_{perp} / L_{par} < 2.1$ for both end-on polymers at 25 and 30 °C and $L_{par} / L_{perp} > 10$ for both side-on polymers at 25 and 30 °C. The conformational anisotropy of the end-on polymers is relatively insensitive to temperature (Figure 5.7a), and the correlation lengths of both side-on and end-on polymers are systematically larger at higher molecular weight (Figure 5.7).

Although L_{par} cannot be measured for side-on polymers, their relative anisotropies from one temperature to the next can still be estimated from the SANS data and it is found that side-on polymer anisotropy is highly sensitive to temperature changes. Assuming C_2 does not change significantly when the temperature is increased from 25 to 30 °C, Equation 5.2 in the high-q limit where $C_1 / q^n \approx 0$ gives the ratio of I_{par} at 25 °C to I_{par} at 30 °C:

$$\frac{I_{par}^{25°C}}{I_{par}^{30°C}} = \frac{{C_2} \big/ {\left(L_{par}^{25°C}\right)^m} \, q^{-m}}{{C_2} \big/ {\left(L_{par}^{30°C}\right)^m} \, q^{-m}} = \left(\frac{L_{par}^{30°C}}{L_{par}^{25°C}}\right)^m . \tag{5.3}$$

For 500HSiBB, the ratio is $L_{par}^{30°C} / L_{par}^{25°C} = 0.55$ (Figure 5.3) and for 990HSiBB the ratio is $L_{par}^{30°C} / L_{par}^{25°C} = 0.82$ (Figure 5.4). The relative changes in anisotropy, $x = L_{par} / L_{perp}$ at 30 °C relative to that at 25 °C, may then be calculated from

$$x = \left(\frac{L_{par}^{30°C}}{L_{par}^{25°C}}\right)\left(\frac{L_{perp}^{25°C}}{L_{perp}^{30°C}}\right), \tag{5.4}$$

giving $x = 0.53$ for 500HSiBB and $x = 0.77$ for 990HSiBB. The anisotropy of 500HSiBB is twice as large at 25 °C as it is at 30 °C and 990HSiBB is 1.5 times as anisotropic at 25 °C as it is at 30 °C.

The correlation lengths, L_{iso}, of polymers in isotropic solution are similar regardless of whether mesogens are attached end-on or side-on (Figure 5.7). Comparing polymers with the same degree of polymerization, 350HSiCB4 and 500HSiBB both have $L_{iso} \approx 35$ Å while 760HSiCB4 and 990HSiBB both have $L_{iso} \approx 50$ Å.

5.4 Discussion

Solutions of 5 wt % SGLCP are found to be in the semidilute regime, evidenced by the fact that the SANS patterns are virtually independent of molecular weight and supramolecular aggregates are formed by interactions between chains. Individual polymers are indistinguishable and the characteristic length scale for scattering is the distance below which a monomer is surrounded mostly by solvent and monomers belonging to the same chain (the polymer's correlation length). Scattering from a semidilute solution does not allow the chains' overall dimensions to be measured, but the relative magnitudes of the dimensions parallel and perpendicular to the director can still be deduced because the polymer conformation inside a correlation blob is similar to the polymer's conformation in dilute solution,[8] therefore the anisotropy of the correlation lengths may be assumed the same as the anisotropy of the overall polymer chain.

Conformational anisotropy of SGLCP chains in an LC solvent derives from coupling between the orientation of the mesogenic side groups and the trajectory of the polymer backbone. Nematic interactions with the solvent cause the polymer side groups to align with the LC director, and their covalent connectivity to the backbone forces it to follow the path connecting the oriented molecules. The polymer's equilibrium conformation is determined by the thermodynamic tradeoff between the enthalpic benefit of side-group alignment and the entropic penalty of deviation from a spherical random-walk. The sense of the coupling between the side groups and the backbone, end-on or side-on, determines whether the polymer chain extends perpendicular to the director to form an oblate ellipsoid or parallel to the director to form a prolate ellipsoid.

The end-on polymers studied here have weak coupling between the side groups and the backbone, relative to that of the side-on polymers. Orienting the end-on polymer side-groups with the LC solvent results in only mild anisotropy, between 1.8 and 2.1, whereas side-on polymers have aspect ratios exceeding 10. This phenomenon may be understood by the difference in the length of the spacer separating the mesogens from the backbone. End-on side groups are separated from the polymer backbone by a ten atom spacer, whereas side-on mesogens are separated by seven atoms (Figure 5.1). End-on polymer backbones may find easier accord with the side groups' orientation field through the flexibility of a longer spacer. The inherently larger anisotropy of the side-on polymers allows the relative dimensions of the polymer to change drastically with increasing temperature as the LC solvent's orientational order decreases and the polymer approaches its spherical conformation in the isotropic phase. These changes in conformational anisotropy have a strong effect on director relaxation dynamics, as explored in detail in Chapter 6.

A notable trend is observed in the exponent m derived from fitting scattering patterns: $m = 2.0$ for scattering in the direction parallel to the spacer connecting the side groups to the polymer backbone and $m = 1.7$ or 1.8 in the direction perpendicular. This implies that the importance of excluded volume effects is anisotropic, giving some insight into the detailed molecular interactions that give rise to conformational anisotropy. Excluded volume effects appear to arise between mesogens attached adjacent to one another on the same polymer chain, causing the polymer to expand in this direction. One possible explanation is that interactions between polymer side-groups and nematic 5CB are more energetically favorable than interactions between the side-groups themselves,[8] a theory supported by the experiments discussed in Chapter 4.

Once the solutions are heated to the isotropic phase, the end-on and side-on polymers are virtually indistinguishable. The polymers adopt spherical conformations and the correlation lengths are similar at comparable molecular weights. The increased correlation length at higher molecular weight is intuitively understood because the likelihood of surrounding monomers being connected to the same chain increases with the degree of polymerization. In the absence of nematic ordering, excluded volume effects disappear and $m = 2.0$, implying that favorable side-group / solvent interactions derive from nematic cross-interactions being of higher magnitude than nematic interactions in either polymer or solvent alone.

5.5 Conclusions

Small-angle neutron scattering from semidilute solutions of SGLCPs in a small-molecule nematic solvent reveals the conformational anisotropy of the polymer chains. The coupling between the LC solvent's orientational order and the polymer's conformation is mediated by the covalently bonded side groups. The sense (oblate or prolate) and the magnitude of the anisotropy is determined by the sense (end-on or side-on) and the magnitude of the polymer / side-group coupling: end-on polymers with weak coupling adopt mildly oblate conformations while side-on polymers with strong coupling adopt highly prolate conformations. The anisotropy of a side-on polymer is strongly dependent on temperature, but end-on polymers remain mildly oblate throughout the nematic phase. Once heated to the isotropic phase both types of polymer take on spherical conformations. The conformational anisotropy of these polymers in nematic solvent, and its temperature dependence, has a tremendous influence on the dynamics of nematic director fluctuations discussed in Chapter 6.

5.6 Tables

Table 5.1 Molecular weight, conversion, and polydispersity of the side-group liquid crystal homopolymers. Details of the characterization of end-on polymers (350HSiCB4 and 760HSiCB4) may be found in Appendix A.

Name	M_n (kg/mol)	Mole Fraction 1,2 PB	Mole Fraction 1,4 PB	Mole Fraction LC	PDI[a]
350HSiCB4	347	0	0.11	0.89	1.27
760HSiCB4	762	0.06	0.04	0.90	1.11
500HSiBB[b]	497	0.07	0.11	0.82	1.15
990HSiBB[b]	992	0.22	0.04	0.74	1.10

[a] PDI = Polydispersity Index (M_w/M_n)
[b] Synthesized and characterized by Rafael Verduzco[6]

Table 5.2 Fitting parameters used to model scattering data with Equation 5.1

Polymer	I_{par} or I_{perp}[a]	T [°C]	L [Å][b]	m	$C_1 \times 10^7$	C_2
500HSiBB	I_{par}	25	>350	1.7	-	-
500HSiBB	I_{par}	30	>350	1.7	-	-
500HSiBB	I_{perp}	25	31.5(1)	2.0	3.6	16
500HSiBB	I_{perp}	30	33.5(1)	2.0	17	21
500HSiBB	-	50	33.9(1)	2.0	4.3	21
990HSiBB	I_{par}	25	>350	1.7	-	-
990HSiBB	I_{par}	30	>350	1.7	-	-
990HSiBB	I_{perp}	25	30.2(2)	2.0	8.1	12
990HSiBB	I_{perp}	30	32.0(2)	2.0	10	14
990HSiBB	-	50	47.1(4)	2.0	0.63	11
350HSiCB4	I_{par}	25	48.4(2)	2.0	8.2	27
350HSiCB4	I_{par}	30	47.7(2)	2.0	5.3	23
350HSiCB4	I_{perp}	25	97.7(7)	1.8	3.4	33
350HSiCB4	I_{perp}	30	88.0(6)	1.8	2.1	27
350HSiCB4	-	50	39.6(1)	2.0	0.077	11
760HSiCB4	I_{par}	25	56.9(2)	2.0	15	39
760HSiCB4	I_{par}	30	55.1(7)	2.0	16	4.8
760HSiCB4	I_{perp}	25	118(1)	1.8	4.4	48
760HSiCB4	I_{perp}	30	111(1)	1.8	6.5	33
760HSiCB4	-	50	49.7(3)	2.0	0.20	15

[a] The parallel and perpendicular designations do not apply at 50 °C, where there is no nematic director and the data are circularly averaged.

[b] The number in parentheses is the standard deviation in the last digit of the value of *L*.

5.7 Figures

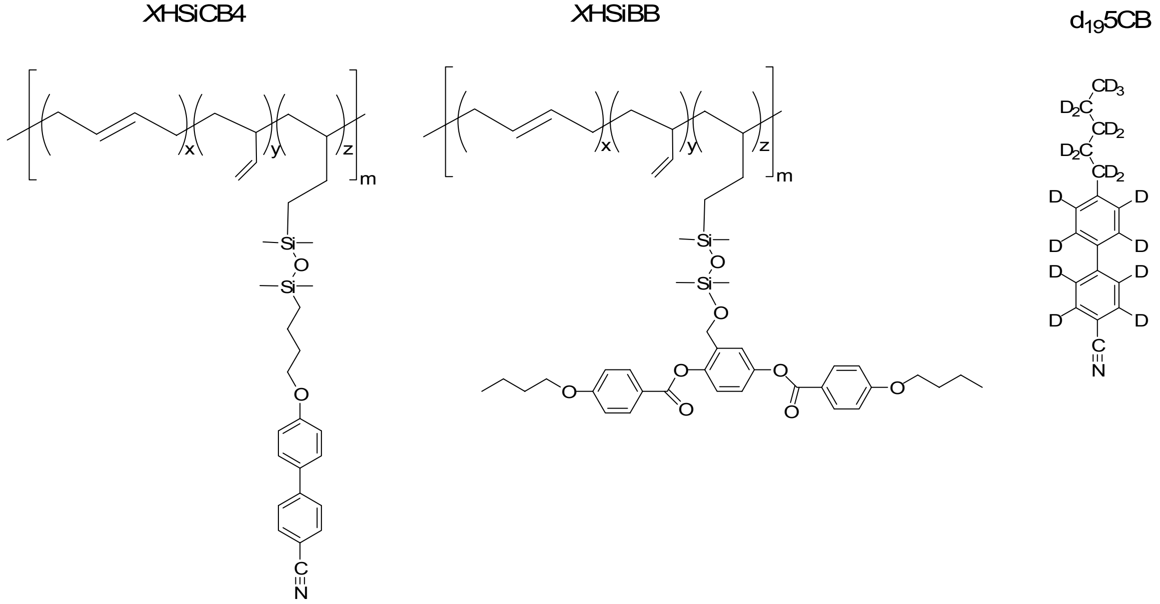

Figure 5.1 Chemical structures of end-on (*X*HSiCB4) and side-on (*X*HSiBB) side-group liquid crystal homopolymers and the perdeuterated nematic liquid crystal solvent (d_{19}5CB). A polymer's name is derived from its molecular weight (*X*) in units of kg/mol, the letter "H" to indicate a homopolymer, and either "SiCB4" or "SiBB" to indicate either end-on or side-on mesogens, respectively. In addition to monomers having an attached mesogen, the polymer also contains some residual 1,2- and 1,4-butadiene monomers. Compositions, expressed as the mole fractions *x*,*y*, and *z*, are given in Table 5.1. Details of end-on polymer characterization are presented in Appendix A, and synthesis of d_{19}5CB is described in Appendix B.

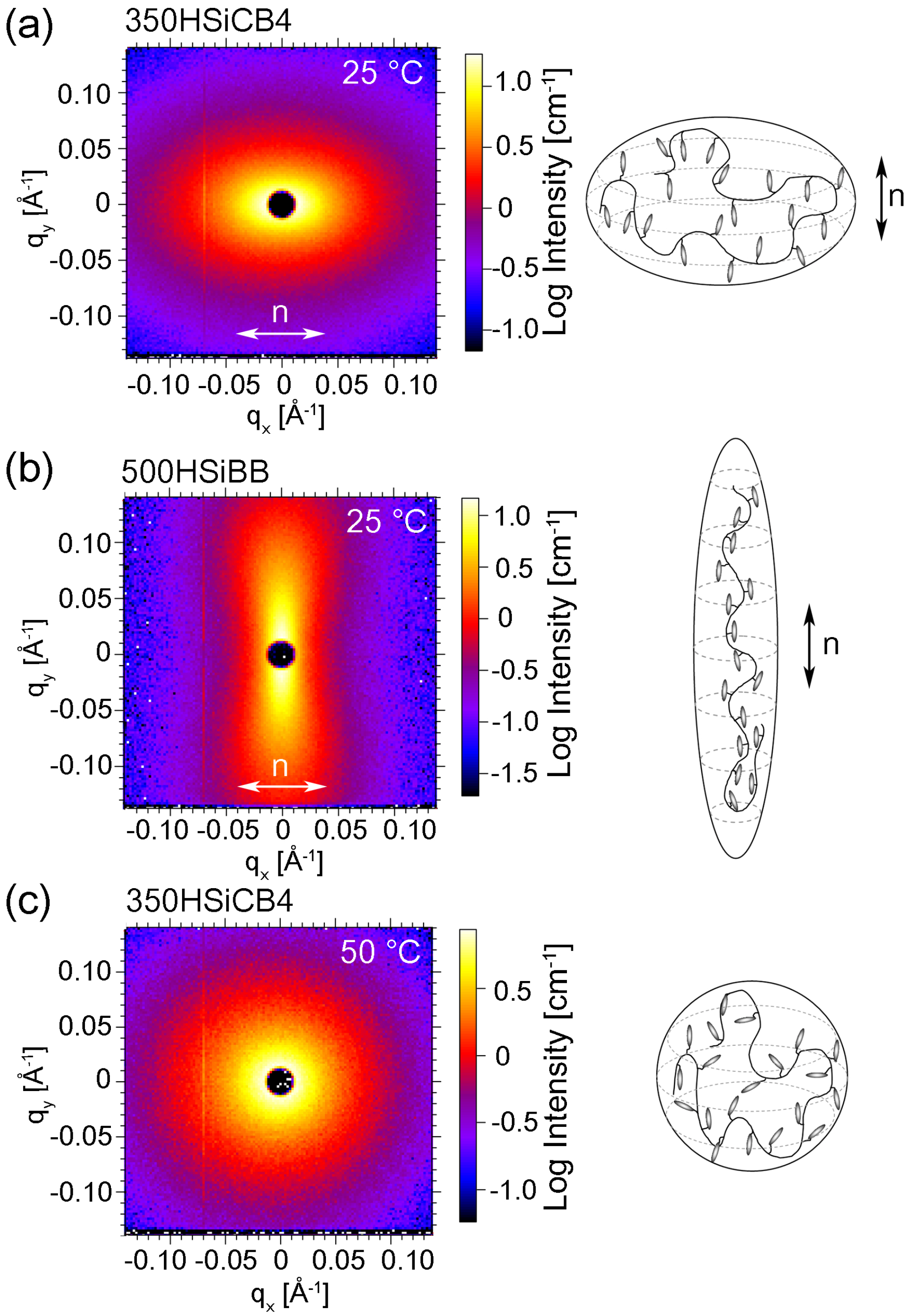

Figure 5.2 Two-dimensional small-angle neutron scattering patterns from 5 wt % solutions of (a) oblate end-on and (b) prolate side-on homopolymers in d_{19}5CB in the nematic phase (25 °C). The orientation of the nematic director, ***n***, is indicated by the double-headed arrows. When heated above the nematic-isotropic transition temperature, the polymers adopt a spherical conformation and the scattering patterns become circularly symmetric as illustrated with (c) end-on homopolymer solution at 50 °C.

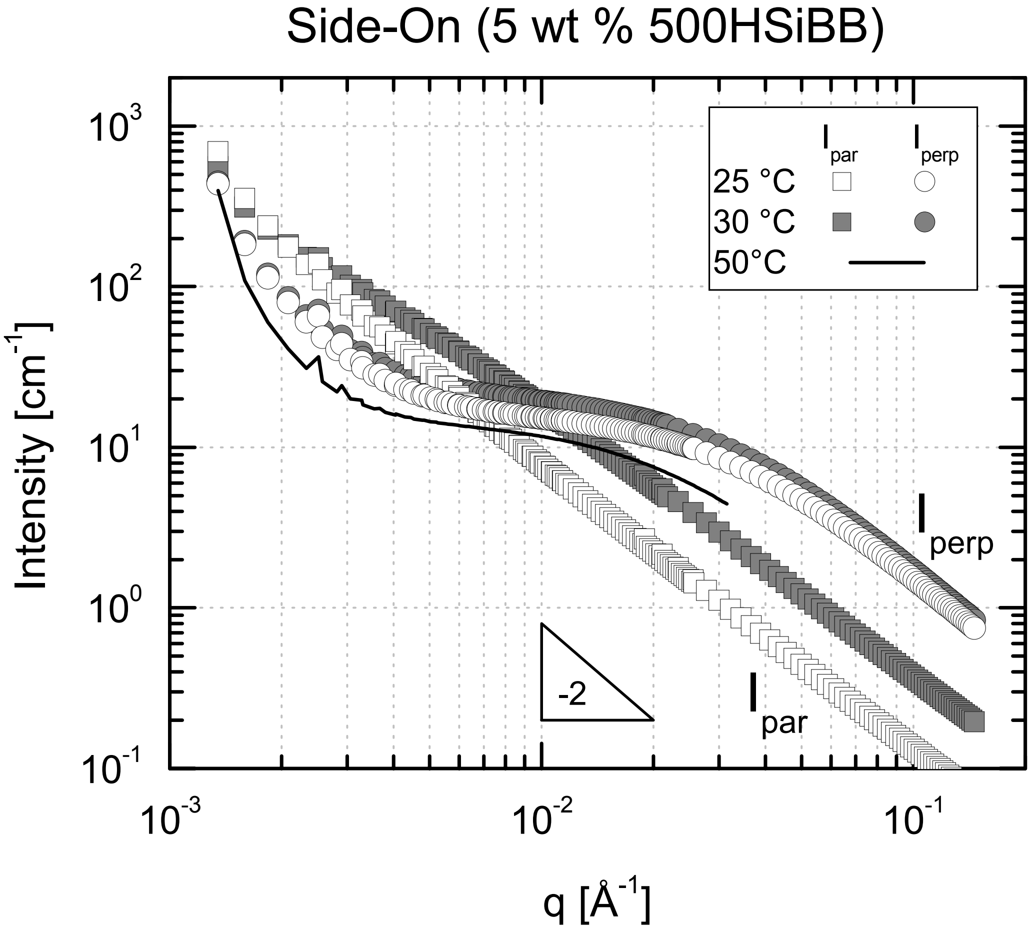

Figure 5.3 Sector-averaged small-angle neutron scattering patterns from 5 wt % 500 HSiBB in d_{19}5CB at two temperatures in the nematic phase (25 and 30 °C) and circularly averaged scattering pattern from the sample in the isotropic phase (50 °C). "I_{par}" and "I_{perp}" denote sector averaging in a ± 15° wedge parallel and perpendicular to the LC director, respectively. For the sake of clarity, a solid line is used to represent data at 50 °C even though the intensity was measured at the same discrete values of *q* as for 25 and 30 °C data sets.

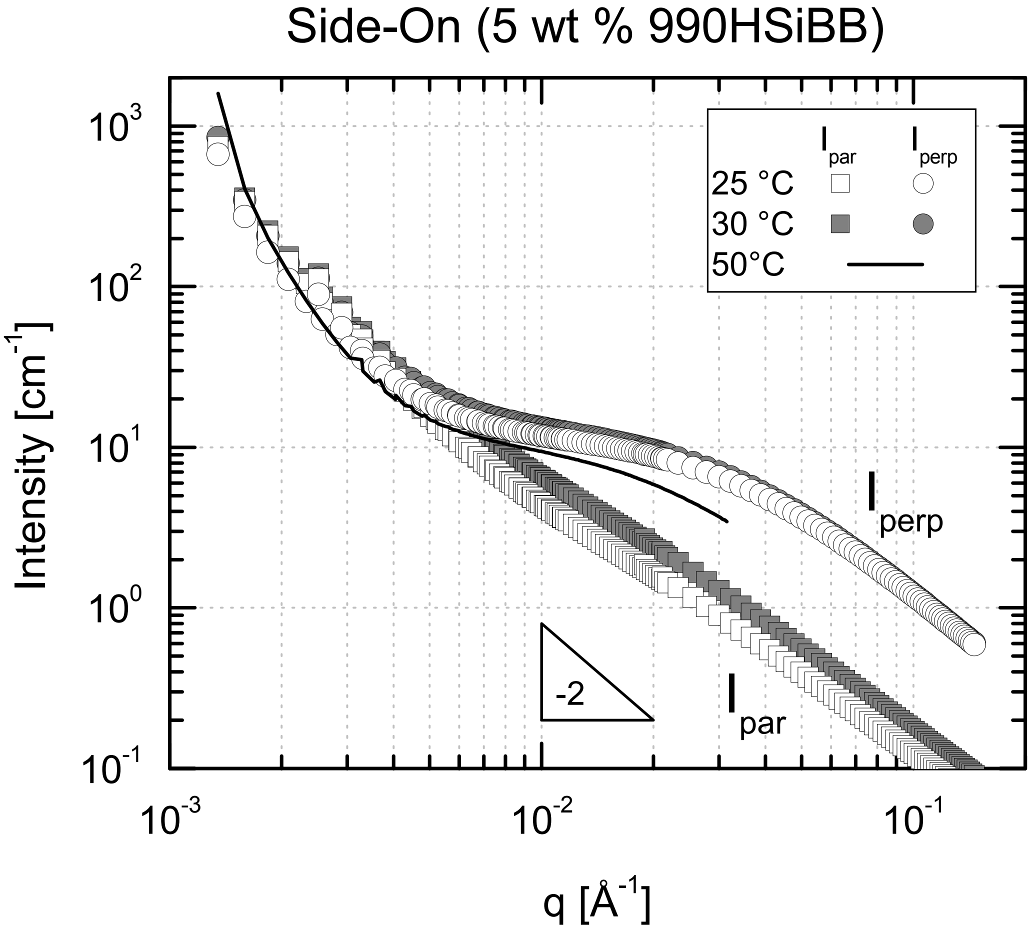

Figure 5.4 Sector-averaged small-angle neutron scattering patterns from 5 wt % 990 HSiBB in d_{19}5CB at two temperatures in the nematic phase (25 and 30 °C) and circularly averaged scattering pattern from the sample in the isotropic phase (50 °C). "I_{par}" and "I_{perp}" denote sector averaging in a ± 15° wedge parallel and perpendicular to the LC director, respectively. For the sake of clarity, a solid line is used to represent data at 50 °C even though the intensity was measured at the same discrete values of q as for 25 and 30 °C data sets.

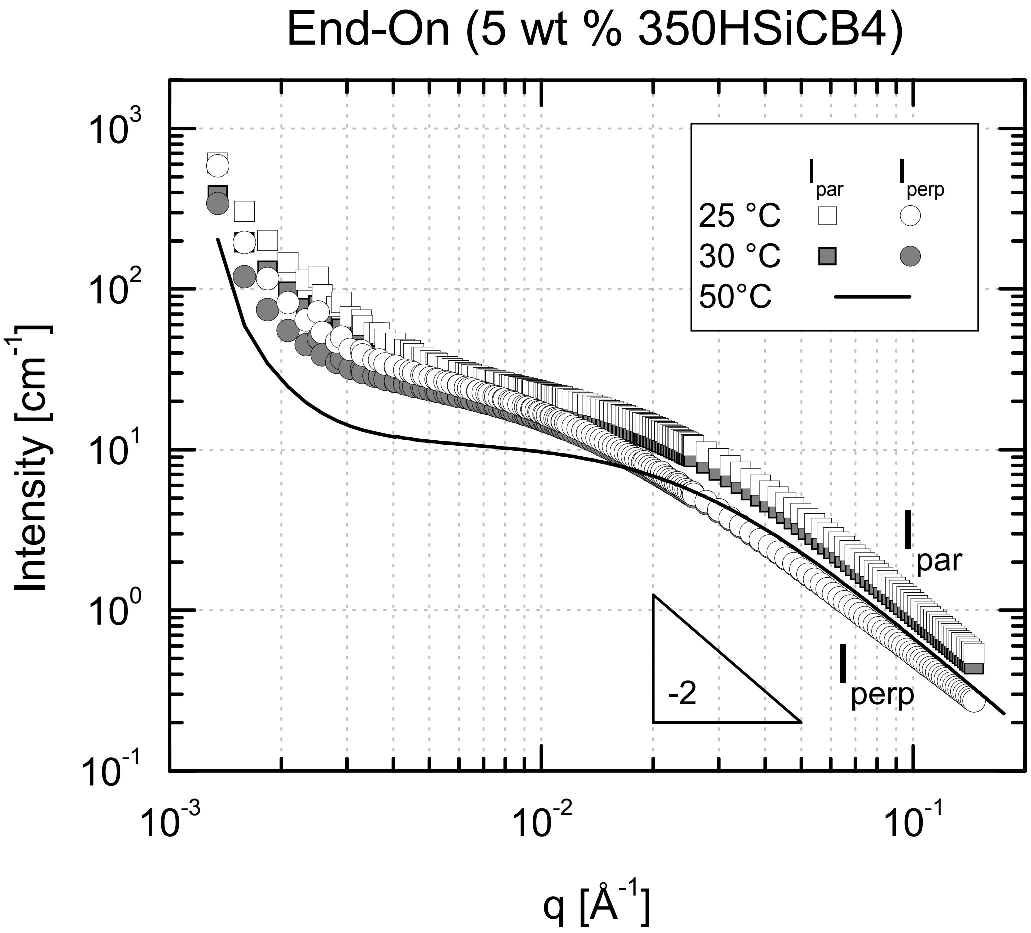

Figure 5.5 Sector-averaged small-angle neutron scattering patterns from 5 wt % 350 HSiCB4 in d_{19}5CB at two temperatures in the nematic phase (25 and 30 °C) and circularly averaged scattering pattern from the sample in the isotropic phase (50 °C). "I_{par}" and "I_{perp}" denote sector averaging in a ± 15° wedge parallel and perpendicular to the LC director, respectively. For the sake of clarity, a solid line is used to represent data at 50 °C even though the intensity was measured at the same discrete values of *q* as for 25 and 30 °C data sets.

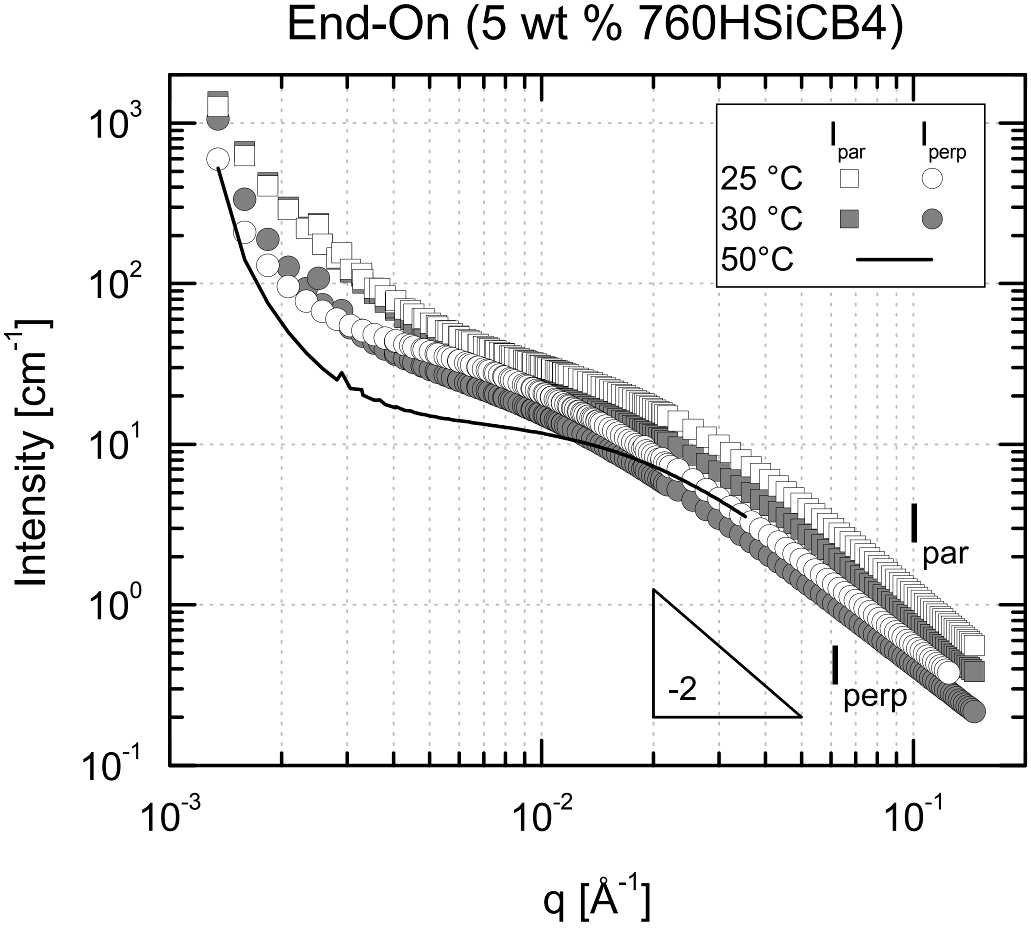

Figure 5.6 Sector-averaged small-angle neutron scattering patterns from 5 wt % 760 HSiCB4 in d_{19}5CB at two temperatures in the nematic phase (25 and 30 °C) and circularly averaged scattering pattern from the sample in the isotropic phase (50 °C). "I_{par}" and "I_{perp}" denote sector averaging in a ± 15° wedge parallel and perpendicular to the LC director, respectively. For the sake of clarity, a solid line is used to represent data at 50 °C even though the intensity was measured at the same discrete values of *q* as for 25 and 30 °C data sets.

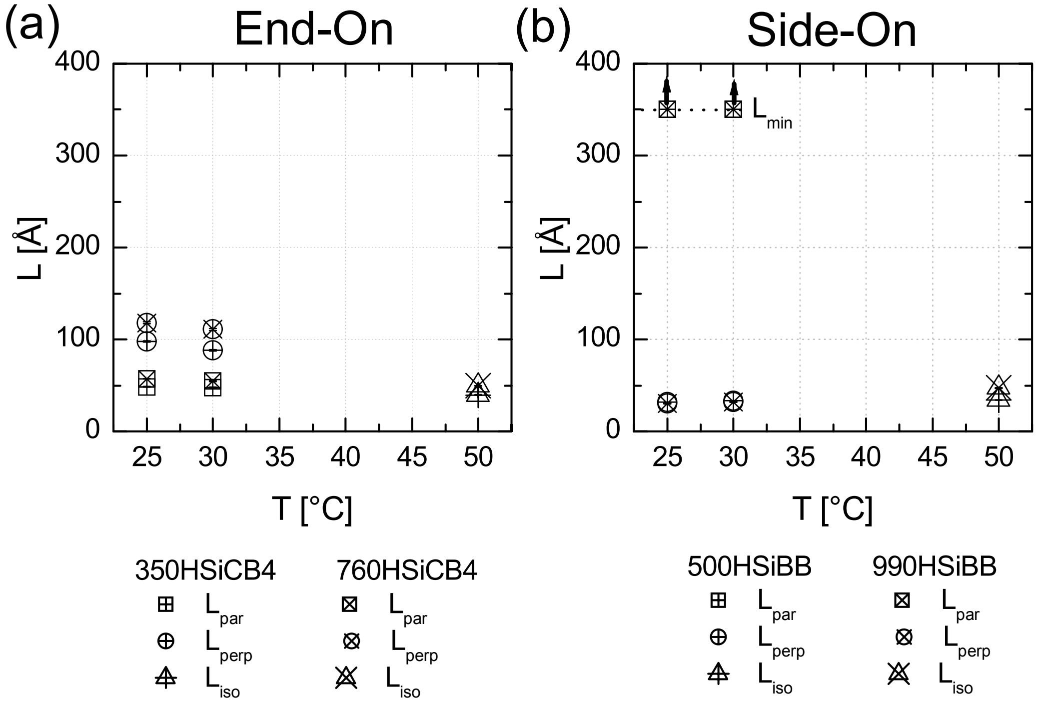

Figure 5.7 Correlation lengths, L, in the directions perpendicular to (L_{perp}) and parallel to (L_{par}) the nematic director for 5 wt % solutions of (a) end-on and (b) side-on homopolymers derived from fits to scattering data using Equation 5.1. The correlation length in the isotropic phase is denoted L_{iso}. In side-on polymers, L_{par} cannot be determined by fitting, but a lower bound of L_{min} = 350 Å has been established. Fitting parameters are given in Table 5.2.

5.8 References

[1] Kempe, M. D.; Kornfield, J. A.; Lal, J. Chain Anisotropy Side-Group Liquid Crystalline Polymers in Nematic Solvents. *Macromolecules* **2004**, *37*, 8730-8738.

[2] Matoussi, H.; Ober, R.; Veyssie, M.; Finkelmann, H. Conformation of Side Chain Nematic Polymers in Nematic Solutions: a Small-Angle X-Ray Scattering Study: SAXS. *Europhys. Lett.* **1986**, *2*, 233-240.

[3] Mattoussi, H.; Ober, R. Conformation of Comblike Liquid-Crystalline Macromolecules. *Macromolecules* **1990**, *23*, 1809-1816.

[4] Carri, G. A.; Muthukumar, M. Configurations of liquid crystalline polymers in nematic solvents. *J. Chem. Phys.* **1998**, *109*, 11117-11128.

[5] Brochard, F.; Jouffroy, J.; Levinson, P. Phase diagrams of mesomorphic mixtures. *J. Physique* **1984**, *45*, 1125-1136.

[6] Verduzco, R. Texture Transitions, Electro-Optics, and Dynamics of Liquid Crystal Gels with Novel Network Architectures. Ph.D. Thesis, California Institute of Technology, Pasadena, CA, February 5, 2007.

[7] Kempe, M. D.; Scruggs, N. R.; Verduzco, R.; Lal, J.; Kornfield, J. A. Self-assembled liquid-crystalline gels designed from the bottom up. *Nat. Mater.* **2004**, *3*, 177-182.

[8] Rubinstein, M.; Colby, R. H. *Polymer Physics*, 1st ed; Oxford University Press: New York, 2003.

[9] Higgins, J. S.; Benoit, H. C. *Polymers and Neutron Scattering*, Oxford Series on Neutron Scattering in Condensed Matter, ed. S.W. Lovesey; E.W.J. Mitchell; Oxford University Press: New York, NY, 1996.

[10] Hammouda, B.; Ho, D. L.; Kline, S. Insight into Clustering in Poly(ethylene oxide) Solutions. *Macromolecules* **2004**, *37*, 6932-6937.

[11] Hammouda, B.; Ho, D.; Kline, S. SANS from Poly(ethylene oxide)/Water Systems. *Macromolecules* **2002**, *35*, 8578-8585.

[12] Richtering, W.; Gleim, W.; Burchard, W. Semidilute Solutions of Liquid Crystalline Polymers. *Macromolecules* **1992**, *25*, 3795-3801.

[13] Viertler, K.; Wewerka, A.; Stelzer, F.; Fytas, G.; Vlassopoulos, D. Macromolecular Anisotropic Association in Isotropic Solutions of a Liquid Crystal Side Chain Polymer. *Macromol. Chem. Phys.* **2001**, *202*, 3174-3179.

[14] Magnago, R. F.; Merlo, A. A.; Vollmer, A. F.; Mauler, R. S.; Vargas, F.; Pesco da Silveira, N. Synthesis, mesomorphic properties and light scattering of polyacrylates liquid crystals. *Polym. Bull. (Heidelberg, Ger.)* **1999**, *42*, 551-557.

[15] Pereira, F. V.; Merlo, A. A.; Pesco da Silveira, N. Behaviour of mesogenic side group polyacrylates in dilute and semidilute regime. *Polymer* **2002**, *43*, 3901-3908.

[16] Gallani, J. L.; Hilliou, L.; Martinoty, P. Abnormal Viscoelastic Behavior of Side-Chain Liquid-Crystal Polymers. *Phys. Rev. Lett.* **1994**, *72*, 2109-2112.

Chapter 6

COUPLING LIQUID CRYSTAL ORIENTATION TO AN ASSOCIATING POLYMER NETWORK: MULTIPLE RELAXATION PROCESSES IN LIQUID CRYSTALLINE PHYSICAL GELS

6.1 Introduction......144
6.2 Experimental......146
6.3 Results......148
6.4 Discussion......153
6.5 Conclusions......156
6.6 Tables......158
6.7 Figures......159
6.8 References......175

The work presented in this chapter was done jointly with Rafael Verduzco and in collaboration with Sam Sprunt (Dept. of Physics, Kent State University) and Peter Palffy-Muhoray (Liquid Crystal Institute, Kent State University). Rafael Verduzco synthesized the side-on polymers (names ending with "BB") and we collected the light scattering data together in Sam Sprunt's lab. Sam Sprunt and Peter Palffy-Muhoray contributed to the experimental design and interpretation of the results. We thank Prof. Sprunt's students, Sunil Sharma and Krishna Neupane, for their help with light scattering experiments.

6.1 Introduction

Dispersing a physically crosslinked network of associating polymer in a small-molecule nematic liquid crystal (LC) solvent couples the network's elasticity with the LC's orientational order, giving rise to electro-optic and mechano-optic properties not present in either material alone. For example, the gel can be aligned into a uniform monodomain simply by applying mechanical shear, and the gel's optical response is fast enough to track a 1 kHz alternating electric field.[1] This coupling between the polymer network and the LC solvent also gives rise to rich dynamic processes in LC physical gels. The physically associated network is capable of dynamic restructuring: on short time scales the network is unchanging, as though it were chemically crosslinked, but the slow process of breaking and reforming crosslinks allows the network to rearrange on long time scales. The orientation of the LC solvent fluctuates with thermal energy and these fluctuations are translated to the network via liquid crystalline side-groups covalently attached to the polymer chains.

The dynamics of LC orientation fluctuations has been extensively studied using dynamic light scattering.[2] When the LC orientation, described by the nematic director, ***n***, fluctuates away from its equilibrium orientation, $\boldsymbol{n_0}$, the resulting distortion can be expressed as the sum of a splay, twist, and bend distortion (Figure 6.1) and the elastic penalty is expressed by the Frank elastic free energy per unit volume, F_V:

$$F_V = \tfrac{1}{2}\left[K_1(\nabla\cdot\mathbf{n})^2 + K_2(\mathbf{n}\cdot(\nabla\times\mathbf{n}))^2 + K_3|\mathbf{n}\times(\nabla\times\mathbf{n})|^2\right] \tag{6.1}$$

where K_1, K_2, and K_3 are the splay, twist, and bend elastic constants, respectively.[3] Frank elasticity drives the director to return to $\boldsymbol{n_0}$ at a rate, τ_ν^{-1}, determined by the ratio of K_ν to the LC's corresponding anisotropic viscosity η_{splay}, η_{twist}, and η_{bend}:

$$\tau_\nu^{-1} = \frac{K_\nu}{\eta_\nu} q^2, \quad \nu = \text{splay, twist, or bend,}^{[2,4]} \tag{6.2}$$

where q is the magnitude of the scattering vector. Choosing the correct geometry can isolate light scattering from fluctuations of splay, twist, and bend distortions in a nematic LC[2] (Figure 6.2) and the time correlation of the scattered light reveals the dynamics of the distortion's relaxation.

Coupling of LC order to a polymer network has previously been accomplished by chemically crosslinking polymers bearing covalently attached liquid crystalline side groups to create a solvent-free LC elastomer, as reviewed by Warner and Terentjev.[5] The theory of nematic LC elastomers[5-9] predicts the network to provide a restoring torque to director fluctuations, in addition to Frank elasticity, which is a function of the anisotropy of the network's polymer chains. Despite the existence of extensive theory, there exists only one experimental investigation of director dynamics in an LC elastomer.[10] This is due, in part, to the difficulty in preparing uniformly aligned monodomain elastomers that are suitable for dynamic light scattering experiments.

LC physical gels are ideal candidates for dynamic light scattering experiments because they are relatively easy to align. A triblock copolymer having random-coil polymer endblocks (polystyrene, PS) and a side-group liquid crystal polymer (SGLCP) midblock self-assembles in nematic LC solvent to create a physical gel.[1, 11] When the solvent is heated to the isotropic phase, the endblocks become soluble and the network dissolves. Cooling a PS-SGLCP-PS triblock copolymer solution from the isotropic to the nematic phase in the presence of a biasing electromagnetic field causes the gel to form in an aligned solvent and provides an optically uniform monodomain. These gels are similar to nematic elastomers in that mechanical strain is coupled to LC order,[12] but they are orders of magnitude softer by virtue of their solvent content: the modulus of an LC physical gel is approximately 10^2 Pa[11] while the modulus of an LC elastomer is typically greater than 10^5 Pa.[10] The network elasticity in an LC gel is, therefore, comparable to the Frank elasticity of a nematic LC ($\sim 10^2 - 10^3$ Pa on ~1 μm length scales),[3] in contrast to LC elastomers where Frank elasticity is orders of magnitude less than network elasticity.

The dynamics of director fluctuations in LC gels and, for the purposes of comparison, analogous side-group liquid crystal polymer (SGLCP) solutions are explored here using dynamic light scattering from uniform monodomains. Both network elasticity and Frank elasticity contribute to relaxation dynamics, and the network's ability to rearrange with time contributes an additional process for director relaxation. In qualitative agreement with the theory of nematic elastomers, gel relaxation dynamics are found to be dependent on the anisotropy of the network chains.

6.2 Experimental

6.2.1 Materials

Two different triblock copolymers having random coil endblocks and a side-group liquid crystal polymer (SGLCP) midblock were synthesized (Figure 6.3) along with two analogous SGLCP homopolymers (Figure 6.4). An anionically polymerized poly[styrene-b-(1,2-butadiene)- b-styrene] (57 kg/mol PS, 146 kg/mol PB, 67 kg/mol PS) triblock copolymer was purchased from Polymer Source (Montreal, Quebec) and functionalized with end-on (SiCB4) mesogens according to the methods described in Appendix A. Side-on (SiBB) mesogens were attached to the same prepolymer by Rafael Verduzco.[13] An anionically polymerized, 63 kg/mol 1,2-polybutadiene prepolymer provided by Steve Smith of Proctor and Gamble, Inc. was used to make the homopolymers. The characteristics of these four polymers are summarized in Table 6.1 and the details of characterization of end-on polymers are given in Appendix A.

Solutions of polymers in the nematic LC 4-pentyl-4′-cyanobiphenyl (5CB, purchased and used as received from TCI America) were prepared by dissolving the polymer and 5CB together in dichloromethane (DCM), then evaporating the DCM under a stream of air followed by drying in vacuum overnight.

6.2.2 Methods

Solutions of polymer in 5CB were loaded into cells consisting of glass plates separated by 4, 9, or 25 μm spacers. Cells having 4 or 9 μm gaps were purchased from LC Vision (Boulder, CO) and have SiO_2 alignment layers for homogeneous (planar) alignment. Cells having a 25 μm gap were purchased from EHC (Japan) and have rubbed polyimide alignment layers for homogeneous alignment. All three cell types have 5 mm x 5 mm transparent indium-tin oxide (ITO) electrodes in their centers. Cells were filled with polymer / LC solutions by capillary action; homopolymer solutions readily flowed in at room temperature and triblock gels flowed readily when heated above the gel point (35 °C for 5 wt % 1100ABASiCB4 and 33 °C for 5 wt % 1400ABASiBB). Homopolymer solutions spontaneously aligned into a monodomain under the influence of the alignment layers. Gels were aligned into a homogeneous monodomain (LC director parallel to the cell surface) by heating them above the gel point then slowly cooling them inside the bore of an 8 T NMR magnet. Alternatively, gels were aligned into homeotropic monodomains (LC director perpendicular to the cell surface) by heating them above the gel point then cooling while applying a 15 V_{rms} potential difference to the ITO electrodes.

Aligned samples were mounted in a temperature controlled oven with optical access that was stabilized to better than ± 0.01 °C and illuminated with a focused, polarized 20 mW HeNe laser (wavelength λ = 633 nm) incident perpendicular to the cell surface. The incident polarization was vertical, orthogonal to the horizontal scattering plane. Monodomain LC samples were placed in the beam oriented so their director was either parallel to the incident polarization (vertical, V), perpendicular to both the incident polarization and the incident beam (horizontal, H), or parallel to the incident beam (parallel, P) (Figure 6.2). Depolarized light scattering was collected at various scattering angles, θ_s, with the optical scattering vector $\boldsymbol{q}$ ($|\boldsymbol{q}| = q = 4\pi n/\lambda \sin(\theta_s/2)$, where $n \approx 1.55$ is the sample's refractive index) lying in the horizontal plane. The time correlation of the scattered intensity ($g_2(t) = \langle I(q,0)I(q,t)\rangle$) was recorded in the homodyne regime. The resulting intensity autocorrelation functions were normalized by their maximum value, typically 1.95.

Prior to initiating a time correlation experiment, the sample position was adjusted to find a well-aligned region of the sample that minimized the static intensity of the scattered light. Monodomains of homopolymer solutions were highly uniform and required little adjustment. On the other hand, it was more difficult to achieve high-quality monodomains with gels, and more sample adjustment was required prior to each experiment.

On small (< 100 nm) length scales, the gels have a heterogeneous structure that consists of a LC midblock dissolved in LC and phase-separated endblocks swollen with LC.

Significantly, the length scales probed by the experiment are large enough that the system can be considered homogeneous. The light scattering experiments probe length scales ranging between 350 nm (q = 0.018 nm^{-1}) and 2.9 μm (q = 0.002 nm^{-1}). The data may be interpreted on the basis of a uniform material because the length scale of the spatial fluctuations that scatter light are much greater than the length scale of a single micelle.

In some samples, the intensity autocorrelation function did not decay completely even after several hours. Due to the large number of experiments, all samples could not be independently verified for ergodicity. However, selected samples that were chosen to verify ergodicity did manifest a complete decay of the intensity autocorrelation function after a sufficiently long time, up to several weeks.

6.3 Results

6.3.1 Comparison of Gels to Homopolymer Solutions

The relaxation dynamics of liquid crystalline gels are qualitatively different from those of homopolymer solutions or 5CB alone. Pure 5CB exhibits a single, exponential relaxation that fully decays on time scales on the order of 10^{-3} s. Homopolymer solutions behave the same way but the relaxation is shifted towards longer times (10^{-2} - 10^{-1} s). In contrast to both of these, correlations in gels decay non-exponentially and often relax over much longer time scales (> 1 s) (Figure 6.5). In some cases there are two distinct relaxation processes observed; the correlation function nearly overlaps that of the homopolymer solution at short times, but decays slowly at long times (Figure 6.5a).

The degree to which relaxation is slowed in homopolymer solutions relative to pure 5CB depends on the scattering geometry. End-on homopolymer (5 wt % 490HSiCB4) slows relaxation more in the H geometry than in V (Figure 6.5a and b). Side-on homopolymer (5 wt % HiBB) has the opposite effect, slowing relaxation more strongly in the V geometry (Figure 6.5c and d). Anisotropy of the relaxation dynamics is also observed in gels; end-on gels (5 wt % 1100ABASiCB4) have longer-lived correlations in the H geometry and side-on gels in the V geometry (5% 1400ABASiBB) (Figure 6.6). The correlation functions of end-on gels overlap those of end-on homopolymers at short times (Figure 6.5a and b). In the case of side-on gels, the short time relaxation is slower than the homopolymer in the H geometry (Figure 6.5c) and faster in the V geometry (Figure 6.5d).

6.3.2 Comparison of End-On and Side-On Gels

Examining the correlation functions of gels at a variety of scattering angles further demonstrates anisotropy in their relaxation dynamics: both the qualitative shape of the correlation functions and the time scales for relaxation are dependent on the scattering geometry (H or V). The time correlation functions from the end-on gel strongly deviate from single exponential decay at all scattering angles in the H geometry with crossover from fast relaxation to slow relaxation occurring between ~10^{-3} and 10^{-2} s (Figure 6.6a). In the V geometry relaxation closely resembles a single exponential, albeit a stretched exponential, for $\theta_s \geq 30°$ and transitions to relaxation by two processes for $\theta_s < 30°$ (Figure 6.6b). Correlations in the end-on gel are significantly longer-lived in the H geometry than in the V; over the dynamic range studied here, correlation functions in the H geometry do not decay to a baseline of $g_2(t) = 1$ when θ_s is less than ~30° but complete decay is observed at all scattering angles in the V geometry. These trends are reversed in the side-on gel where the relaxation is clearly non-exponential for all scattering angles in the V geometry (Figure 6.6d) but closely resembles a stretched exponential for $\theta_s \geq 16°$ in the H geometry (Figure 6.6c). Long-lived correlations are evident in the V geometry, but in the H geometry the correlation functions completely decay to $g_2(t) = 1$, except at $\theta_s = 8°$. Unlike the end-on gel there is no clear inflection point signaling a crossover from a fast relaxation process to a slow relaxation process in the side-on gel. Instead, the correlation functions in the V geometry are highly stretched to long times.

The sense of the dynamical anisotropy in the gels is identical to that of the homopolymer solutions: the end-on gel has slower dynamics in the bend (H) geometry and the side-on gel has slower dynamics in the splay (V) geometry. The relative contribution of the fast and slow processes is also dependent on the scattering geometry with the slow process playing a more prominent role in the geometry where dynamics are slowest. The relative contribution of the processes is independent of the scattering angle in side-on gels, but in end-on gels the slow process becomes more prominent at smaller angles.

6.3.3 *q*-Dependence of the Relaxation Dynamics

The scaling of relaxation rate with q is revealed by plotting a series of correlation functions at different scattering angles versus rescaled delay time, $t^R = t\ (\sin(\theta_s)/\sin(\theta_{s,0}))^2$, where $\theta_{s,0}$ is a reference angle of $\theta_s = 8°$, thus collapsing them onto a single curve when the relaxation rate depends on q^2. Correlation functions from end-on (Figure 6.7a and b) and side-on on (Figure 6.8a and b) homopolymer solutions superimpose well with this rescaling, but such is not always the case with gels. Correlation functions from end-on gels in the V geometry superimpose well when $\theta_s \geq 30°$. At smaller scattering angles they superimpose well at short times ($t^R < 10^{-2}$ s) but deviate towards higher values of $g_2(t)$ at longer times (Figure 6.7d). The H geometry is similar; correlation functions superimpose well at large scattering angles, but deviate at smaller θ_s (Figure 6.7c). In side-on gels, the correlation functions are found to superimpose well at all scattering angles in both H and V geometries, the only exception being when $\theta_s = 8°$ in the H geometry (Figure 6.8c and d).

Comparing the time scale for relaxation of the gels to that of the corresponding homopolymer solutions shows that the gel slows relaxation in one scattering geometry more strongly than the other. The time scale for complete loss of correlation ($g_2(t) = 1$) is approximately the same for end-on gel and homopolymer solution at $\theta_s < 22°$ in the V geometry ($t^R \approx 10^{-1}$ s) (Figure 6.7b and d), but the gel has much longer-lived correlations ($t^R \approx 10^3$ s) in the H geometry when compared to the homopolymer solution (Figure 6.7a and c). Opposite to what is observed for end-on polymers, the time scale for complete loss of correlation in side-on gel is approximately equal to that of the side-on homopolymer solution ($t^R \approx 10^{-2} – 10^{-1}$ s) in the H geometry (Figure 6.8a and c), but is shifted to much longer time scales in the V geometry ($t^R \approx 10^3$ s) (Figure 6.8b and d).

6.3.4 Concentration Dependence of the Relaxation Dynamics

The time correlation functions from solutions of end-on triblock copolymers are qualitatively different above and below the gel point (~ 5 wt % polymer) (Figure 6.9). A solution of 1 wt % 1100ABASiCB4 in 5CB has a single, exponential relaxation similar in shape to an end-on homopolymer solution. Above the gel point the shape of the correlation function is relatively insensitive to concentration and the dynamics get slower as concentration is increased; correlations are longer-lived in 15 wt % 1100ABASiCB4 than 5 wt % 1100ABASiCB4.

6.3.5 Temperature Dependence of the Relaxation Dynamics

The dynamics of the end-on homopolymer solution and gel are relatively insensitive to changes in temperature. Time correlation functions are virtually superimposable in the temperature range from 25.0 to 33.5 °C (Figure 6.10). In contrast, director relaxation in side-on polymer solutions gets faster as temperature is increased (Figure 6.11). Most dramatically, the relaxation rate of 5 wt % side-on homopolymer in the V geometry increases by almost two orders of magnitude as temperature is increased from 25.0 to 33.5 °C (Figure 6.11b). In the H geometry, however, there is no observable change in this temperature range (Figure 6.11a). Increasing the temperature of the side-on gel has the strongest effect on long-time relaxation dynamics; correlation functions are shifted toward shorter times at higher temperatures, especially in the H geometry (Figure 6.11c). Examining the entire range of scattering angles makes temperature-induced changes in side-on polymer solutions more evident (Figure 6.12). At the highest temperature studied (33.5 °C), homopolymer correlation functions are shifted towards smaller times in the V geometry, but unchanged in the H geometry (Figure 6.12a and b) relative to the data at 25 °C (Figure 6.8a and b). The correlation functions from side-on gels in the H geometry at 31.5 °C in the H geometry more closely resemble a single exponential decay and are shifted towards shorter times relative to the 25 °C data (Figure 6.12c and Figure 6.8c). In the V geometry there is a similar shift and change in shape for correlation functions at $\theta_s \geq 30°$, but when $\theta_s \leq 22°$, the correlation functions are dramatically different from those at high angle: they do not superimpose with the $(\sin(\theta_s)/\sin(\theta_{s,0}))^2$ rescaling and correlations persist to longer time scales (Figure 6.12d).

6.3.6 Relaxation Dynamics of Gels in the P Geometry

Correlation functions from gels in the P geometry have many of the same characteristics observed in the H and V geometries (Figure 6.13). Both gels' correlation functions decay by a combination of a fast and a slow process, the slow process being most prominent at small scattering angles. Long-lived correlations are observed in the side-on gel when $\theta_s \leq 16°$ but are not observed in the end-on gel. The time scale for complete loss of correlation in the P geometry is similar for both gels ($t^R \sim 10^3$ s); for the end-on gel it is similar to that in the H geometry and for the side-on gel it is similar to that in the V geometry.

6.3.7 Fitting Correlation Functions to Determine Relaxation Rates

Correlation functions from homopolymer solutions were fit to the empirical Williams-Watts function:[14, 15]

$$g_2(t) = 1 + \left[e^{-\left(t/\tau\right)^{\beta}} \right]^2 \tag{6.3}$$

where τ is the relaxation rate and $0 < \beta \leq 1$ is a stretching exponent equal to one for purely exponential relaxation. If $\beta < 1$ is assumed to derive from a spectrum of relaxation times, the average relaxation time $<\tau>$ may be calculated:[16]

$$\langle \tau \rangle = \frac{\tau}{\beta} \Gamma\left(\beta^{-1}\right) \tag{6.4}$$

where Γ denotes the Gamma function. Plotting the inverse of $<\tau>$ versus q^2 gives a straight line for homopolymer solutions (Figure 6.14), further demonstrating the expected scaling between relaxation rate and q (equation 6.2). The anisotropy of the relaxation dynamics is evident in the relaxation rates, as well. Relaxation rates of end-on homopolymer solution are faster in the V geometry (Figure 6.14a), but side-on homopolymer solution relaxes faster in the H geometry (Figure 6.14b). The anisotropy is much greater in side-on homopolymer solution; relaxation in the H geometry is about two orders of magnitude faster than in the V geometry whereas the difference is approximately tenfold for end-on homopolymer. The change in the relaxation rates with temperature is negligible in end-on homopolymer solution (Figure 6.14a), but relaxation dynamics get much faster in side-on solution when temperature is increased to 33.5 °C (Figure 6.14b).

The value of the stretching exponent used to fit correlation functions from homopolymer solutions ranged from 0.8 to 1.0, except when fitting end-on solution in the H geometry; in this case the exponent was as low as 0.6. These exponents correlate with the polymers' polydispersities (Table 6.1) and are consistent with a spectrum of relaxation times that would result from a broad distribution of molecular weight. Attempts to use the Williams-Watts function to fit data from gels resulted in β values as low as 0.3, too low to be accounted for by polydispersity alone. Furthermore, the Williams-Watts function fails to describe the two relaxation processes often observed in gels.

6.4 Discussion

6.4.1 Dynamics of Homopolymer Solutions

Director relaxation in solutions of SGLCP homopolymers is a hydrodynamically controlled process: just like small-molecule LCs, Frank elasticity of the director field provides the restoring torque to a director fluctuation and the LC's viscosity resists the return to equilibrium. Thus, the relaxation rate of homopolymer solutions scales with q^2 (Equation 6.2). Numerous studies on SGLCP solutions have found similar hydrodynamic relaxation and shown that dissolving an SGLCP in a nematic LC increases the viscosity without significantly changing the Frank elastic constants.[4, 17-21]

The dynamical anisotropy observed in homopolymer solutions is consistent with the Brochard theory,[22] which predicts the viscosity to be affected anisotropically depending on the dissolved polymer's conformation in solution: prolate SGLCPs have the greatest effect on the splay viscosity (η_{splay}) while oblate SGLCPs affect the bend viscosity (η_{bend}) more. The end-on homopolymer, which has been shown by small-angle neutron scattering (SANS) to have a mildly oblate conformation in solution with 5CB (Chapter 5), has a greater effect on the dynamics of relaxation in the bend geometry ($\tau / \tau_{5CB} = 120$) than in the splay geometry ($\tau / \tau_{5CB} = 3$). Similarly, the side-on homopolymer has been shown by SANS to adopt a strongly prolate conformation (Chapter 5) and has a larger effect on the dynamics of relaxation in the splay geometry (τ / τ_{5CB} = 90) than in the bend geometry (τ / τ_{5CB} = 3).

The temperature dependence of relaxation dynamics in homopolymer solutions may be interpreted within the Brochard theory to indicate a change in the polymer's conformational anisotropy; the theory predicts the anisotropy in the increase of viscosity to vanish as $R_{||}$ / $R_{\perp}$ approaches unity ($R_{||}$ and $R_{\perp}$ denote the polymer's radii of gyration parallel and perpendicular to the director, respectively). The temperature dependence of end-on homopolymer solution is small, but when side-on homopolymer solution is heated from 31.5 to 33. 5 °C the anisotropy in the relaxation rate, τ_H / τ_V, goes from 60 to 5. This dramatic decrease in dynamical anisotropy is attributed to a decrease in $R_{||}$ / $R_{\perp}$ as the polymer approaches an isotropic conformation near T_{NI} (35 °C). The effect is not evident in end-on polymer where the room-temperature anisotropy is small ($R_{||}$ / $R_{\perp}$ $\approx$ 0.6) compared to that of side-on polymer ($R_{||}$ / $R_{\perp}$ $\approx$ 5-7)[1] and large changes in anisotropy are therefore not possible.

6.4.2 Dynamics of Gels

In contrast to the single hydrodynamic relaxation process observed in homopolymer solutions, relaxation in gels takes place via two distinct processs. The qualitative change in behavior is clearly a consequence of network formation since triblock copolymer solutions below the gel point behave similarly to homopolymers. The gels' fast relaxation process retains the q^2 scaling observed in homopolymer solutions, characteristic of hydrodynamic relaxation, but the slow process has a stronger q dependence and is non-hydrodynamic. The slow process is reminiscent of relaxation dynamics of non-LC physical gels[23-27] but, significantly, light scattering in an LC gel arises from nematic director fluctuations, not from density fluctuations. The LC gels' structural changes are revealed indirectly by their effect on director dynamics. The slow process is attributed to reorganization of the physically associated polymer network: director relaxation via the fast, hydrodynamic process can only proceed to a certain extent because of its coupling to the local orientation of the underlying network. At long times the network structure can rearrange and allow the director to completely lose correlation with its initial orientation.

The proposed mechanism of director relaxation via two processs is illustrated schematically in Figure 6.15. A spontaneous thermal fluctuation causes a distortion to the director field that is translated to the polymer network by the coupling between the director and the network, mediated by the mesogens attached to the polymer midblock. The network distortion causes the local concentration of SGLCP chains to increase or decrease as the crosslinks are pushed together or pulled apart. Relaxation of the distortion takes place by a fast process that does not change the network's connectivity and by a slow restructuring of the network to relieve crowding of adjacent micellar crosslinks and stretching or compressing of chains spanning between two crosslinks. The PS blocks that make up a physical crosslink are constantly disengaging and reengaging, and when one disengages from a crosslink that is in a high energy environment due to polymer crowding or depletion, or chain stretching or compression, it is more likely to reengage in a crosslink that mitigates those osmotic and elastic penalties. The schematic captures the basic physics, but the ordered structure depicted is simply for the sake of clarity. Small-angle neutron scattering from the gel shows no evidence of such long-range order on a cubic lattice.

The dynamical anisotropy that is present in homopolymer solutions translates to the gels, suggesting some anisotropy in the network structure, as well. The SGLCP blocks that make up the network strands have a preferred conformation that balances the alignment of the polymer's mesogens and the director with the backbone's conformational entropy. It is plausible that SGLCPs radiating from a crosslink are, therefore, more likely to connect to another crosslink that is positioned in a way that accommodates that preferred conformation, leading to higher crosslink density perpendicular to the director in the case of end-on polymers and parallel to the director in the case of side-on polymers. This effect also results in an anisotropic distance between crosslinks. The underlying physics for dynamical anisotropy in gels may be understood in terms of the dynamic restructuring of an anisotropic network (Figure 6.16). Distortions to the director field couple to the polymer network and force the physical crosslinks to shift position. The deformation is easily accommodated when the network can undulate along its long axis without significantly changing the average distance between crosslinks. However, when the wavevector of the deformation is along the short axis, crosslinking domains are pushed close together or pulled far apart and the SGLCP network strands are forced to stretch and compress, accordingly. The free energy cost of changing the equilibrium chain conformation, combined with the osmotic resistance to increasing SGLCP overlap, creates a driving force for network rearrangement. Thus, when an end-on gel composed of oblate polymer strands is subjected to a bend distortion, the spreading out and pushing together of crosslink points causes network rearrangement to be an important mechanism for relaxation, but splay distortions are more easily accommodated and relaxation can take place without rearranging the connectivity. The opposite holds true for side-on gels composed of prolate polymer strands where splay distortions more severely perturb the network and bend distortions are relatively easily tolerated. Twist distortions significantly perturb the network in both gels.

Further evidence for anisotropic network structure is found in the temperature dependence of gel relaxation dynamics. The temperature dependence observed in homopolymer solutions carries over to gels: end-on gels are insensitive to temperature, but the relaxation of the side-on gel in the V geometry gets slower with increased temperature, opposite to what is observed in the corresponding homopolymer solution. This is consistent with Lubensky's theory of nematic elastomers,[7] which predicts that the network provides an additional restoring torque on director fluctuations that is highly dependent on its anisotropy. As the side-on gel transitions from being highly anisotropic at low temperature to being mildly anisotropic near T_{NI}, the decrease in the network's restoring torque results in slower relaxation.

6.5 Conclusions

The dynamics of director relaxation in liquid crystalline physical gels are governed by two processes: a fast, hydrodynamic relaxation process similar to homopolymer solutions and a slow relaxation process resulting from the network's ability to rearrange itself. The dynamical anisotropy observed in liquid crystalline gels suggests an anisotropic network structure resulting from the anisotropy of the polymer chains that comprise the network strands. Bend distortions relax slowly in networks composed of oblate polymers because the distortion perturbs the arrangement of the network, but when the polymer chains are prolate, splay distortions are more strongly affected.

The existing theories of LC elastomers and gels[5, 7, 9] cannot be directly applied to a physical gel because the finite lifetime of the crosslinks modifies the director dynamics. An interesting avenue of research would be to combine the theory of LC gels with the theory of associating polymers[28] to predict director dynamics in LC physical gels.

6.6 Tables

Table 6.1 Molecular weight, conversion, and polydispersity of side-group liquid crystal polymers. The full details of characterization are given in Appendix A.

Name	PS Blocks	SGLCP Block				PDI[a]
	M_n [kg/mol]	M_n [kg/mol]	Mole Fraction 1,2 PB	Mole Fraction 1,4 PB	Mole Fraction LC	
490HSiCB4	--	489	0.01	0.03	0.96	1.48
710HSiBB[b]	--	711	0.08	0.03	0.89	1.08
1100ABASiCB4	57,67	1,012	0.02	0.14	0.84	1.16
1400ABASiBB[b]	57,67	1367	0.21	0.14	0.65	1.50

[a] PDI = Polydispersity Index (M_w/M_n)

[b] Synthesized and characterized by Rafael Verduzco[13]

6.7 Figures

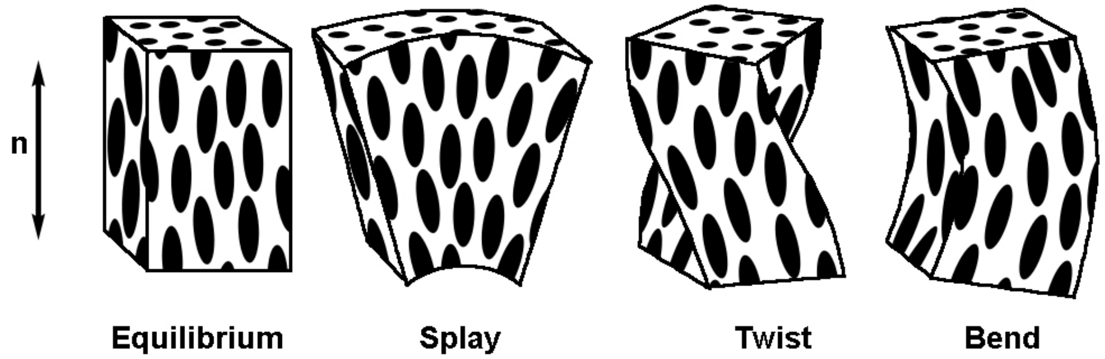

Figure 6.1 Schematic diagrams of the splay, twist, and bend distortions in a nematic liquid crystal. The spatially varying nematic director is represented by ellipses and the equilibrium director is denoted ***n***.

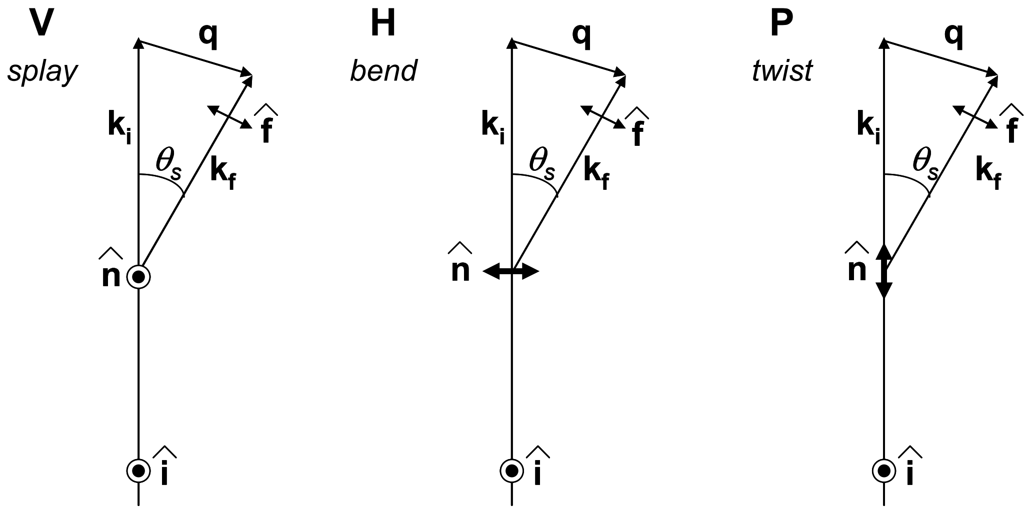

Figure 6.2 Top-view schematic of the three scattering geometries used. The scattering plane, which contains **q**, is in the plane of the page, perpendicular to **i**. Relative to the incident polarization, **i**, and wavevector $\mathbf{k_i}$, the LC director, **n**, is oriented parallel to **i** ("V" for "vertical"), perpendicular to both **i** and $\mathbf{k_i}$ ("H" for "horizontal"), or parallel to $\mathbf{k_i}$ ("P" for "parallel"). The polarization direction of the analyzer, **f**, is horizontal, perpendicular to **i**. The intensity of the scattered, depolarized light is recorded at a discrete angle, θ_s, in the laboratory frame, corresponding to a final wavevector, $\mathbf{k_f}$, and scattering vector $\mathbf{q} = \mathbf{k_f} - \mathbf{k_i}$. The V, H, and P geometries are typically known as the splay, bend, and twist geometries, respectively.

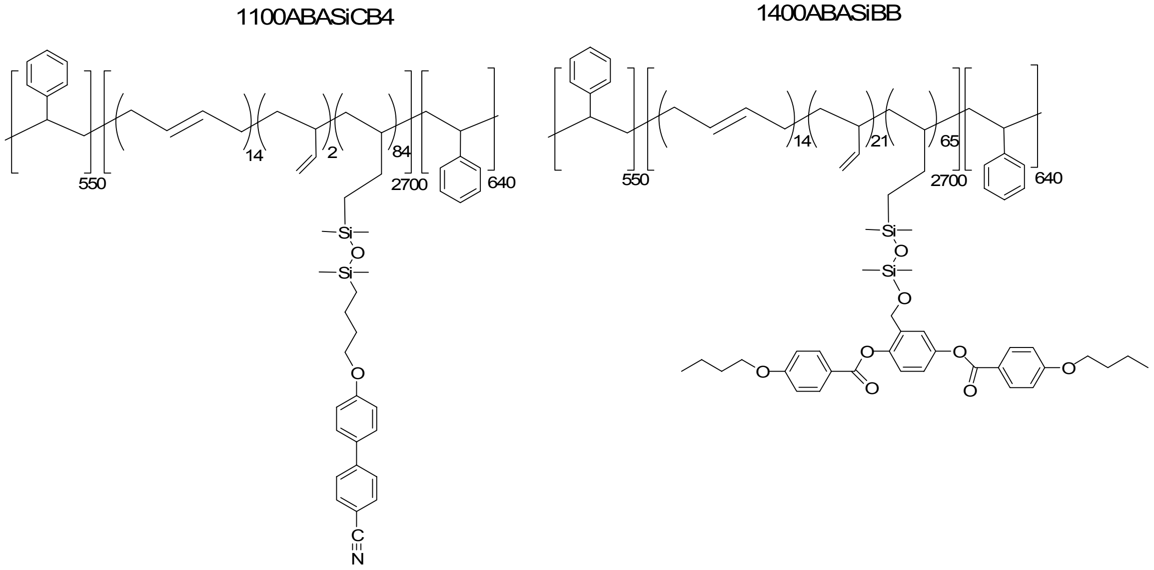

Figure 6.3 Chemical structures of end-on (1100ABASiCB4) and side-on (1400ABASiBB) side-group liquid crystal triblock copolymers with polystyrene endblocks. A polymer's name is derived from its molecular weight in units of kg/mol, the letters "ABA" to indicate a triblock copolymer, and either "SiCB4" or "SiBB" to indicate either end-on or side-on mesogens, respectively. In addition to monomers having an attached mesogen, the midblock also contains some residual 1,2- and 1,4-butadiene monomers. These polymers' properties are summarized in Table 6.1.

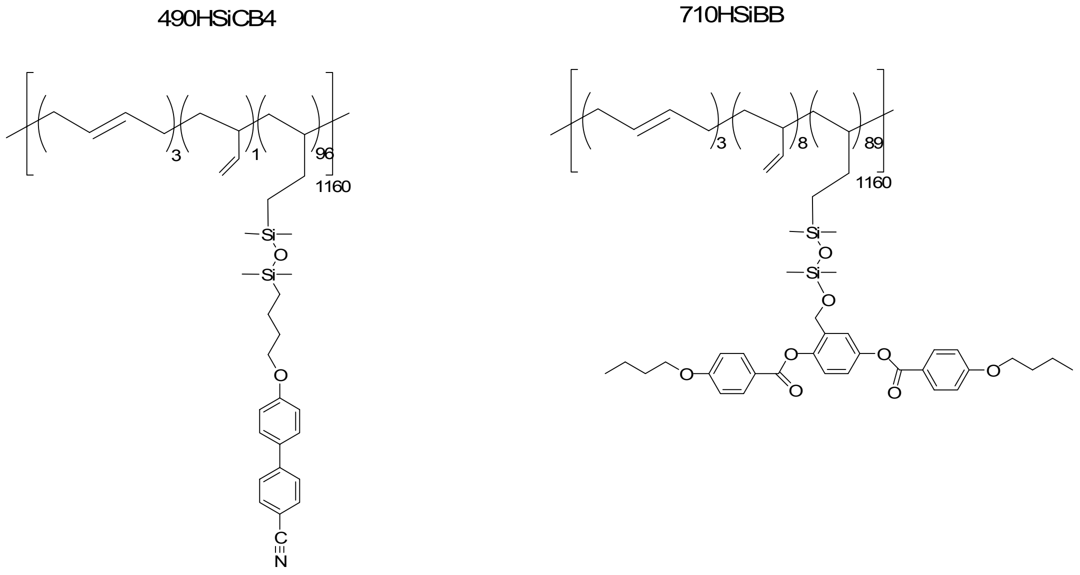

Figure 6.4 Chemical structures of end-on (490HSiCB4) and side-on (710HSiBB) side-group liquid crystal homopolymers. A polymer's name is derived from its molecular weight in units of kg/mol, the letter "H" to indicate a homopolymer, and either "SiCB4" or "SiBB" to indicate either end-on or side-on mesogens, respectively. In addition to monomers having an attached mesogen, the polymer also contains some residual 1,2- and 1,4-butadiene monomers. These polymers' properties are summarized in Table 6.1.

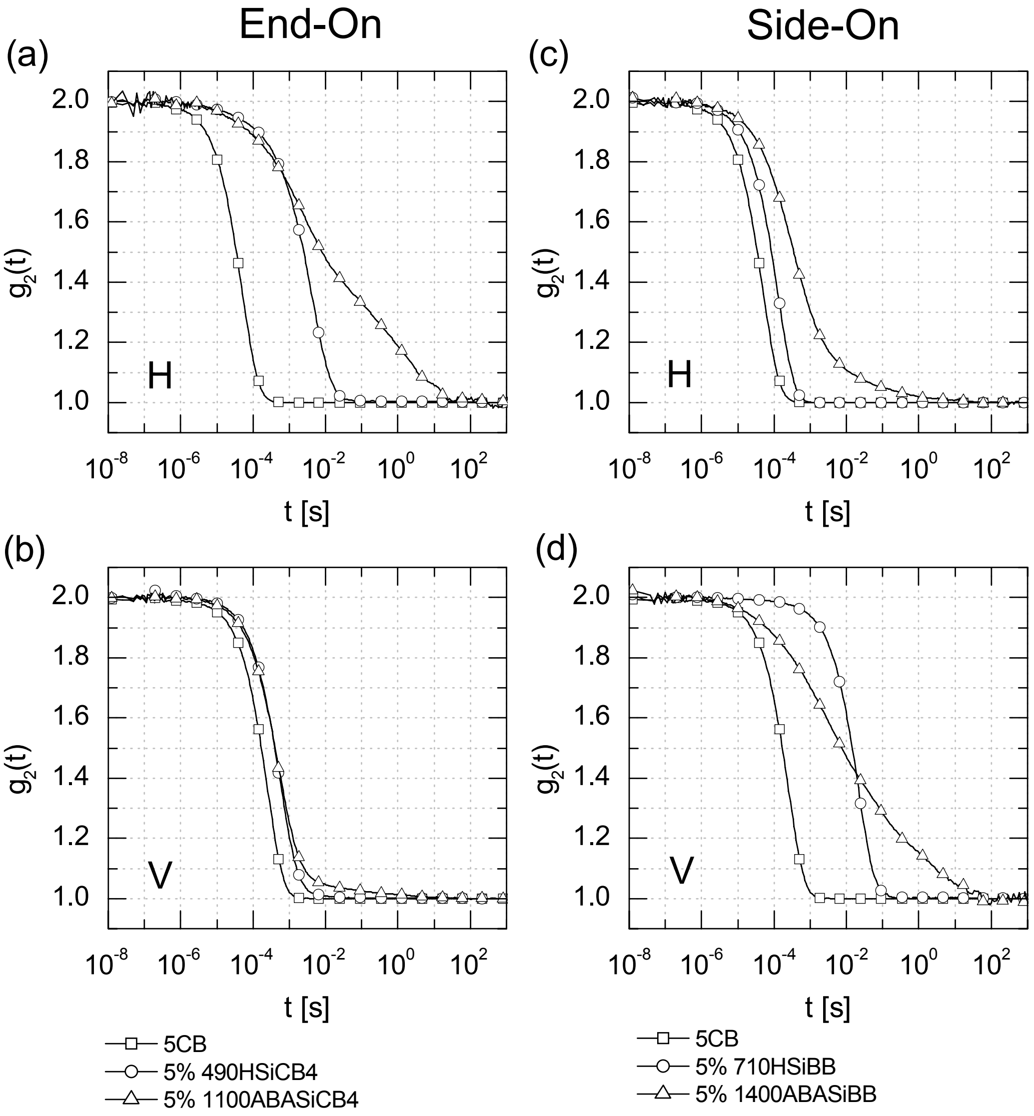

Figure 6.5 Normalized time correlation functions, $g_2(t)$, at 25 °C and $\theta_s = 30°$ for 5CB, 5 wt % homopolymer solutions, and 5 wt % triblock copolymer gels in the H and V orientations

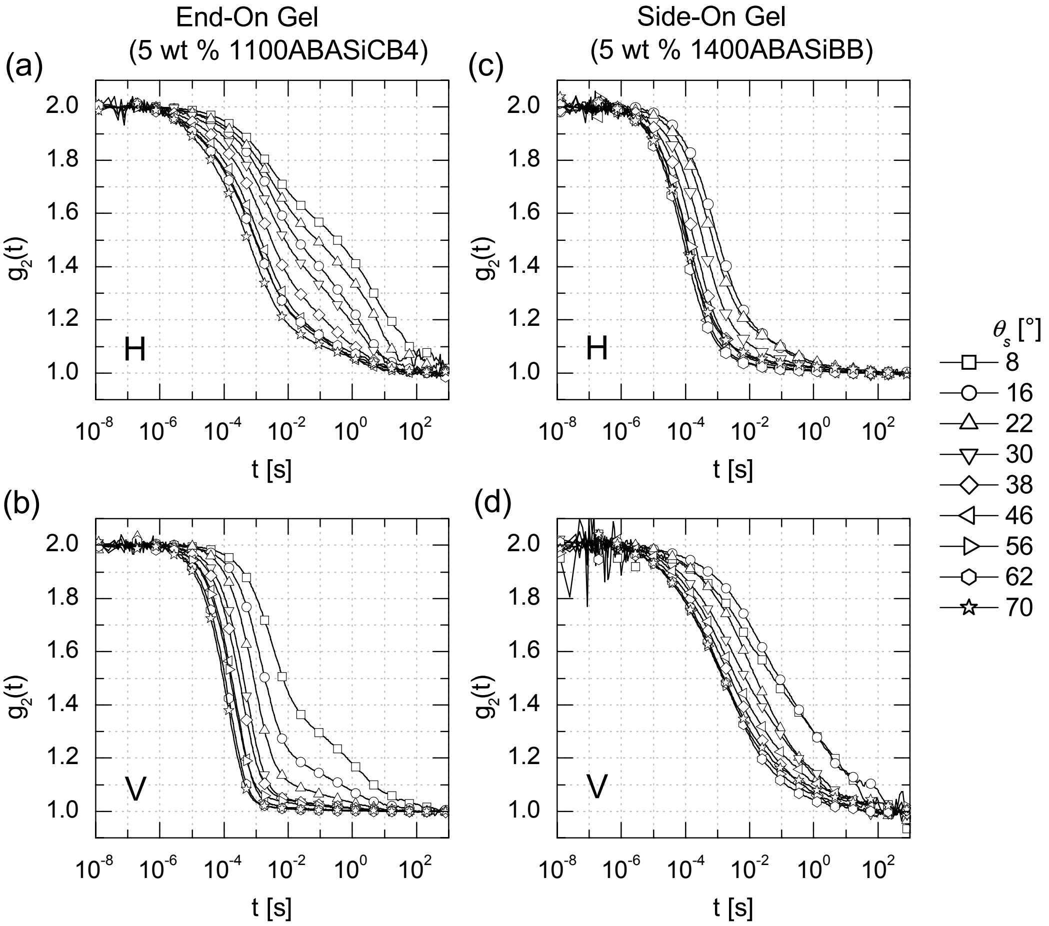

Figure 6.6 Normalized time correlation functions, $g_2(t)$, at 25 °C for end-on and side-on gels (5 wt % 1100ABASiCB4 and 5 wt % 1400ABASiBB, respectively) in the H and V orientations

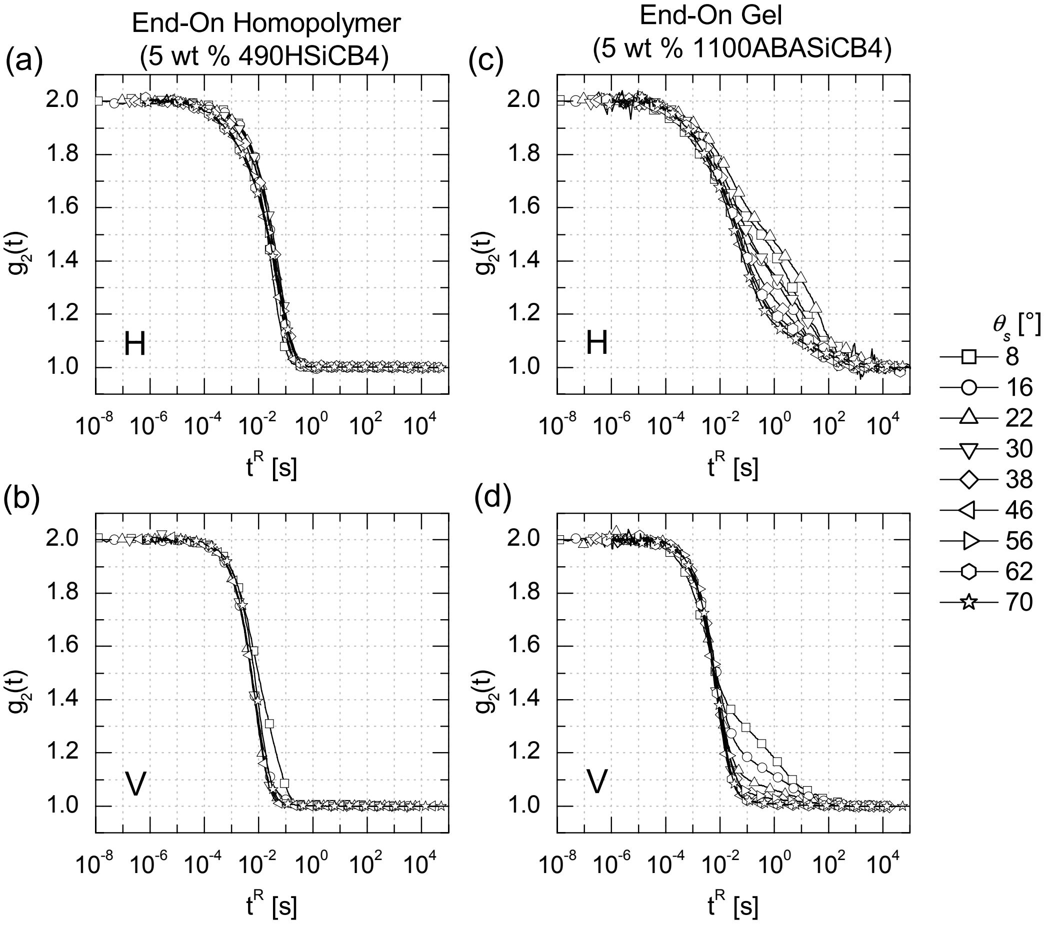

Figure 6.7 Normalized time correlation functions, $g_2(t)$, at 25 °C of end-on polymers at a variety of scattering angles as a function of rescaled delay time, $t^R = t\ (\sin(\theta_s)/\sin(\theta_{s,0}))^2$, where $\theta_{s,0} = 8°$. 5 wt % end-on homopolymer (490HSiCB4) in (a) H orientation and (b) V orientation; and 5 wt % end-on triblock copolymer (1100ABASiCB4) gel in (c) H orientation and (d) V orientation

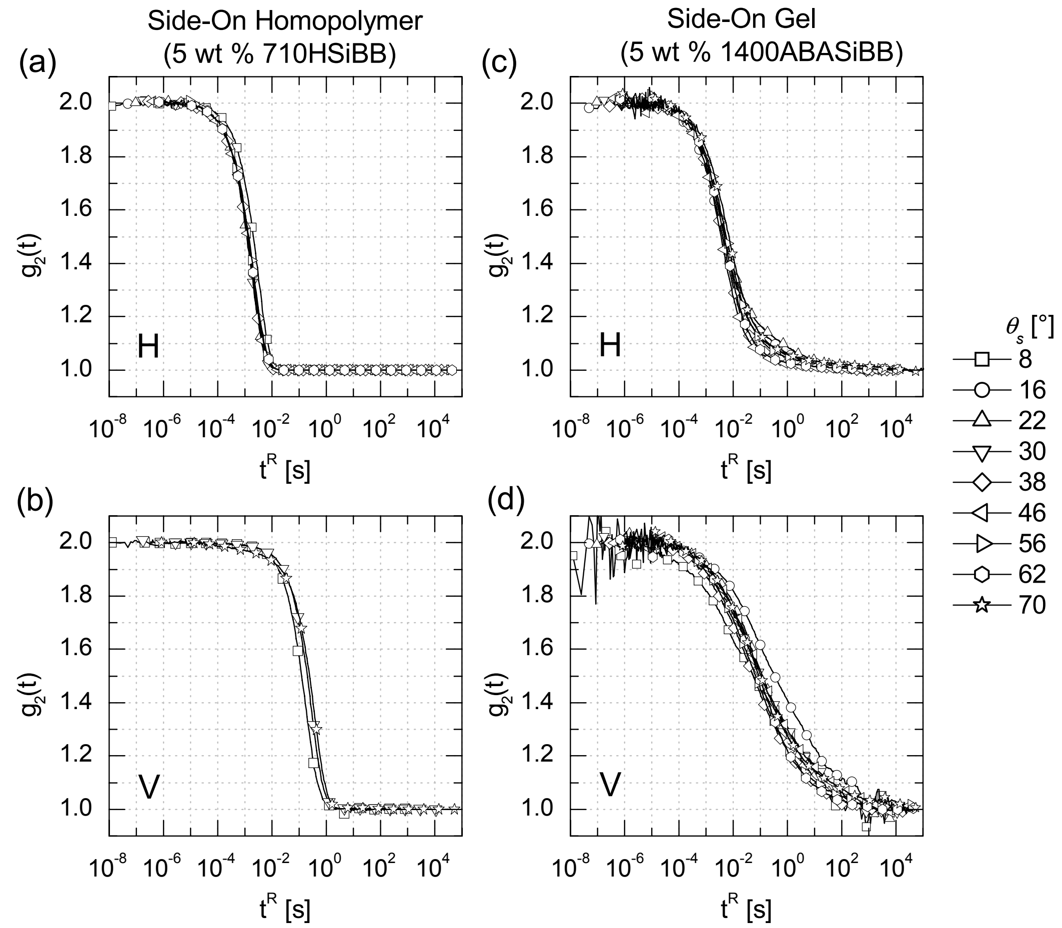

Figure 6.8 Normalized time correlation functions, $g_2(t)$, at 25 °C of side-on polymers at a variety of scattering angles as a function of rescaled delay time, $t^R = t\ (\sin(\theta_s)/\sin(\theta_{s,0}))^2$, where $\theta_{s,0} = 8°$. 5 wt % side-on homopolymer (710HSiBB) in (a) H orientation and (b) V orientation; and 5 wt % side-on triblock copolymer (1400ABASiBB) gel in (c) H orientation and (d) V orientation

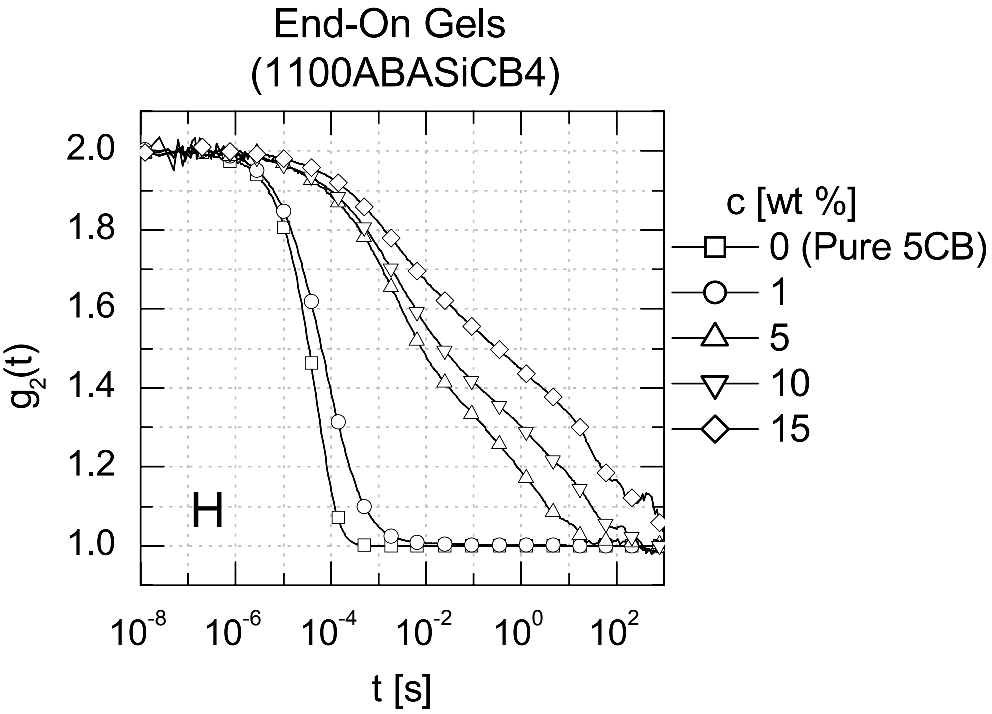

Figure 6.9 Concentration dependence of the normalized time correlation functions, $g_2(t)$, at 25 °C and $\theta_s = 30°$ of end-on triblock copolymer gels (solutions of 1100ABASiCB4) in the H orientation

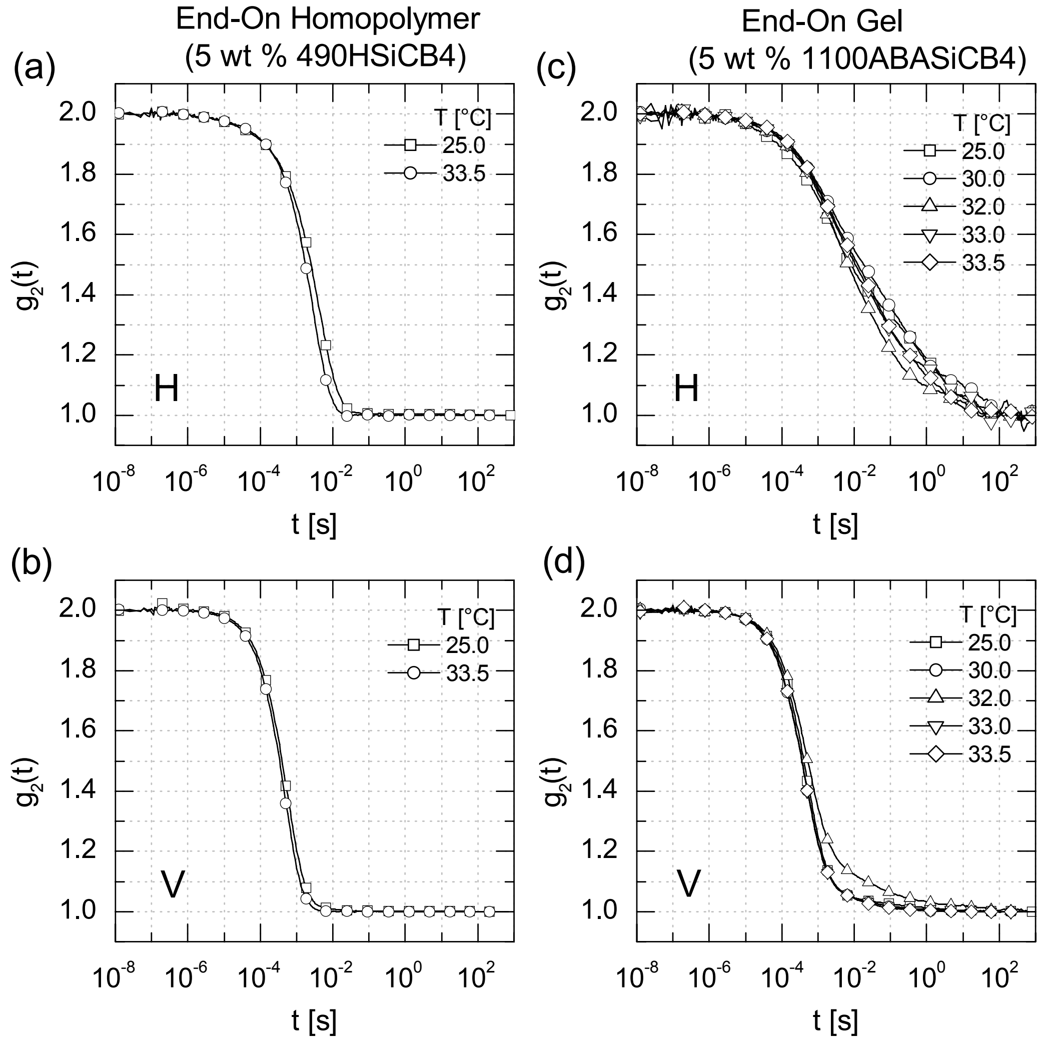

Figure 6.10 Temperature dependence of the normalized time correlation functions, $g_2(t)$, at θ_s = 30° of 5 wt % end-on homopolymer (490HSiCB4) in (a) H orientation and (b) V orientation and 5 wt % end-on triblock copolymer (1100ABASiCB4) gel in (c) H orientation and (d) V orientation

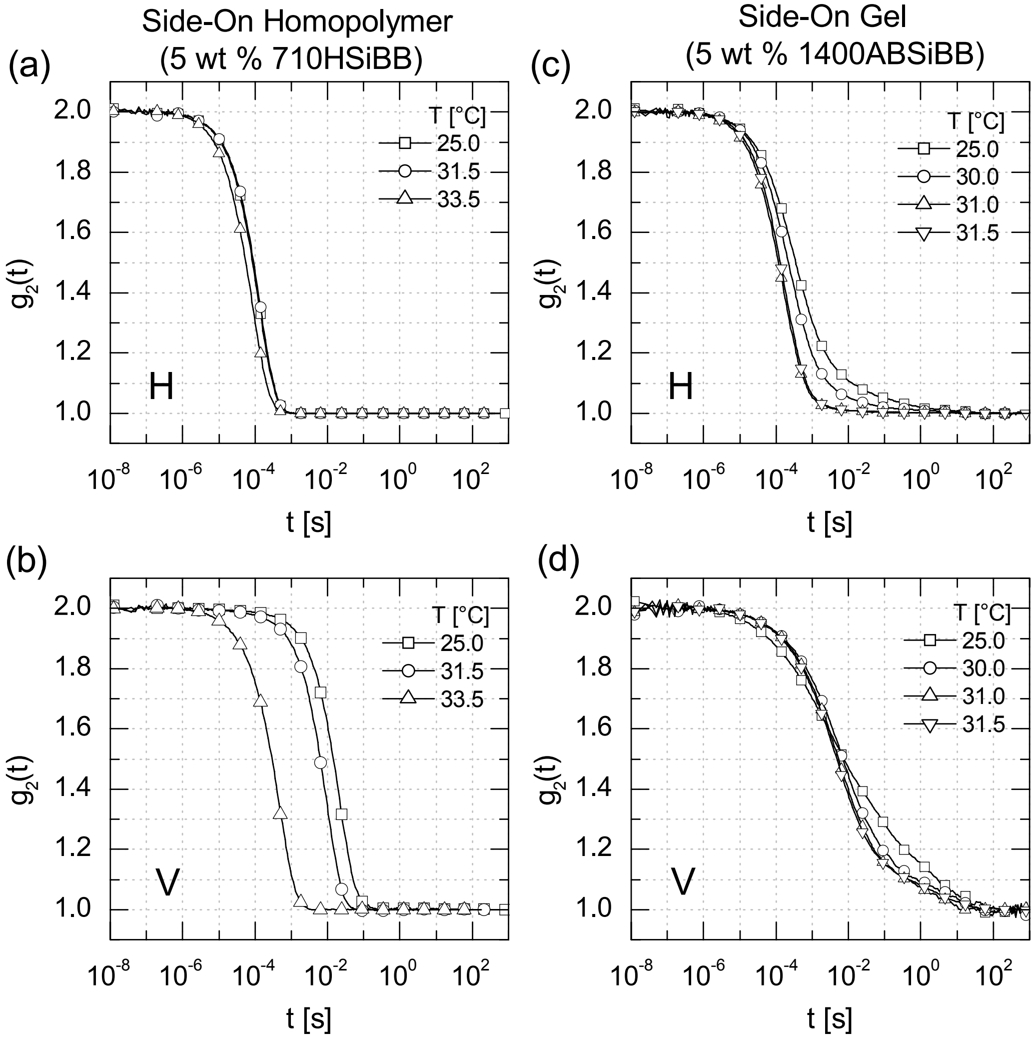

Figure 6.11 Temperature dependence of the normalized time correlation functions, $g_2(t)$, at θ_s = 30° of 5% side-on homopolymer (710HSiBB) in (a) H orientation and (b) V orientation and 5% side-on triblock copolymer (1400ABASiBB) gel in (c) H orientation and (d) V orientation

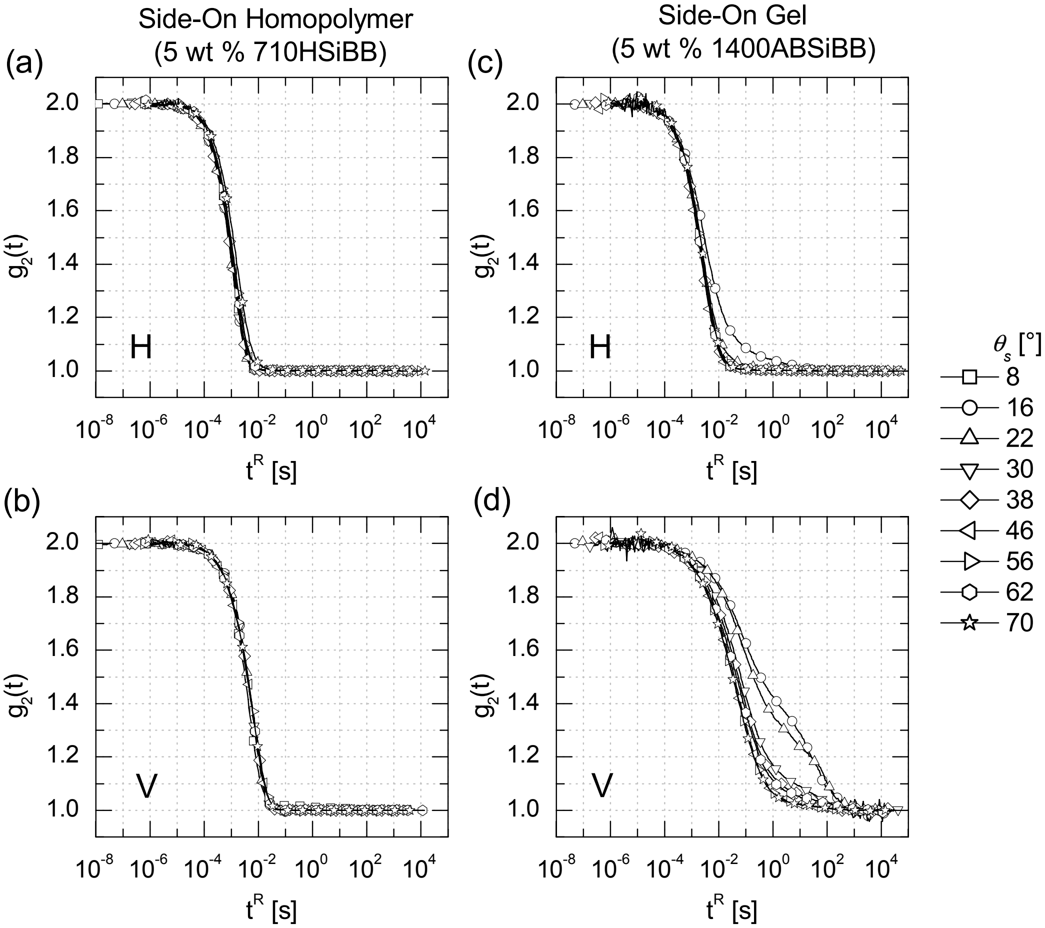

Figure 6.12 Normalized time correlation functions, $g_2(t)$, of side-on homopolymer solution and triblock polymer gel at a variety of scattering angles as a function of rescaled delay time, $t^R = t\ (\sin(\theta_s)/\sin(\theta_{s,0}))^2$, where $\theta_{s,0} = 8°$. 5 wt % side-on homopolymer (710HSiBB) solution at 33.5 °C in (a) H orientation and (b) V orientation and 5 wt % side-on triblock copolymer (1400ABASiBB) gel at 31.5 °C in (c) H orientation and (d) V orientation

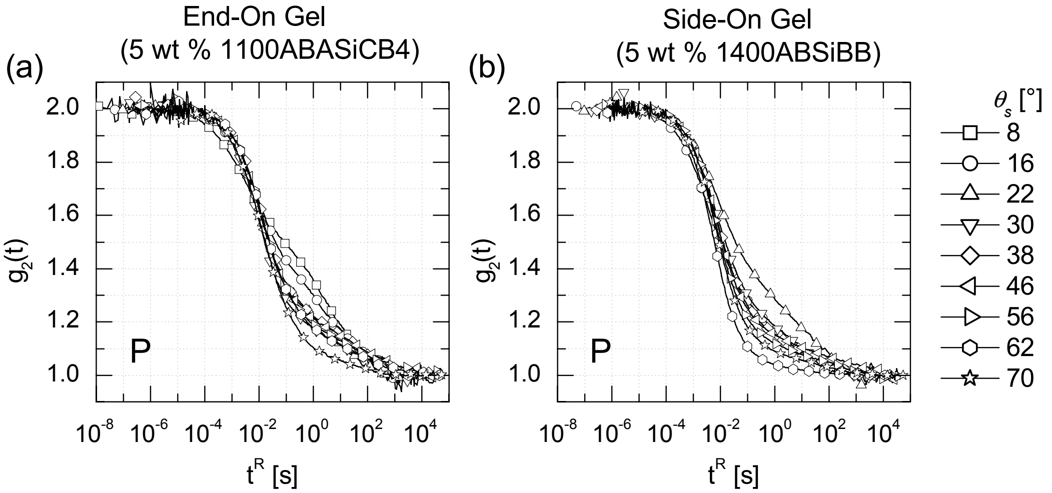

Figure 6.13 Normalized time correlation functions, $g_2(t)$, at 25 °C of triblock copolymer gels in P orientation at a variety of scattering angles as a function of rescaled delay time, $t^R = t\,(\sin(\theta_s)/\sin(\theta_{s,0}))^2$, where $\theta_{s,0} = 8°$. (a) 5 wt % end-on triblock (1100ABASiCB4) and (b) 5 wt % side-on triblock (1400ABASiBB)

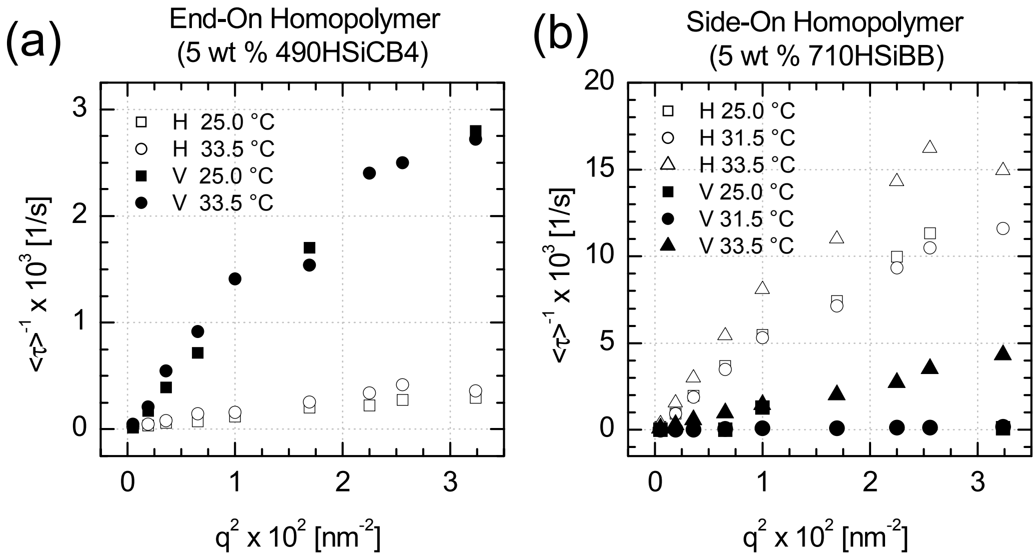

Figure 6.14 Average relaxation rates ($<\tau>^{-1}$) of (a) end-on and (b) side-on homopolymer solutions at various temperatures in the H and V scattering geometries derived from fitting time correlation functions to an empirical Williams-Watts function

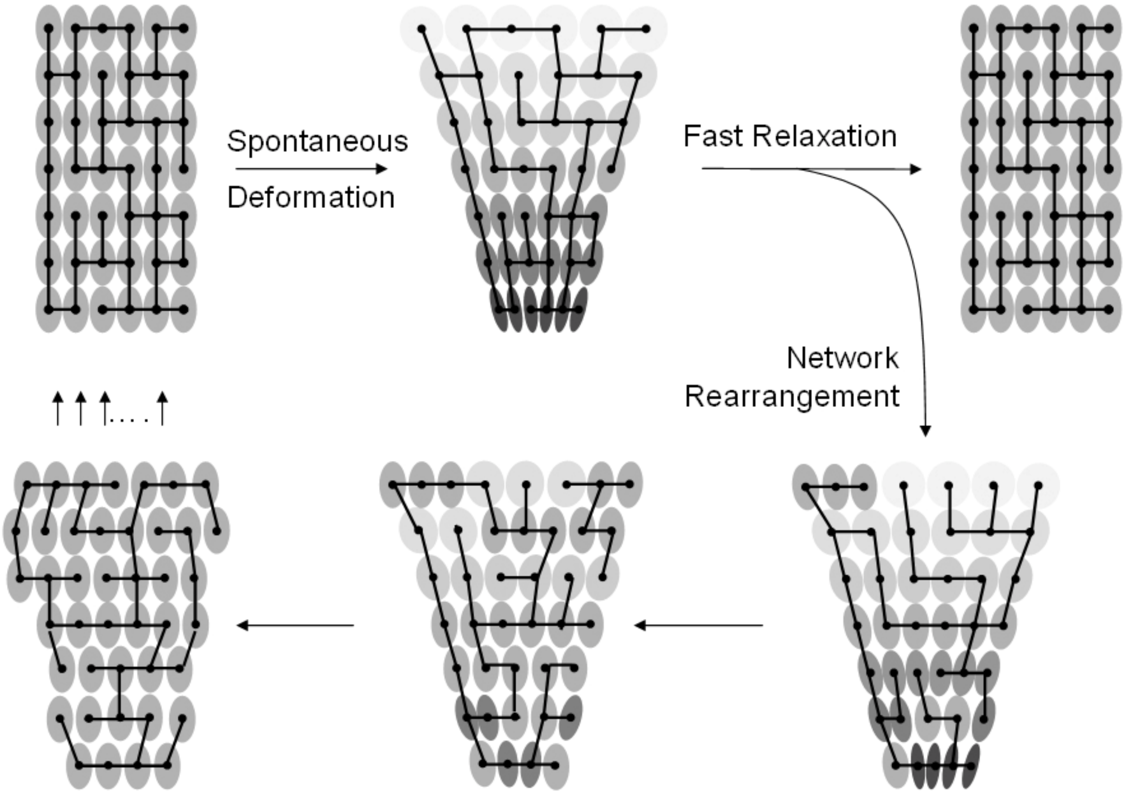

Figure 6.15 Schematic illustrating the two director relaxation processes in LC physical gels. Physical crosslinks consisting of microphase separated polystyrene are represented by black circles and the connections between them, comprised of SGLCP strands, are represented as black lines. The shading of the gray ellipses represents the local density of SGLCP chains. When the network undergoes a spontaneous deformation, it can relax by a fast process that does not require network rearrangement, and by a slow process in which the physical crosslinks break and reform to reestablish a uniform density of SGLCP and mitigate chain stretching.

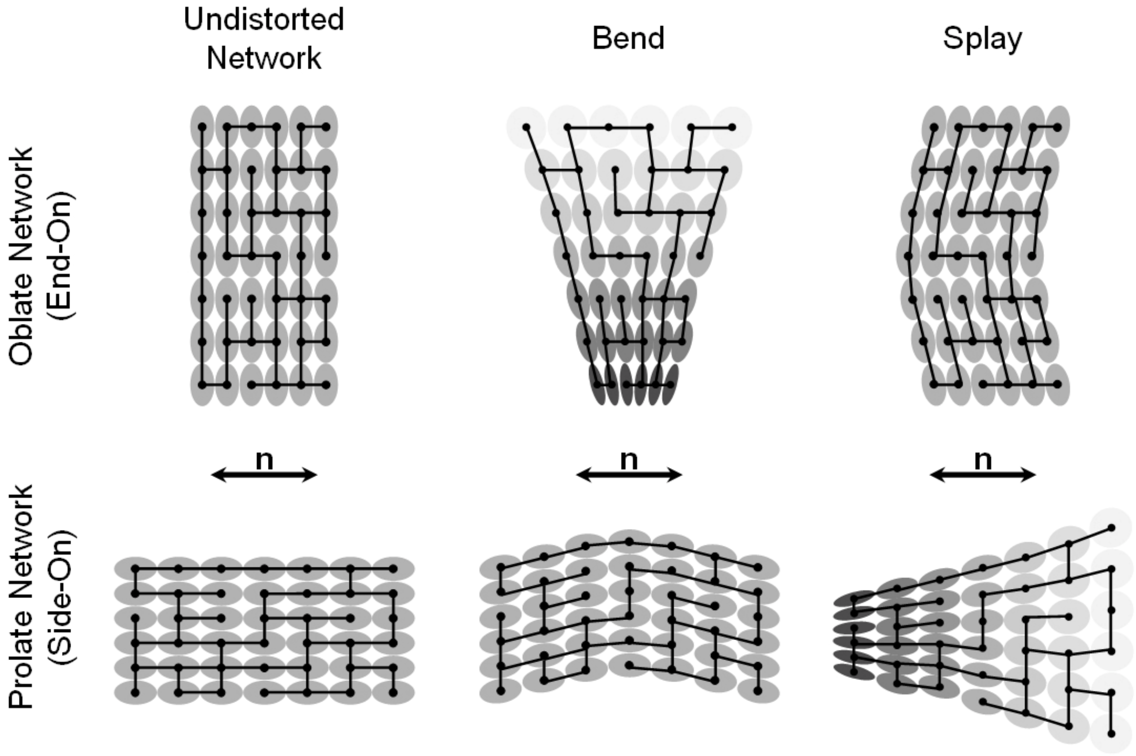

Figure 6.16 Schematic illustrating the effects of bend and splay distortions on an anisotropic network. Physical crosslinks consisting of microphase separated polystyrene are represented by black circles and the connections between them, comprised of SGLCP strands, are represented as black lines. The shading of the gray ellipses represents the local density of SGLCP chains. When an oblate network, such as an end-on LC gel, is subjected to a bend distortion, the local density of SGLCP chains and the average distance between crosslinks are significantly perturbed, but a splay distortion is accommodated by undulation of the network. The effects are reversed in a prolate network, such as a side-on LC gel, where bend distortions are more easily accommodated. The LC director, ***n***, is indicated by the double-headed arrow.

6.8 References

[1] Kempe, M. D.; Scruggs, N. R.; Verduzco, R.; Lal, J.; Kornfield, J. A. Self-assembled liquid-crystalline gels designed from the bottom up. *Nat. Mater.* **2004**, *3*, 177-182.

[2] Ho, J. T. Light scattering and quasielastic spectroscopy. In *Liquid Crystals*; S. Kumar, Editor; Cambridge University Press: Cambridge, 2001.

[3] de Gennes, P.-G. *The Physics of Liquid Crystals*, 2nd ed; Clarendon Press: Oxford, 1993.

[4] Jamieson, A. M.; Gu, D. F.; Chen, F. L.; Smith, S. Viscoelastic behavior of nematic monodomains containing liquid crystal polymers. *Prog. Polym. Sci.* **1996**, *21*, 981-1033.

[5] Warner, M.; Terentjev, E. M. Nematic elastomers- a new state of matter? *Prog. Polym. Sci.* **1996**, *21*, 853-891.

[6] Olmsted, P. D. Rotational invariance and Goldstone modes in nematic elastomers and gels. *J. Phys. II France* **1994**, *4*, 2215-2230.

[7] Stenull, O.; Lubensky, T. C. Dynamics of nematic elastomers. *Phys. Rev. E* **2004**, *69*, 051801.

[8] Terentjev, E. M.; Warner, M. Linear hydrodynamics and viscoelasticity of nematic elastomers. *Eur. Phys. J. E* **2001**, *4*, 343-353.

[9] Warner, M.; Terentjev, E. M. *Liquid Crystal Elastomers*, Oxford University Press: Oxford, 2003.

[10] Schöenstein, M.; Stille, W.; Strobl, G. Effect of the network on the director fluctuations in a nematic side-group elastomer analysed by static and dynamic light scattering. *Eur. Phys. J. E* **2001**, *5*, 511-517.

[11] Kempe, M. D.; Verduzco, R.; Scruggs, N. R.; Kornfield, J. A. Rheological study of structural transitions in triblock copolymers in a liquid crystal solvent. *Soft Matter* **2006**, *2*, 422-431.

[12] Verduzco, R.; Meng, G.; Kornfield, J. A.; Meyer, R. B. Buckling instability in liquid crystalline physical gels. *Phys. Rev. Lett.* **2006**, *96*, 147802.

[13] Verduzco, R. Texture Transitions, Electro-Optics, and Dynamics of Liquid Crystal Gels with Novel Network Architectures. Ph.D. Thesis, California Institute of Technology, Pasadena, CA, February 5, 2007.

[14] Williams, G.; Watts, D. C. Non-Symmetrical Dielectric Relaxation Behaviour Arising from a Simple Empirical Decay Function. *Trans. Faraday Soc.* **1970**, *66*, 80-85.

[15] Williams, G.; Watts, D. C.; Dev, S. B.; North, A. M. Further Considerations of Non Symmetrical Dielectric Relaxation Behaviour arising from a Simple Empirical Decay Function. *Trans. Faraday Soc.* **1977**, *67*, 1323-1335.

[16] Lindsey, C. P.; Patterson, G. D. Detailed comparison of the Williams-Watts and Cole-Davidson functions. *J. Chem. Phys.* **1980**, *73*, 3348-3357.

[17] Gu, D. F.; Jamieson, A. M.; Kawasumi, M.; Lee, M.; Percec, V. Dynamic Light Scattering from Nematic Monodomains Containing Mesogenic Polymers of Differing Architectures. *Macromolecules* **1992**, *25*, 2151-2155.

[18] Gu, D. F.; Jamieson, A. M.; Rosenblatt, C.; Tomazos, D.; Lee, M.; Percec, V. Dynamic Light Scattering from a Nematic Monodomain Containing a Side-Chain Liquid Crystal Polymer in a Nematic Solvent. *Macromolecules* **1991**, *24*, 2385-2390.

[19] Chiang, Y.-C.; Jamieson, A. M.; Campbell, S.; Tong, T. H.; Sidocky, N. D.; Chien, L. C.; Kawasumi, M.; Percec, V. Electro-rheological behavior of liquid crystal polymers dissolved in a nematic solvent: dependence on temperatrue and LCP structure. *Polymer* **2000**, *41*, 4127-4135.

[20] Chiang, Y.-C.; Jamieson, A. M.; Campbell, S.; Lin, Y.; O'Sidocky, N.; Chien, L. C.; Kawasumi, M.; Percec, V. Effect of molecular architecture on the electrorheological behavior of liquid crystal polymers in nematic solvents. *Rheological Acta* **1997**, *36*, 505-512.

[21] Chen, F.-L.; Jamieson, A. M.; Kawasumi, M.; Percec, V. Viscoelastic properties of dilute nematic mixtures containing cyclic and hyperbranched liquid crystal polymers dissolved in a nematic solvent. *Journal of Polymer Science: Part B: Polymer Physics* **1995**, *33*, 1213-1223.

[22] Brochard, F. Viscosities of Dilute Polymer-Solutions in Nematic Liquids. *J. Polym. Sci. Pt. B-Polym. Phys.* **1979**, *17*, 1367-1374.

[23] Blanco, M. C.; Leisner, D.; Vazquez, C.; Lopez-Quintela, M. A. Dynamic Light Scattering in Transient Reversible Gels. *Langmuir* **2000**, *16*, 8585-8594.

[24] Castelletto, V.; Hamley, I. W.; Waigh, T. A. Dynamic light scattering study of the dynamics of a gelled polymeric micellar system. *J. Chem. Phys.* **2004**, *121*, 11474-11480.

[25] Konak, C.; Fleischer, G.; Tuzar, Z.; Bansil, R. Dynamics of Solutions of Triblock Copolymers in a Selective Solvent: Effect of Varying Copolymer Concentration. *J. Polym. Sci., Part B: Polym. Phys.* **2000**, *38*, 1312-1322.

[26] Konak, C.; Helmstedt, M.; Bansil, R. Dynamics in Solutions of Associating Statistical Copolymers. *Macromolecules* **1997**, *30*, 4342-4346.

[27] Raspaud, E.; Lairez, D.; Adam, M.; Carton, J.-P. Triblock Copolymers in a Selective Solvent. 2. Semidilute Solutions. *Macromolecules* **1996**, *29*, 1269-1277.

[28] Tanaka, F. Theoretical Study of Molecular Association and Thermoreversible Gelation in Polymers. *Polym. J. (Tokyo, Jpn.)* **2002**, *34*, 479-509.

Chapter 7

ELECTRIC-FIELD IMPRINTING OF LIQUID CRYSTAL GELS SELF-ASSEMBLED FROM DIBLOCK AND TRIBLOCK COPOLYMERS IN NEMATIC SOLVENT

7.1 Introduction........177
7.2 Experimental........178
7.3 Results........179
7.4 Discussion........181
7.5 Conclusions........182
7.6 Tables........183
7.7 Figures........184
7.8 References........190

7.1 Introduction

When a block copolymer having a side-group liquid crystal polymer (SGLCP) block and a random-coil polymer block is dissolved in a small-molecule liquid crystal (LC) solvent, the polymer self-assembles to segregate the random-coil block from the ordered solvent. Self-assembly of a coil-SGLCP diblock copolymer results in the formation of micelles and, at sufficiently high concentration, the osmotic repulsion between neighboring micelles causes the solution to behave rheologically as a gel:[1] the elastic modulus is greater than the storage modulus and is virtually independent of frequency.[2] Self-assembly of a coil-SGLCP-coil triblock copolymer results in the formation of a percolated polymer network because a single polymer chain can participate in up to two different coil-block domains. Triblock copolymer solutions also behave rheologically as gels above a critical concentration.[3, 4]

Although diblock and triblock copolymer gels are rheologically similar, the two are in stark contrast when it comes to their electro-optic performance. Triblock copolymer gels preserve a memory of the LC orientation field present when they self-assemble,[3, 5] but this memory is absent in diblock copolymer gels. These experiments compare the relaxation of diblock and triblock copolymer gels after removal of an orienting electric field as a function of the orienting field's duration.

7.2 Experimental

7.2.1 Materials

Diblock copolymers having a side-group liquid crystal polymer (SGLCP) block and a random coil block (polystyrene, PS) (Figure 7.1) were synthesized according to the methods described in Appendix A from poly[styrene-*b*-1,2-butadiene] prepolymers supplied by David Uhrig (Oak Ridge National Laboratory's Center for Nanophase Materials Sciences). A PS-SGLCP-PS triblock copolymer (Figure 7.1) was synthesized according to the methods described in Appendix A from a poly[styrene-*b*-1,2-butadiene-*b*-styrene] prepolymer purchased from Polymer Source (Montreal, Quebec). The properties of these polymers are summarized in Table 7.1.

Solutions of these polymers in 4-pentyl-4′-cyanobiphenyl (5CB, purchased and used as received from TCI America) were prepared by dissolving the polymer and 5CB together in dichloromethane (DCM) then evaporating the DCM under a stream of air, followed by drying in vacuum overnight. Polymer concentrations were chosen such that the polymers would form gels: 10 wt % for diblocks and 5 wt % for the triblock.

7.2.2 Methods

Solutions of polymer in 5CB were loaded into cells purchased from LC Vision (Boulder, CO) consisting of glass plates with 5 mm x 5 mm transparent indium-tin oxide (ITO) electrodes in their centers and separated by spacers 9 μm thick. Cells were filled with polymer / LC solutions by capillary action: when heated above the gel point (35 °C) the gels transition to liquids and readily flow into the gap. Cooling to the nematic phase produces unaligned, polydomain gels. Cells were mounted in an aluminum block equipped with electrical heaters and a temperature controller stable to within ± 1 °C. Before beginning an experiment, the sample's history was erased by annealing to 50 °C for approximately 15 minutes, then annealing at 25 °C for approximately 15 minutes.

Samples were illuminated through the ITO electrodes with a 10 mW polarized HeNe laser (λ = 633 nm) and the transmitted intensity was measured using a Thorlabs PDA55 photodiode detector. The output of the detector was recorded by a computer using a National Instruments PCI-MIO-16XE-10 data acquisition card. A potential difference was applied to the cell's electrodes using a computer-controlled California Instruments 251TL alternating current power source set to a frequency of 1 kHz.

7.3 Results

Before applying the electric field, diblock and triblock copolymer gels are unaligned and the polydomain orientation of the LC director causes light to be scattered as it passes through the samples. The intensity that reaches the detector in the polydomain state is minimal. When a sufficiently large potential difference is applied across the sample, the LC is uniformly aligned with its optic axis perpendicular to the electrodes, by virtue of the LC's positive dielectric anisotropy. Aligned samples are optically clear and the detected intensity reaches a maximum with the applied field. The transmitted intensity as a function of field strength was recorded for each gel and a representative voltage sweep is presented in Figure 7.2.

A 50 V_{rms} potential difference, far above all three gels' switching thresholds, was applied to initially polydomain gels for increasing durations ranging from one minute to four days. The transmitted intensity was measured at periodic intervals both during the application of the field and for at least six hours after the field was removed, and was converted to percent transmittance by subtracting the initial baseline intensity in the polydomain state (I_0) then dividing by the maximum intensity achieved during application of the field (I_{max}). The transmittance of all three gels changes from 0 to 100% when the field is applied. When the field is removed, the transmittance decreases with time from 100% to value that depends on the duration of the previously applied field (Figure 7.3 - Figure 7.5).

The field-induced orientation is imprinted on diblock copolymer gels: neither 10 wt % 390(60)ABSiCB4 nor 10 wt % 320(120)ABSiCB4 return to 0% transmittance when the field is removed (Figure 7.3 and Figure 7.4). The field-off transmittance increases with the duration of the applied field. When 10 wt % 390(60)ABSiCB4 is exposed to the 50 V_{rms} potential difference for 1 min the transmittance remains above 40% for the entire six-hour window of field-off observation. After exposure for 1 day, the gel's transmittance remains above 85% in the field-off state. 10 wt % 320(120)ABSiCB4 is even more susceptible to imprinting. Applying the field for 1 min causes the field-off transmittance to remain above 50% in the six-hour window of observation, and field durations of 1 hour or more peg the field-off transmittance at greater than 80%.

In contrast to diblock gels, the triblock gel resists imprinting and retains a "memory" of its polydomain field-off orientation. When the 50 V_{rms} potential difference is applied for less than 1 day the transmittance returns to less than 5% within an hour of removing the field. Even when the field-on time is increased to 4 days the triblock gel returns to less than 25% transmittance within the six-hour window of observation.

7.4 Discussion

The presence of an interconnected polymer network in triblock copolymer gels provides a memory of the gel's orientation that is absent in diblock copolymer gels (Figure 7.6). When the orientation of the LC solvent is changed, diblock micelles reorient to align their corona chains with the new director. The required rotation does not change the micelles' positions relative to one another. When the field is removed the micelles return to a random orientation distribution by Brownian diffusion, but the return is slow because the micelles are large and packed relatively close together. In the triblock gel, changing the orientation of the LC solvent causes the conformations of polymer chains spanning between two crosslinks to be significantly distorted and the stresses cannot be relieved without changing the network's connectivity because the positions and orientations of the physical crosslinks are highly correlated with one another.

These electric field imprinting experiments give an order of magnitude estimate of the triblock copolymer network's reorganization time. The network's physical junctions continuously break and reform with a characteristic time scale, t_R, and when a strong bias voltage is used to torque the LC away from its equilibrium orientation it creates a driving force for a broken junction to reform in way that accommodates the new director field. However, network restructuring can only play a role when the field-on time is sufficiently long compared to t_R. The observation that triblock gels retain no memory of field-induced orientation when the field on time is less than or equal to six hours demonstrates that t_R is greater than six hours, in agreement with the order of magnitude ($> 10^3$ s) of the reorganization time scale measured by dynamic light scattering in Chapter 6.

Amongst diblock copolymer gels, the observation that 10 wt % 390(60)ABSiCB4 is less susceptible to imprinting than 10 wt % 320(120)ABSiCB4 may be related to the size of the micelles and the modulus of the gel. SANS from the two gels (Chapter 4) demonstrates that micelles in 10 wt % 320(120)ABSiCB4 are larger than in 10 wt % 390(60)ABSiCB4, and rheology (Appendix E) demonstrates that 10 wt % 320(120)ABSiCB4 is more viscous. Assuming the bias field provides the same degree of orientation in both gels, the relaxation time to return to the polydomain state would be much longer in 10 wt % 320(120)ABSiCB4 because the diffusion of larger micelles in a more viscous medium is slower. Anisotropy of the micelle structure may also play a role. If the aspect ratio of micelles in 10 wt % 320(120)ABSiCB4 is larger than those in 10 wt % 390(60)ABSiCB4, their field-on reorientation may be much faster.[6] At equal field-on times, the micelles in 10 wt % 320(120)ABSiCB4 would be more strongly oriented than those in 10 wt % 390(60)ABSiCB4 and would, therefore, better serve to reinforce the LC's uniform orientation after the field was removed.

7.5 Conclusions

The network structure in an LC gel self-assembled from a triblock copolymer serves to reinforce the alignment state present when the gel is formed. When an orienting electric field is removed from an initially polydomain gel, the network causes the alignment to return to the polydomain state. When the field is left on for very long times, the network can restructure to accommodate the new director field. In contrast, gels formed from diblock copolymers, in which the micelles are not interconnected, do not return to their polydomain alignment state when the electric field is removed. Instead, the slow diffusion of the micelles back to a random orientation distribution serves to preserve the field-on orientation.

7.6 Tables

Table 7.1 Molecular weight, conversion, and polydispersity of the side-group liquid crystal block copolymers. Details of their characterization may be found in Appendix A.

Name	PS Block	SGLCP Block				PDI[a]
	M_n [kg/mol]	M_n [kg/mol]	Mole Fraction 1,2 PB	Mole Fraction 1,4 PB	Mole Fraction LC	
390(60)ABSiCB4	59	388	0.15	0.03	0.85	1.11
320(120)ABSiCB4	121	323	0.22	0.01	0.77	1.05
1100ABASiCB4	57,67	1,012	0.02	0.14	0.84	1.16

[a] PDI = Polydispersity Index (M_w/M_n)

7.7 Figures

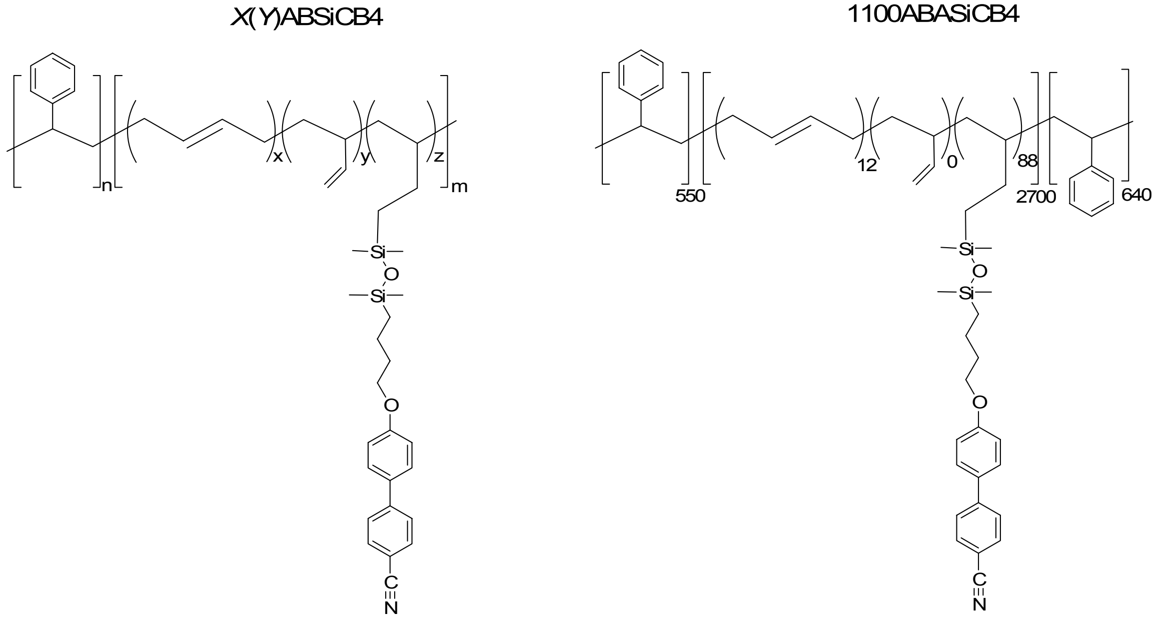

Figure 7.1 Chemical structures of side-group liquid crystal diblock (*X*(*Y*)ABSiCB4) and triblock (1100ABASiCB4) copolymers. The diblocks' names are derived from the molecular weights of the SGLCP block (*X*) and the PS block (*Y*) in units of kg/mol, the letters "AB" to indicate a diblock copolymer, and "SiCB4" to indicate end-on mesogens. The triblock's name derives from its total molecular weight (1100 kg/mol) and the letters "ABA" to indicate a triblock copolymer. In addition to monomers having an attached mesogen, the polymers also contain some residual 1,2- and 1,4-butadiene monomers. Compositions, expressed as the mole fractions *x*,*y*, and *z*, are given in Table 7.1. Details of polymer characterization are presented in Appendix A.

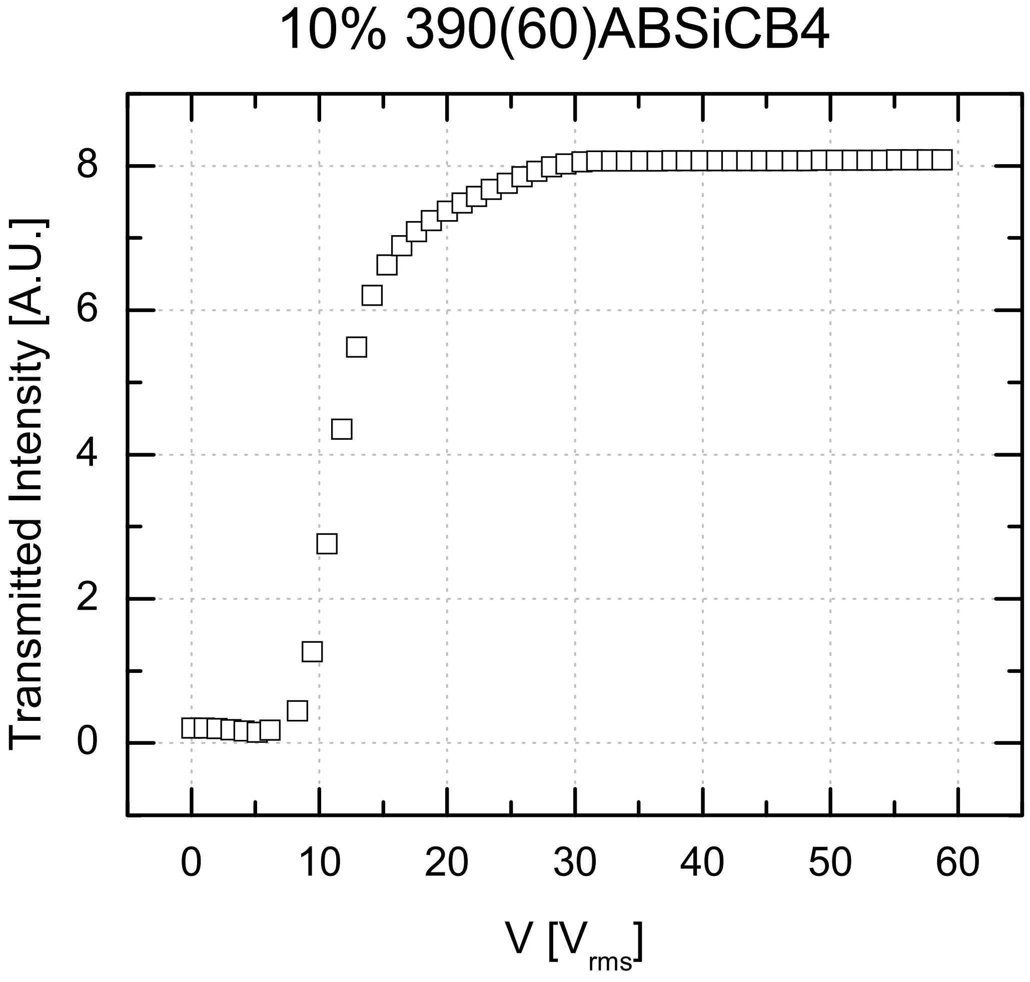

Figure 7.2 Representative voltage sweep performed on a 10 wt % 390(60)ABSiCB4 gel. A potential difference of 50 V_{rms} is well above the threshold field for switching. Voltage sweeps from 10 wt % 320(120)ABSiCB4 and 5 wt % 1100ABASiCB4 gels were similar.

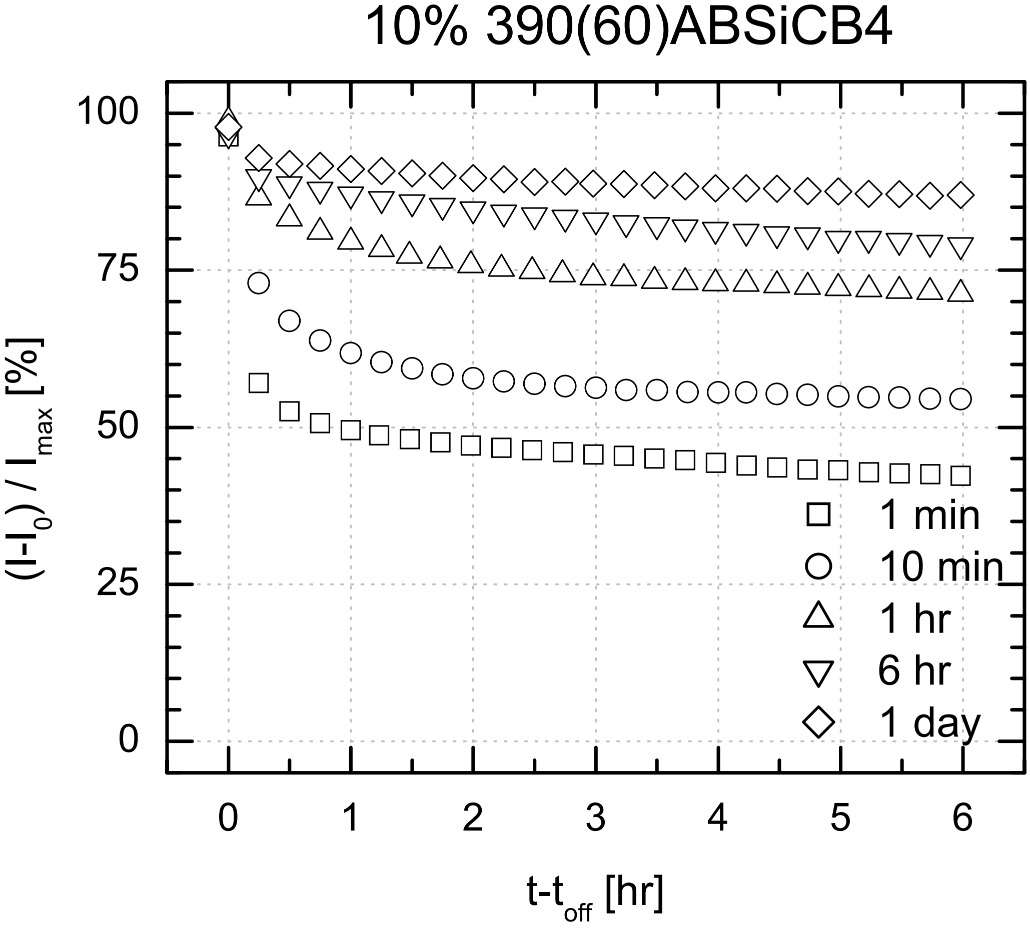

Figure 7.3 Time-dependence of the percent transmittance of light ($(I\text{-}I_0)/I_{max}$) through a gel composed of 10 wt % 390(60)ABSiCB4 in 5CB after applying a 50 V_{rms} potential difference for 1 min, 10 min, 1 hr, 6, hr, or 1 day then removing it at time $t = t_{off}$.

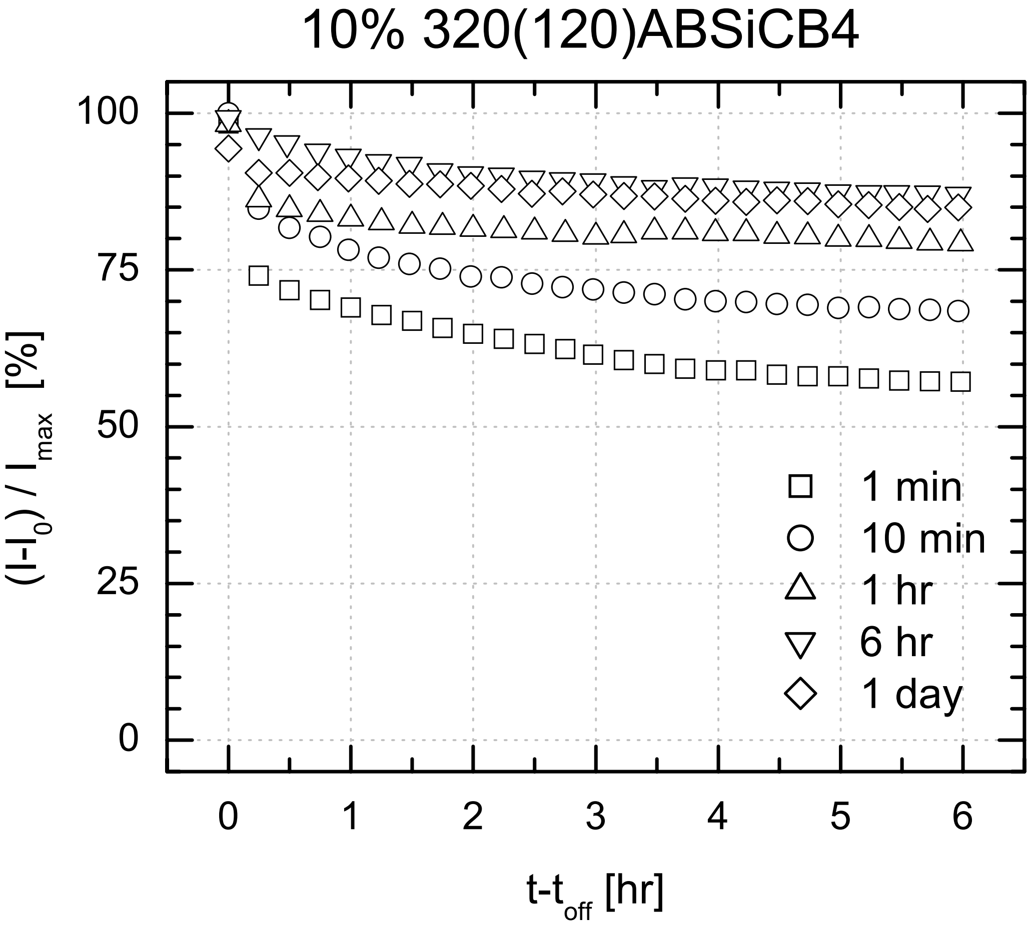

Figure 7.4 Time-dependence of the percent transmittance of light ($(I\text{-}I_0)/I_{max}$) through a gel composed of 10 wt % 320(120)ABSiCB4 in 5CB after applying a 50 V_{rms} potential difference for 1 min, 10 min, 1 hr, 6, hr, or 1 day then removing it at time $t = t_{off}$.

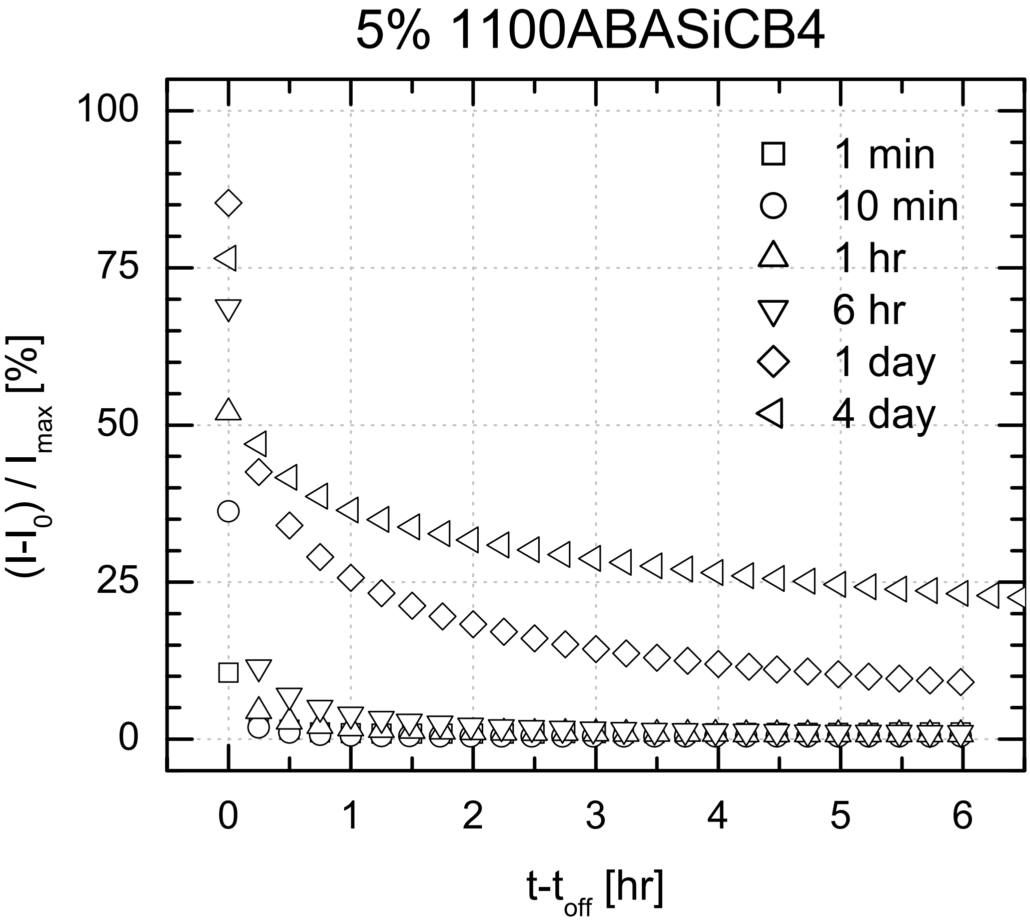

Figure 7.5 Time-dependence of the percent transmittance of light ($(I\text{-}I_0)/I_{max}$) through a gel composed of 5 wt % 1100ABSiCB4 in 5CB after applying a 50 V_{rms} potential difference for 1 min, 10 min, 1 hr, 6, hr, 1 day, or 4 days then removing it at time $t = t_{off}$.

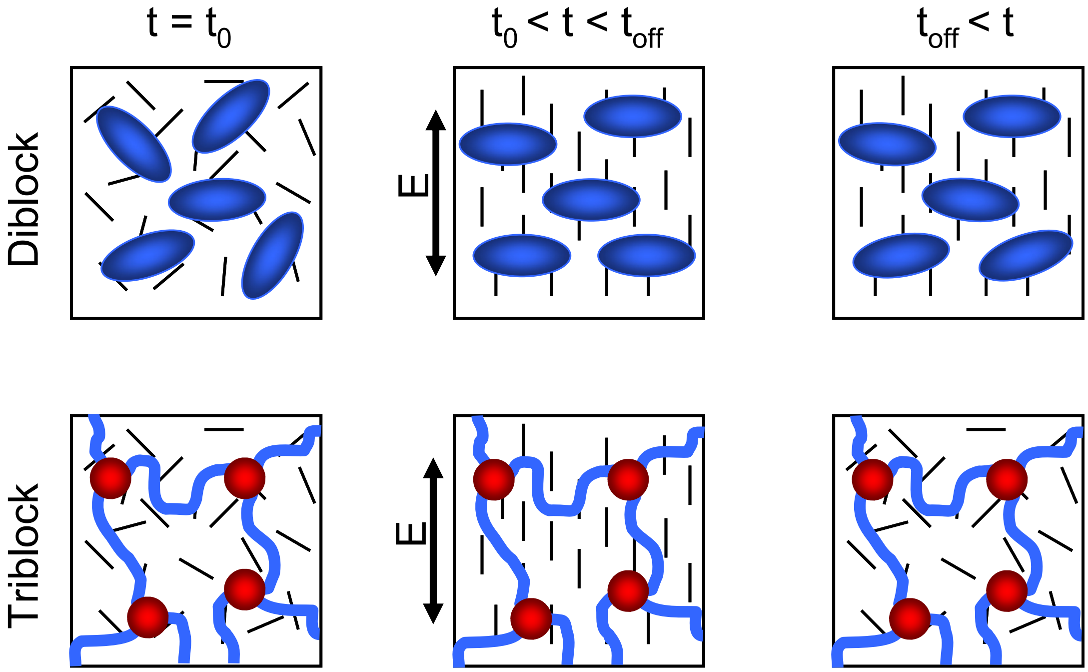

Figure 7.6 Schematic illustrating the reorientation of liquid crystalline gels before applying an electric field ($t = t_0$), during field application ($t_0 < t < t_{off}$), and after removing the electric field ($t_{off} < t$). The micelles in the diblock copolymer gel can rotate to align with the field, then diffuse slowly back to a random distribution when the field is removed. The network structure in the triblock copolymer gel provides memory of the initial polydomain alignment state, unless the field is applied long enough to allow the network to restructure.

7.8 References

[1] Scruggs, N. R.; Kornfield, J. A.; Lal, J. Using the "Switchable" Quality of Liquid Crystal Solvents to Mediate Segregation between Coil and Liquid-Crystalline Polymers. *Macromolecules* **2006**, *39*, 3921-3926.

[2] Almdal, K.; Dyre, J.; Hvidt, S.; Kramer, O. What is a gel? *Makromol. Chem. - M. Symp.* **1993**, *76*, 49-51.

[3] Kempe, M. D.; Scruggs, N. R.; Verduzco, R.; Lal, J.; Kornfield, J. A. Self-assembled liquid-crystalline gels designed from the bottom up. *Nat. Mater.* **2004**, *3*, 177-182.

[4] Kempe, M. D.; Verduzco, R.; Scruggs, N. R.; Kornfield, J. A. Rheological study of structural transitions in triblock copolymers in a liquid crystal solvent. *Soft Matter* **2006**, *2*, 422-431.

[5] Verduzco, R.; Meng, G.; Kornfield, J. A.; Meyer, R. B. Buckling instability in liquid crystalline physical gels. *Phys. Rev. Lett.* **2006**, *96*, 147802.

[6] Hsu, H.-Y.; Sharma, N.; Ruoff, R. S.; Patankar, N. A. Electro-orientation in particle light valves. *Nanotechnology* **2005**, *16*, 312-319.

Appendix A

SYNTHESIS AND CHARACTERIZATION OF SIDE-GROUP LIQUID CRYSTAL POLYMERS

A.1 Appendix 191

A.2 Tables 197

A.3 Schemes 203

A.4 Figures 205

A.5 References 230

A.1 Appendix

All reagents were purchased and used as received from Aldrich, unless otherwise noted.

A.1.1 Strategy for Synthesis of Side-Group Liquid Crystal Polymers

Polymer-analogous synthesis is used to attach liquid crystalline side-groups to existing polymer backbones. A library of polybutadiene (PB) homopolymers (Figure A.1-Figure A.3) and PB-containing block copolymers (Figure A.4-Figure A.12) was obtained from various sources. The PB portion of every polymer contains a high percentage (> 80 mol %) of 1,2-addition monomers. A cyanobiphenyl-based mesogen is synthesized separately and attached in one step to the pendant vinyl groups of 1,2-PB, yielding a side-group liquid crystal polymer (SGLCP).

A.1.2 Synthesis of Cyanobiphenyl-Based Mesogenic Side Groups

A cyanobiphenyl-based mesogen is synthesized by Mitsunobu reaction[1, 2] between 4-cyano-4′-hydroxybiphenyl (CHB) and 3-buten-1-ol (4OH) (Scheme A.1). CHB (1.3 g, 6.2

mmol, purchased and used as received from TCI America) and 1.1 equivalents each of 4OH (0.60 mL, 6.8 mmol) and triphenylphosphine (TPP) (1.8 g, 6.8 mmol) are dissolved together in 50 mL anhydrous tetrahydrofuran (THF). The solution is chilled in an ice water bath followed by the dropwise addition of 1.1 equivalents of diisopropyl azodicarboxylate (DIAD) (1.3 mL, 6.8 mmol). The reaction flask is then removed from the ice water bath and the reaction proceeds at room temperature until thin-layer chromatography no longer reveals the presence of CHB (approximately 3-5 hours). Upon completion, the THF is evaporated and the product, 4-cyano-4′-(3-butenoxy)-biphenyl (CBV4), is dissolved in dichloromethane (DCM) and purified on a silica gel column using 5% ethyl acetate in hexane as the mobile phase. CBV4 is further purified by recrystallization from hexane, achieving 77% yield overall (1.2 g, 4.7 mmol).

The phenolic Mitsunobu reaction (Scheme A.1) is the preferred scheme for synthesizing CBV4 because relatively high yield is achieved in a single reaction. However, an alternate scheme is Williamson ether synthesis (Scheme A.2).[3, 4] 4OH (10. mL, 120 mmol) is first converted to 3-butenyl-1-tosylate (4OTs) by reaction with two equivalents of p-toluenesulfonyl chloride (tosyl chloride, TsCl) (44 g, 230 mmol) in 150 mL DCM along with one equivalent of pyridine (9.4 mL, 120 mmol).[5, 6] Reagents are mixed at 0 °C then the reaction flask is removed to room temperature and the reaction proceeds for approximately ten hours. The product, 4OTs, is purified by liquid-liquid extraction. After adding an excess of pyridine (100 mL), the DCM solution is washed with 400 mL of aqueous hydrochloric acid (5% HCl). 4OTs remaining in the aqueous layer is extracted with DCM then the combined organic layers are washed once more with 5% HCl. The organic layer is dried with anhydrous sodium sulfate and the DCM evaporated to recover the product (83% yield, 22 g, 96 mmol). Williamson ether synthesis yields the final product, CBV4. A seventy percent excess of 4OTs (22 g, 96 mmol) is added to a solution of CHB (11 g, 57 mmol) in 50 mL of *N*,*N*-dimethylformamide (DMF). A seventy percent excess of anhydrous potassium carbonate is added (13 g, 96 mmol) and the mixture heated at 90 °C for eight hours. Upon completion, the potassium tosylate byproduct is precipitated with an excess of DCM and removed by filtration. After evaporating the majority of the solvent the remaining CBV4 is purified on a silica gel column using ten percent ethyl acetate in hexane, then recrystallized from hexane for an overall yield of 43% (6.1 g, 25 mmol).

A siloxane linking group is attached to the cyanobiphenyl mesogen, CBV4, by hydrosilylation (Scheme A.3). A tenfold excess of 1,1,3,3-tetramethyldisiloxane (TMDS) (18 mL, 99 mmol) is dissolved together with CBV4 (2.5 g, 9.9 mmol) in 20 mL anhydrous toluene. A drop of platinum catalyst (PC072 platinum divinyl complex in xylene, United Chemical Technologies, Bristol, PA) is added and the mixture is stirred at room temperature for 16 hours under inert gas. Upon completion, the solvent and excess TMDS are evaporated at 80 °C under vacuum and the product, 4-cyano-4′-(5-(1,1,3,3,-tetramethyldisiloxane)butoxy)biphenyl (SiCB4), is purified by column chromatography. An anhydrous chromatography column is prepared in order to prevent the degradation of SiCB4 by reaction with water. The column is filled with silica gel dried in a 150 °C oven and then repeatedly flamed with a propane torch while dry, inert gas flows through the silica. The column is then filled with anhydrous hexane and mixed to create a slurry of silica gel in hexane. Once the silica gel settles, the SiCB4 is loaded onto the column and eluted with an anhydrous mixture of 10% ethyl acetate in hexane. Anhydrous column chromatography is sometimes repeated to recover a clear, liquid product (75% yield, 2.1 g, 7.4 mmol).

A.1.3 Attaching Side Groups to Polymer

The cyanobiphenyl-based mesogen with attached siloxane linking group (SiCB4) is suitable for attachment to the pendant vinyl groups of a 1,2-polybutadiene polymer by platinum-catalyzed hydrosilylation (Scheme A.4) in manner similar to the synthesis of SiCB4. 1,2-Polybutadiene (0.14 g, 2.5 mmol) is dissolved in 5 mL of anhydrous tetrahydrofuran (THF) in inert atmosphere. A threefold excess of freshly purified SiCB4 (2.1 g, 7.4 mmol) is added along with a drop of platinum catalyst (PC085 platinum cyclovinyl complex in vinylmehtylsiloxanes, United Chemical Technologies, Bristol, PA) and the mixture heated at 50 °C for between four and seven days. Reaction progress is monitored periodically by proton NMR. When the reaction is complete, as evidenced by the disappearance of the 1,2-PB vinyl resonance peak at $\delta = 4.9$ ppm, it is quenched by heating at 50 °C overnight after addition of excess styrene (~2-5 mL).

After quenching with styrene the polymer is concentrated by evaporating approximately half the solvent under vacuum. Unreacted mesogen is removed by precipitating the polymer from solution using an excess of methanol. The precipitated polymer is then repeatedly dissolved in THF and precipitated with methanol. The methanol used for precipitation contains 10 ppm of a radical inhibitor (BHT) to improve stability during long-term storage. After the final precipitation the solid polymer is dried in vacuum. Polymer conversion is nearly quantitative; yield is greater than 95% of the theoretical value.

Cross-linking reactions are seemingly unavoidable; polymers almost always have a bimodal molecular weight distribution with a small fraction of high molecular weight, cross-linked polymers, which is removed by solvent fractionation. A solution of approximately ten percent polymer in THF is passed through a 0.45 μm syringe filter then diluted with toluene and THF for a final composition of 0.5% polymer dissolved in a mixture of 60% THF and 40% toluene. While stirring vigorously, methanol is added until the solution becomes cloudy (the amount of methanol required is typically almost equal to the volume of the solution). THF is then slowly added until the solution becomes clear; at this point it is very near its room-temperature cloud point. Next, a small amount of methanol is added, usually between 5 and 15 mL. The amount of methanol added determines the degree to which the polymer will fractionate: more methanol will result in more polymer dropping out of solution. The cloudy solution is heated to 70 °C and stirred until it becomes clear again. Finally, the clear, hot solution is poured into a hot separatory funnel wrapped in plenty of insulation. The insulated funnel is isolated from air currents and left to cool very slowly overnight. A viscous syrup composed largely of high molecular weight polymer separates into the bottom of the separatory funnel while low molecular weight polymer remains in the dilute solution above. The high molecular weight fraction is easily drained off, precipitated with methanol, and dried in vacuum. The low molecular weight fraction is recovered by evaporating the solvent and drying in vacuum.

A.1.4 Characterization of Polybutadiene-Containing Prepolymers

The molecular weight of the SGLCP precursor polymers is measured by the manufacturer using light scattering. Proton NMR is used to measure the percentage of 1,2-PB monomers and to verify the mass fraction of PB in block copolymers (Figure A.1-Figure A.12). A 300 MHz Varian NMR spectrometer is used to collect proton NMR spectra from solutions of polymers in deuterated chloroform ($CDCl_3$). Hydrogen atoms in the vinyl group of 1,2-butadiene contribute to the intensities of peaks at $\delta = 4.9$ ppm (two hydrogens) and $\delta = 5.4$ ppm (one hydrogen). The two hydrogen atoms attached to the double-bonded carbons of 1,4-butadiene contribute to the peak intensity at $\delta = 5.4$ ppm. The 1,2-butadiene content is calculated from these peak intensities: $x_{1,2} = I_{\delta=4.9ppm} / (I_{\delta=4.9ppm} + I_{\delta=5.4ppm} - \frac{1}{2} I_{\delta=4.9ppm})$. The mole fraction of PB in a PB-polystyrene (PS) block copolymer is computed by comparing the intensity per mole of hydrogen of PB peaks (both 1,4- and 1,2- addition) to that of aromatic peaks in the range of $\delta = 6.2 - 7.4$ ppm. The mole fraction is easily converted to the mass fraction using the monomers' molar masses.

The polymers' molecular weight distributions, characterized by the polydispersity index (PDI = M_w / M_n), is measured using gel permeation chromatography (GPC) (Figure A.1-Figure A.12). A dilute solution of the polymer in THF is eluted through four gel columns (Polymer Laboratories PLgel 10 μm analytical columns, 30 cm long) using THF flowing at a rate of 0.9 mL/min and is detected at the outlet by a Waters 410 differential refractometer. The chromatograph is calibrated with monodisperse PS standards and the PDI is calculated using the Millenium® software from Waters. The total time to traverse all four columns is approximately 45 minutes. In some cases (when the GPC trace only goes from zero to 30 minutes) only two columns were used.

Prepolymer properties are summarized in Table A.1-Table A.4. NMR and GPC data from prepolymers are presented in Figure A.1-Figure A.12.

A.1.5 Characterization of Side-Group Liquid Crystal Polymers

The degree of conversion (percentage of reacted 1,2-PB monomers) of SGLCPs is measured by proton NMR (Figure A.13-Figure A.25). Just as was the case in the prepolymer, the mole fraction of unreacted 1,2-buatdiene monomers is quantified by the intensity of the peak at $\delta = 4.9$ ppm. Using the peak at $\delta = 3.9$ ppm (two alkyl hydrogens adjacent to the cyanobiphenyl core) as a convenient measure of the mesogenic side groups, the degree of conversion is the ratio of this peak intensity to that of 1,2 PB: $x_{LC} = I_{\delta=3.9ppm} / (I_{\delta=4.9ppm} + I_{\delta=3.9ppm})$. The mole fraction of unreactive 1,4-PB and the molecular weight of the coil block(s) is assumed to be the same as in the prepolymer. The molecular weight of SGLCP block is calculated using the measured composition and the known molecular weight of polybutadiene in the prepolymer. Polydispersity of the SGLCPs is measured by GPC, just like the prepolymer (Figure A.13-Figure A.25).

SGLCP properties are summarized in Table A.5-Table A.8. NMR and GPC data from SGLCPs are presented in Figure A.13-Figure A.25.

A.2 Tables

Table A.1 Molecular weight, composition, and polydispersity of 1,2-polybuatdiene prepolymers used to synthesize side-group liquid crystalline homopolymers in Table A.5. See Figure A.1-Figure A.3 for data used to calculate and composition of the PB block and polydispersity.

Name	M_n [kg/mol]	Mole Fraction 1,2 PB	Mole Fraction 1,4 PB	PDI[a]
50H	47.5[b]	0.89	0.11	1.06
60H	63[c]	0.97	0.03	1.05
100H	104[b]	0.96	0.04	1.05

[a] PDI = Polydispersity Index (M_w/M_n)

[b] Information provided by the supplier, Polymer Source (Montreal, Quebec)

[c] Polymer synthesized by Steven Smith (Proctor and Gamble, Inc.), M_n independently measured by Michael Kempe using multi-angle laser light scattering[4]

Table A.2 Molecular weight, composition, and polydispersity of poly[styrene-*b*-1,2-butadiene] diblock prepolymers used to synthesize PS-SGLCP diblock copolymers in Table A.6. See Figure A.4-Figure A.10 for data used to calculate and composition of the PB block and polydispersity.

	PS Block	PB Block			
Name	M_n [kg/mol]	M_n [kg/mol]	Mole Fraction 1,2 PB	Mole Fraction 1,4 PB	PDI[a]
30(60)AB	33[b]	63.5[b]	0.85	0.15	1.12
100(70)AB	97[b]	70[b]	0.88	0.12	1.19
100(190)AB	97[b]	191[b]	0.77	0.23	1.42
60(40)AB	59[c]	43[c]	0.99	0.01	1.04
60(60)AB	57[c]	59[c]	0.97	0.03	1.08
60(80)AB	57[c]	83[c]	0.95	0.05	1.09
50(120)AB	50[c]	121[c]	0.99	0.01	1.06

[a] PDI = Polydispersity Index (M_w/M_n)

[b] Information provided by the supplier, Polymer Source (Montreal, Quebec)

[c] Information provided by the supplier, David Uhrig (Center for Nanophase Materials Sciences, Oak Ridge National Laboratory)

Table A.3 Molecular weight, composition, and polydispersity of poly[styrene-*b*-1,2-butadiene-*b*-styrene] triblock prepolymer used to synthesize the PS-SGLCP-PS triblock copolymer in Table A.7. See Figure A.11 for data used to calculate and composition of the PB block and polydispersity.

	PS Blocks	PB Block			
Name	M_n [kg/mol]	M_n [kg/mol]	Mole Fraction 1,2 PB	Mole Fraction 1,4 PB	PDI[a]
(60)150(70)ABA	57, 67[b]	146[b]	0.86	0.14	1.43

[a] PDI = Polydispersity Index (M_w/M_n)

[b] Polymer purchased from Polymer Source (Montreal, Quebec), M_n independently measured by Michael Kempe using multi-angle laser light scattering[4]

Table A.4 Molecular weight, composition, and polydispersity of poly[(methyl methacrylate)-*b*-1,2-butadiene] diblock prepolymer used to synthesize the PMMA-SGLCP diblock copolymer in Table A.8. See Figure A.12 for data used to calculate and composition of the PB block and polydispersity.

	PMMA Block	PB Block			
Name	M_n [kg/mol]	M_n [kg/mol]	Mole Fraction 1,2 PB	Mole Fraction 1,4 PB	PDI[a]
140(70)BdMMA	68[b]	142[b]	0.87	0.13	1.24

[a] PDI = Polydispersity Index (M_w/M_n)

[b] Information provided by the supplier, Polymer Source (Montreal, Quebec)

Table A.5 Molecular weight, composition, and polydispersity of the side-group liquid crystal homopolymers synthesized from prepolymers in Table A.1. See Figure A.4-Figure A.10 and Figure A.17-Figure A.23 for data used to calculate composition, polydispersity, and the molecular weight of the SGLCP block.

Name	M_n [kg/mol]	Mole Fraction 1,2 PB	Mole Fraction 1,4 PB	Mole Fraction LC	PDI[a]
350HSiCB4	347	0	0.11	0.89	1.27
$d_2$350HSiCB4	348	0	0.11	0.89	1.27
490HSiCB4	489	0.01	0.03	0.96	1.48
760HSiCB4	762	0.06	0.04	0.90	1.11

[a] PDI = Polydispersity Index (M_w/M_n)

Table A.6 Molecular weight, composition, and polydispersity of the side-group liquid crystal diblock copolymers with coil block composed of polystyrene (PS), synthesized from prepolymers in Table A.2 . See Figure A.4-Figure A.10 and Figure A.17-Figure A.23 for data used to calculate composition, polydispersity, and the molecular weight of the SGLCP block.

Name	PS Block M_n [kg/mol]	SGLCP Block M_n [kg/mol]	SGLCP Block Mole Fraction 1,2 PB	SGLCP Block Mole Fraction 1,4 PB	SGLCP Block Mole Fraction LC	PDI[a]
210(60)ABSiCB4	63.5	205	0.13	0.15	0.72	1.22
700(70)ABSiCB4	70	700	0	0.11	0.89	1.50
580(190)ABSiCB4	191	577	0.09	0.23	0.68	1.56
470(40)ABSiCB4	43	472	0	0.01	0.99	1.19
390(60)ABSiCB4	59	388	0.15	0.03	0.85	1.11
420(80)ABSiCB4	83	422	0.05	0.05	0.90	1.07
320(120)ABSiCB4	121	323	0.22	0.01	0.77	1.05

[a] PDI = Polydispersity Index (M_w/M_n)

Table A.7 Molecular weight, composition, and polydispersity of the side-group liquid crystal triblock copolymer with polystyrene endblocks, synthesized from the prepolymer in Table A.3. See Figure A.11 and Figure A.24 for data used to calculate composition, polydispersity, and the molecular weight of the SGLCP block.

Name	PS Blocks	SGLCP Block				PDI[a]
	M_n [kg/mol]	M_n [kg/mol]	Mole Fraction 1,2 PB	Mole Fraction 1,4 PB	Mole Fraction LC	
1100ABASiCB4	57,67	1,012	0.02	0.14	0.84	1.16

[a]PDI = Polydispersity Index (M_w/M_n)

Table A.8 Molecular weight, composition, and polydispersity of the side-group liquid crystal diblock copolymer with coil block composed of poly(methyl methacrylate) (PMMA), synthesized from the prepolymer in Table A.4. See Figure A.12 and Figure A.25 for data used to calculate composition, polydispersity, and the molecular weight of the SGLCP block.

Name	PMMA Block	SGLCP Block				PDI[a]
	M_n [kg/mol]	M_n [kg/mol]	Mole Fraction 1,2 PB	Mole Fraction 1,4 PB	Mole Fraction LC	
950(70)BdMMASiCB4	68	954	0.07	0.13	0.80	1.11

[a]PDI = Polydispersity Index (M_w/M_n)

A.3 Schemes

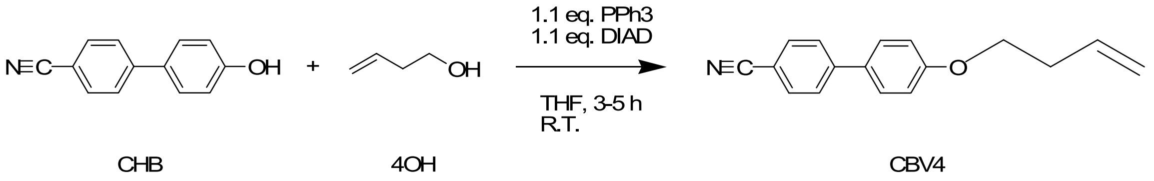

Scheme A.1 Synthesis of 4-cyano-4′-(3-butenoxy)-biphenyl (CBV4) by Mitsunobu reaction between 4-cyano-4′-hydroxybiphenyl (CHB) and 3-buten-1-ol (4OH) using diisopropyl azodicarboxylate (DIAD) and triphenylphosphine (TPP) in tetrahydrofuran (THF) at room temperature

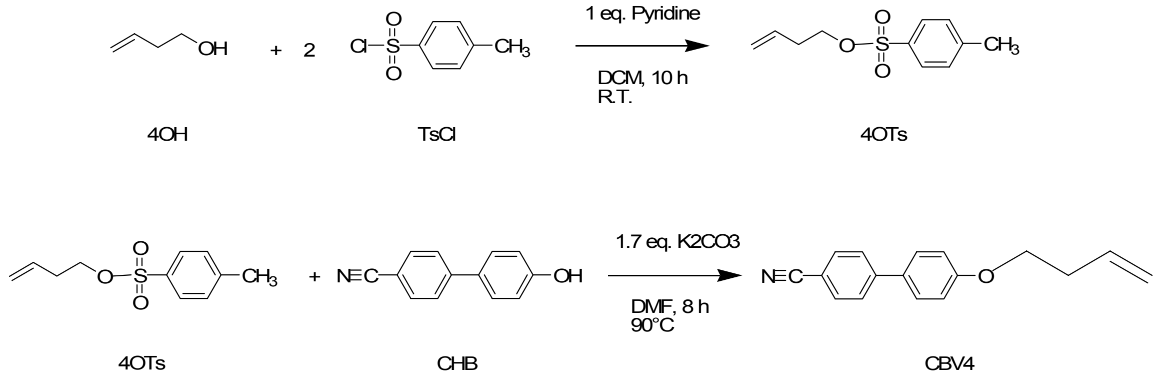

Scheme A.2 Synthesis of 4-cyano-4′-(3-butenoxy)-biphenyl (CBV4) by Williamson ether synthesis. 3-buten-1-ol (4OH) is first converted to 3-butenyl-1-tosylate (4OTs) by reaction with p-toluenesulfonyl chloride (TsCl) and is subsequently reacted with 4-cyano-4′-hydroxybiphenyl (CHB) to yield the final product.

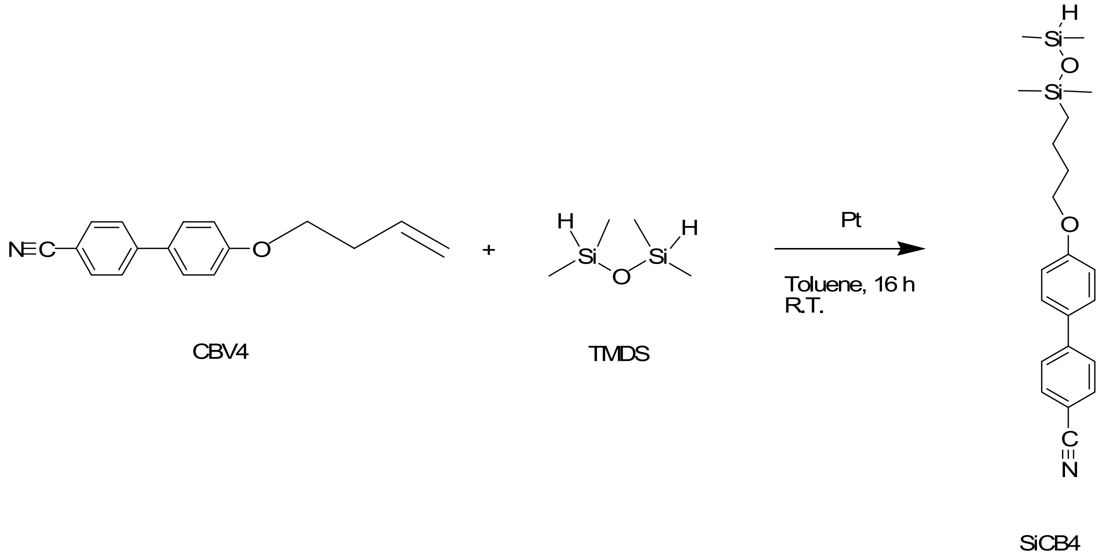

Scheme A.3 Synthesis of 4-cyano-4′-(5-(1,1,3,3,-tetramethyldisiloxane)butoxy)biphenyl (SiCB4) by platinum-catalyzed hydrosilylation

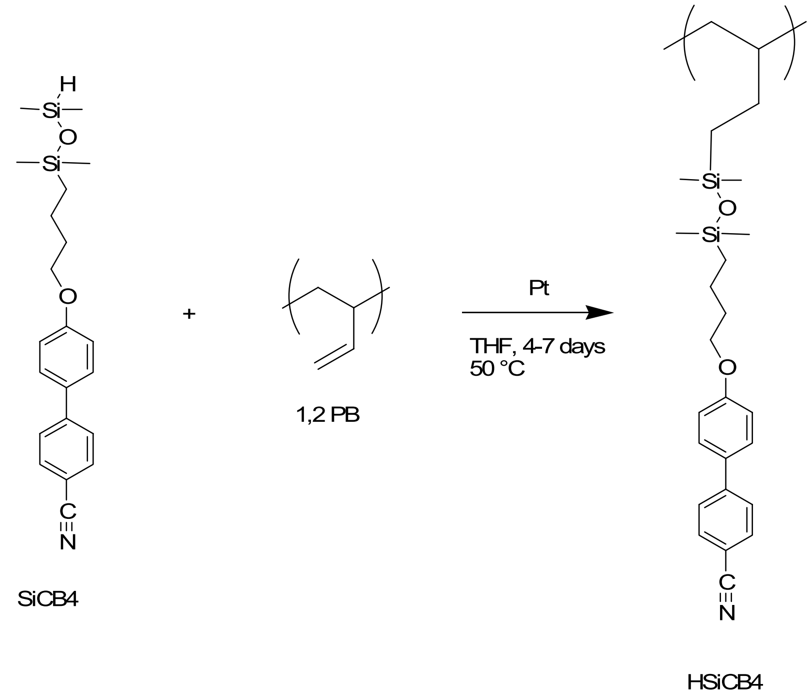

Scheme A.4 Attachment of SiCB4 to a 1,2-polybutadiene monomer by platinum-catalyzed hydrosilylation

A.4 Figures

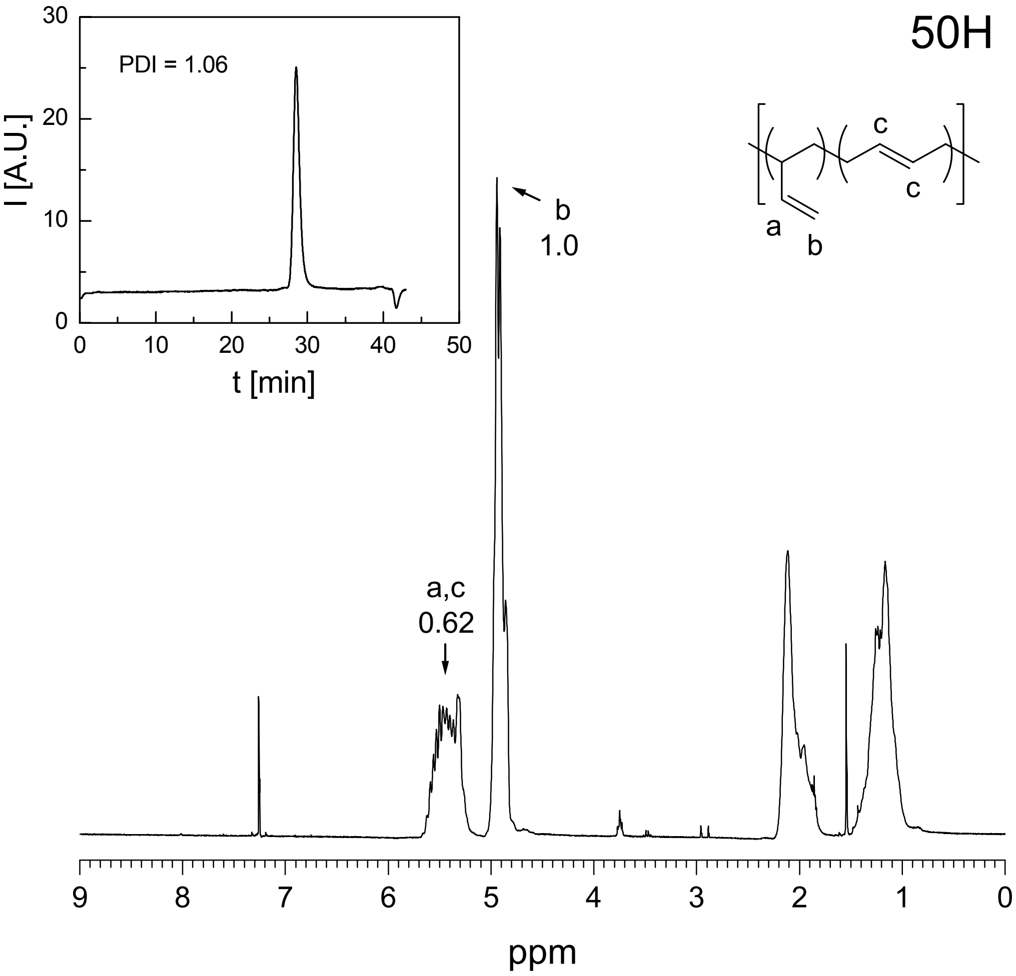

Figure A.1 300 MHz proton NMR spectrum of 50H, a 1,2-polybutadiene homopolymer with M_n = 47.5 kg/mol, in $CDCl_3$. Peak labels include the relative intensity (integrated area) and their assignments. This data was used to calculate the polymer composition reported in Table A.1. The GPC chromatograph used to measure polydispersity is shown in the inset.

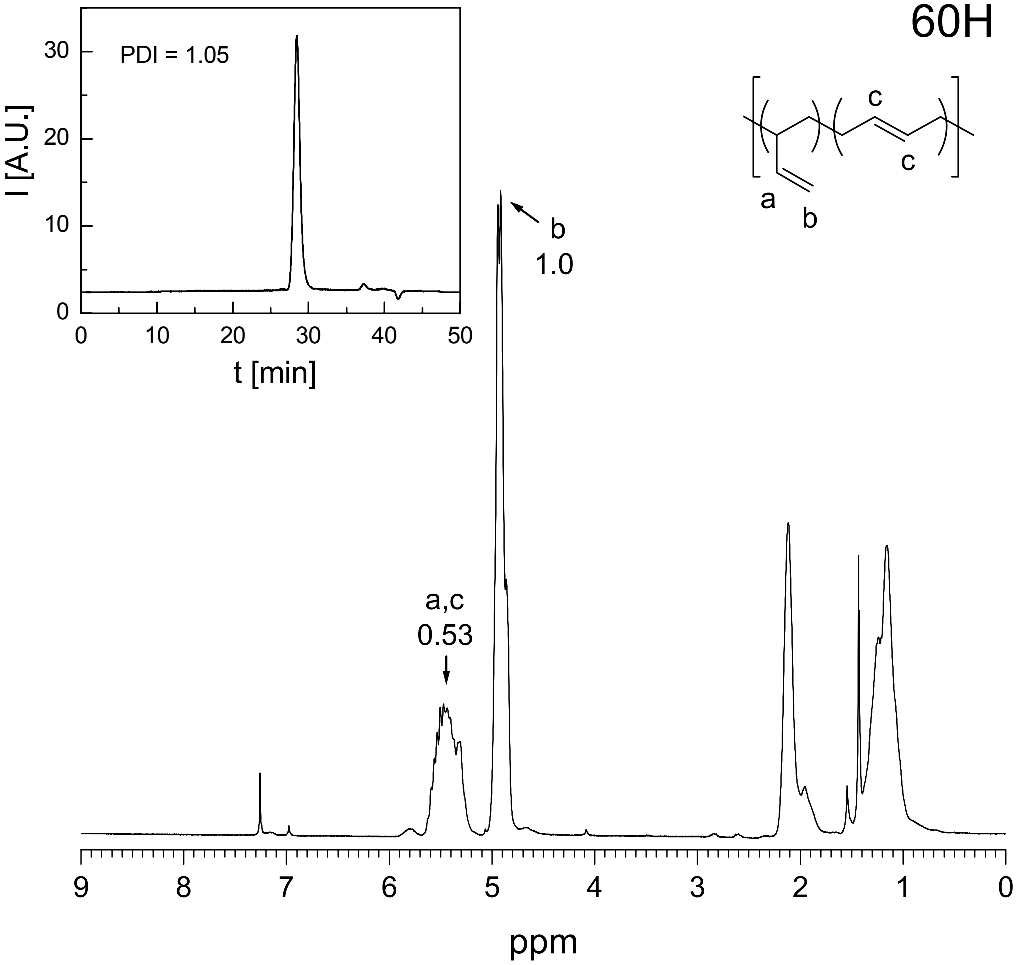

Figure A.2 300 MHz proton NMR spectrum of 60H, a 1,2-polybutadiene homopolymer with M_n = 63 kg/mol, in $CDCl_3$. Peak labels include the relative intensity (integrated area) and their assignments. This data was used to calculate the polymer composition reported in Table A.1. The GPC chromatograph used to measure polydispersity is shown in the inset.

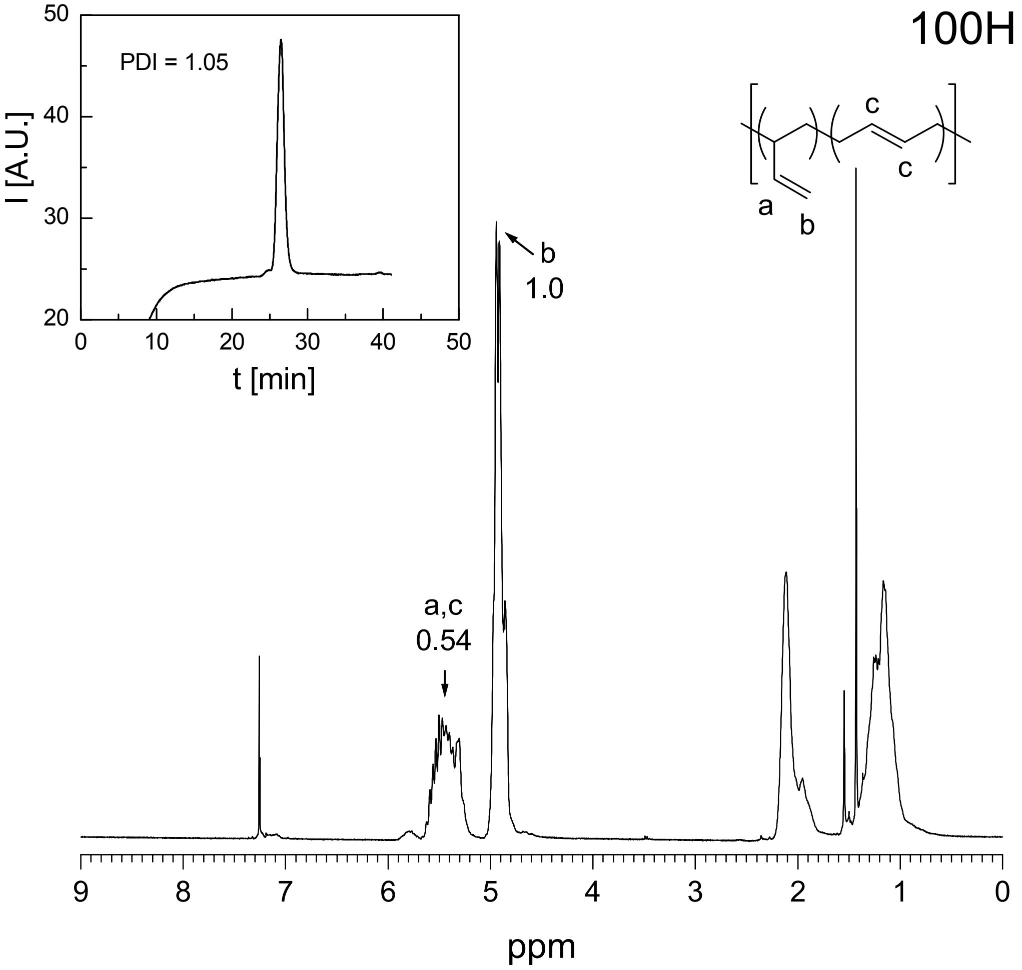

Figure A.3 300 MHz proton NMR spectrum of 100H, a 1,2-polybutadiene homopolymer with M_n = 104 kg/mol, in $CDCl_3$. Peak labels include the relative intensity (integrated area) and their assignments. This data was used to calculate the polymer composition reported in Table A.1. The GPC chromatograph used to measure polydispersity is shown in the inset.

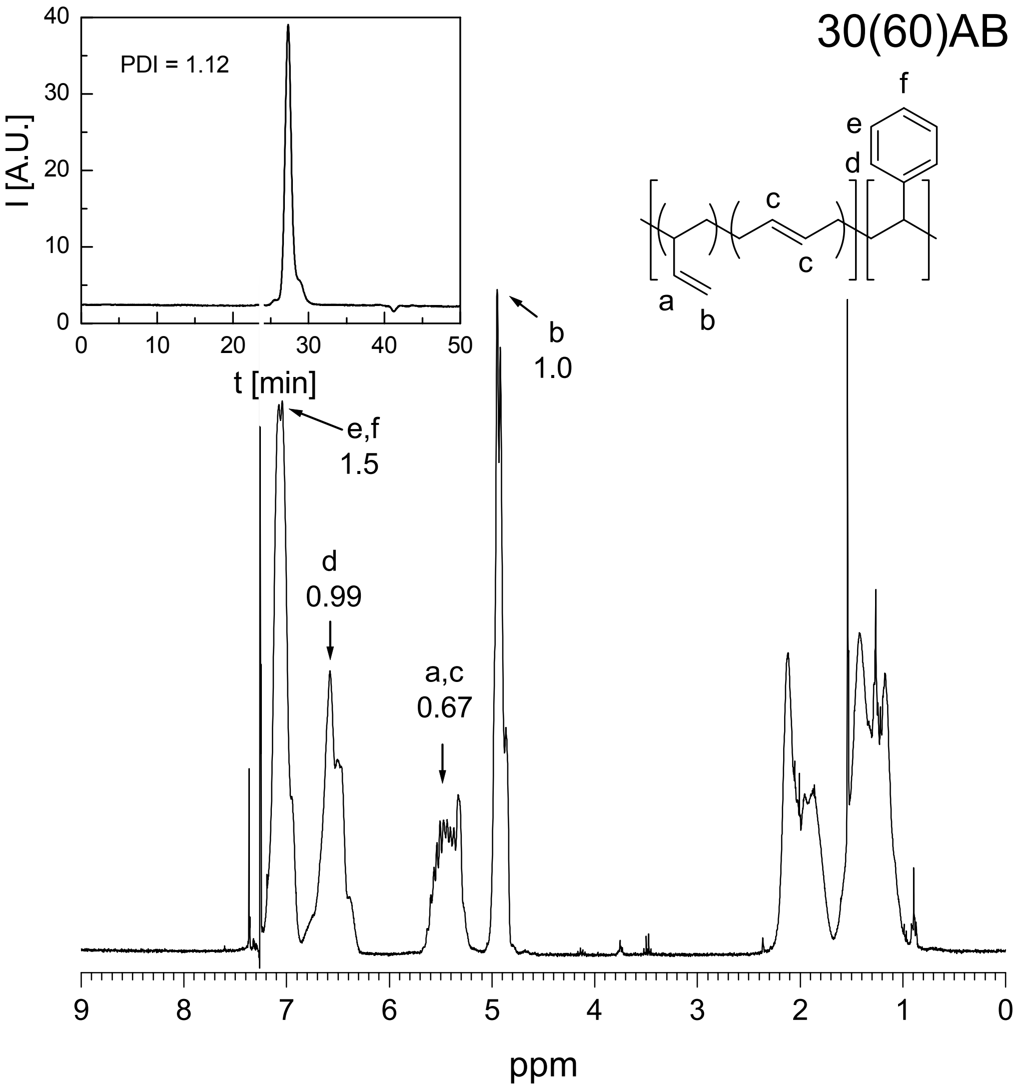

Figure A.4 300 MHz proton NMR spectrum of 30(60)AB, a poly[styrene-*b*-1,2-butadiene] block copolymer with M_{PS} = 63.5 kg/mol and M_{PB} = 33 kg/mol, in $CDCl_3$. Peak labels include the relative intensity (integrated area) and their assignments. This data was used to calculate the polymer composition reported in Table A.2. The GPC chromatograph used to measure polydispersity is shown in the inset.

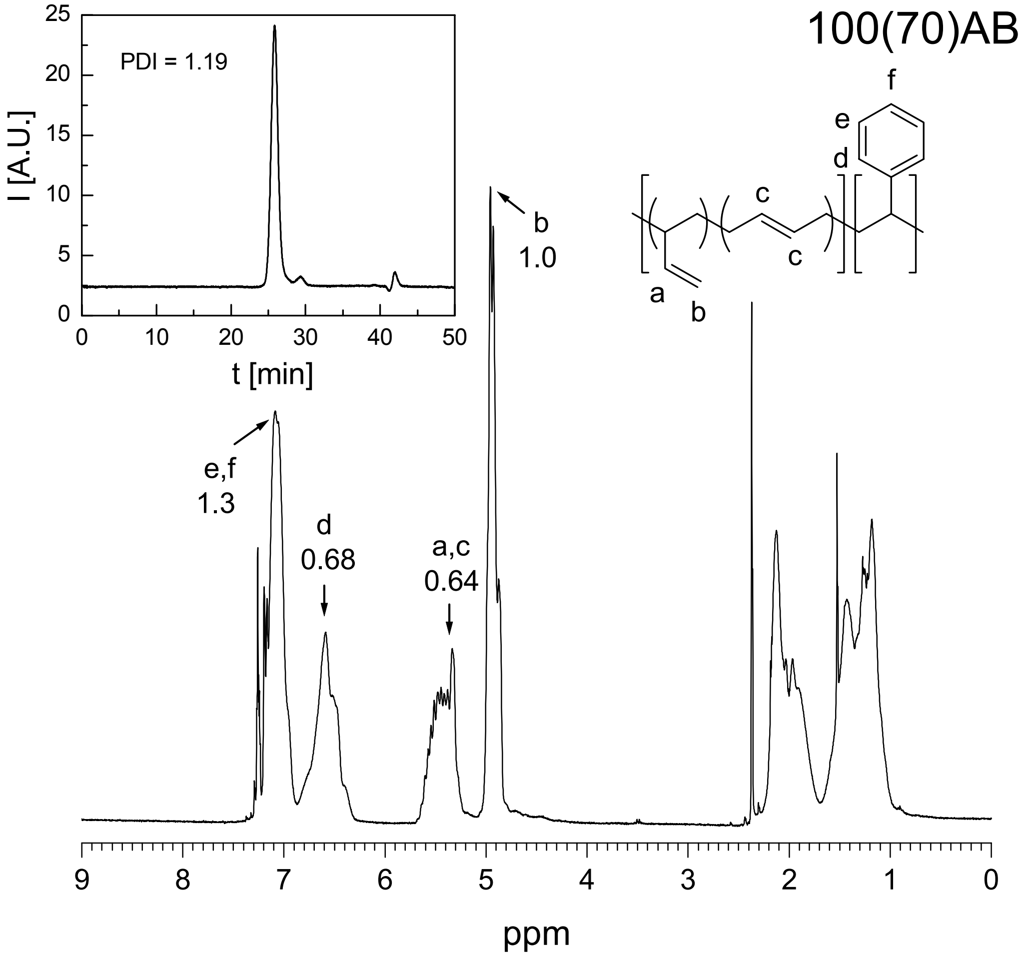

Figure A.5 300 MHz proton NMR spectrum of 100(70)AB, a poly[styrene-*b*-1,2-butadiene] block copolymer with M_{PS} = 70 kg/mol and M_{PB} = 97 kg/mol, in $CDCl_3$. Peak labels include the relative intensity (integrated area) and their assignments. This data was used to calculate the polymer composition reported in Table A.2. The GPC chromatograph used to measure polydispersity is shown in the inset.

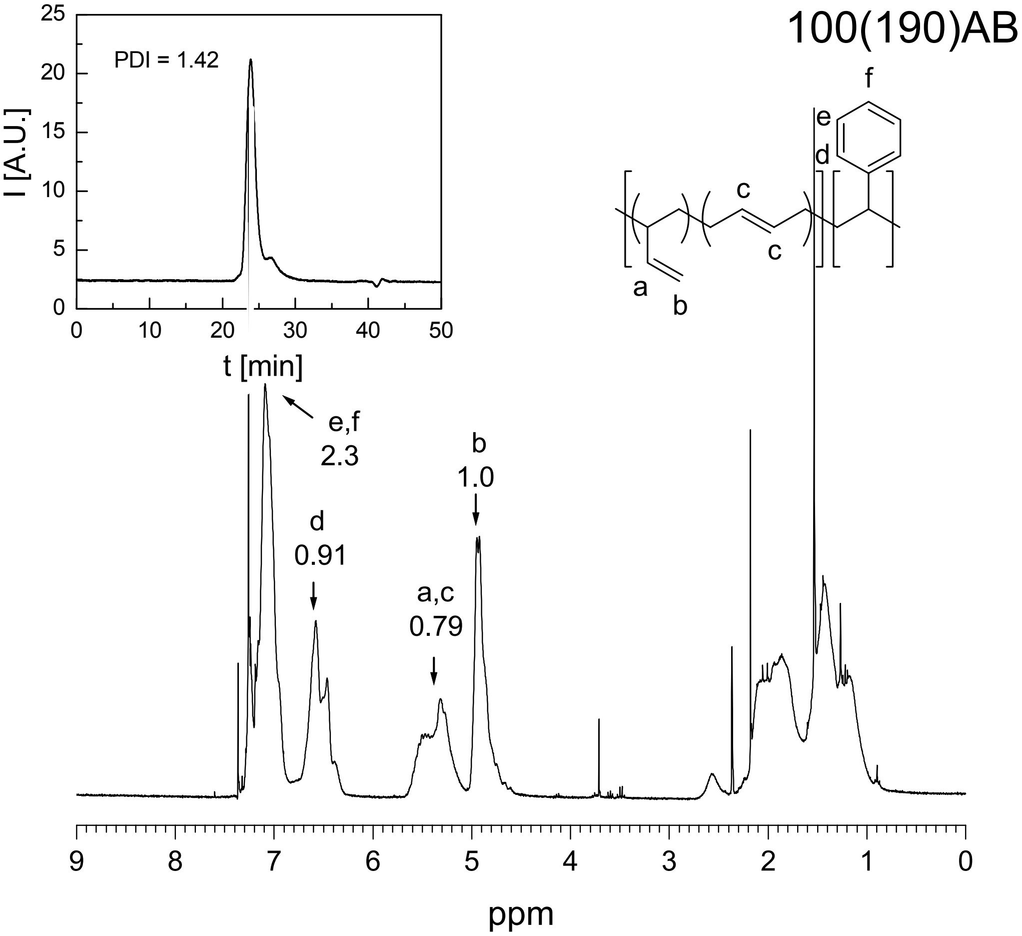

Figure A.6 300 MHz proton NMR spectrum of 100(190)AB, a poly[styrene-b-1,2-butadiene] block copolymer with M_{PS} = 191 kg/mol and M_{PB} = 97 kg/mol, in CDCl3. Peak labels include the relative intensity (integrated area) and their assignments. This data was used to calculate the polymer composition reported in Table A.2. The GPC chromatograph used to measure polydispersity is shown in the inset.

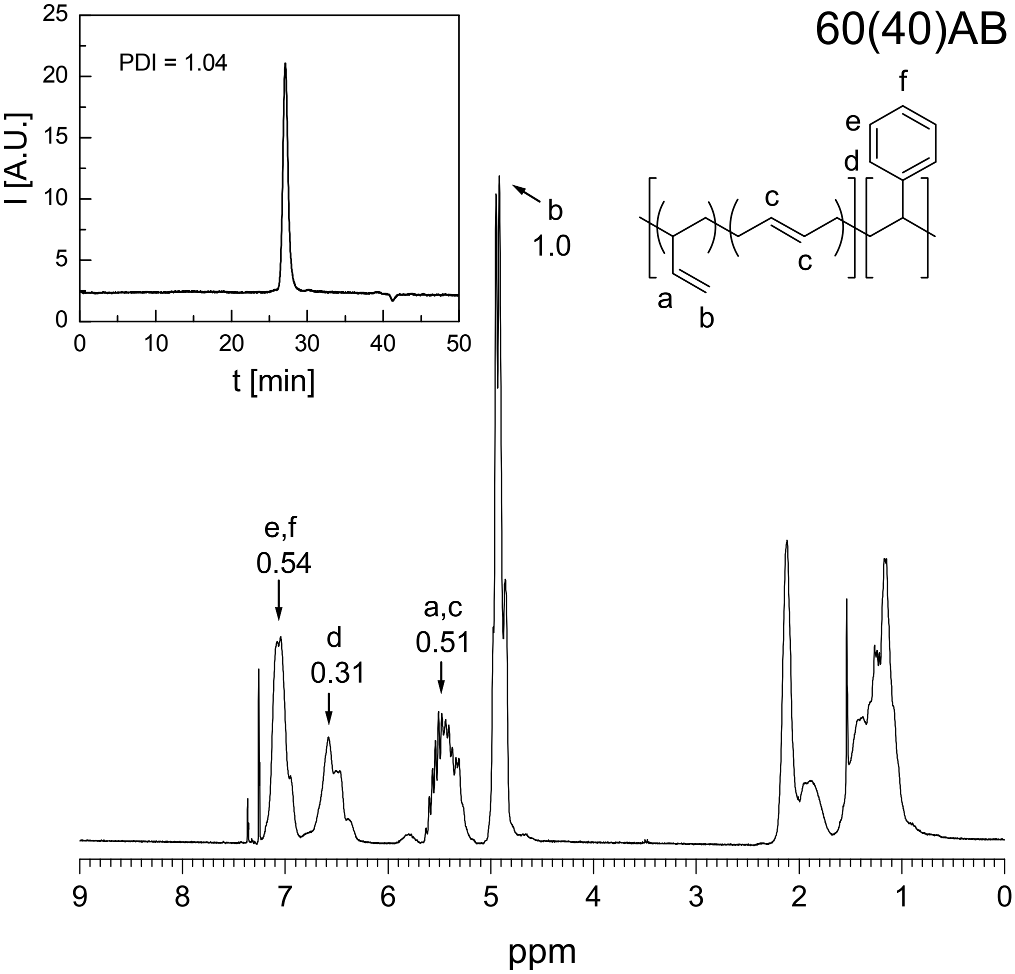

Figure A.7 300 MHz proton NMR spectrum of 60(40)AB, a poly[styrene-b-1,2-butadiene] block copolymer with M_{PS} = 43 kg/mol and M_{PB} = 59 kg/mol, in CDCl3. Peak labels include the relative intensity (integrated area) and their assignments. This data was used to calculate the polymer composition reported in Table A.2. The GPC chromatograph used to measure polydispersity is shown in the inset.

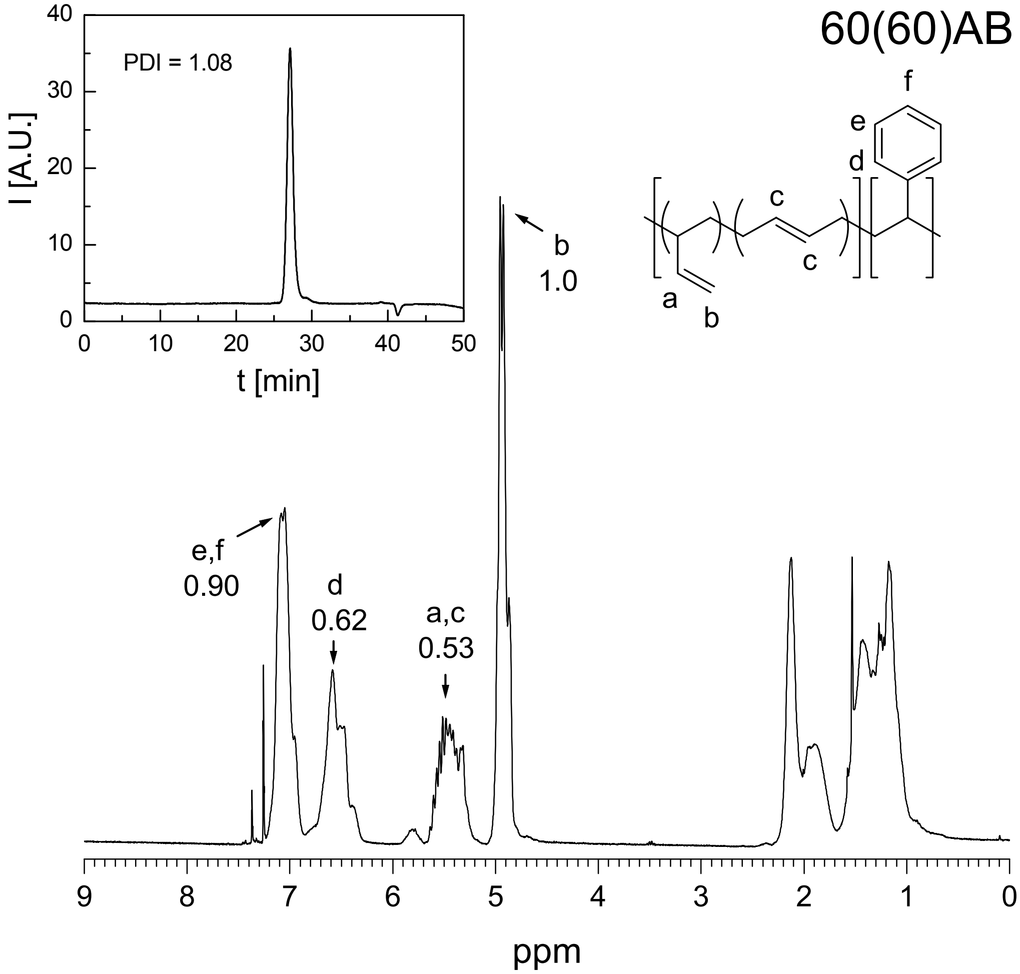

Figure A.8 300 MHz proton NMR spectrum of 60(60)AB, a poly[styrene-b-1,2-butadiene] block copolymer with M_{PS} = 59 kg/mol and M_{PB} = 57 kg/mol, in CDCl3. Peak labels include the relative intensity (integrated area) and their assignments. This data was used to calculate the polymer composition reported in Table A.2. The GPC chromatograph used to measure polydispersity is shown in the inset.

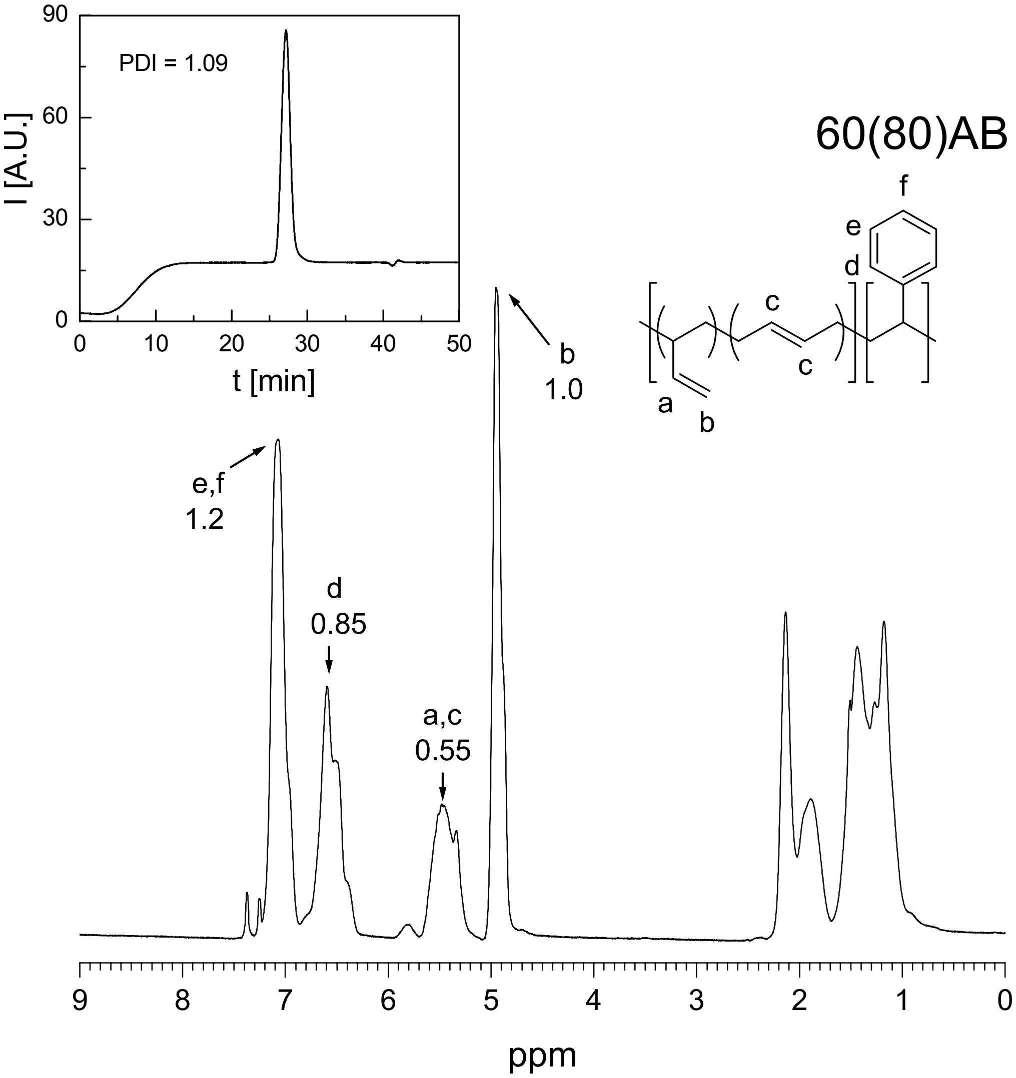

Figure A.9 300 MHz proton NMR spectrum of 60(80)AB, a poly[styrene-b-1,2-butadiene] block copolymer with M_{PS} = 83 kg/mol and M_{PB} = 57 kg/mol, in CDCl3. Peak labels include the relative intensity (integrated area) and their assignments. This data was used to calculate the polymer composition reported in Table A.2. The GPC chromatograph used to measure polydispersity is shown in the inset.

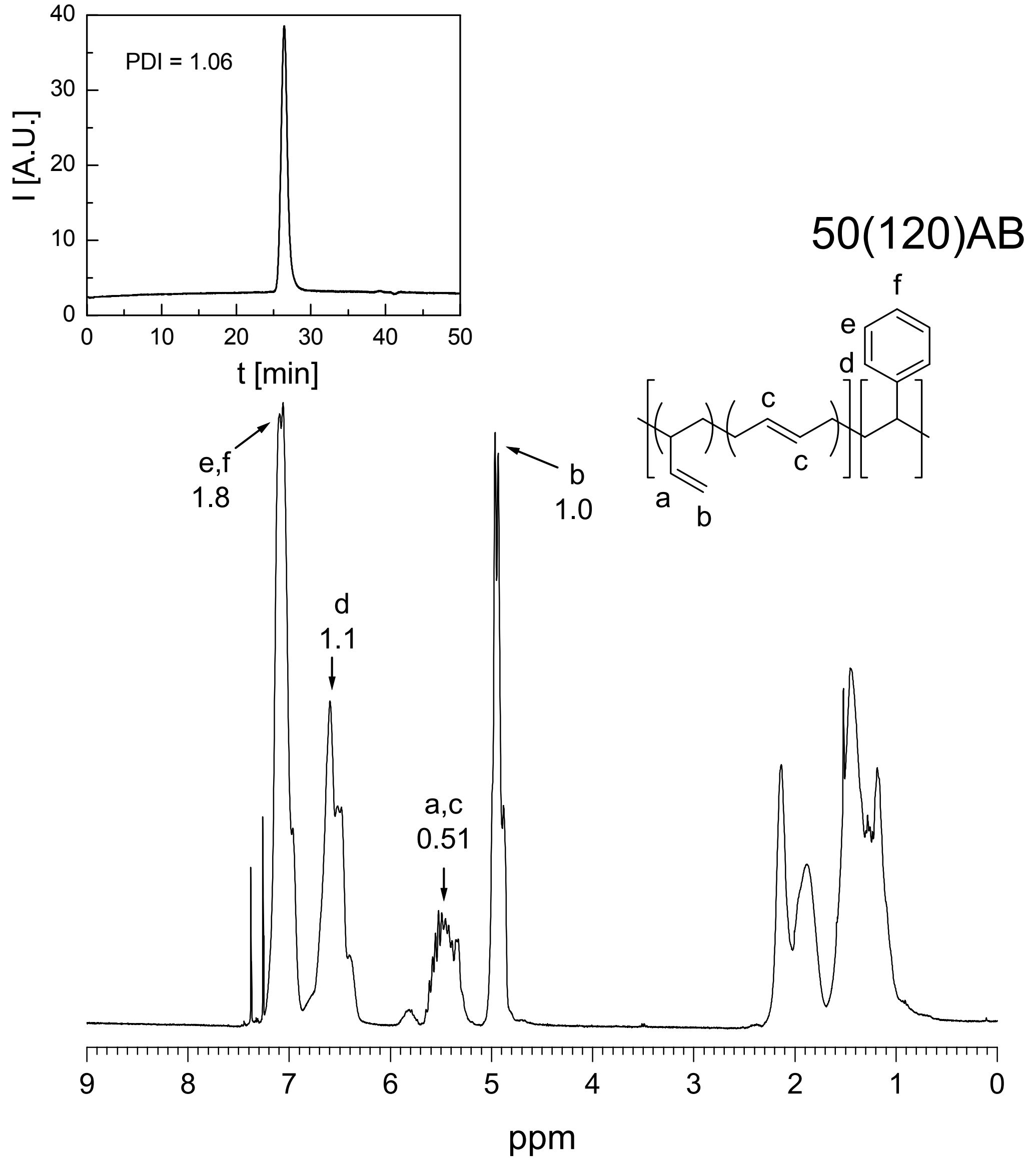

Figure A.10 300 MHz proton NMR spectrum of 50(120)AB, a poly[styrene-b-1,2-butadiene] block copolymer with M_{PS} = 121 kg/mol and M_{PB} = 50 kg/mol, in CDCl3. Peak labels include the relative intensity (integrated area) and their assignments. This data was used to calculate the polymer composition reported in Table A.2. The GPC chromatograph used to measure polydispersity is shown in the inset.

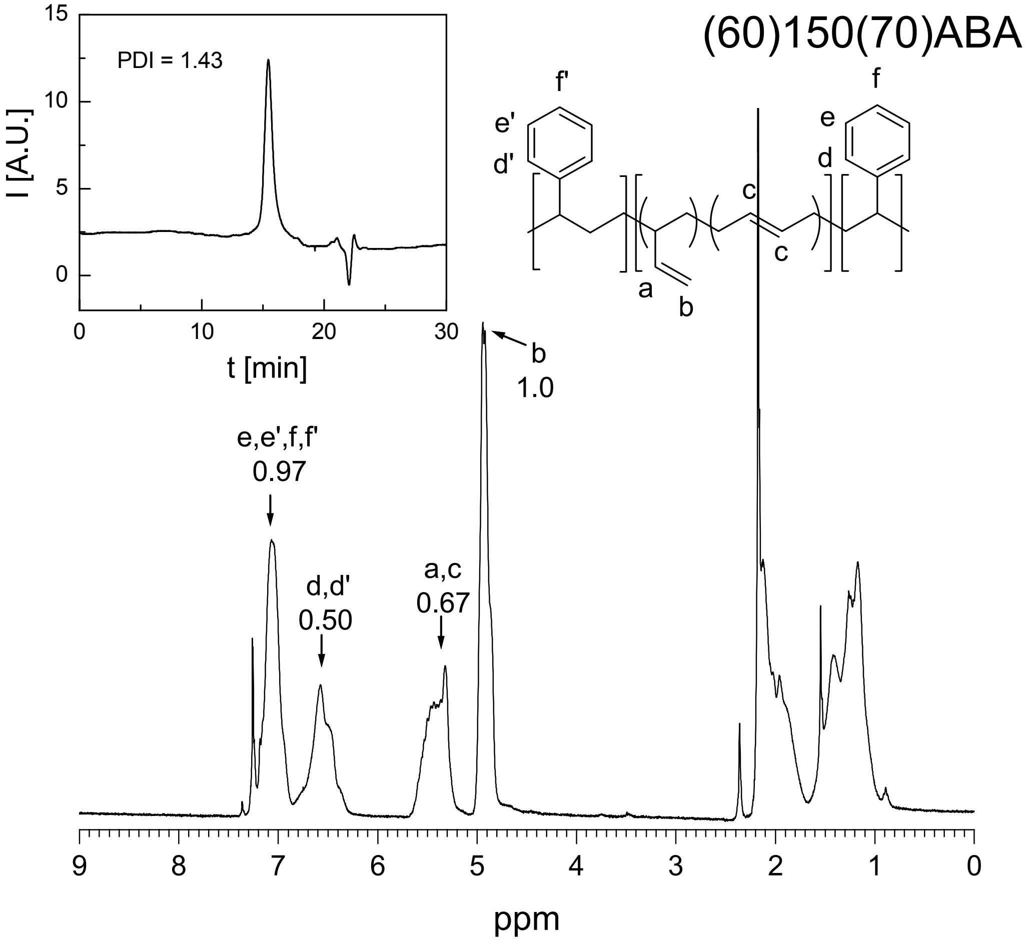

Figure A.11 300 MHz proton NMR spectrum of (60)150(70)ABA, a poly[styrene-*b*-1,2-butadiene-*b*-styrene] triblock copolymer with M_{PS} = 57 and 67 kg/mol and M_{PB} = 146 kg/mol, in $CDCl_3$. Peak labels include the relative intensity (integrated area) and their assignments. This data was used to calculate the polymer composition reported in Table A.3. The GPC chromatograph used to measure polydispersity is shown in the inset.

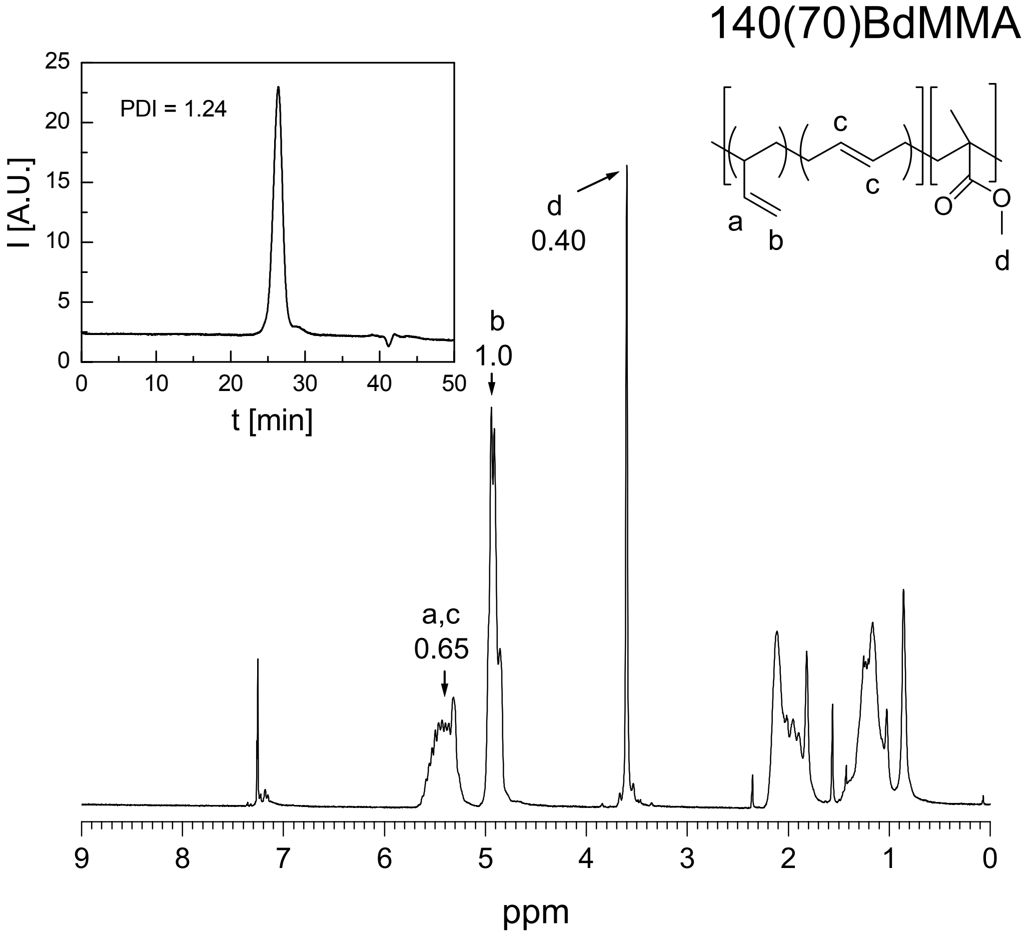

Figure A.12 300 MHz proton NMR spectrum of 140(70)BdMMA, a poly[(methyl methacrylate)-*b*-1,2-butadiene] block copolymer with M_{PMMA} = 68 kg/mol and M_{PB} = 142 kg/mol, in $CDCl_3$. Peak labels include the relative intensity (integrated area) and their assignments. This data was used to calculate the polymer composition reported in Table A.4. The GPC chromatograph used to measure polydispersity is shown in the inset.

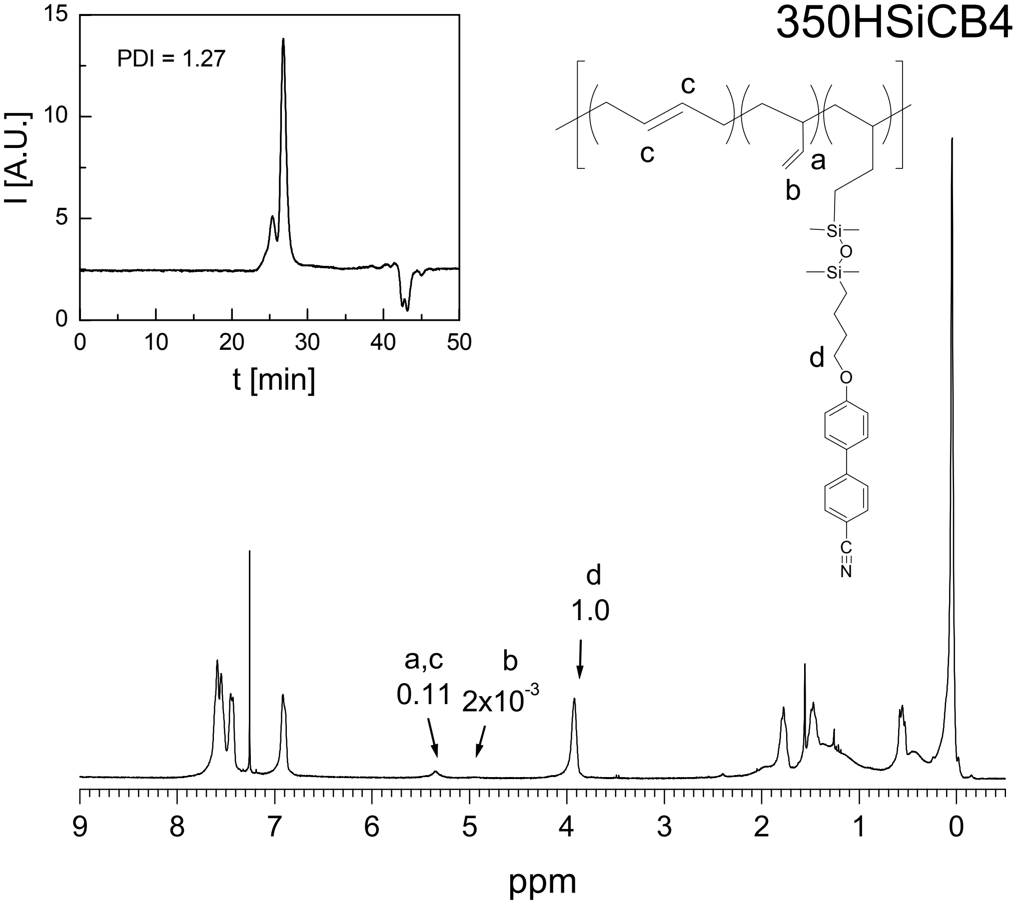

Figure A.13 300 MHz proton NMR spectrum of 350HSiCB4, an SGLCP homopolymer synthesized from 50H, in $CDCl_3$. Peak labels include the relative intensity (integrated area) and their assignments. This data was used to calculate the polymer composition and molecular weight reported in Table A.5. The GPC chromatograph used to measure polydispersity is shown in the inset.

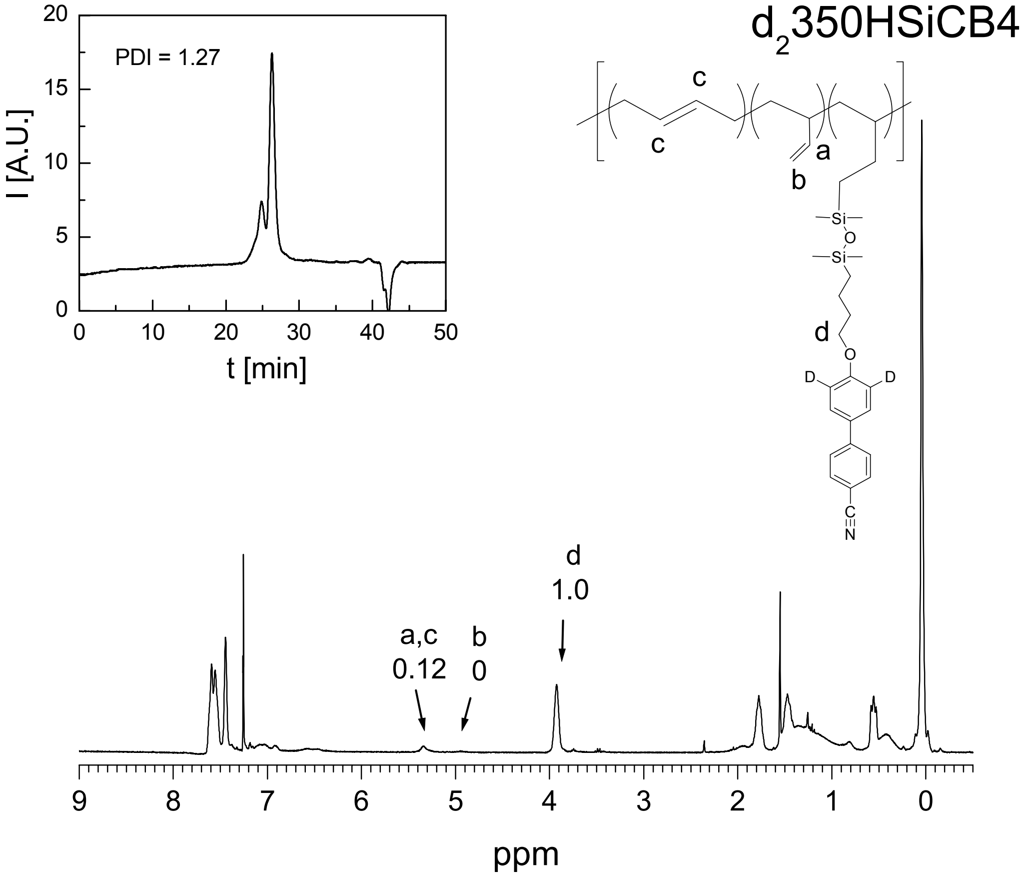

Figure A.14 300 MHz proton NMR spectrum of d$_2$350HSiCB4, a deuterium-labeled SGLCP homopolymer synthesized from 50H, in CDCl$_3$. Peak labels include the relative intensity (integrated area) and their assignments. This data was used to calculate the polymer composition and molecular weight reported in Table A.5. The GPC chromatograph used to measure polydispersity is shown in the inset.

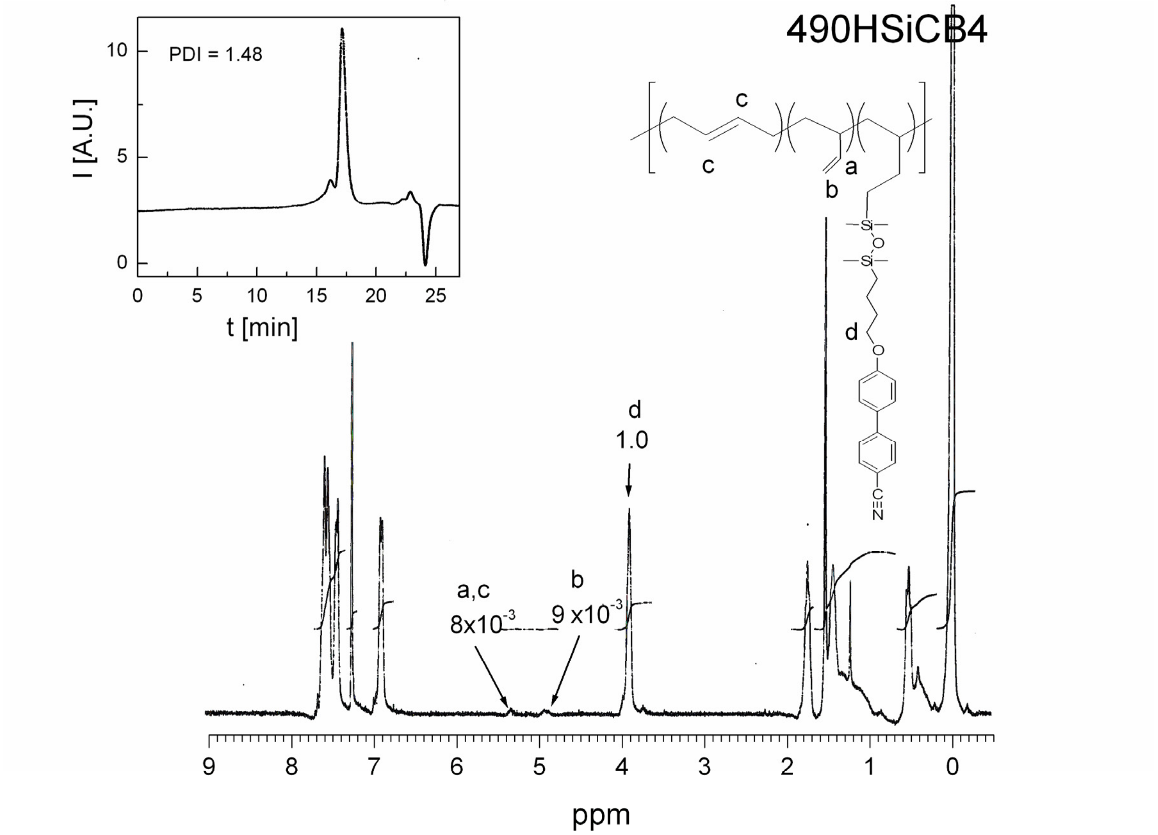

Figure A.15 300 MHz proton NMR spectrum of 490HSiCB4, an SGLCP homopolymer synthesized from 60H, in $CDCl_3$. Peak labels include the relative intensity (integrated area) and their assignments. This data was used to calculate the polymer composition and molecular weight reported in Table A.5. The GPC chromatograph used to measure polydispersity is shown in the inset. The relative intensity of peak ***d*** may be anomalously high due to incomplete removal of unreacted mesogen in this particular sample.

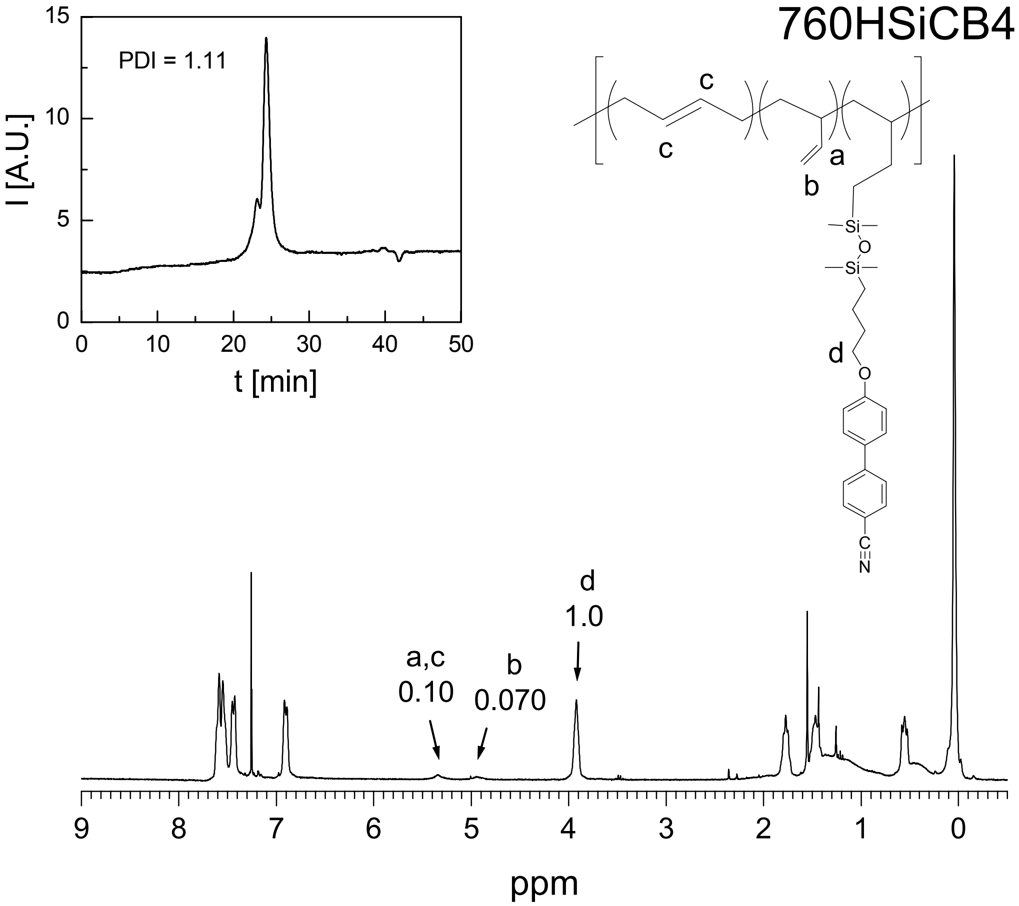

Figure A.16 300 MHz proton NMR spectrum of 760HSiCB4, an SGLCP homopolymer synthesized from 100H, in $CDCl_3$. Peak labels include the relative intensity (integrated area) and their assignments. This data was used to calculate the polymer composition and molecular weight reported in Table A.5. The GPC chromatograph used to measure polydispersity is shown in the inset.

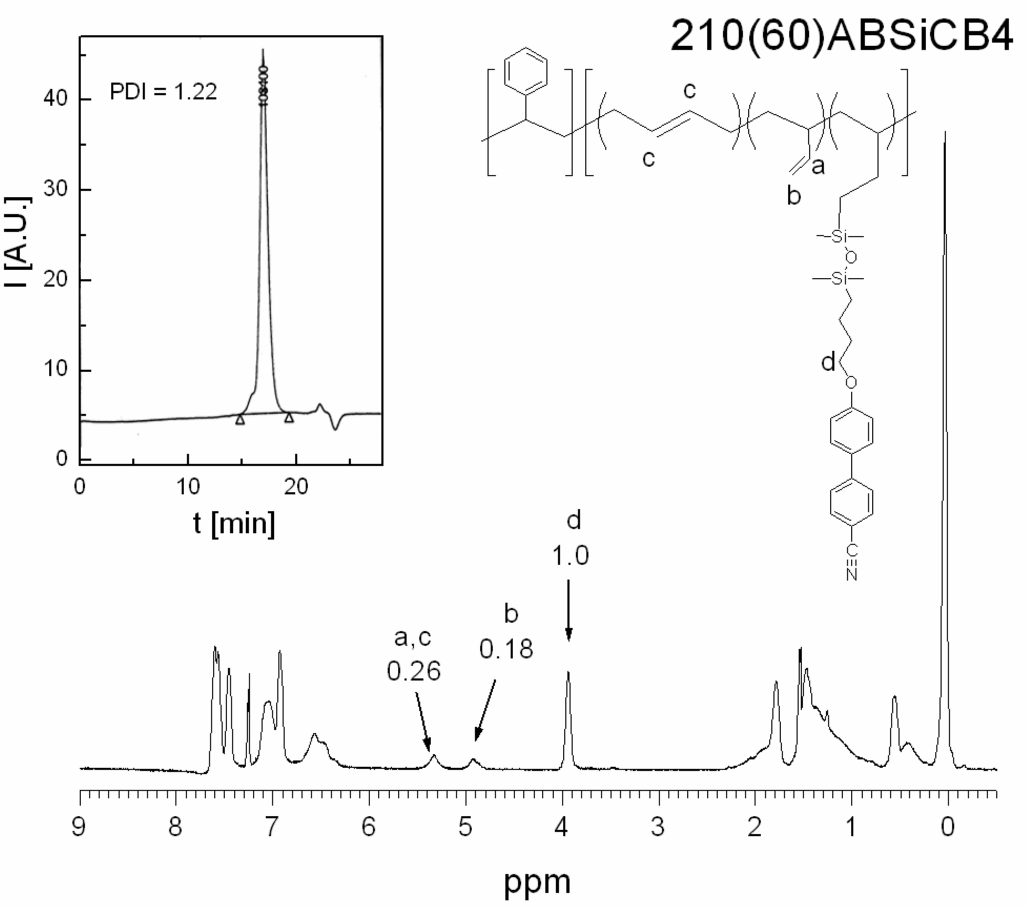

Figure A.17 300 MHz proton NMR spectrum of 210(60)ABSiCB4, a PS-SGLCP diblock copolymer synthesized from 30(60)AB, in $CDCl_3$. Peak labels include the relative intensity (integrated area) and their assignments. This data was used to calculate the polymer composition and molecular weight of the SGLCP block reported in Table A.6. The GPC chromatograph used to measure polydispersity is shown in the inset.

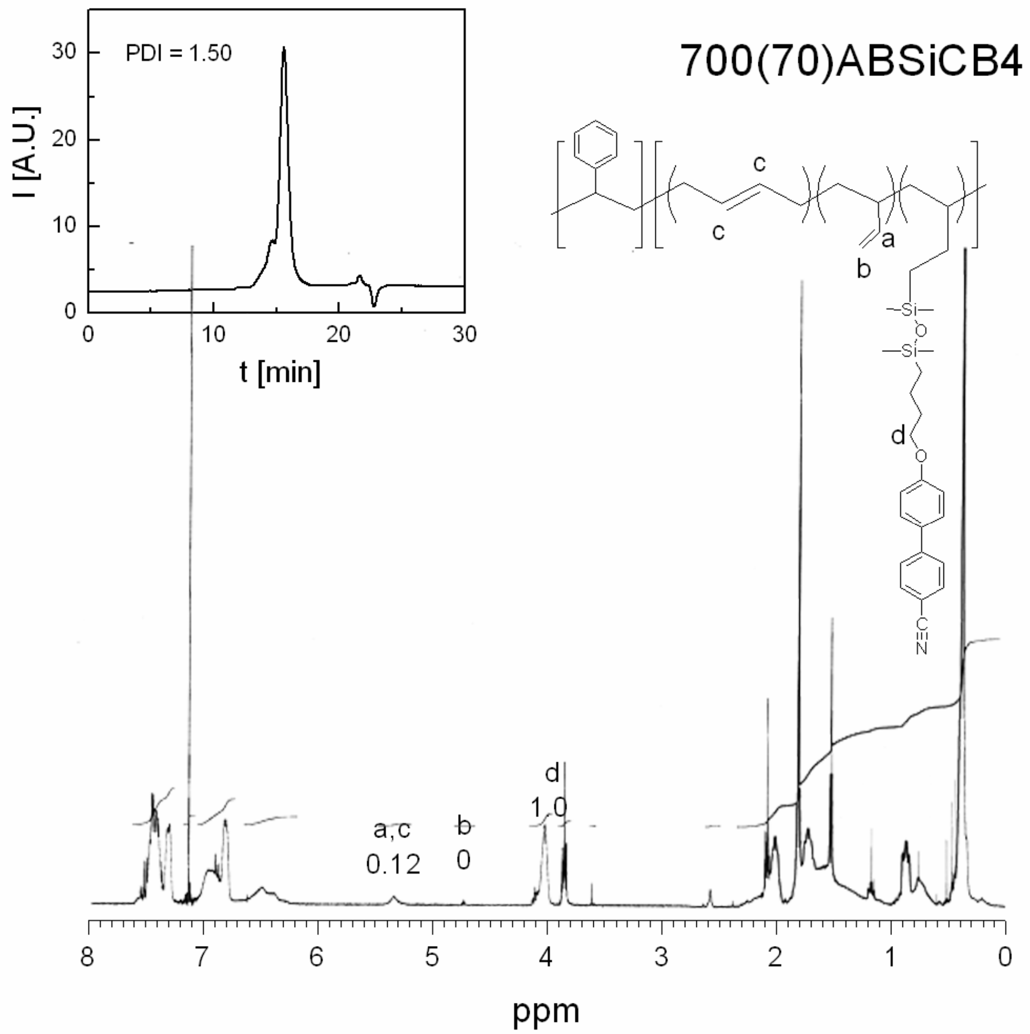

Figure A.18 300 MHz proton NMR spectrum of 700(70)ABSiCB4, a PS-SGLCP diblock copolymer synthesized from 100(70)AB, in $CDCl_3$. Peak labels include the relative intensity (integrated area) and their assignments. This data was used to calculate the polymer composition and molecular weight of the SGLCP block reported in Table A.6. The GPC chromatograph used to measure polydispersity is shown in the inset. The relative intensity of peak ***d*** may be anomalously high and the presence of a peak at $\delta =$ 3.85 ppm may be due to incomplete removal of unreacted mesogen in this particular sample.

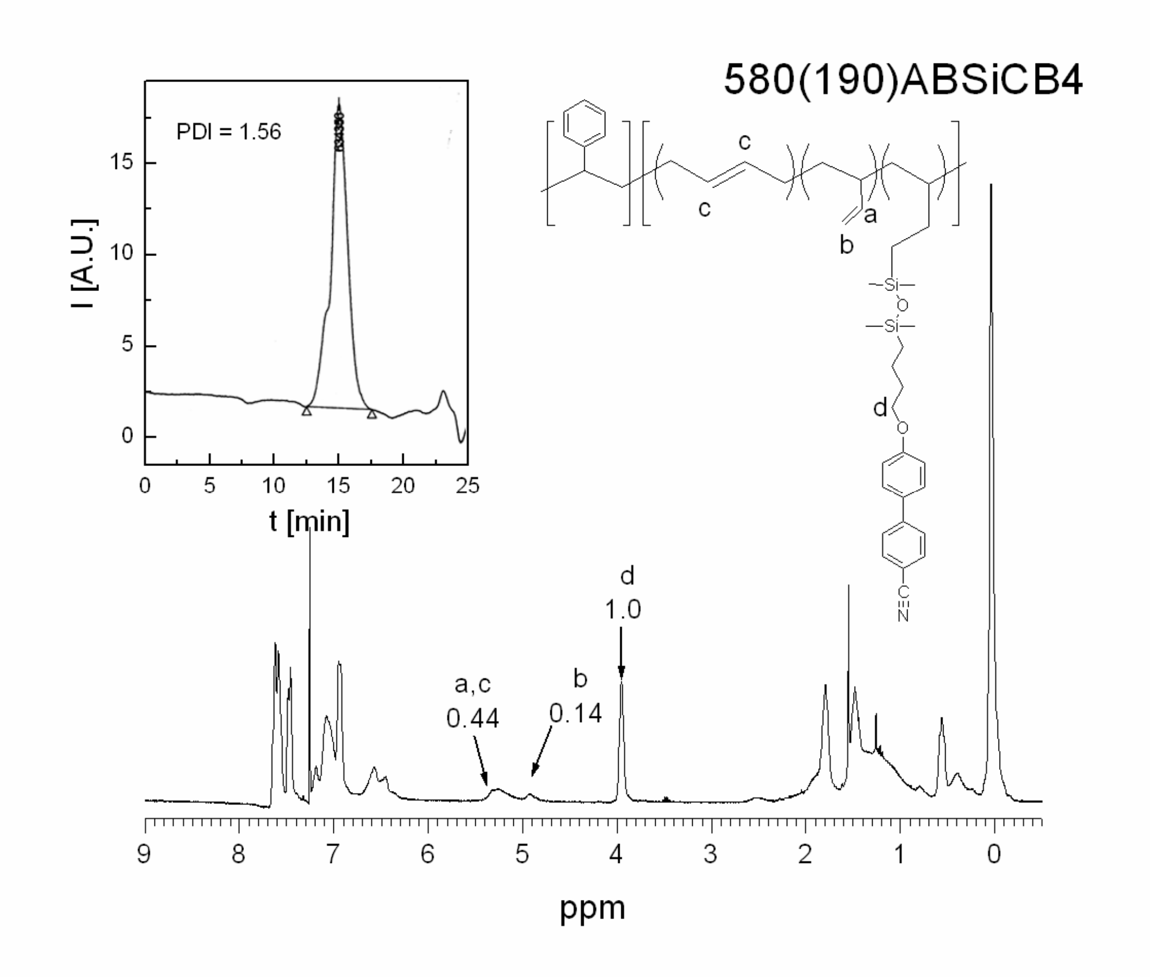

Figure A.19 300 MHz proton NMR spectrum of 580(190)ABSiCB4, a PS-SGLCP diblock copolymer synthesized from 100(190)AB, in $CDCl_3$. Peak labels include the relative intensity (integrated area) and their assignments. This data was used to calculate the polymer composition and molecular weight of the SGLCP block reported in Table A.6. The GPC chromatograph used to measure polydispersity is shown in the inset.

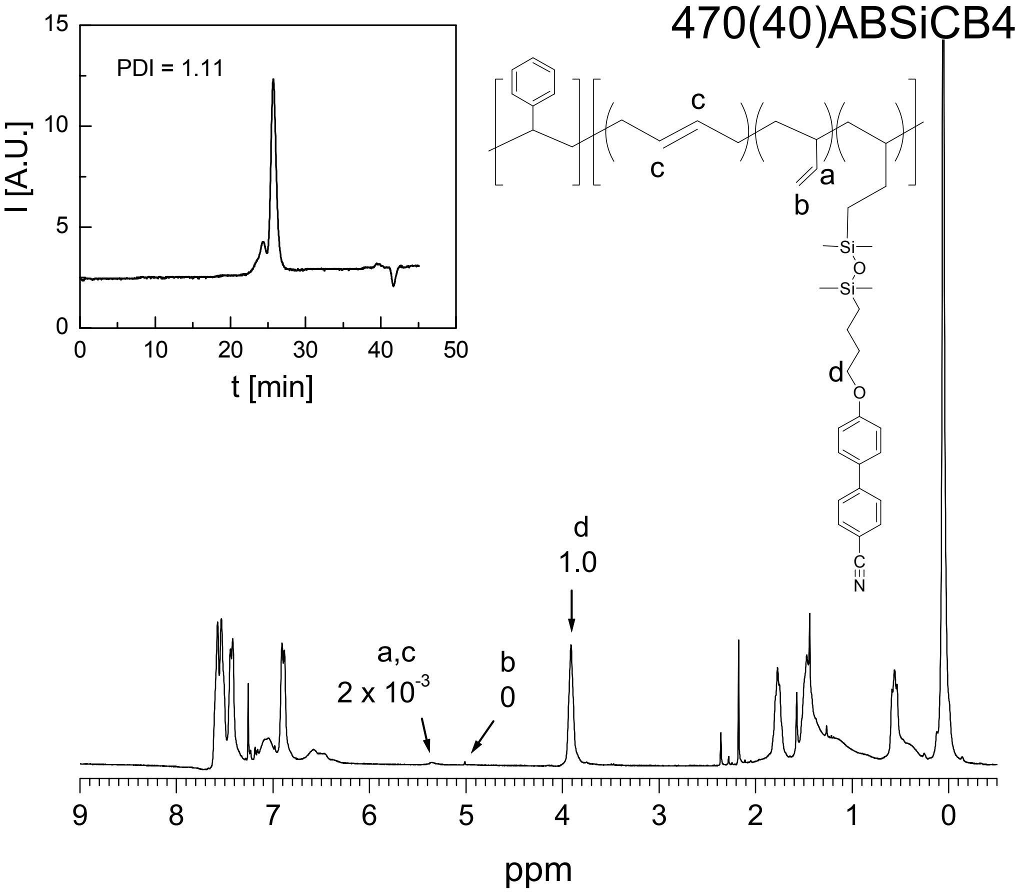

Figure A.20 300 MHz proton NMR spectrum of 470(40)ABSiCB4, a PS-SGLCP diblock copolymer synthesized from 60(40)AB, in $CDCl_3$. Peak labels include the relative intensity (integrated area) and their assignments. This data was used to calculate the polymer composition and molecular weight of the SGLCP block reported in Table A.6. The GPC chromatograph used to measure polydispersity is shown in the inset.

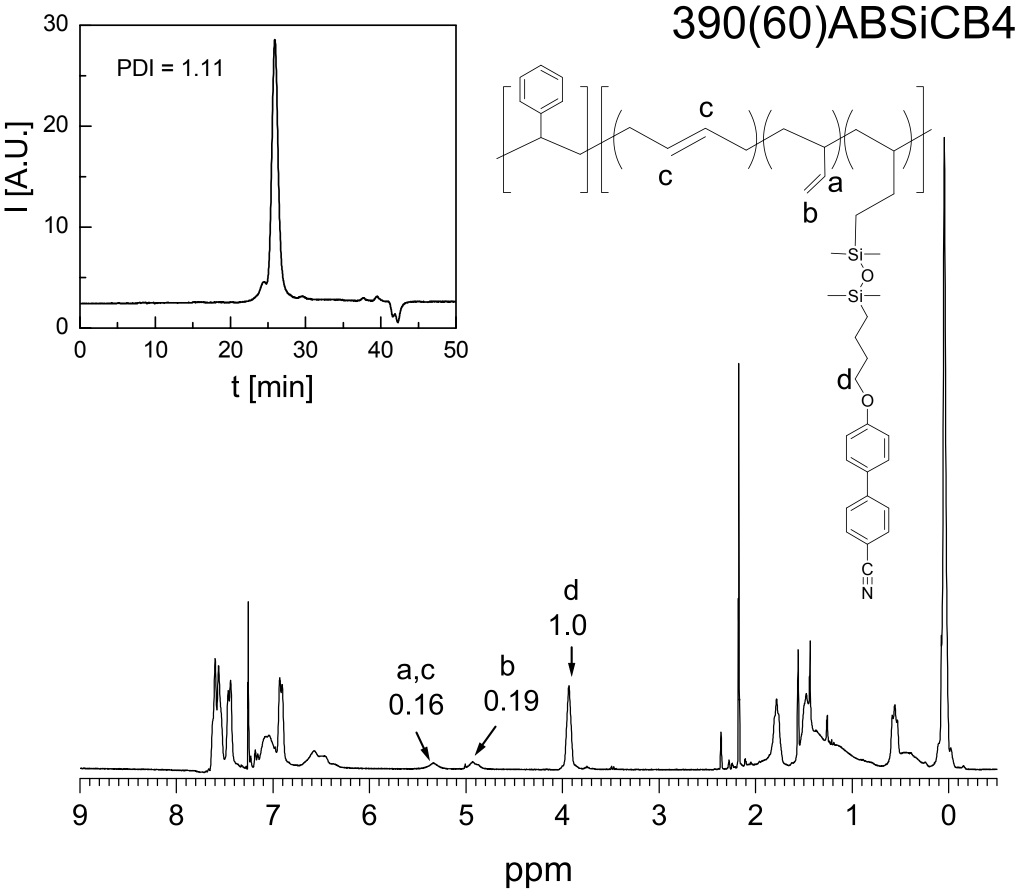

Figure A.21 300 MHz proton NMR spectrum of 390(60)ABSiCB4, a PS-SGLCP diblock copolymer synthesized from 60(60)AB, in $CDCl_3$. Peak labels include the relative intensity (integrated area) and their assignments. This data was used to calculate the polymer composition and molecular weight of the SGLCP block reported in Table A.6. The GPC chromatograph used to measure polydispersity is shown in the inset.

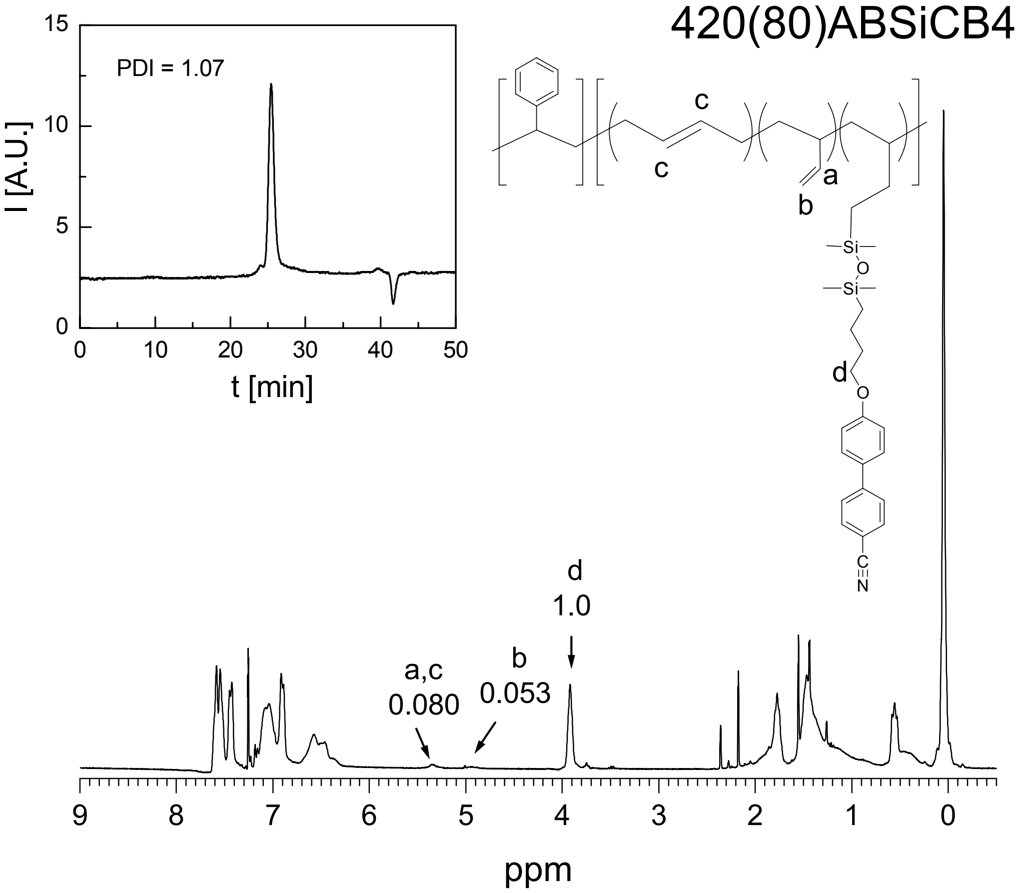

Figure A.22 300 MHz proton NMR spectrum of 420(80)ABSiCB4, a PS-SGLCP diblock copolymer synthesized from 60(80)AB, in $CDCl_3$. Peak labels include the relative intensity (integrated area) and their assignments. This data was used to calculate the polymer composition and molecular weight of the SGLCP block reported in Table A.6. The GPC chromatograph used to measure polydispersity is shown in the inset.

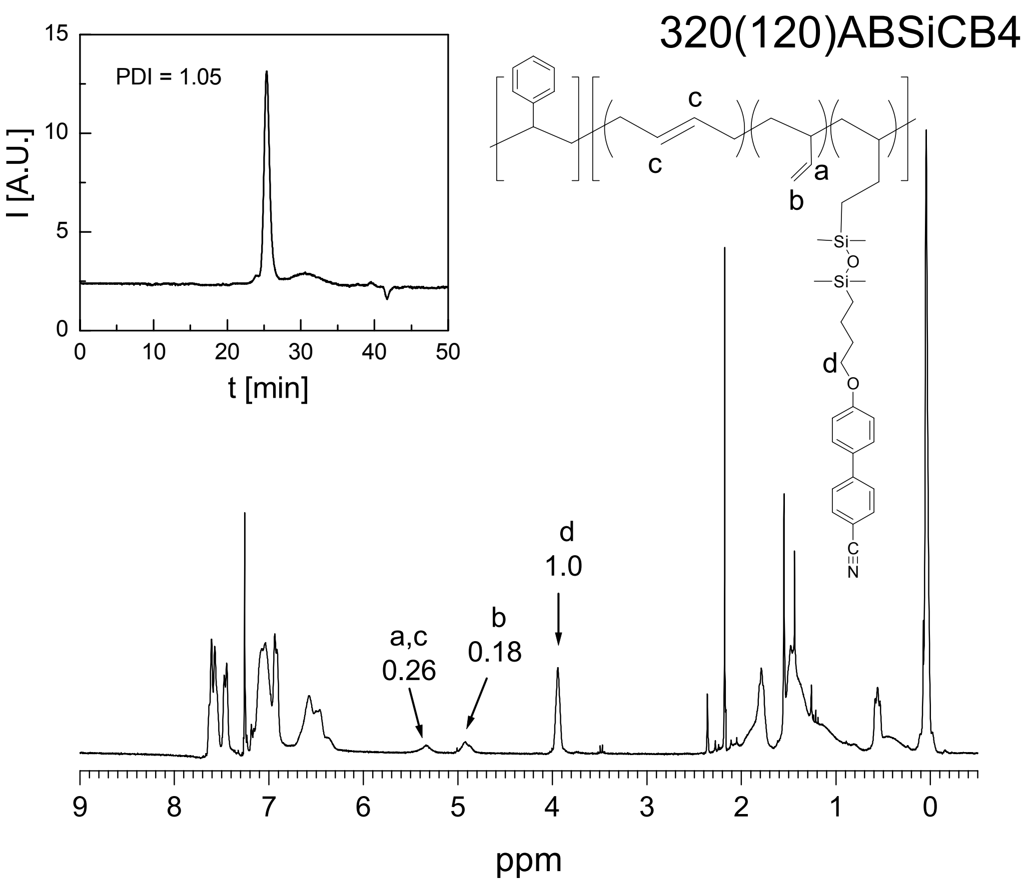

Figure A.23 300 MHz proton NMR spectrum of 320(120)ABSiCB4, a PS-SGLCP diblock copolymer synthesized from 50(120)AB, in $CDCl_3$. Peak labels include the relative intensity (integrated area) and their assignments. This data was used to calculate the polymer composition and molecular weight of the SGLCP block reported in Table A.6. The GPC chromatograph used to measure polydispersity is shown in the inset.

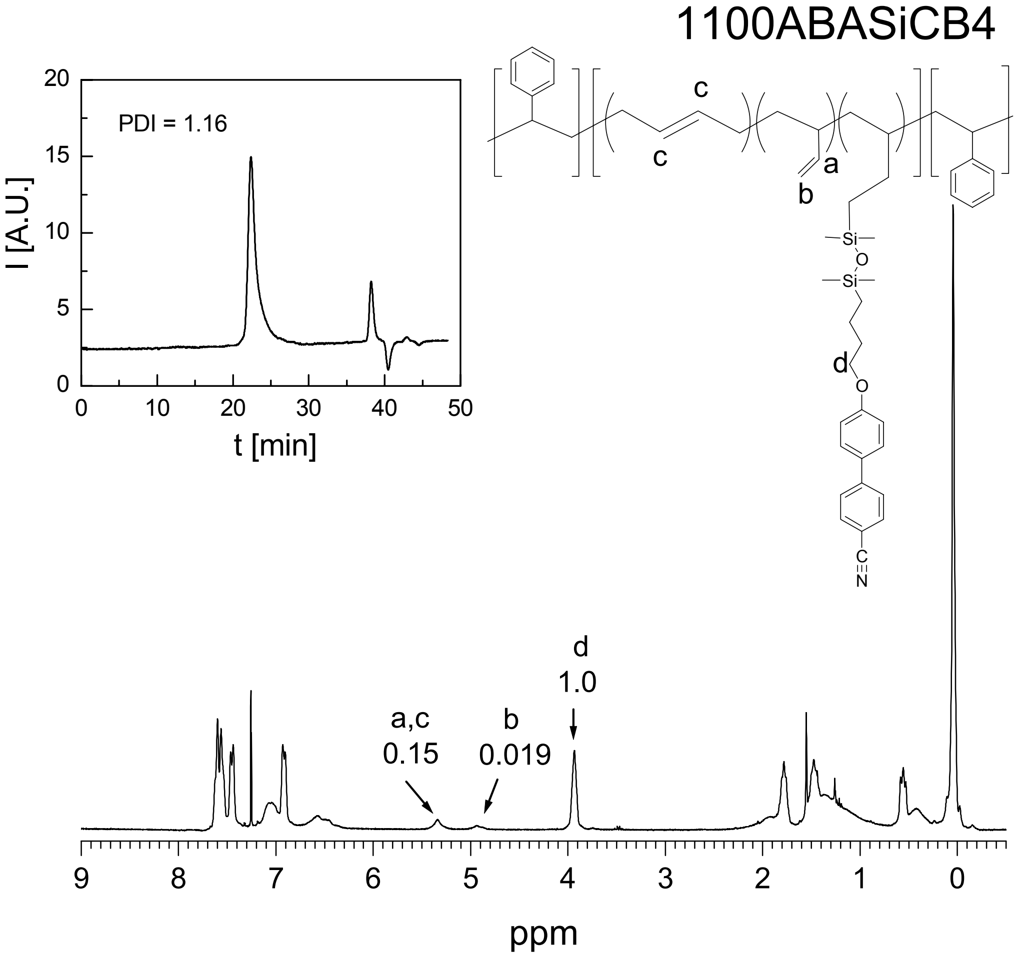

Figure A.24 300 MHz proton NMR spectrum of 1100ABASiCB4, a PS-SGLCP-PS triblock copolymer synthesized from (60)150(70)ABA, in $CDCl_3$. Peak labels include the relative intensity (integrated area) and their assignments. This data was used to calculate the polymer composition and molecular weight of the SGLCP block reported in Table A.7. The GPC chromatograph used to measure polydispersity is shown in the inset.

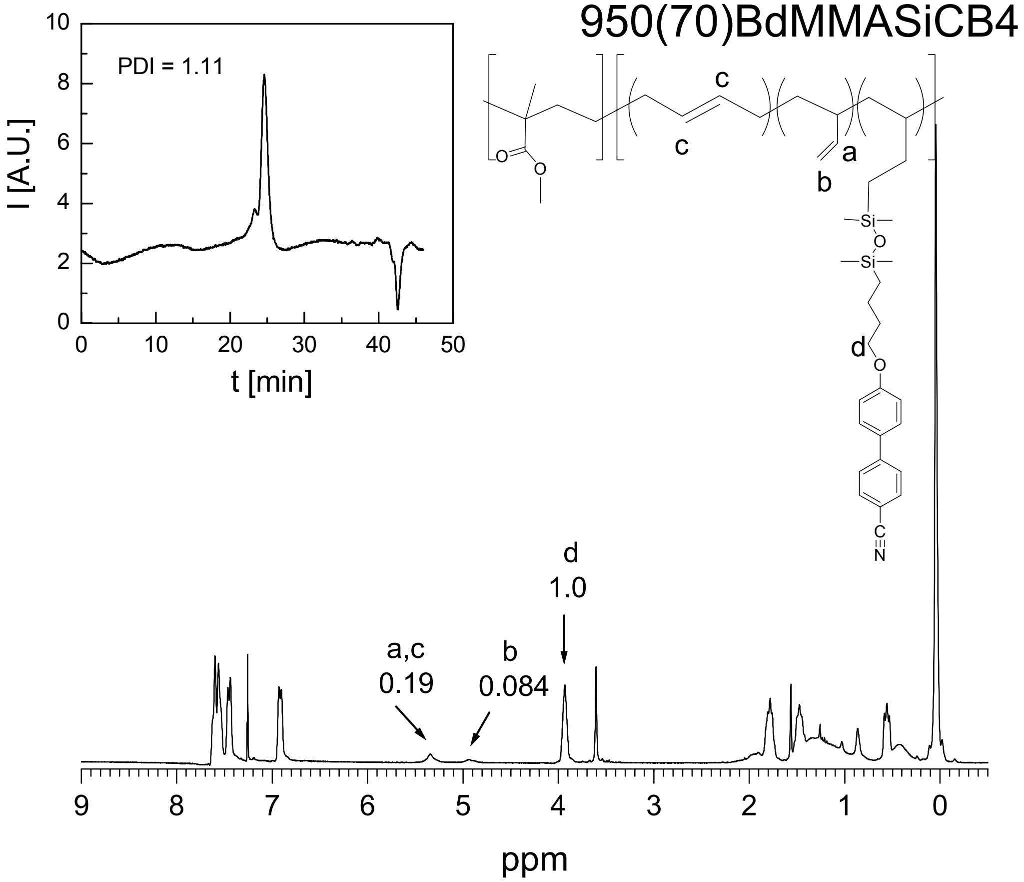

Figure A.25 300 MHz proton NMR spectrum of 950(70)BdMMASiCB4, a PMMA-SGLCP diblock copolymer synthesized from 140(70)BdMMA, in $CDCl_3$. Peak labels include the relative intensity (integrated area) and their assignments. This data was used to calculate the polymer composition and molecular weight of the SGLCP block reported in Table A.8. The GPC chromatograph used to measure polydispersity is shown in the inset.

A.5 References

[1] Lepore, S. D.; He, Y. Use of Sonication for the Coupling of Sterically Hindered Substrates in the Phenolic Mitsunobu Reaction. *J. Org. Chem.* **2003**, *68*, 8261-8263.

[2] Mitsunobu, O. The Use of Diethyl Azodicarboxylate and Triphenylphosphine in Synthesis and Transformation of Natural Products. *Synthesis* **1981**, *1*, 1-28.

[3] Kempe, M. D.; Verduzco, R.; Scruggs, N. R.; Kornfield, J. A. Rheological study of structural transitions in triblock copolymers in a liquid crystal solvent. *Soft Matter* **2006**, *2*, 422-431.

[4] Kempe, M. D. Rheology and dynamics of side-group liquid crystalline polymers in nematic solvents. Ph.D. Thesis, California Institute of Technology, Pasadena, CA,

[5] van Hest, J. C. M.; Kiick, K. L.; Tirrell, D. A. Efficient Incorporation of Unsaturated Methionine Analogues into Proteins in Vivo. *J. Am. Chem. Soc.* **2000**, *122*, 1282-1288.

[6] Ren, X. F.; Turos, E.; Lake, C. H.; Churchill, M. R. Regiochemical and Stereochemical Studies on Halocyclization Reactions of Unsaturated Sulfides. *J. Org. Chem.* **1995**, *60*, 6468-6483.

Appendix B

ISOTOPIC LABELLING FOR SANS AND NMR

B.1 Appendix 231

B.2 Schemes 234

B.3 Figures 235

B.4 References 237

B.1 Appendix

All reagents were purchased and used as received from Aldrich, unless otherwise noted.

B.1.1 Synthesis of Perdeuterated 4-Pentyl-4′-Cyanobiphenyl (d_{19}5CB)

Using the same method employed by Michael Kempe[1, 2], a platinum-catalyzed deuterium exchange is used to perdeuterate 4-pentylbiphenyl (5B) (Scheme B.1).[3] 5B (20 mL, purchased from TCI America and used as received) is combined with deuterium oxide (D_2O, 20 mL), platinum black (400 mg), and a piece of aluminum foil (approximately 2 cm^2) in a high-pressure, Teflon-lined reaction vessel. The vessel is mounted on a rotating arm inside an oven, where it is continually agitated and held at a temperature between 170 and 200 °C. Approximately once every seven days, the vessel is removed from the oven and, after cooling to room temperature, it is opened and the water inside is replaced with fresh D_2O. At this time, a small sample of 5B is taken and the deuterium content is measured by NMR spectroscopy: a proton NMR spectrum is collected from a solution containing known quantities of 5B (~ 100 mg) and DCM (~ 1 mg) in deuterated chloroform ($CDCl_3$) and the DCM peak is used as a standard to calculate the degree of deuteration.

The process is repeated for approximately eight weeks until a high degree of deuterium substitution is achieved, typically 95 mol %.

After completing the deuterium substitution, perdeuterated 5B (d_{20}5B) is converted to perdeuterated 4-pentyl-4-cyanobiphenyl (d_{19}5CB) in two steps (Scheme B.1). First, d_{20}5B (26 g, 110 mmol) is reacted with one equivalent of elemental bromine (5.4 mL, 110 mmol) catalyzed by $FeBr_3$ (900 mg, 3.0 mmol). The d_{20}5B and $FeBr_3$ are dissolved together in 50 mL chloroform then Br_2 is added dropwise at room temperature. The mixture is allowed to stir at room temperature for 30 minutes after completing the Br_2 addition. The product, perdeuterated 4-pentyl-4-bromobiphenyl (d_{19}5BBr), is precipitated with water, filtered, and dried. The dry product is recrystallized from hot hexane (200 mL heated to 40 °C), achieving 31% yield overall (11 g, 34 mmol). Next, d_{19}5BBr is reacted with potassium cyanide to yield the final product, d_{19}5CB. A palladium catalyst ($Pd(TPP)_2$) is synthesized by dissolving palladium II acetate ($Pd(OAc)_2$, 180 mg, 0.80 mmol) together with triphenyl phosphine (TPP, 420 mg, 1.6 mmol) in 40 mL anhydrous toluene and heated at 50 °C until the mixture turns bright red. The remaining reagents are then added directly to the catalyst solution: d_{19}5BBr (1.8 g, 5.5 mmol), KCN (360 mg, 5.5 mmol), and the phase-transfer catalyst *N*, *N*, *N′*, *N′*-tetramethylethylenediamine (TMEDA, 160 μL, 1.1 mmol), which promotes the solubility of KCN in organic solvent.[4] The reaction flask is purged with inert gas, then sealed and heated at 90 °C for approximately 18 hours. The product is purified on a silica gel column using 1% ethyl acetate in hexane as the mobile phase, and the typical yield is approximately 75%. The d_{19}5CB is often repeatedly fractionated on a silica gel column and fractions having very low nematic-isotropic transition temperatures (T_{NI}) are discarded. The T_{NI} of the final product, obtained by combining d_{19}5CB from several separate syntheses, is usually between 32.0 and 33.5 °C, slightly below that of hydrogenous 5CB ($T_{NI} = 35$ °C). The deuterium content of d_{19}5CB is measured by proton NMR in the same way as for d_{20}5B (Figure B.1).

B.1.2 Synthesis of Deuterium-Labeled 4-Cyano-4′-hydroxybiphenyl (d_2CHB)

Deuterium atoms are incorporated into 4-cyano-4′-hydroxybiphenyl (CHB) by acid-catalyzed deuterium exchange.[3] A solution of deuterium bromide (DBr) and deuterium phosphate (D_3PO_4) is synthesized by dropwise addition of phosphorus tribromide (2.1g, 7.8 mmol) to D_2O (3.4g, 170 mmol) at 0 °C. Excess PBr_3 is removed from the DBr / D_3PO_4 solution by extraction with ether. The DBr / D_3PO_4 solution is added to a solution of CHB (1.9g, 9.7 mmol, purchased from TCI America and used as received) in 13 g perdeuterated acetone. The mixture is refluxed for approximately 72 hours, during which time a dark brown tar forms in the reaction flask. The product is selectively dissolved in ether and the tar separated by filtration. The ether solution is extracted repeatedly with water until the aqueous layer ceases to become yellow during washing. The ether layer is then dried with anhydrous Na_2SO_4 and the product is applied to approximately 100 mL of silica gel by evaporating the ether. The product-loaded silica gel is eluted with hexane, followed by 5% ethyl acetate in hexane, followed by 50% ethyl acetate in hexane. The waxy, orange product is purified on another silica gel column using 50% ethyl acetate in hexane as the mobile phase then recrystallized from toluene heated to 100 °C. The overall yield is approximately 20%, and the deuterium content is measured by proton NMR (Figure B.2). Deuterium-labeled CHB is attached to a polymer according to the methods described in Appendix A.

B.2 Schemes

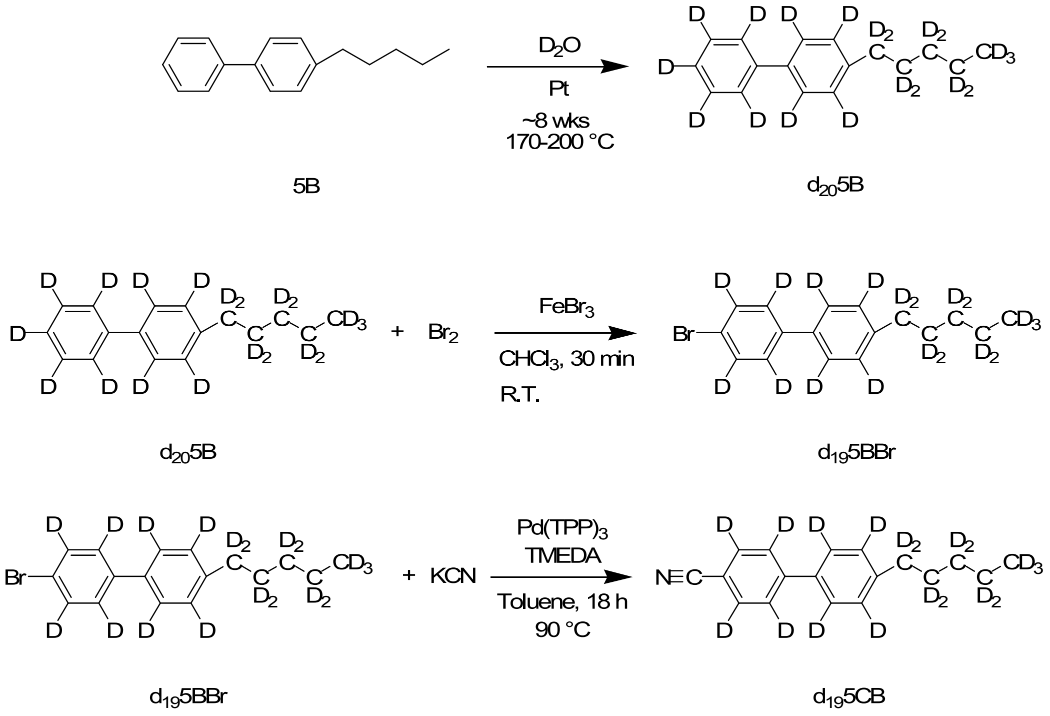

Scheme B.1 Synthesis of perdeuterated 4-pentyl-4′-cyanobiphenyl (d_{19}5CB). The hydrogen atoms of 4-pentylbiphenyl (5B) are exchanged for deuterium via platinum-catalyzed exchange with D_2O to make perdeuterated 4-pentylbiphenyl (d_{20}5B). This is then reacted with elemental bromine to make 4-pentyl-4′-bromobiphenyl (d_{19}5BBr), which is subsequently reacted with potassium cyanide to yield the product. Typically, between 90 and 95 mol % of the hydrogen atoms are replaced with deuterium in the final product.

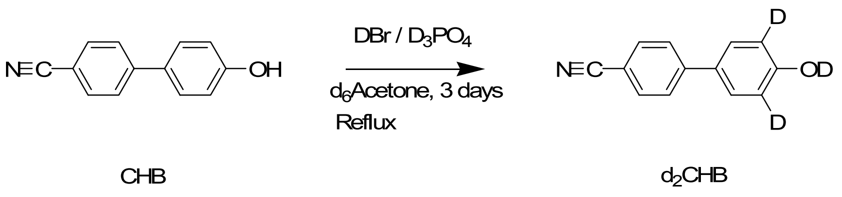

Scheme B.2 Deuterium labeling of 4-cyano-4′-hydroxybiphenyl (d_2CHB). Heating CHB in perdeuterated, acidic solution results in exchange of the hydrogens *ortho-* to the hydroxyl group.

B.3 Figures

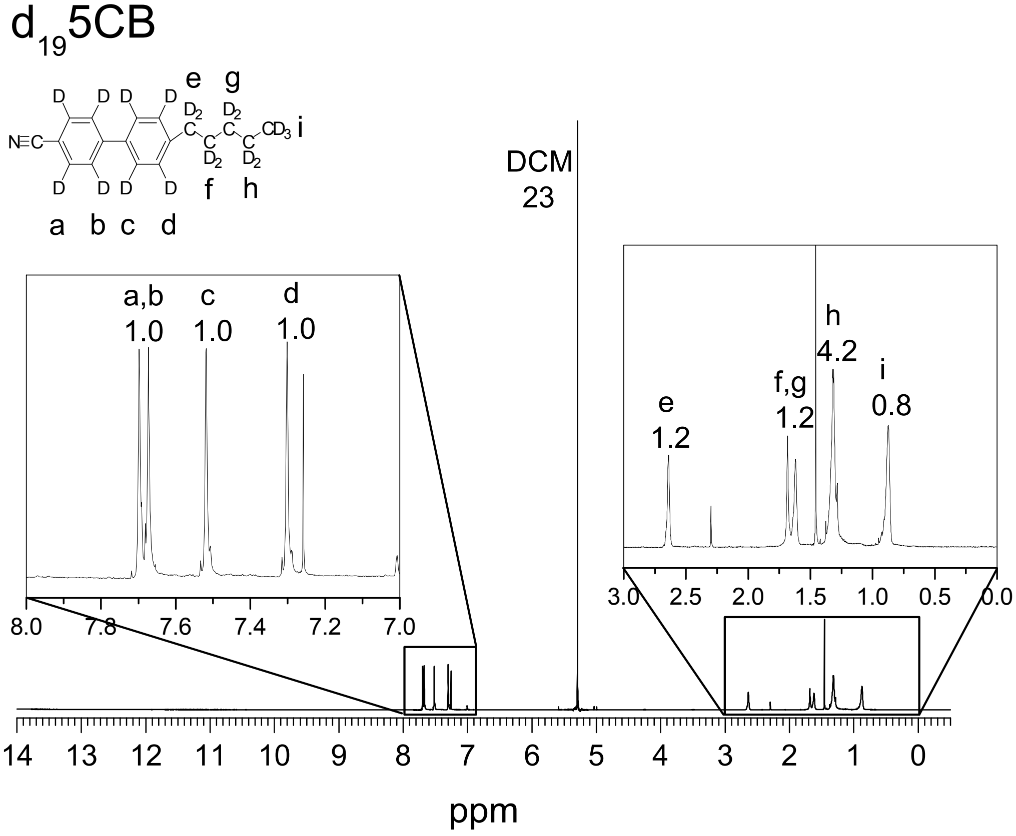

Figure B.1 300 MHz proton NMR spectrum of d_{19}5CB and dichloromethane (DCM) in $CDCl_3$ used to calculate the deuterium content. The number under each peak assignment is the relative intensity (integrated area) per mole of hydrogen at that site, taking into account the relative amounts of d_{19}5CB and DCM in the sample. The mole fraction of hydrogen at a specific site on the d_{19}5CB molecule is calculated by dividing its relative intensity by that of DCM. In this particular sample, 94 mol % of the total hydrogen atoms have been replaced with deuterium.

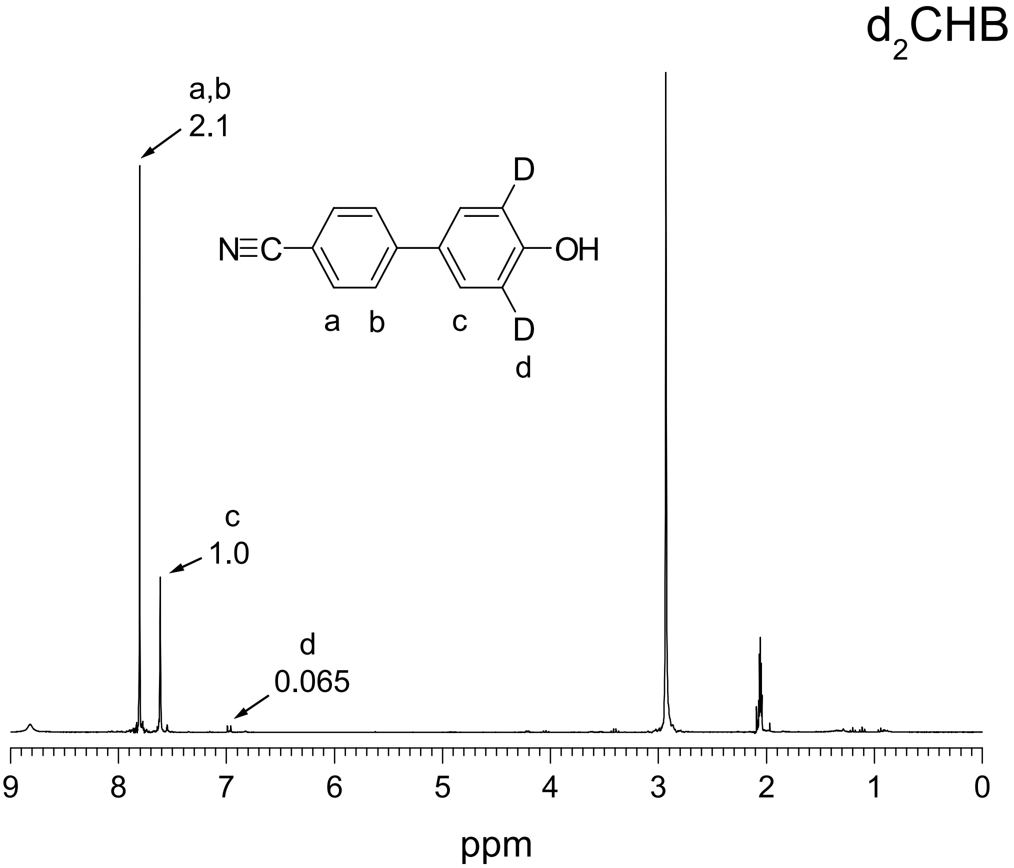

Figure B.2 300MHz proton NMR spectrum of d_2CHB in d_6-acetone. The number under each peak assignment gives the relative intensity (integrated area). The molecule's deuterium content is measured from the ratio of the peak intensity at $\delta = 7.0$ ppm to that at $\delta = 7.6$ ppm, or half that at $\delta = 7.8$ ppm. In this case, 94 mol % of the hydrogen atoms in the position *para-* to the hydroxyl group have been replaced with deuterium.

B.4 References

[1] Wu, S. T.; Wang, Q. H.; Kempe, M. D.; Kornfield, J. A. Perdeuterated cyanobiphenyl liquid crystals for infrared applications. *J. Appl. Phys.* **2002**, *92*, 7146-7148.

[2] Kempe, M. D. Rheology and dynamics of side-group liquid crystalline polymers in nematic solvents. Ph.D. Thesis, California Institute of Technology, Pasadena, CA,

[3] Thomas, A. F. *Deuterium Labeling in Organic Chemistry*, Appleton-Century-Crofts: New York, 1971.

[4] Sundermeier, M.; Zapf, A.; Beller, M. Palladium-Catalyzed Cyanation of Aryl Halides: Recent Developments and Perspectives. *Eur. J. Inorg. Chem.* **2003**, *19*, 3513-3526.

Appendix C

FITTING SANS DATA FROM COIL-LIQUID CRYSTALLINE DIBLOCK COPOLYMER SOLUTIONS

C.1 Appendix 238

C.2 Tables 246

C.3 Figures 247

C.4 References 253

C.1 Appendix

Small-angle neutron scattering (SANS) data from solutions of diblock copolymers having a side-group liquid crystal polymer (SGLCP) block and a random-coil polymer (polystyrene, PS) in a small-molecule liquid crystal (LC) solvent is presented in Chapter 3. The diblock copolymers self-assemble in LC solvent to form micelles composed of PS-rich cores surrounded by SGLCP-rich coronas. Extensive efforts were made to fit the SANS data to structural models in order to extract parameters such as the core radius, the corona thickness, and the aggregation number, but the results are inconclusive. This appendix details the successes and failures of the data-fitting methods used.

C.1.1 Theory of Scattering from Block Copolymer Micelles

The differential scattering cross-section, $\partial\Sigma/\partial\Omega(q)$, from a solution of N mondisperse, spherically symmetric particles of volume V and with neutron scattering contrast $(\Delta\rho)^2$ is given by the product of a form factor, $P(q)$, and a structure factor $S(q)$:

$$\frac{\partial\Sigma}{\partial\Omega}(q) = N(\Delta\rho)^2 V^2 P(q) S(q), \tag{C.1}$$

where $q = 4\pi/\lambda \sin(\theta_s / 2)$ is the magnitude of the scattering vector at an angle, θ_s.[1, 2] The form factor accounts for intra-particle scattering and depends on the shape and composition of the particle. The structure factor accounts for interference between particles and depends on the inter-particle potential. In the case of a solution of polydisperse, interacting particles, a decoupling approximation[3] may be used to write the scattered intensity

$$\frac{\partial \Sigma}{\partial \Omega}(q) = N(\Delta\rho)^2 V^2 P(q)[1 + \beta(q)(S(q) - 1)], \tag{C.2}$$

where $\beta(q)$ is a factor between 0 and 1 that dampens the structure factor oscillations. Interparticle interference becomes negligible when the volume fraction of particles is very small or when particles are correlated on length scales much larger than q. In this case, $S(q) = 1$ and the differential scattering cross-section from a solution of uncorrelated particles, whether monodisperse or polydisperse, is simply

$$\frac{\partial \Sigma}{\partial \Omega}(q) = N(\Delta\rho)^2 V^2 P(q). \tag{C.3}$$

Numerous form factors are available for modeling block copolymer micelles with varying levels of structural detail (Figure C.1). In the simplest case, a micelle may be modeled as a spherical core of homogeneous scattering length density surrounded by a concentric shell of homogeneous scattering length density (Figure C.1a).[4, 5] This model is extended to anisotropic micelles by using ellipsoidal or cylindrical cores and shells, for examples (Figure C.1b,c).[5] More detailed models take into account the polymeric nature of the material in the shell and treat the micelle as a homogeneous core with chains attached to the surface (Figure C.1d)[6, 7] or account for a radial density profile of the polymer in the shell (Figure C.1e).[8-10] These models are extended to anisotropic micelles, as well.[11] Choosing a very detailed form factor can yield more structural information about the micelles, but it also introduces an increasing number of fitting parameters and requires increasingly high-resolution scattering experiments to be confident in the physical significance of the resulting fit. In practice, one narrows the field to physically realistic form factors for the system of interest then chooses the simplest one that can be used to fit the data with consistency between different samples.

The structure factor most commonly employed for block copolymer micelles is the Percus-Yevick model for hard spheres[12, 13] because fits to SANS data are usually equally good regardless of the interparticle potential invoked.[5] For example, Castelletto, Hamley, and Pedersen[14] found that highly swollen micelles formed the BCC lattice expected for soft spheres, but the scattering was equally well modeled with the hard-sphere structure factor as with the soft-sphere structure factor. The Percus-Yevick model is, therefore, preferred because it is one of the few structure factors that can be calculated analytically, thus saving computing time.

Polydispersity of particle size and the limitations of instrumental resolution[15] cause smearing of the intensity profile, and these effects must be accounted for when modeling experimental data. The distribution of block copolymer micelle radii, R, is typically modeled with a Schultz distribution:[3, 4]

$$n(R) = \frac{\left(\dfrac{\mu+1}{\langle R\rangle}\right)^{\mu+1} R^{\mu} \exp\left[-\left(\dfrac{\mu+1}{\langle R\rangle}\right)R\right]}{\Gamma(\mu+1)} \tag{C.4}$$

$$\mu = \frac{\left(1 - \beta^2 \big/ \langle R\rangle^2\right)}{\beta^2 \big/ \langle R\rangle^2},$$

where n is the population of micelles with radius R, $\langle R\rangle$ is the average radius, β is a width parameter, and Γ denotes the gamma function. Applying this distribution to the differential scattering cross-section from uncorrelated micelles (Equation C.3) gives:

$$\frac{\partial\Sigma}{\partial\Omega}(q) = \int_0^{\infty} n(R) N (\Delta\rho)^2 V^2 P(q,R)\, dR\,; \tag{C.5}$$

higher-order corrections must be made when $S(q) \neq 1$.[3, 5] The instrument used to measure the scattering pattern has a particular resolution function, $\sigma(q)$, that must be applied to simulate experimentally measured data. The resolution-smeared differential scattering cross-section, $\partial\Sigma/\partial\Omega(q)_{smeared}$, is

$$\frac{\partial \Sigma}{\partial \Omega}(q)_{smeared} = \frac{\int_0^\infty \frac{\partial \Sigma}{\partial \Omega}(q')\exp\left[-\frac{(q'-q)^2}{2\sigma(q)^2}\right]dq'}{\int_0^\infty \exp\left[-\frac{(q'-q)^2}{2\sigma(q)^2}\right]dq'}. \tag{C.6}$$

C.1.2 Fitting Scattering Data from PS-SGLCP Diblock Copolymer Micelles with the Spherical Core-Shell Form Factor Including Polydispersity and Instrumental Smearing

In practice, the experimentally measured intensity, $I(q)$, is not necessarily in absolute units. $I(q)$ is assumed to be proportional to $\partial\Sigma/\partial\Omega(q)$ and the proportionality constant is lumped together with the product $N(\Delta\rho)^2V^2$ into an overall multiplicative factor, K. Physical parameters are extracted from the data by hypothesizing a form factor and structure factor then using least-squares algorithms to determine the model parameters that give the best fit to the experimental data.[5]

The structure factor was found to make a negligible contribution to the scattering from coil-SGLCP diblocks dissolved in LC solvent. The peaks often observed at low q are insensitive to concentration, in opposition to the strong concentration dependence predicted by the hard-sphere structure factor model. Indeed, in a series of diblock solutions ranging from 2 to 20 wt % polymer, the peak positions do not change with concentration and the maximum intensity (normalized by concentration) varies by less than 40%, implying that $S(q)$ is, at most, 1.4.[16] These structure factor contributions are ignored and scattering patterns are modeled as the product of a form factor and a multiplicative constant.

The spherical core-shell form factor for coil-SGLCP diblock micelles is derived in Appendix D to be

$$\frac{1}{f_{PS}^2}P(q) = \left[V_c^2 K_c \psi_c^2 + 2V_c V_s K_{cs}\psi_c\psi_s + V_s^2 K_s \psi_s^2\right], \tag{C.7}$$

where

$$\psi_x = \frac{3[\sin(qR_x) - qR_x \cos(qR_x)]}{(qR_x)^3},$$

$$K_c = \left[(\rho_{PS} - \rho_{d_{19}5CB}) - \frac{v_{LCP}}{v_{PS}} \frac{R_c^3}{R_s^3 - R_c^3} (\rho_{LCP} - \rho_{d_{19}5CB}) \right]^2,$$

$$K_{cs} = \left[(\rho_{PS} - \rho_{d_{19}5CB}) - \frac{v_{LCP}}{v_{PS}} \frac{R_c^3}{R_s^3 - R_c^3} (\rho_{LCP} - \rho_{d_{19}5CB}) \right] \left[\frac{v_{LCP}}{v_{PS}} \frac{R_c^3}{R_s^3 - R_c^3} (\rho_{LCP} - \rho_{d_{19}5CB}) \right],$$

and

$$K_s = \left[\frac{v_{LCP}}{v_{PS}} \frac{R_c^3}{R_s^3 - R_c^3} (\rho_{LCP} - \rho_{d_{19}5CB}) \right]^2.$$

Equation C.7 contains only two adjustable parameters: R_c and R_s, the radius of the core and overall micelle, respectively (Figure C.1a). ρ_{PS}, ρ_{LCP}, and $\rho_{d_{19}5CB}$ denote the scattering length densities of pure PS, SGLCP, and d$_{19}$5CB, respectively, while v_{PS} and v_{LCP} denote the volumes of one polystyrene block and one SGLCP block, respectively. The scattering length densities are listed in Table D.1 and the polymer volumes are calculated from the molecular weights and the densities listed in Table D.1. Keeping the ratio of R_s / R_c constant, a Schultz distribution (Equation C.4) of core sizes is used to calculate the unsmeared intensity with Equation C.5 and Equation C.7, absorbing the volume fraction of PS in the core, f_{PS}, into a constant $K' = K / f_{PS}^2$. A Lorentzian describing the monomer-level scattering of a polymer with correlation length ξ is added to describe the high-q scattering:

$$I(q) = \frac{K_L}{\left(1 + (q\xi)^2\right)}, \tag{C.8}$$

where K_L is a weighting factor for this term. Equation C.8 was used to model scattering from SGLCP homopolymers in Chapter 5. The total intensity is smeared with the resolution function of the Small-Angle Scattering Instrument (SASI) at Argonne National Laboratory's Intense Pulsed Neutron Source, which has been previously reported[17] and is interpolated for numeric integration with a sixth degree polynomial (Figure C.2). In summary, the total calculated intensity is

$$I(q)=\frac{\int_0^\infty\left[\int_0^\infty n(R_c)K'P(q',R_c)dR_c+\frac{K_L}{\left(1+(q'\xi)^2\right)}\right]\exp\left[-\frac{(q'-q)^2}{2\sigma(q)^2}\right]dq'}{\int_0^\infty\exp\left[-\frac{(q'-q)^2}{2\sigma(q)^2}\right]dq'}+I_{inc} \qquad \text{(C.9)}$$

with $K' = K / f_{PS}^2$, $n(R_c)$ given by Equation C.4, and $P(q, R_c)$ given by Equation C.7. I_{inc} accounts for q-independent background scattering. Least-squares fitting of Equation C.9 to the experimental scattering patterns is performed with WaveMetrics IGOR Pro® using procedures available from the NIST Center for Neutron Research,[18, 19] modified to include Equation C.7.

SANS patterns are well-described by Equation C.9 (Figure C.3), and the fits give values of R_c and R_s (Figure C.4 and Figure C.5). Least-squares fitting was initially performed allowing all the variables, K', R_c, R_s, β, K_L, ξ, and I_{inc}, to float freely. A second round of data fitting was performed at fixed polydispersities, $p = (1+\beta)^{-1/2}$. The quality of fit changes with p, but the values of R_c and R_s are insensitive to this parameter. Mean values of R_c and R_s (such as those reported in Figure C.4 and Figure C.5) are calculated by averaging R_c and R_s values obtained from fits with p fixed at various values between 0.01 and 0.45. The average is weighted by the sum of the square of the residuals, χ^2, between the fit and the experimental data.

C.1.3 Checking Fits for Self-Consistency and Physical Significance

The length scales extracted from fits to Equation C.9 must be checked for realism and self-consistency. The aggregation number, N_{agg}, is related to R_c and f_{PS} by

$$N_{agg}=\frac{f_{PS}\,{}^4\!/_3\,\pi R_c^3}{v_{PS}}, \qquad \text{(C.10)}$$

allowing an upper limit on N_{agg} to be estimated assuming the core is solvent-free ($f_{PS} = 1$). An upper limit on N_{agg} may also be estimated from the thickness of the shell, using the analogous relation,

$$N_{agg}=\frac{f_{LCP}\,{}^4\!/_3\,\pi\left(R_s^3-R_c^3\right)}{v_{LCP}}, \qquad \text{(C.11)}$$

and assuming the shell is solvent-free ($f_{LCP} = 1$). The upper limits on N_{agg} for 5 wt % diblock solutions in Figure C.4, estimated from Equations C.10 and C.11, jar the intuition (Table C.1). Qualtitative trends in the micelle sizes and aggregation numbers for 5 wt % diblock solutions are in agreement with the conclusions drawn from the raw data (Chapter 3). N_{agg} increases with the size of the PS block (Figure C.4) and decreases with increasing temperature (Figure C.5). However, the values of N_{agg} estimated for the core and corona are not consistent with one another. The corona is expected to be highly swollen with solvent, and the upper limit of N_{agg} estimated from Equation C.11 should, therefore, be much larger than that estimated from Equation C.10, but the data show the opposite trend: N_{agg} estimated from the shell dimension is, at most, 50% of that estimated from the core. In the physically unrealistic case that the corona is composed of pure SGLCP, these values of N_{agg} would require between 50 and 70% of the core's volume to be occupied by solvent (Table C.1). In a more realistic scenario, if the volume fraction of SGLCP in the shell is 0.5, the core would have to be composed of more than 70% solvent (Table C.1).

A fundamental assumption of the core-shell model may be responsible for the discrepancy between N_{agg} estimated from the core and the corona. In applying this model it was assumed that there is a well-defined interface between the surface of the micelle and a matrix composed of pure d_{19}5CB. In reality, one expects the volume fraction of SGLCP in the corona to decay with increasing distance from the core.[20-22] The high-density layer of polymer immediately adjacent to the core surface may constitute and effective shell in an effective matrix of SGLCP/d195CB solution; this phenomenon has been observed before in aqueous solutions of PEO-PPO-PEO micelles.[23] A better model for PS-SGLCP micelles may be a core-shell model with a density profile (Figure C.1e), but attempts to fit the data with such models fail because the selection of a functional form for the density decay is arbitrary and introduces additional fitting parameters.[9] Since equality of the aggregation number in the core and shell was imposed in deriving the form factor (Appendix D), the accuracy of R_c derived from the core-shell model relies on the accuracy of the shell thickness and both length scales are therefore suspect.

Confidence in the extracted length scales is further called into doubt by the observation that different form factors can provide equally good fits to the data (Figure C.6). The form factor for a homogenous cylinder with radius of 185 Å and length of 545 Å provides a description of data from 5 wt % 320(120)ABSiCB4 just as well as the spherical core-shell model. Without data from monodomain samples it is impossible to determine whether an anisotropic model is more appropriate for these micelles. Even if this were the case, models for elliptical core-shell structures are extremely difficult to fit because there are twice as many length scales involved (Figure C.1b).

C.1.4 Conclusions

SANS data from solutions of PS-SGLCP diblock copolymer micelles can be fit with a spherical core-shell model, but the length scales extracted from the fits are highly suspect. The corresponding aggregation numbers estimated for the core and shell are inconsistent with one another and the radial density profile of SGLCP in the corona that likely exists is not considered at all by the model. Furthermore, it is unknown whether a spherical model is even appropriate for these micelles; the orientation of the LC solvent probably causes them to adopt anisotropic forms.[24, 25]

The limited range of scattering vectors is, perhaps, the biggest obstacle standing in the way of extracting meaningful length scales from this data. The size of these micelles is greater than 150 Å according to every form factor that was attempted. To get unambiguous fits to a form factor, plenty of data should be available in a range of $q < L^{-1}$, where L is the characteristic length scale. The minimum value of q that was accessed in these experiments is 0.00666 Å^{-1}, giving *q equal* to L^{-1} at best. Perhaps data fitting would be more successful if the experiments were repeated at a facility giving access to lower values of q (e.g., the NIST Center for Neutron Research or, perhaps, a small-angle x-ray scattering beamline).

C.2 Tables

Table C.1 Upper bounds on the aggregation number (N_{agg}) in 5 wt % solutions of diblock copolymers estimated from the size of the core using Equation C.10 and from the size of the shell using Equation C.11. The volume fraction of polystyrene in the core (f_{PS}) is estimated from N_{agg} of the shell for two cases: a shell composed of pure SGLCP (f_{LCP} = 1.0) and a shell composed of 50% SGLCP and 50% solvent (f_{LCP} = 0.5).

Polymer	Max N_{agg} (core)	Max N_{agg} (shell)	f_{PS} (f_{LCP} = 1.0)	f_{PS} (f_{LCP} = 0.5)
470(40)ABSiCB4	210	58	0.52	0.14
390(60)ABSiCB4	240	95	0.34	0.20
420(80)ABSiCB4	2200	760	0.40	0.17
320(120)ABSiCB4	4200	2200	0.27	0.26

C.3 Figures

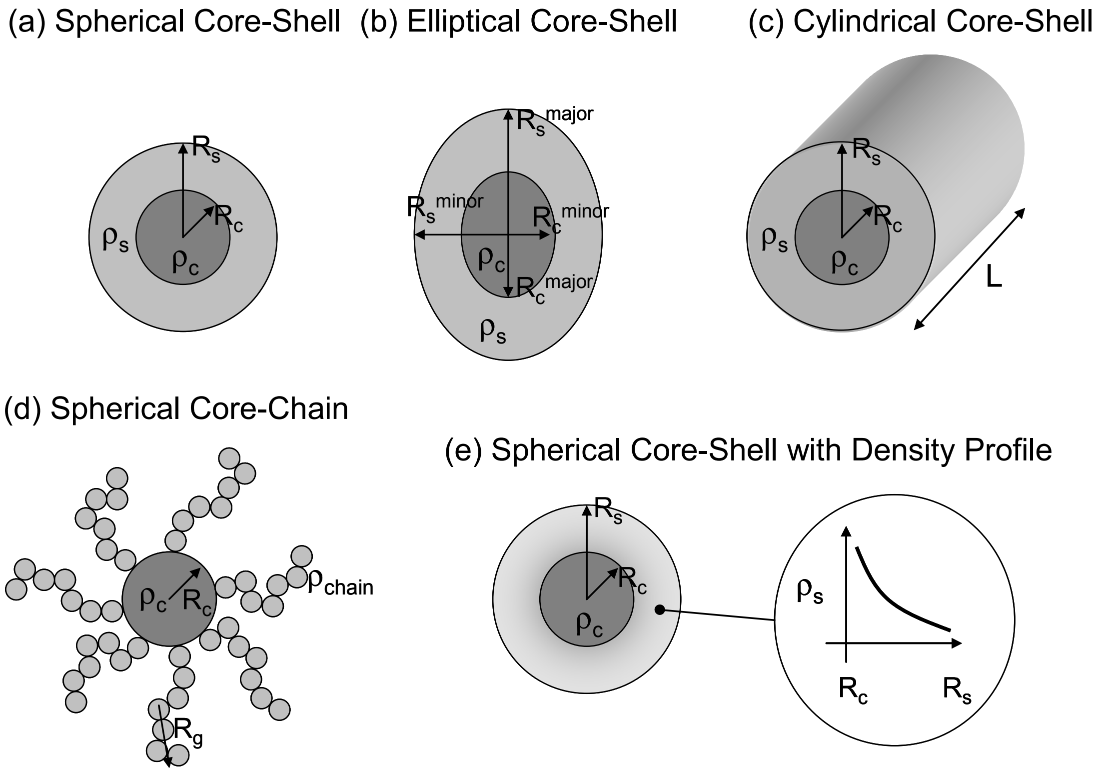

Figure C.1 Schematic drawings of examples of structural models that may be used to calculate form factors of block copolymer micelles. These examples all assume a core of radius R_c with homogenous neutron scattering length density, ρ_c. (a,b,c,e) The core-shell models assume the core is surrounded by a concentric shell with scattering length density ρ_s such that the overall micelle's radius is R_s. (d) In the core-chain model, the core is surrounded by a corona of polymer chains having neutron scattering length density ρ_{chain} and radii of gyration R_g.

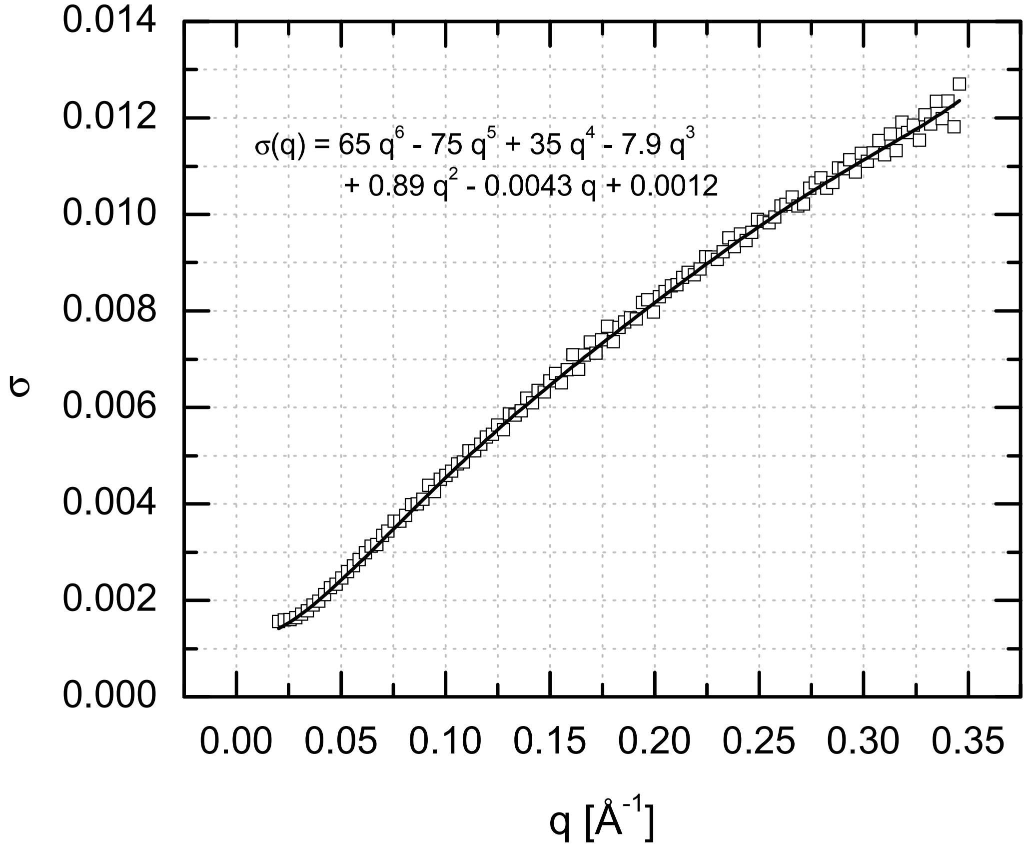

Figure C.2 Resolution function of the Small-Angle Scattering Instrument (SASI) at Argonne National Laboratory's Intense Pulsed Neutron Source. Experimentally determined[17] values of σ(square symbols) were interpolated with a sixth degree polynomial (line).

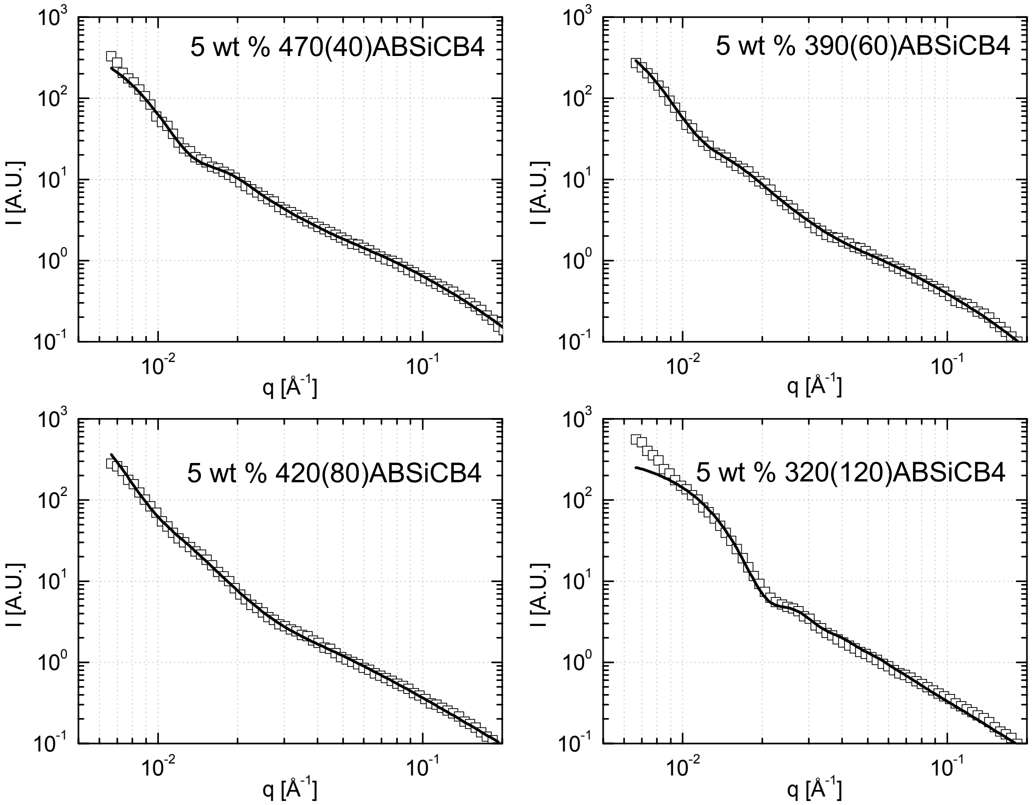

Figure C.3 Small-angle neutron scattering data from 5 wt % diblock copolymer solutions at 25 °C (square symbols) together with representative fits (lines) obtained using the spherical core-shell form factor (Equation D.9).

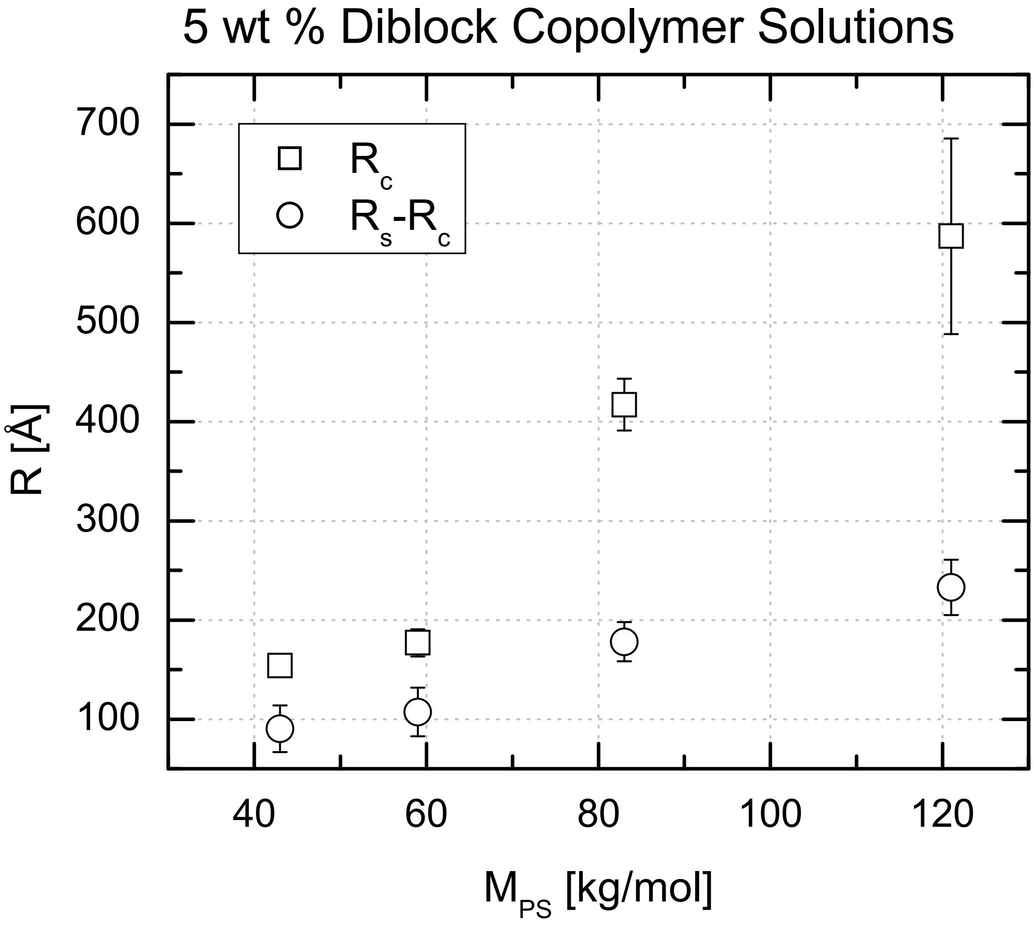

Figure C.4 Values of the core radius (R_c) and shell thickness (R_s - R_c) for 5 wt % solutions of 470(40)ABSiCB4, 390(60)ABSiCB4, 420(80)ABSiCB4, and 320(120)ABSiCB4 at 25 °C as a function of the molecular weight of the polystyrene block (M_{PS}). Values are derived from fitting neutron scattering data to the spherical core-shell model (Equation D.9). Error bars represent the standard deviation of an average from fits using different polydispersities, weighted by the fits' χ^2.

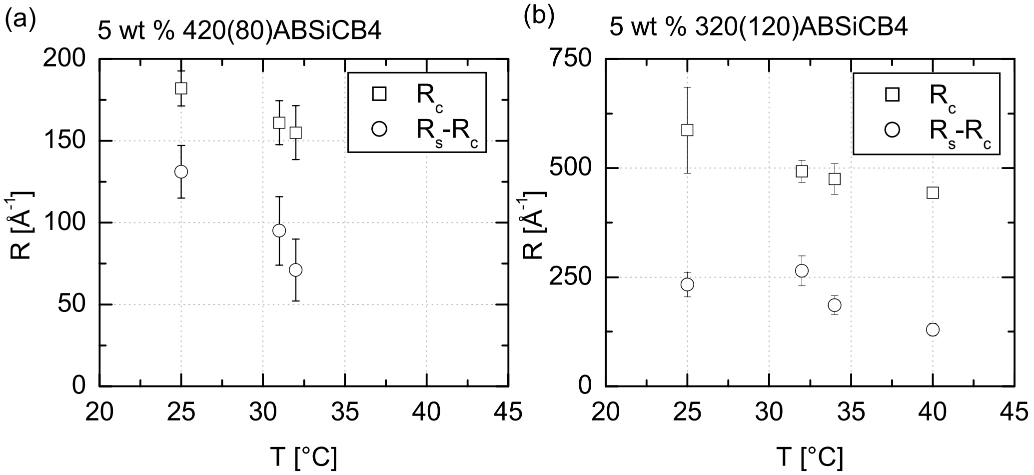

Figure C.5 Values of the core radius (*R*$_c$) and shell thickness (*R*$_s$ - *R*$_c$) for (a) 5 wt % 420(80)ABSiCB4 and (b) 5 wt % 320(120)ABSiCB4 as a function of temperature. Values are derived from fitting neutron scattering data to the spherical core-shell model (Equation D.9). Error bars represent the standard deviation of an average from fits using different polydispersities, weighted by the fits' χ^2.

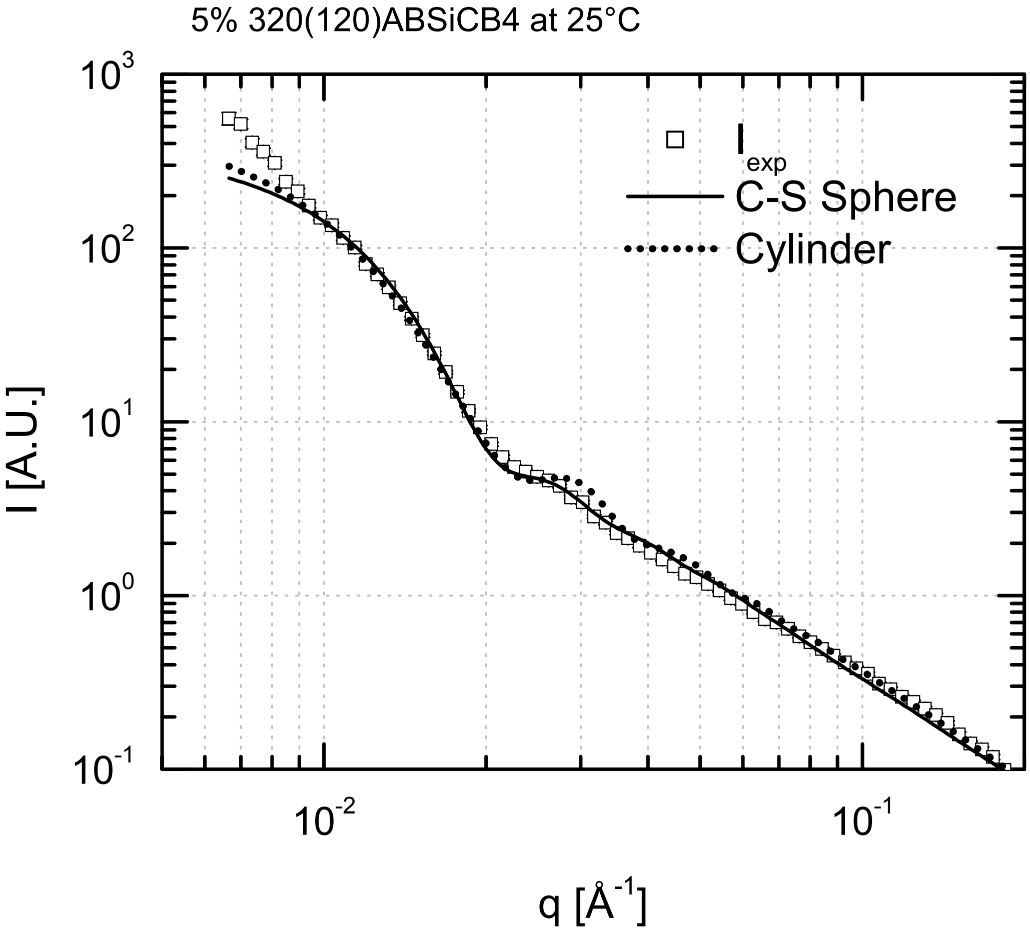

Figure C.6 Small-angle neutron scattering data from 5 wt % 320(120)ABSiCB4 at 25 °C (I_{exp}) shown together with a representative fit using the spherical core-shell model (Equation D.9) and the form factor for a cylinder of homogeneous scattering length density.

C.4 References

[1] Glatter, O.; Kratky, O., eds. *Small Angle X-Ray Scattering*. 1982, Academic Press: London.

[2] Higgins, J. S.; Benoit, H. C. *Polymers and Neutron Scattering*, Oxford Series on Neutron Scattering in Condensed Matter, ed. S.W. Lovesey; E.W.J. Mitchell; Oxford University Press: New York, NY, 1996.

[3] Kotlarchyk, M.; Chen, S.-H. Analysis of small angle neutron scattering spectra from polydisperse interacting colloids. *J. Chem. Phys.* **1983**, *79*, 2461-2469.

[4] King, S. M.; Griffiths, P. C.; Cosgrove, T. Using SANS to Study Adsorbed Layers in Colloidal Dispersions. In *Applications of Neutron Scattering to Soft Condensed Matter*; B.J. Gabrys, Editor; Gordon and Breach Science Publishers: Amsterdam, 2000.

[5] Pedersen, J. S. Analysis of small-angle scattering data from colloids and polymer solutions: modeling and least-squares fitting. *Adv. Colloid Interface Sci.* **1997**, *70*, 171-210.

[6] Pedersen, J. S.; Gerstenberg, M. C. Scattering Form Factor of Block Copolymer Micelles. *Macromolecules* **1996**, *29*, 1363-1365.

[7] Svaneborg, C.; Pedersen, J. S. Form Factors of Block Copolymer Micelles with Excluded-Volume Interactions of the Corona Chains Determined by Monte Carlo Simulations. *Macromolecules* **2002**, *35*, 1028-1037.

[8] Castelletto, V.; Hamley, I. W.; Pedersen, J. S. A small-angle neutron scattering investigation of the structure of highly swollen block copolymer micelles. *J. Chem. Phys.* **2002**, *117*, 8124-8129.

[9] Pedersen, J. S.; Svaneborg, C.; Almdal, K.; Hamley, I. W.; Young, R. N. A Small-Angle Neutron and X-ray Contrast Variation Scattering Study of the Structure of Block Copolymer Micelles: Corona Shape and Excluded Volume Interactions. *Macromolecules* **2003**, *36*, 416-433.

[10] Bang, J.; Viswanathan, K.; Lodge, T. P.; Park, M. J.; Char, K. Temperature-dependent micellar structures in poly(styrene-b-isoprene) diblock copolymer solutions near the critical micelle temperature. *J. Chem. Phys.* **2004**, *121*, 11489-11500.

[11] Pedersen, J. S. Form factors of block copolymer micelles with spherical, ellipsoidal and cylindrical cores. *J. Appl. Crystallogr.* **2000**, *33*, 637-640.

[12] Kinning, D. J.; Thomas, E. L. Hard-Sphere Interactions between Spherical Domains in Diblock Copolymers. *Macromolecules* **1984**, *17*, 1712-1718.

[13] Percus, J. K.; Yevick, G. J. Analysis of Classical Statistical Mechanics by Means of Collective Coordinates. *Phys. Rev.* **1958**, *110*, 1-13.

[14] Castelletto, V.; Hamley, I. W. Small-Angle Neutron Scattering Study of the Structure of Superswollen Micelles Formed by a Highly Asymmetric Poly(oxybutylene)-Poly(oxyethylene) Diblock Copolymer in Aqueous Solution. *Langmuir* **2004**, *20*, 2992-2994.

[15] Wignall, G. D.; Christen, D. K.; Ramakrishnan, V. Instrumental Resolution Effects in Small-Angle Neutron Scatterin. *J. Appl. Crystallogr.* **1988**, *21*, 438-451.

[16] Scruggs, N. R.; Kornfield, J. A.; Lal, J. Using the "Switchable" Quality of Liquid Crystal Solvents to Mediate Segregation between Coil and Liquid-Crystalline Polymers. *Macromolecules* **2006**, *39*, 3921-3926.

[17] Thiyagarajan, P.; Epperson, J. E.; Crawford, R. K.; Carpenter, J. M.; Klippert, T. E.; Wozniak, D. G. The Time-of-Flight Small-Angle Neutron Diffractometer (SAD) at IPNS, Argonne National Laboratory. *J. Appl. Crystallogr.* **1997**, *30*, 280-293.

[18] NIST Center for Neutron Research. *NCNR tools on the web, http://www.ncnr.nist.gov/resources/index.html*. June 30, 2003 [cited November 8 2006].

[19] NIST Center for Neutron Research. *SANS and USANS Data Reduction and Analysis with IGOR Pro, http://www.ncnr.nist.gov/programs/sans/data/red_anal.html*. August 17, 2006 [cited November 8 2006].

[20] Halperin, A. Polymeric Micelles: A Star Model. *Macromolecules* **1987**, *20*, 2943-2946.

[21] Halperin, A.; Tirrell, M.; Lodge, T. P. Tethered Chains in Polymer Microstructures. *Adv. Polym. Sci.* **1992**, *100*, 31-71.

[22] Milner, S. T. Polymer Brushes. *Science* **1991**, *251*, 905-914.

[23] Mortensen, K.; Pedersen, J. S. Structural Study of the Micelle Formation of Poly(ethylene oxide)-Poly(propylene oxide)-Poly(ethylene oxide) Triblock Copolymer in Aqueous Solution. *Macromolecules* **1993**, *26*, 805-812.

[24] Walther, M.; Bohnert, R.; Derow, S.; Finkelmann, H. Structure formation of liquid-crystalline isotropic AB block copolymers in nematic solvents. *Macromol. Rapid Commun.* **1995**, *16*, 621-629.

[25] Walther, M.; Faulhammer, H.; Finkelmann, H. On the thread-like morphology of LC/I block copolymers in nematic solvents. *Macromol. Chem. Phys.* **1998**, *199*, 223-237.

Appendix D

THE SPHERICAL CORE-SHELL FORM FACTOR APPLIED TO COIL-LIQUID CRYSTALLINE DIBLOCK COPOLYMER MICELLES

D.1 Appendix........255

D.2 Tables........260

D.3 Figures........261

D.4 References........263

D.1 Appendix

A spherical particle having a total radius R_s composed of a core of radius R_c surrounded by a shell of thickness $R_s - R_c$ is assumed to have uniform scattering length density in the core, ρ_c, and in the shell, ρ_s. The surrounding solvent has a scattering length density ρ_{solv}. (Figure D.1). The form factor, $P(q)$, of the particle is given by[1]

$$P(q) = \left[V_c^2(\rho_c - \rho_s)^2\psi_c^2 + 2V_cV_s(\rho_c - \rho_s)(\rho_s - \rho_{solv})\psi_c\psi_s + V_s^2(\rho_s - \rho_{solv})^2\psi_s^2\right] \quad \text{(D.1)}$$

where V_c and V_s are the volumes of the core and shell, respectively, and

$$\psi_x = \frac{3\left[\sin(qR_x) - qR_x\cos(qR_x)\right]}{(qR_x)^3}. \quad \text{(D.2)}$$

The first and last terms in Equation D.1 describe the scattering from the core and from the overall particle, respectively. The middle term (cross term) accounts for the interference between the two. The scattered intensity in the absence of interparticle correlations ($S(q) = 1$) is

$$I(q) = KP(q). \quad \text{(D.3)}$$

The proportionality constant K is related to the number of scatterers and is, effectively, simply a fitting parameter.

In the case of a polystyrene (PS) – liquid crystal polymer (LCP) diblock copolymer micelle dissolved in perdeuterated 5CB (d_{19}5CB), PS segregates into the core and the shell contains the LCP block. These cannot be assumed to consist of pure polymer because the penetration of d_{19}5CB into the micelle dilutes the core such that the volume fraction of PS is $f_{PS} < 1$ and the remaining volume is occupied by solvent. Similarly, the volume fraction of LCP in the shell is $f_{LCP} < 1$ and the remaining volume is occupied by solvent. The scattering length density of the core and shell are then calculated from

$$\rho_c = f_{PS}\rho_{PS} + (1 - f_{PS})\rho_{d_{19}5CB} \tag{D.4}$$

$$\rho_s = f_{LCP}\rho_{LCP} + (1 - f_{LCP})\rho_{d_{19}5CB} \tag{D.5}$$

where ρ_{PS} and ρ_{LCP} are the scattering length densities of PS and LCP, respectively, and the scattering length density of the solvent is $\rho_{d_{19}5CB}$. The contrast factors, (ρ_c-ρ_s) and (ρ_s-ρ_{solv}), then become

$$\rho_c - \rho_s = f_{PS}\left(\rho_{PS} - \rho_{d_{19}5CB}\right) - f_{LCP}\left(\rho_{LCP} - \rho_{d_{19}5CB}\right) \tag{D.6}$$

And

$$\rho_c - \rho_{solv} = f_{LCP}\left(\rho_{LCP} - \rho_{d_{19}5CB}\right) \tag{D.7}$$

A relationship between f_{PS} and f_{LCP} is derived from the requirement that the number of LCP chains in the shell must equal the number of PS chains in the core by virtue of the diblock copolymer's connectivity. In other words, the aggregation number of the core must equal that of the shell, expressed mathematically as

$$\frac{f_{PS}\,{}^4\!/_3\,\pi R_c^3}{v_{PS}} = \frac{f_{LCP}\left({}^4\!/_3\,\pi R_s^3 - {}^4\!/_3\,\pi R_c^3\right)}{v_{LCP}} \tag{D.8}$$

where v_{PS} and v_{LCP} are the volumes occupied by a single PS block and LCP block, respectively. Equation D.8 gives the following relationship between f_{PS} and f_{LCP}:

$$f_{LCP} = f_{PS}\frac{v_{LCP}}{v_{PS}}\frac{R_c^3}{R_s^3 - R_c^3}\,. \tag{D.9}$$

Eliminating f_{LCP} from Equations D.6 and D.7 by substituting Equation D.9 gives the contrast factors in terms of f_{PS} alone:

$$\rho_c - \rho_s = f_{PS}\left[\left(\rho_{PS} - \rho_{d_{19}5CB}\right) - \frac{v_{LCP}}{v_{PS}}\frac{R_c^3}{R_s^3 - R_c^3}\left(\rho_{LCP} - \rho_{d_{19}5CB}\right)\right] \tag{D.10}$$

$$\rho_s - \rho_{solv} = f_{PS}\left[\frac{v_{LCP}}{v_{PS}}\frac{R_c^3}{R_s^3 - R_c^3}\left(\rho_{LCP} - \rho_{d_{19}5CB}\right)\right]. \tag{D.11}$$

The form factor for the swollen PS-LCP micelle is now written

$$P(q) = \left[V_c^2 K_c \psi_c^2 + 2V_c V_s K_{cs} \psi_c \psi_s + V_s^2 K_s \psi_s^2\right] \tag{D.12}$$

where

$$K_c = f_{PS}^2\left[\left(\rho_{PS} - \rho_{d_{19}5CB}\right) - \frac{v_{LCP}}{v_{PS}}\frac{R_c^3}{R_s^3 - R_c^3}\left(\rho_{LCP} - \rho_{d_{19}5CB}\right)\right]^2,$$

$$K_{cs} = f_{PS}^2\left[\left(\rho_{PS} - \rho_{d_{19}5CB}\right) - \frac{v_{LCP}}{v_{PS}}\frac{R_c^3}{R_s^3 - R_c^3}\left(\rho_{LCP} - \rho_{d_{19}5CB}\right)\right]\left[\frac{v_{LCP}}{v_{PS}}\frac{R_c^3}{R_s^3 - R_c^3}\left(\rho_{LCP} - \rho_{d_{19}5CB}\right)\right],$$

and

$$K_s = f_{PS}^2\left[\frac{v_{LCP}}{v_{PS}}\frac{R_c^3}{R_s^3 - R_c^3}\left(\rho_{LCP} - \rho_{d_{19}5CB}\right)\right]^2.$$

Evidently, the volume fraction of PS in the core is a multiplicative factor that may be absorbed into the proportionality constant, K, when calculating the scattered intensity (Equation D.3). This implies that the degree to which solvent penetrates the micelle cannot be measured with SANS unless additional information can be gleaned from the interparticle structure factor. The aggregation number is similarly indeterminate from form factor scattering alone, though an upper bound may be established by setting $f_{PS} = 1$.

For the purposes of fitting experimental SANS data the scattered intensity calculated from Equations D.3 and D.12 contains only three adjustable parameters: K, R_c, and R_s. The scattering length densities (ρ_{PS}, ρ_{LCP}, and $\rho_{d_{19}5CB}$) are calculated from the chemical composition of each species using

$$\rho = \frac{\sum_{i=1}^{n} b_{c_i}}{v_m} \tag{D.13}$$

where the b_cs are the bound coherent scattering lengths of the molecule's n atoms and v_m is the molecular volume. Results for the polymers and solvent studied here are summarized in Table D.1.

It is interesting to speculate on the potential use of contrast matching techniques to simplify the scattering from these micelles. If the scattering length density of the shell is equal to that of the solvent, the form factor is reduced to that of a homogeneous sphere,

$$P(q) = V_c^2 (\rho_c - \rho_s)^2 \psi_c^2, \tag{D.14}$$

and the scattering only depends on one length scale, R_c. However, matching the scattering length density of the solvent and the core does not eliminate any terms from the form factor. Only when $\rho_c = \rho_s$ does the form factor get simpler, reducing to that of a homogenous sphere with radius R_s.

The high incoherent scattering length of hydrogen makes it undesirable to use hydrogenated 5CB as the solvent, but mixtures of 5CB and d_{19}5CB could make suitable solvents if the mixture was less than perhaps 50 % 5CB. Deuterium atoms must be incorporated into the polymer in order to achieve a contrast match with the solvent. Polystyrene is the most obvious candidate for deuteration because styrene monomer containing 1, 2, 3, 5, 6, or 8 deuterons (Table D.2) is readily available from chemical suppliers. However, this is not particularly helpful since contrast matching the core does not eliminate a length scale; even an empty shell is still characterized by R_c and R_s. The complete form factor for a diblock micelle having a contrast-matched core is

$$P(q) = f_{PS}^2 \left[\frac{v_{LCP}}{v_{PS}} \frac{R_c^3}{R_s^3 - R_c^3} \left(\rho_{LCP} - \rho_{d_{19}5CB} \right) \right]^2 \left[V_c^2 \psi_c^2 - 2 V_c V_s \psi_c \psi_s + V_s^2 \psi_s^2 \right]. \tag{D.15}$$

The alternative is to incorporate deuterium into the LCP block, a difficult problem from the synthetic point of view. It may be possible to fully deuterate the mesogens' aromatic rings with techniques similar to those used to synthesize d_{19}5CB and d_2HSiCB4 (Appendix B). Additional deuterons could be incorporated by using a perdeuterated polybutadiene (d_8PB) backbone as the prepolymer. If achievable, these two substitutions would raise the scattering length density of HSiCB4 from 0.9×10^{-6} Å^{-2} to 2.8×10^{-6} Å^{-2} which would be contrast matched with a mixture of 30 % d_{19}5CB / 70% 5CB ($\rho_{5CB} = 1.4 \times 10^{-6}$ Å^{-2}), a mixture that is likely too high in hydrogen content. In order to achieve a contrast match between HSiCB4 and a 50/50 mixture of d_{19}5CB/5CB, 22 of the polymer's 35 hydrogens must be replaced with deuterium atoms (Figure D.2). This would require deuterium substitution of all hydrogens except those on the siloxane linking group.

Notably from Figure D.2, the scattering length density of d_2HSiCB4 is almost perfectly matched to that of PS. This match does not, however, imply that a d_2HSiCB4-PS diblock would form a micelle with matched core and shell. Note that all of the contrast terms in Equation D.12 are relative to the solvent; none are between the two polymers. The solvent penetrates the core and shell to different degrees such that $\rho_c \neq \rho_s$, even when $\rho_{LCP} = \rho_{PS}$.

D.2 Tables

Table D.1 Densities and scattering length densities, ρ, of relevant molecules.

	Density [g/cm^3]	$\rho \times 10^6$ [Å^{-2}]
d_{19}5CB	1.1[a]	6.2
HSiCB4	1.0[a]	0.9
HSiBB	1.0[a]	1.0
PS	1.05	1.4
PB	0.9	0.4

[a] Estimated density; actual value unknown

Table D.2 Densities and scattering length densities, ρ, of polystyrene having various levels of deuteration.

Number of Deuterons	Density [g/cm^3]	$\rho \times 10^6$ [Å^{-2}]
0	1.05	1.4
1	1.06[a]	2.0
2	1.07[a]	2.6
3	1.08[a]	3.2
5	1.10[a]	4.4
6	1.11[a]	4.9
8	1.13[a]	6.5

[a] Estimated density; actual value unknown

D.3 Figures

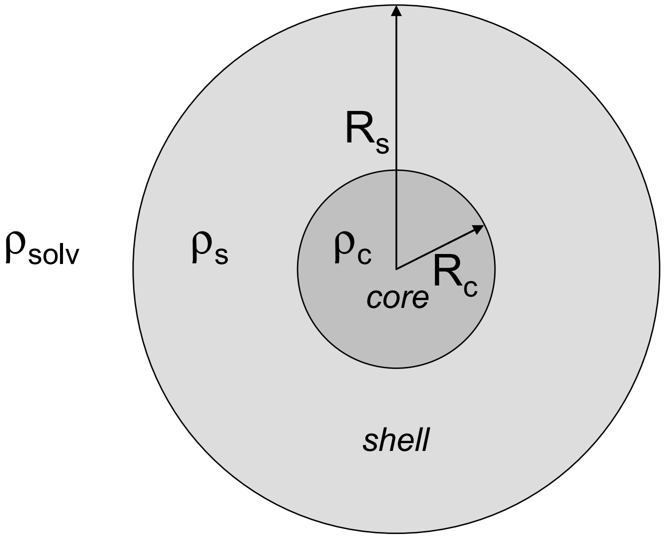

Figure D.1 Schematic diagram of a spherical core-shell particle having an overall radius R_s and a core radius of R_c. The scattering length densities of the core and corona (ρ_c and ρ_s, respectively) are assumed be uniform throughout their respective volumes. The particle is in a solvent with scattering length density ρ_{solv}.

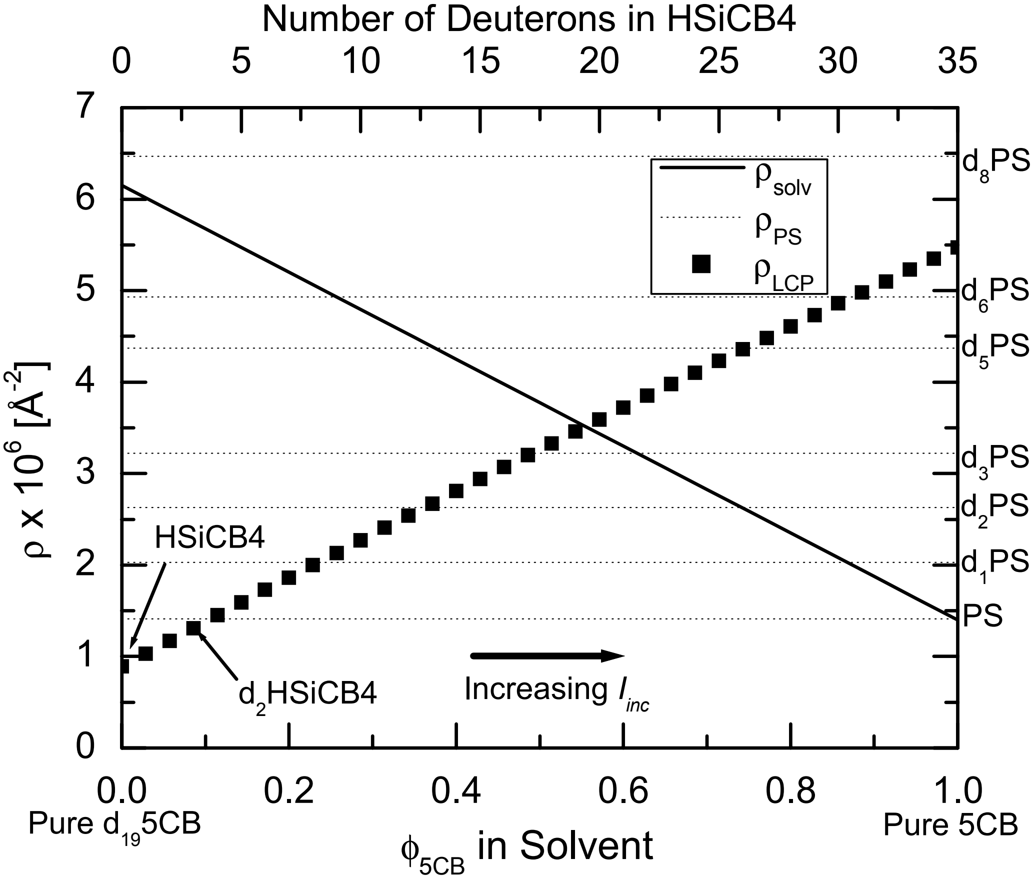

Figure D.2 Achievable neutron scattering length densities of the solvent, side-group liquid crystal polymer (HSiCB4), and polystyrene (PS) by various strategies for changing each component's deuterium content. The deuterium content of the solvent can be varied by mixing d_{19}5CB with 5CB (bottom axis) to achieve $\rho \times 10^6$ anywhere between 1.4 and 6.2 Å^{-2} (solid line). As the 5CB content increases, the incoherent scattering (I_{inc}) increases. Deuterium can be incorporated into polystyrene by polymerizing d_x-styrene where x is the number of deuterium atoms in the monomer (dotted lines). It might be possible to substitute deuterium for some of the 35 hydrogen atoms on the HSiCB4 monomer (squares, top axis). Only one such deuteriated polymer, d_2HSiCB4, has been synthesized to date.

D.4 References

[1] King, S. M.; Griffiths, P. C.; Cosgrove, T. Using SANS to Study Adsorbed Layers in Colloidal Dispersions. In *Applications of Neutron Scattering to Soft Condensed Matter*; B.J. Gabrys, Editor; Gordon and Breach Science Publishers: Amsterdam, 2000.

Appendix E

DYNAMIC STORAGE AND LOSS MODULI OF LIQUID CRYSTALLINE POLYMER SOLUTIONS

E.1 Appendix 264

E.2 Figures 265

E.1 Appendix

A TA Instruments ARES-RFS fluids rheometer was used to measure the dynamic storage modulus, $G'(\omega)$, and loss modulus, $G''(\omega)$, of solutions of side-group liquid crystalline diblock copolymers, triblock copolymers, and homopolymers dissolved in nematic liquid crystal solvent, 4-pentyl-4′-cyanobiphenyl (5CB). Temperature was controlled with the rheometer’s built-in Peltier plate, and before beginning a frequency sweep, the sample was heated to 60 °C then annealed at the desired temperature for at least five minutes. A 25 mm titanium cone-and-plate tool with a cone angle of 0.04 rad was used, which requires approximately 250 mg of sample.

E.2 Figures

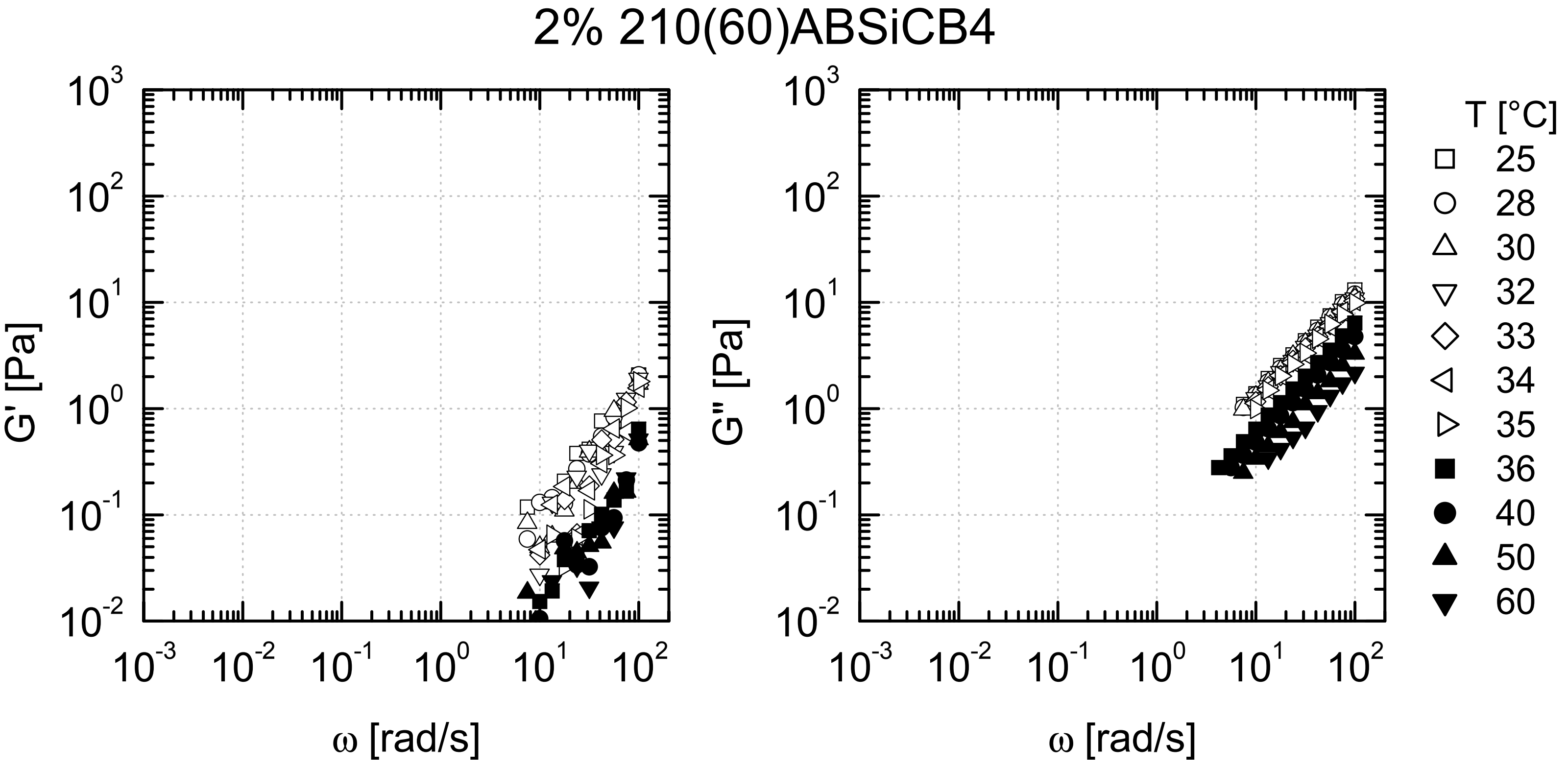

Figure E.1 Frequency (*ω*) dependence of the storage (*G*′) and loss (*G*″) modulus of 2 wt % 210(60)ABSiCB4 in 5CB as a function of temperature (*T*) in the nematic phase (open symbols) and the isotropic phase (closed symbols).

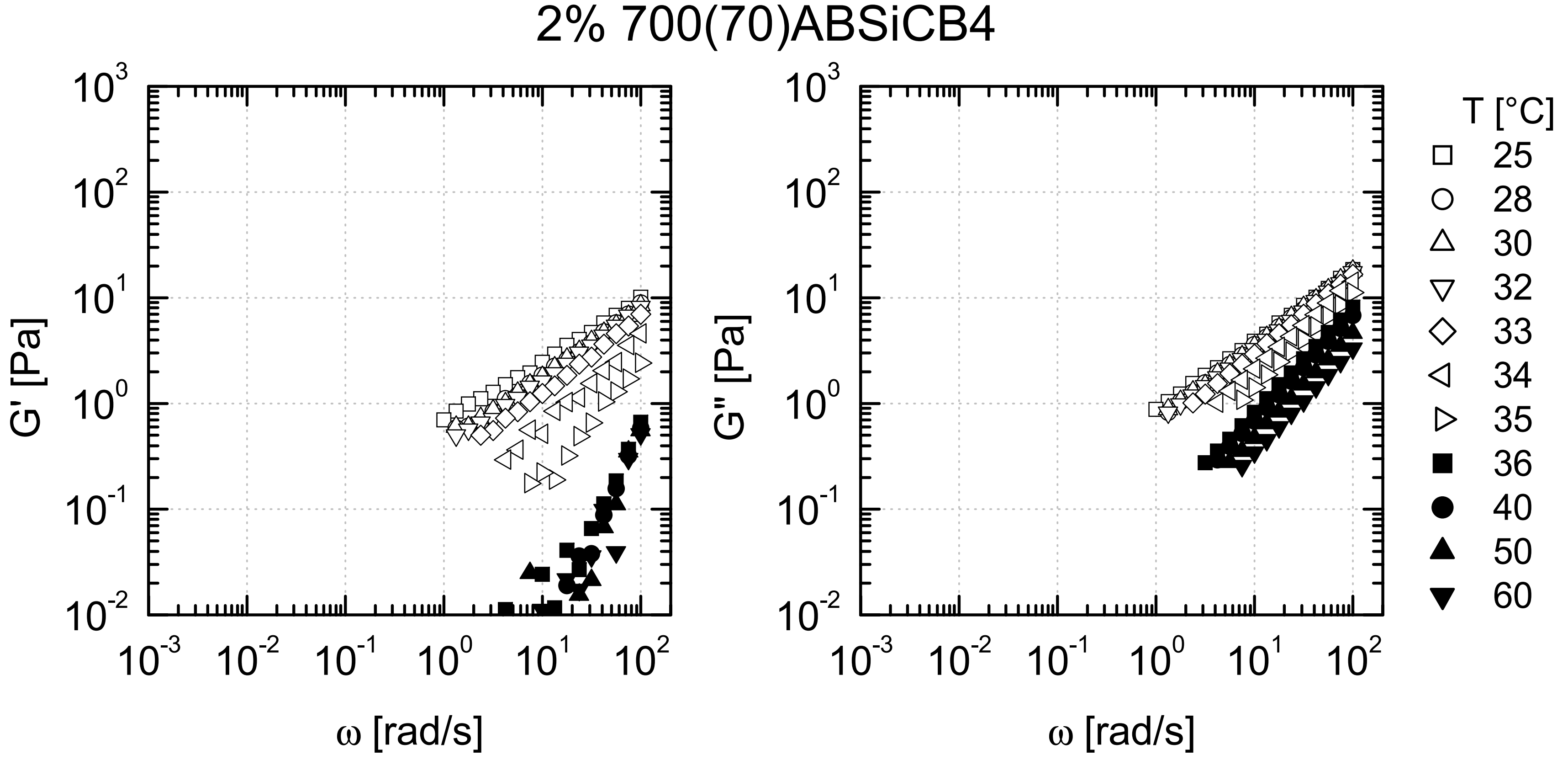

Figure E.2 Frequency (*ω*) dependence of the storage (*G′*) and loss (*G″*) modulus of 2 wt % 700(70)ABSiCB4 in 5CB as a function of temperature (*T*) in the nematic phase (open symbols) and the isotropic phase (closed symbols).

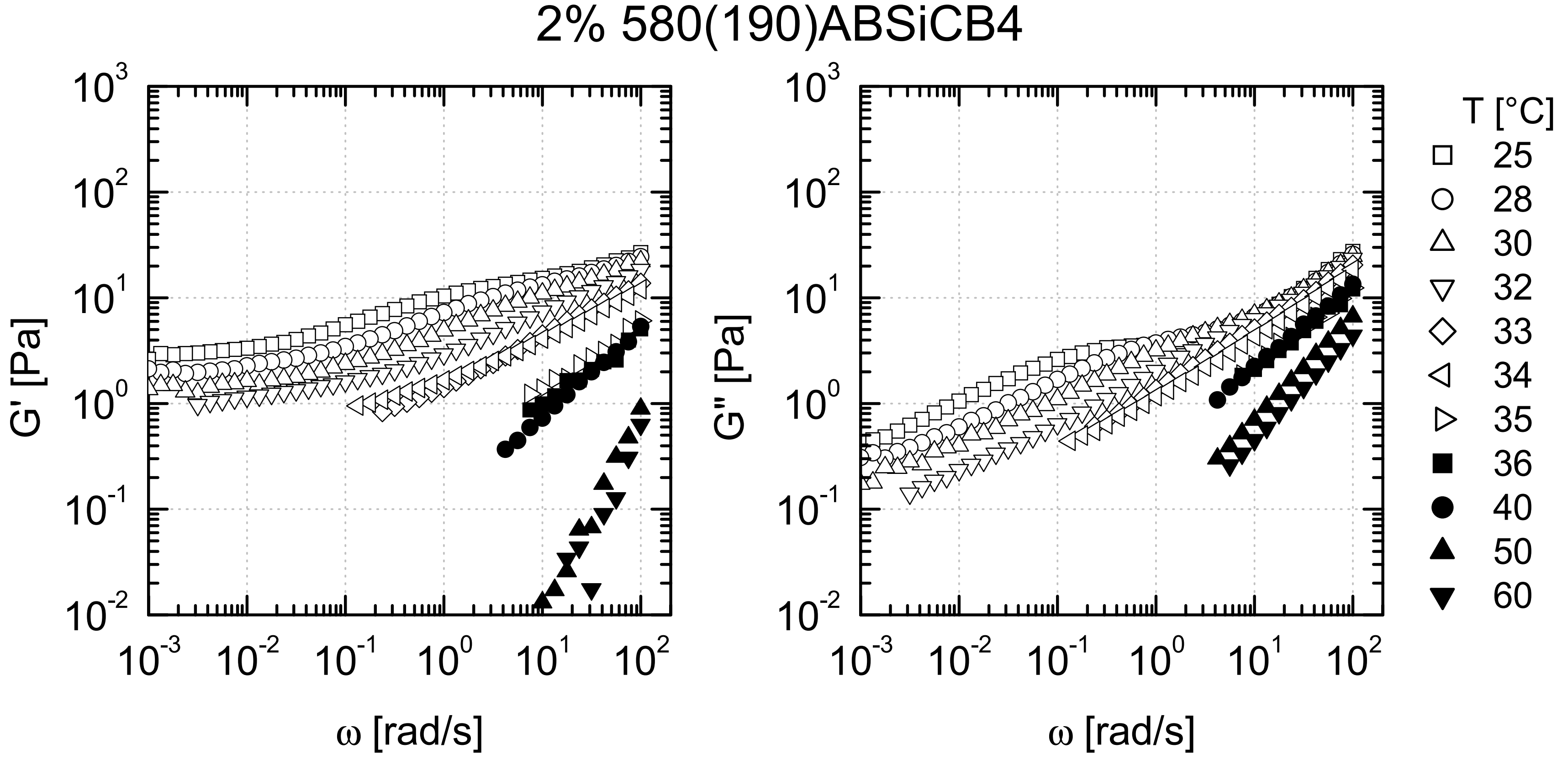

Figure E.3 Frequency (ω) dependence of the storage (G') and loss (G'') modulus of 2 wt % 580(190)ABSiCB4 in 5CB as a function of temperature (T) in the nematic phase (open symbols) and the isotropic phase (closed symbols).

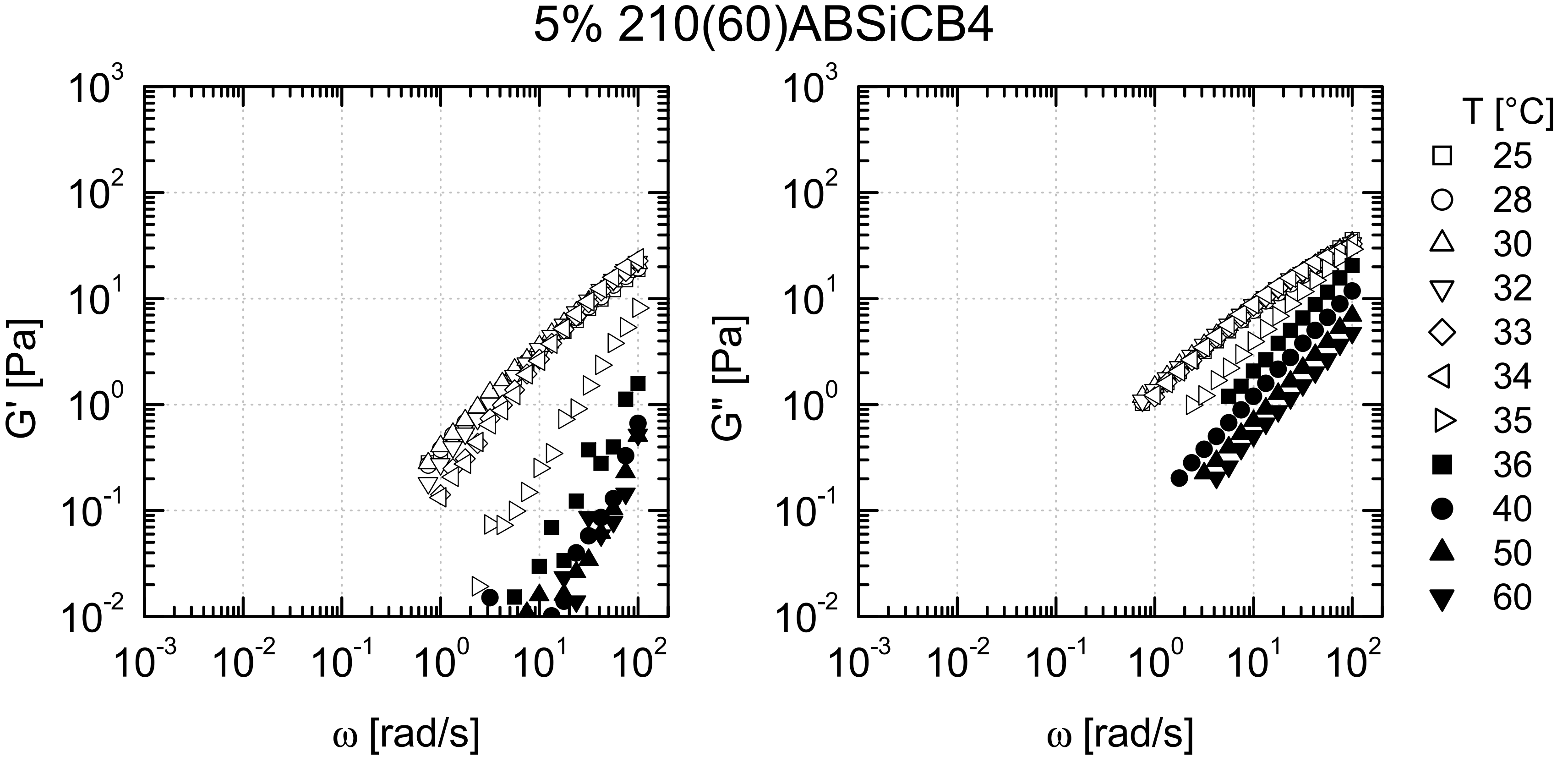

Figure E.4 Frequency (ω) dependence of the storage (G') and loss (G'') modulus of 5 wt % 210(60)ABSiCB4 in 5CB as a function of temperature (T) in the nematic phase (open symbols) and the isotropic phase (closed symbols).

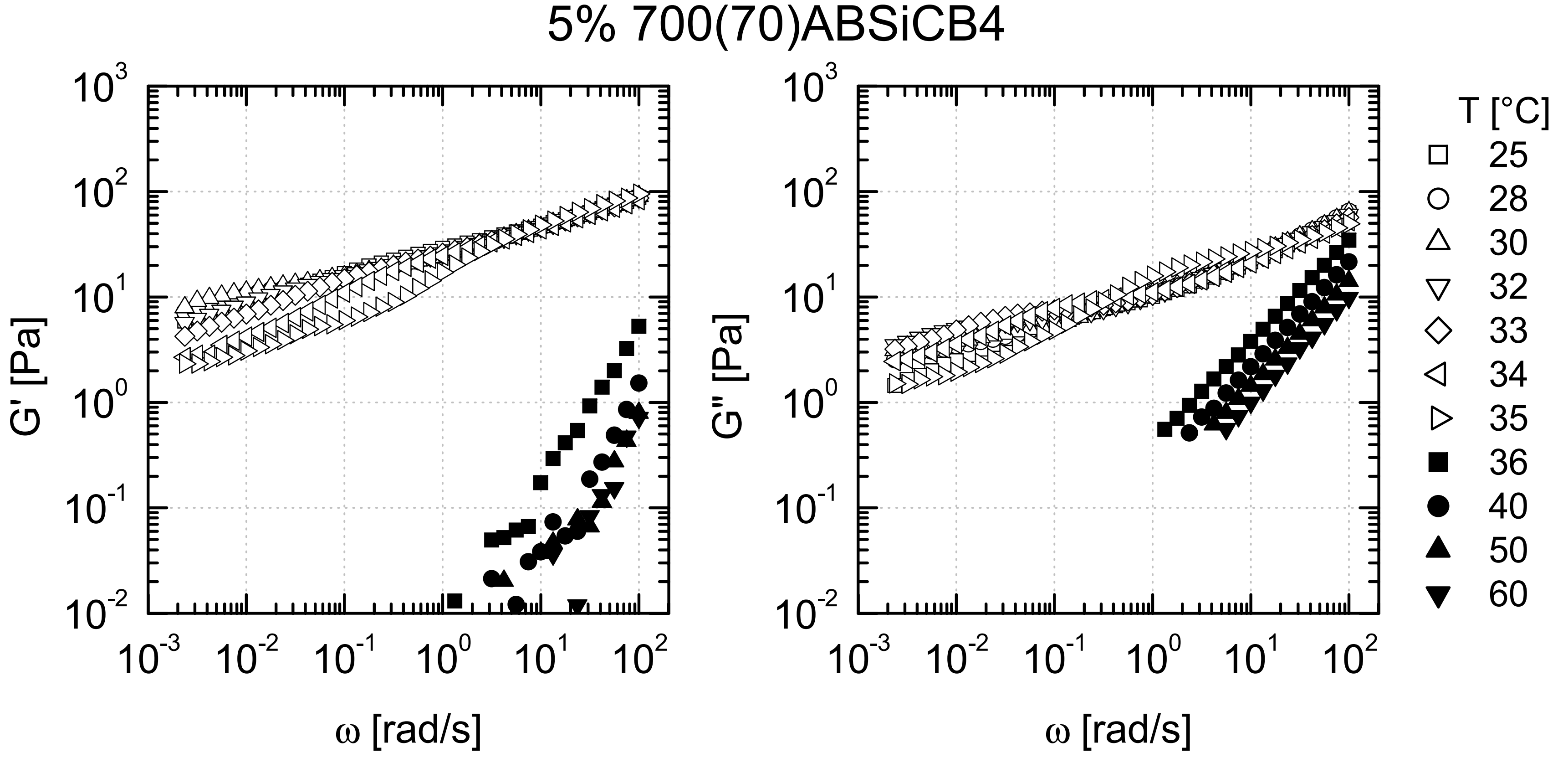

Figure E.5 Frequency (*ω*) dependence of the storage (*G′*) and loss (*G″*) modulus of 5 wt % 700(70)ABSiCB4 in 5CB as a function of temperature (*T*) in the nematic phase (open symbols) and the isotropic phase (closed symbols).

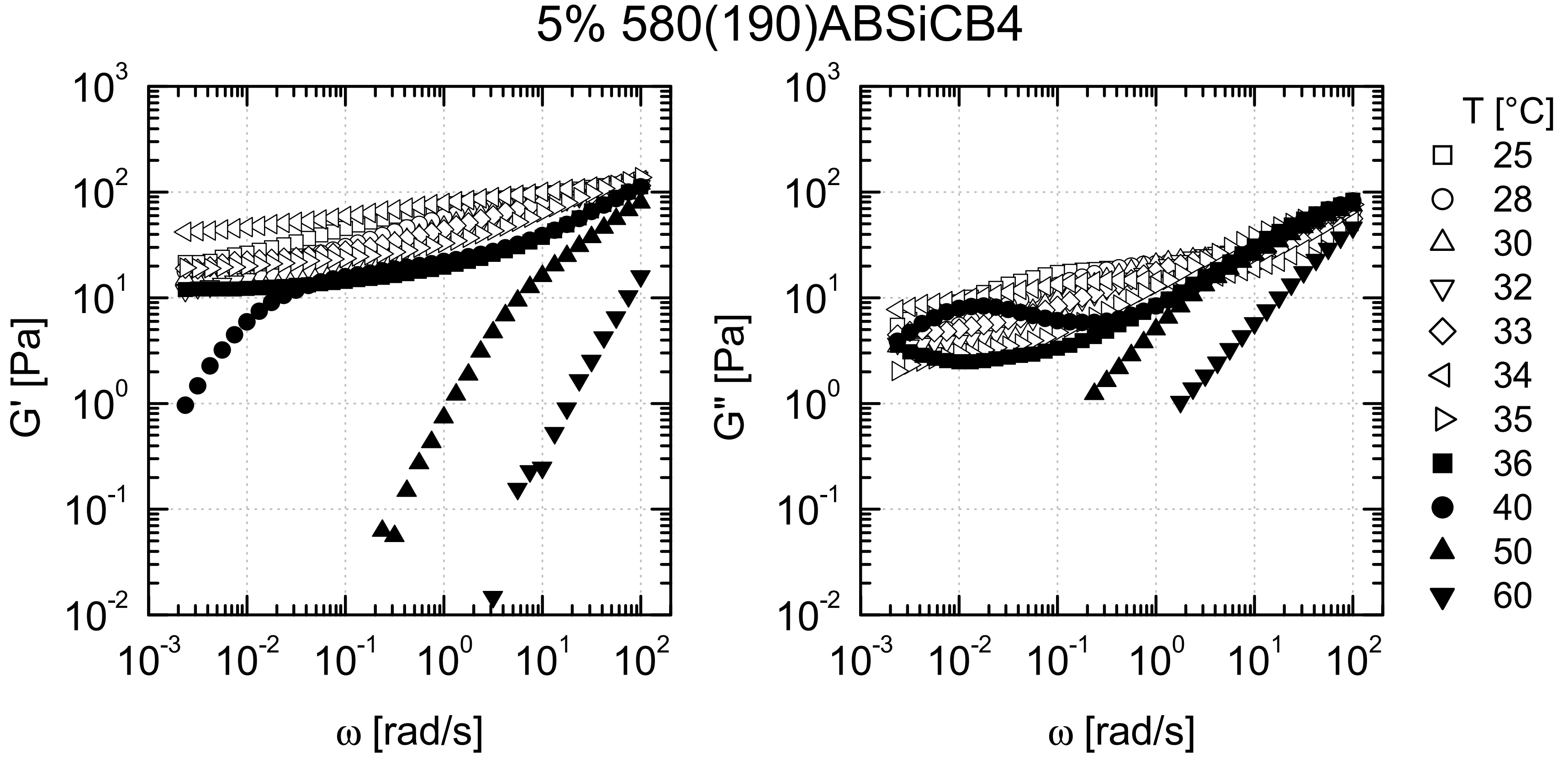

Figure E.6 Frequency (*ω*) dependence of the storage (*G*′) and loss (*G*″) modulus of 5 wt % 580(190)ABSiCB4 in 5CB as a function of temperature (*T*) in the nematic phase (open symbols) and the isotropic phase (closed symbols).

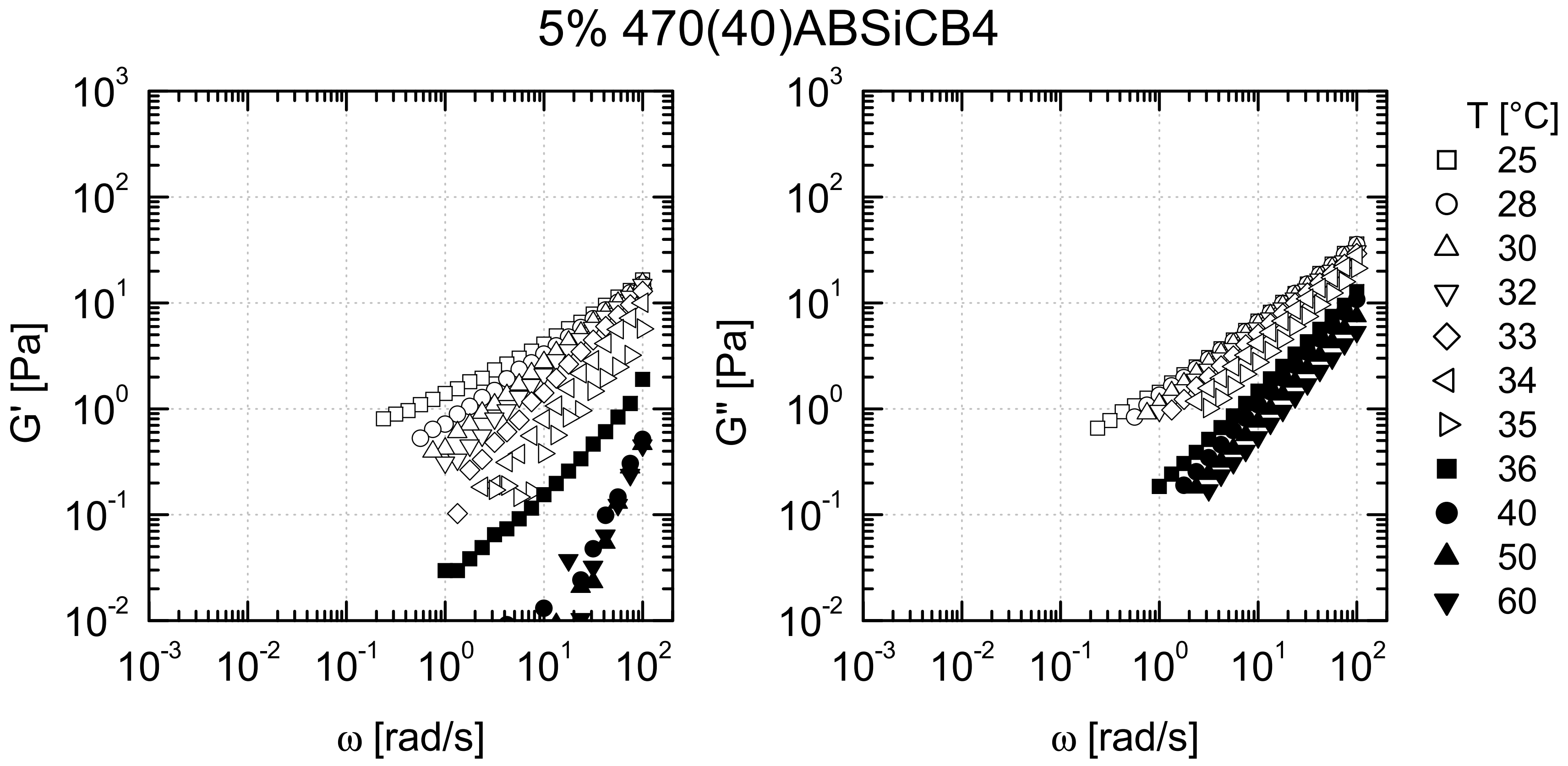

Figure E.7 Frequency (*ω*) dependence of the storage (*G*′) and loss (*G*″) modulus of 5 wt % 470(40)ABSiCB4 in 5CB as a function of temperature (*T*) in the nematic phase (open symbols) and the isotropic phase (closed symbols).

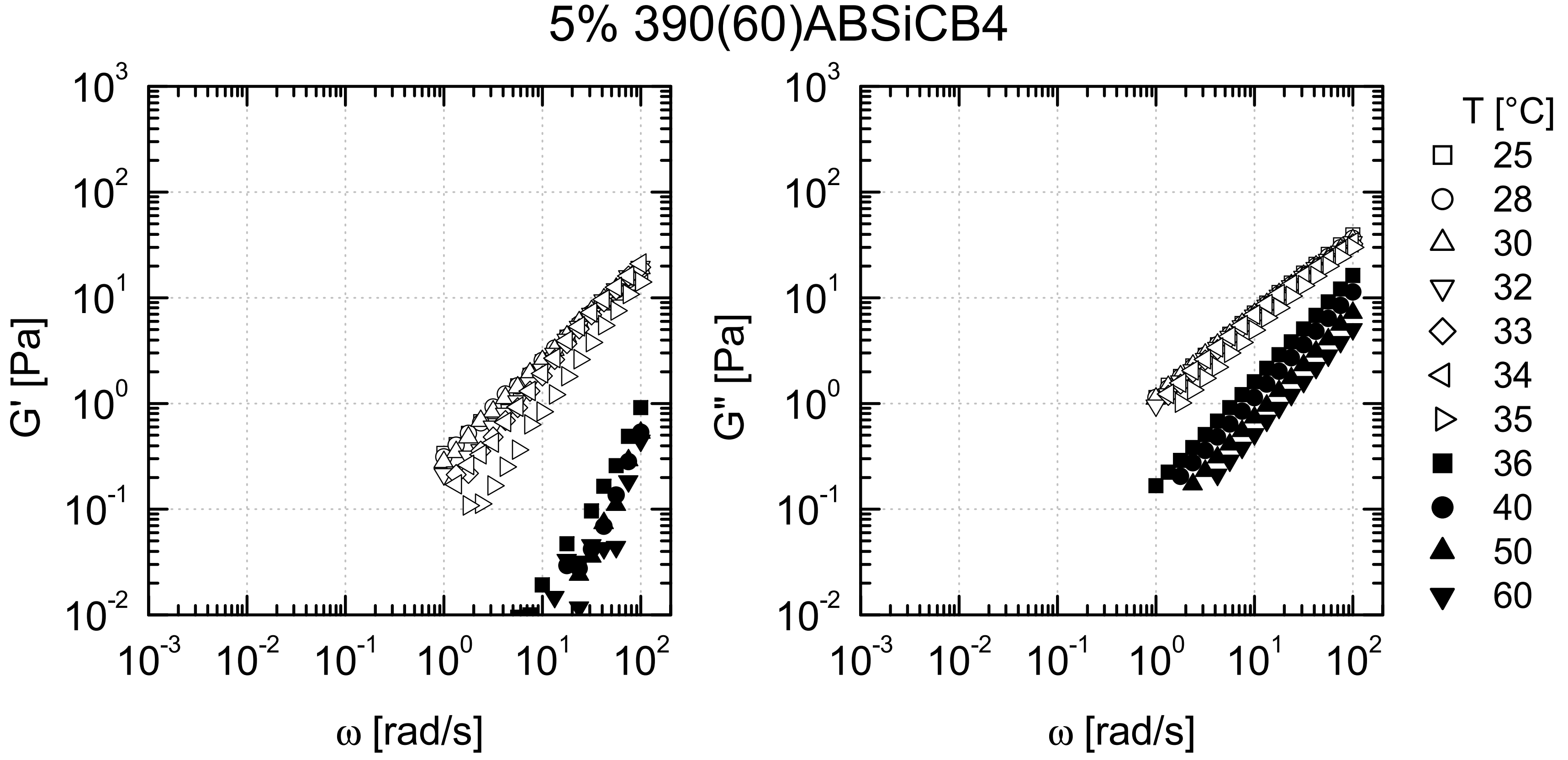

Figure E.8 Frequency (*ω*) dependence of the storage (*G′*) and loss (*G″*) modulus of 5 wt % 390(60)ABSiCB4 in 5CB as a function of temperature (*T*) in the nematic phase (open symbols) and the isotropic phase (closed symbols).

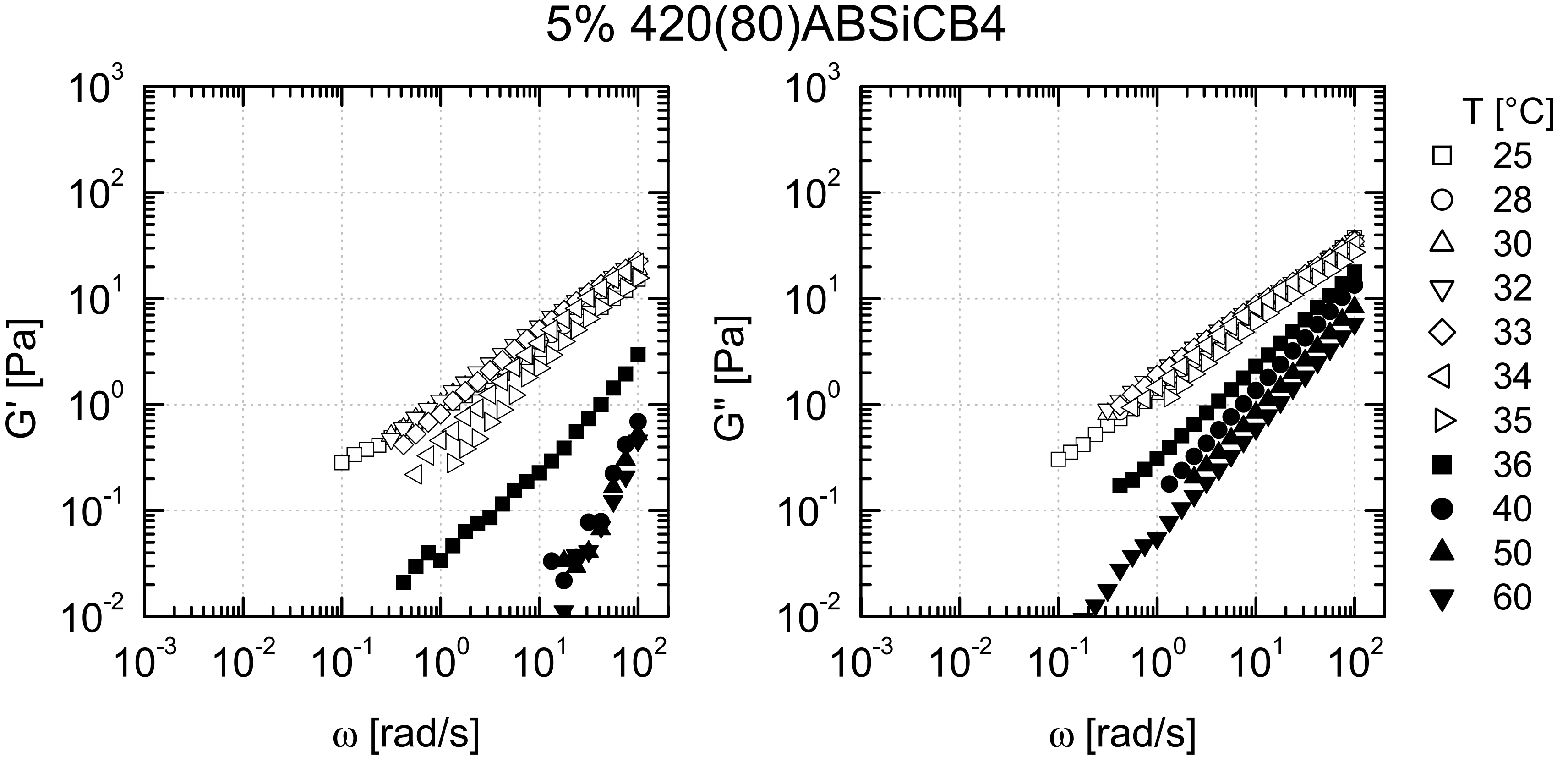

Figure E.9 Frequency (ω) dependence of the storage (G') and loss (G'') modulus of 5 wt % 420(80)ABSiCB4 in 5CB as a function of temperature (T) in the nematic phase (open symbols) and the isotropic phase (closed symbols).

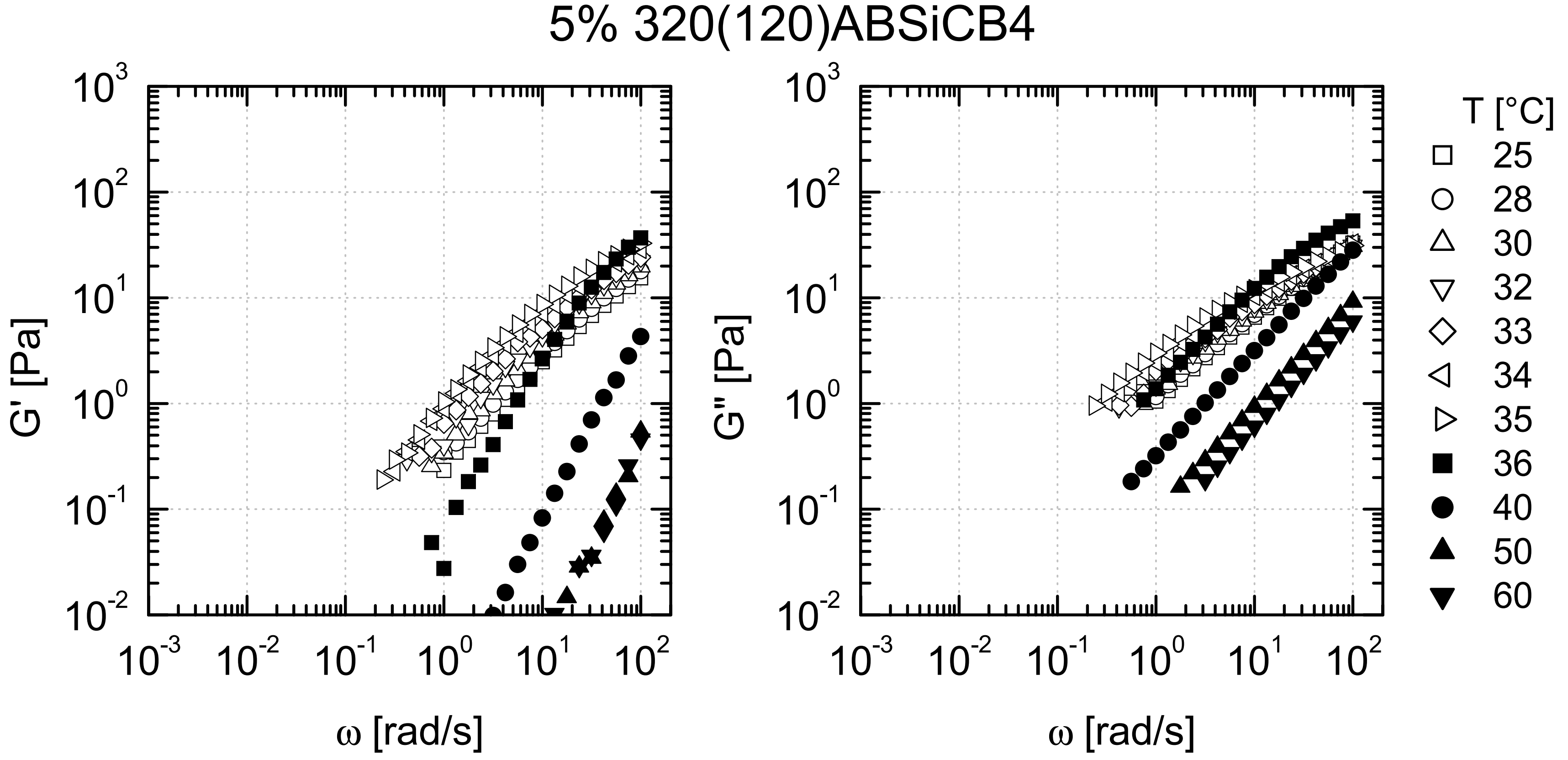

Figure E.10 Frequency (ω) dependence of the storage (G') and loss (G'') modulus of 5 wt % 320(120)ABSiCB4 in 5CB as a function of temperature (T) in the nematic phase (open symbols) and the isotropic phase (closed symbols).

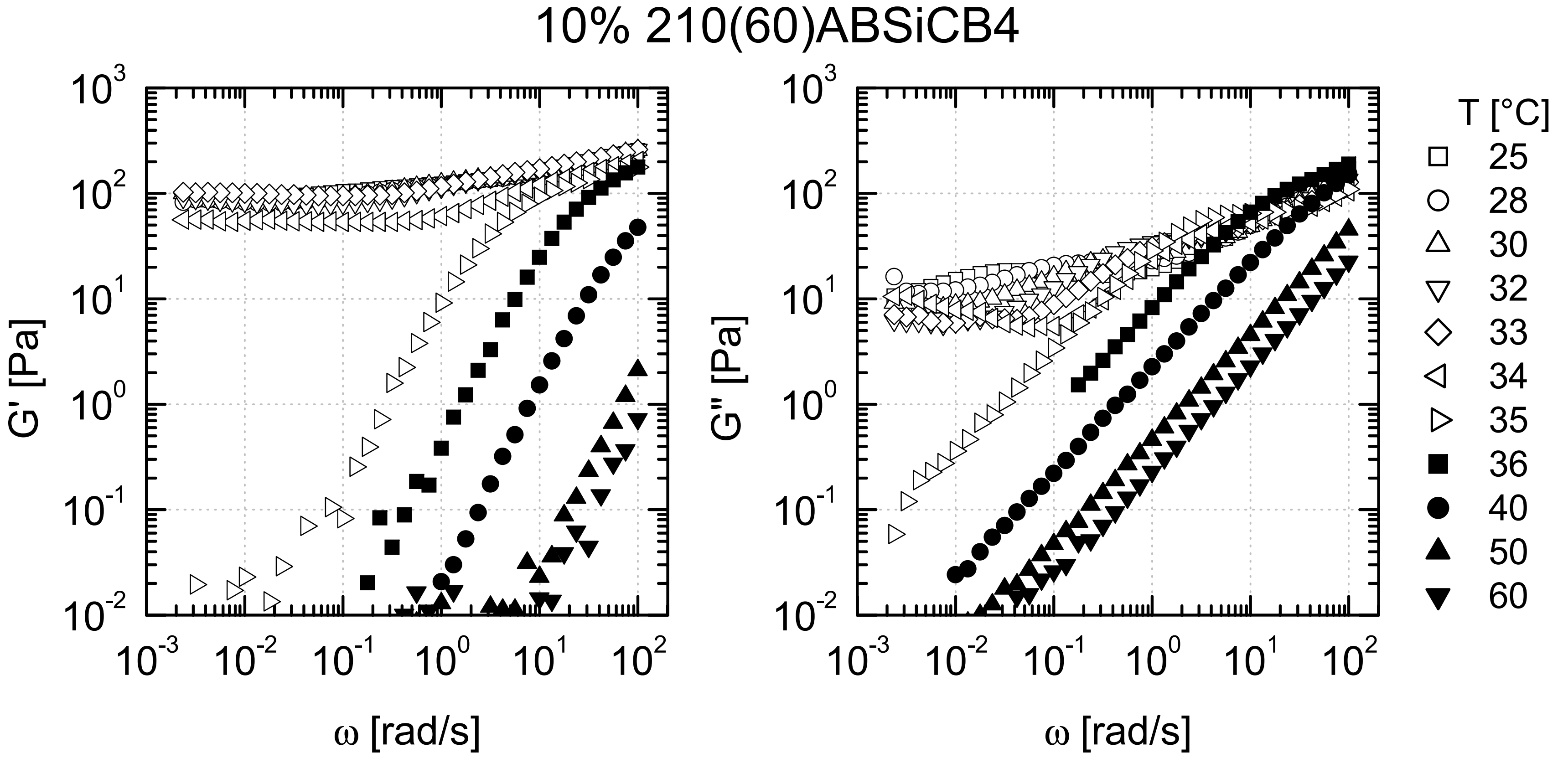

Figure E.11 Frequency (ω) dependence of the storage (G') and loss (G'') modulus of 10 wt % 210(60)ABSiCB4 in 5CB as a function of temperature (T) in the nematic phase (open symbols) and the isotropic phase (closed symbols).

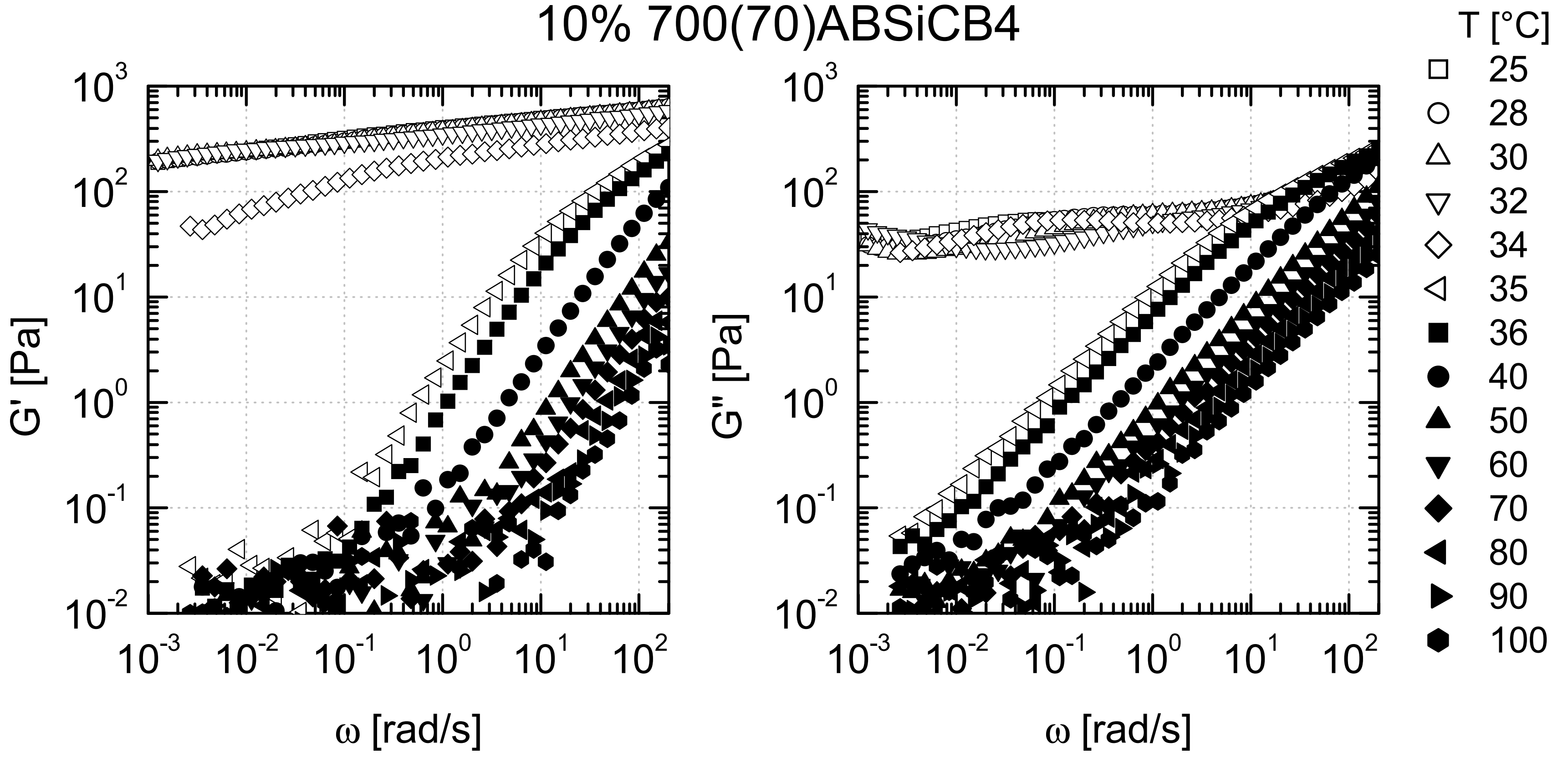

Figure E.12 Frequency (*ω*) dependence of the storage (*G′*) and loss (*G″*) modulus of 10 wt % 700(70)ABSiCB4 in 5CB as a function of temperature (*T*) in the nematic phase (open symbols) and the isotropic phase (closed symbols).

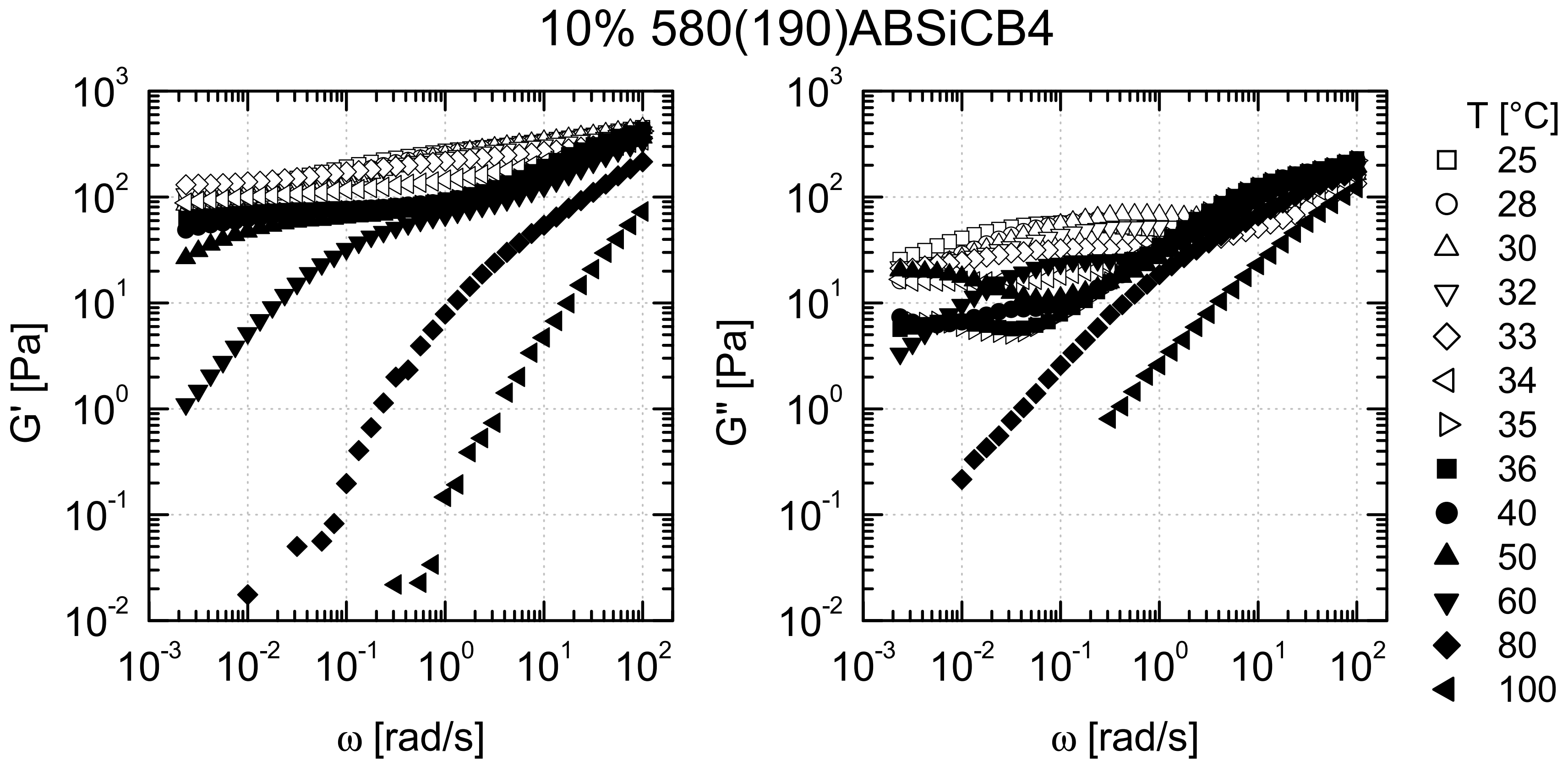

Figure E.13 Frequency (*ω*) dependence of the storage (*G′*) and loss (*G″*) modulus of 10 wt % 580(190)ABSiCB4 in 5CB as a function of temperature (*T*) in the nematic phase (open symbols) and the isotropic phase (closed symbols).

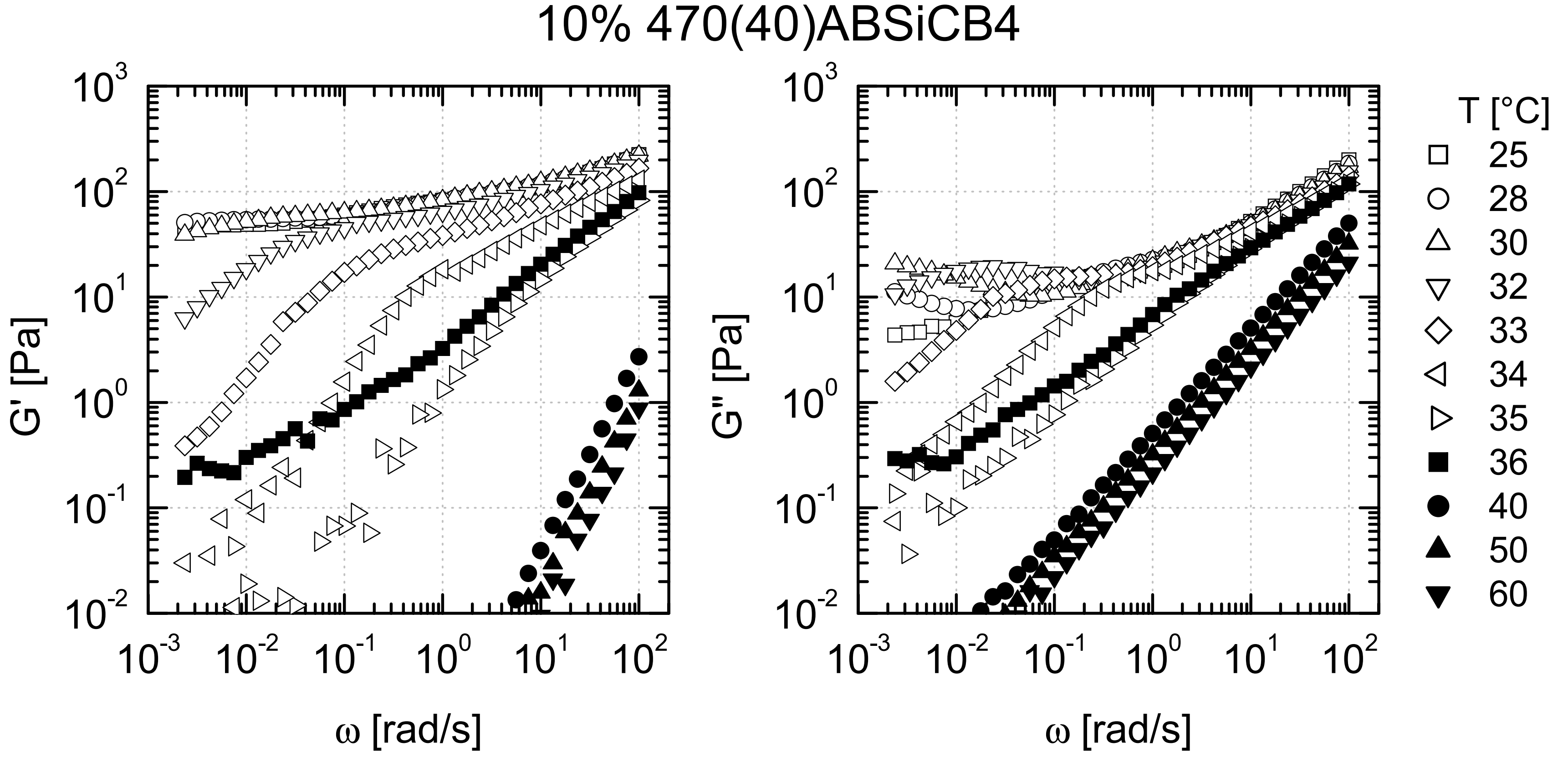

Figure E.14 Frequency (ω) dependence of the storage (G') and loss (G'') modulus of 10 wt % 470(40)ABSiCB4 in 5CB as a function of temperature (T) in the nematic phase (open symbols) and the isotropic phase (closed symbols).

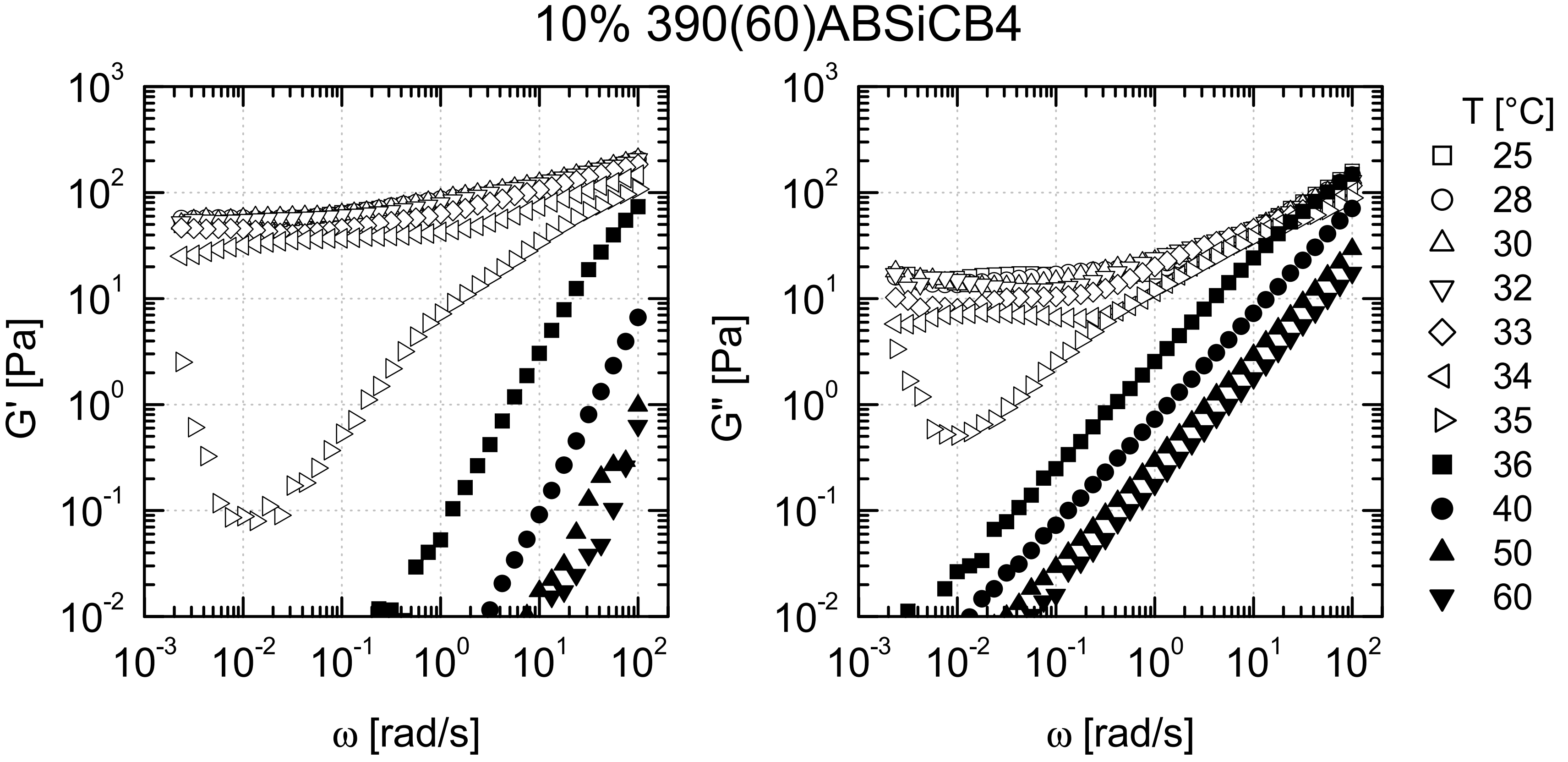

Figure E.15 Frequency (*ω*) dependence of the storage (*G′*) and loss (*G″*) modulus of 10 wt % 390(60)ABSiCB4 in 5CB as a function of temperature (*T*) in the nematic phase (open symbols) and the isotropic phase (closed symbols).

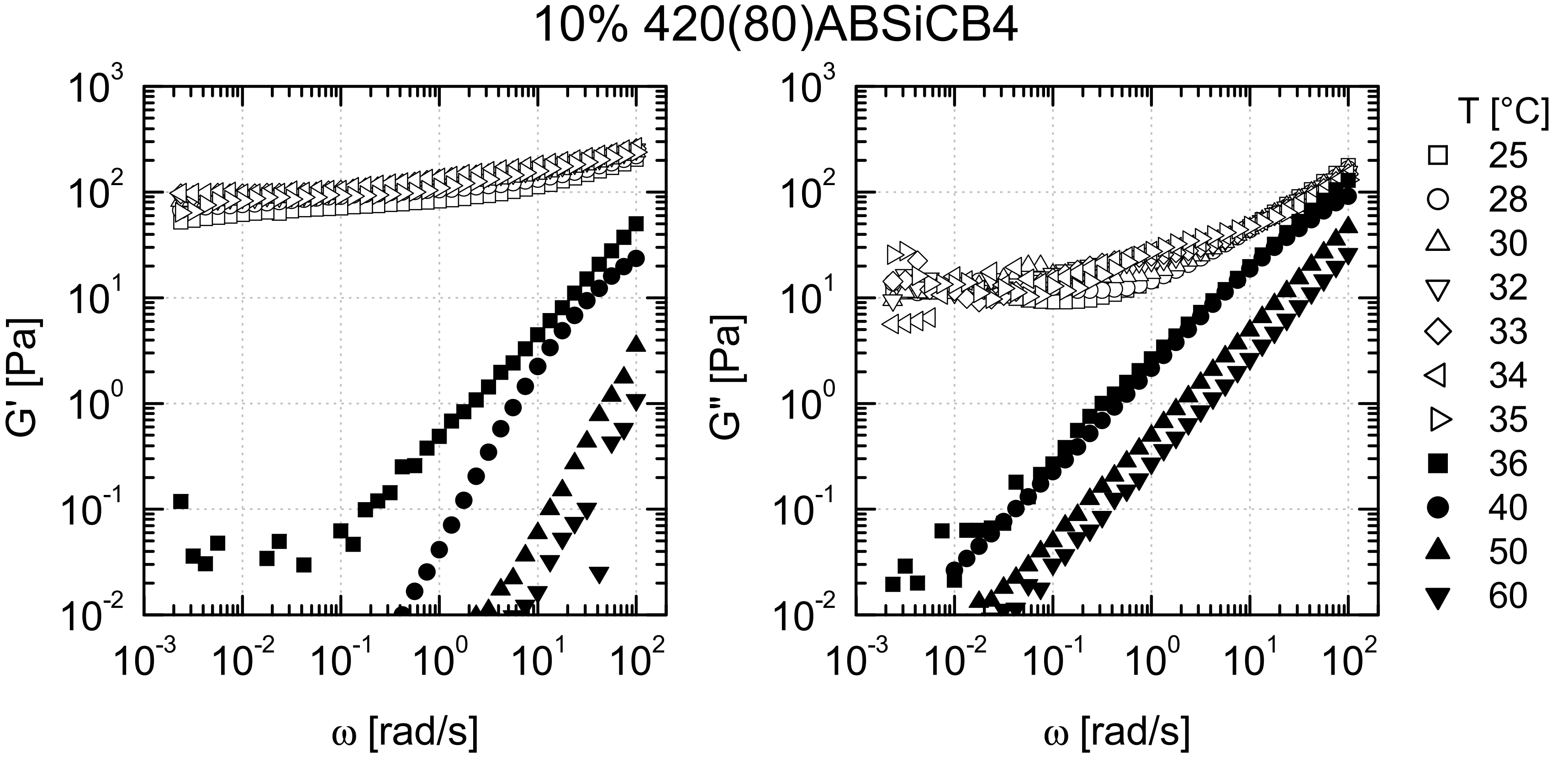

Figure E.16 Frequency (ω) dependence of the storage (G') and loss (G'') modulus of 10 wt % 420(80)ABSiCB4 in 5CB as a function of temperature (T) in the nematic phase (open symbols) and the isotropic phase (closed symbols).

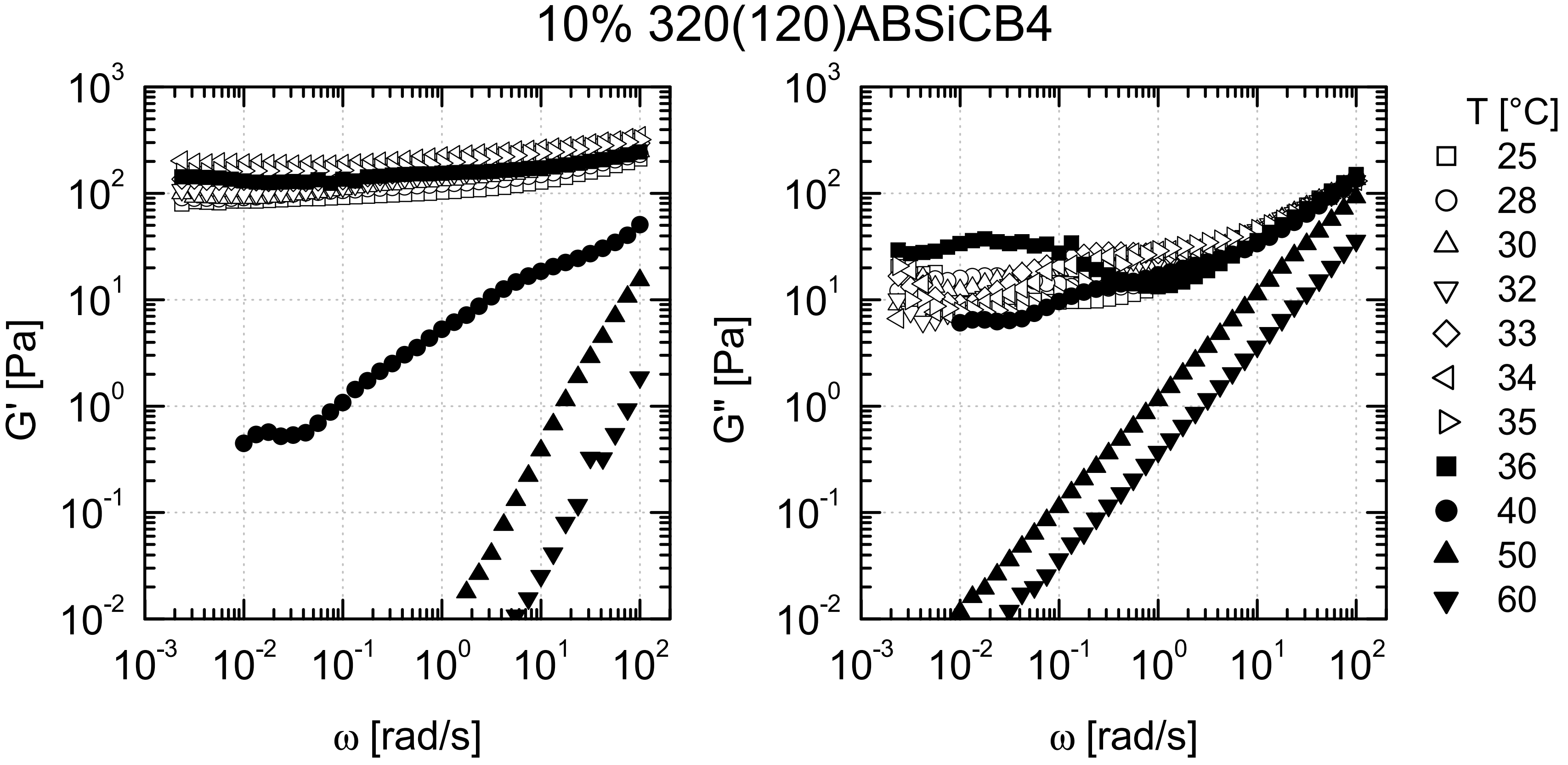

Figure E.17 Frequency (ω) dependence of the storage (G') and loss (G'') modulus of 10 wt % 320(120)ABSiCB4 in 5CB as a function of temperature (T) in the nematic phase (open symbols) and the isotropic phase (closed symbols).

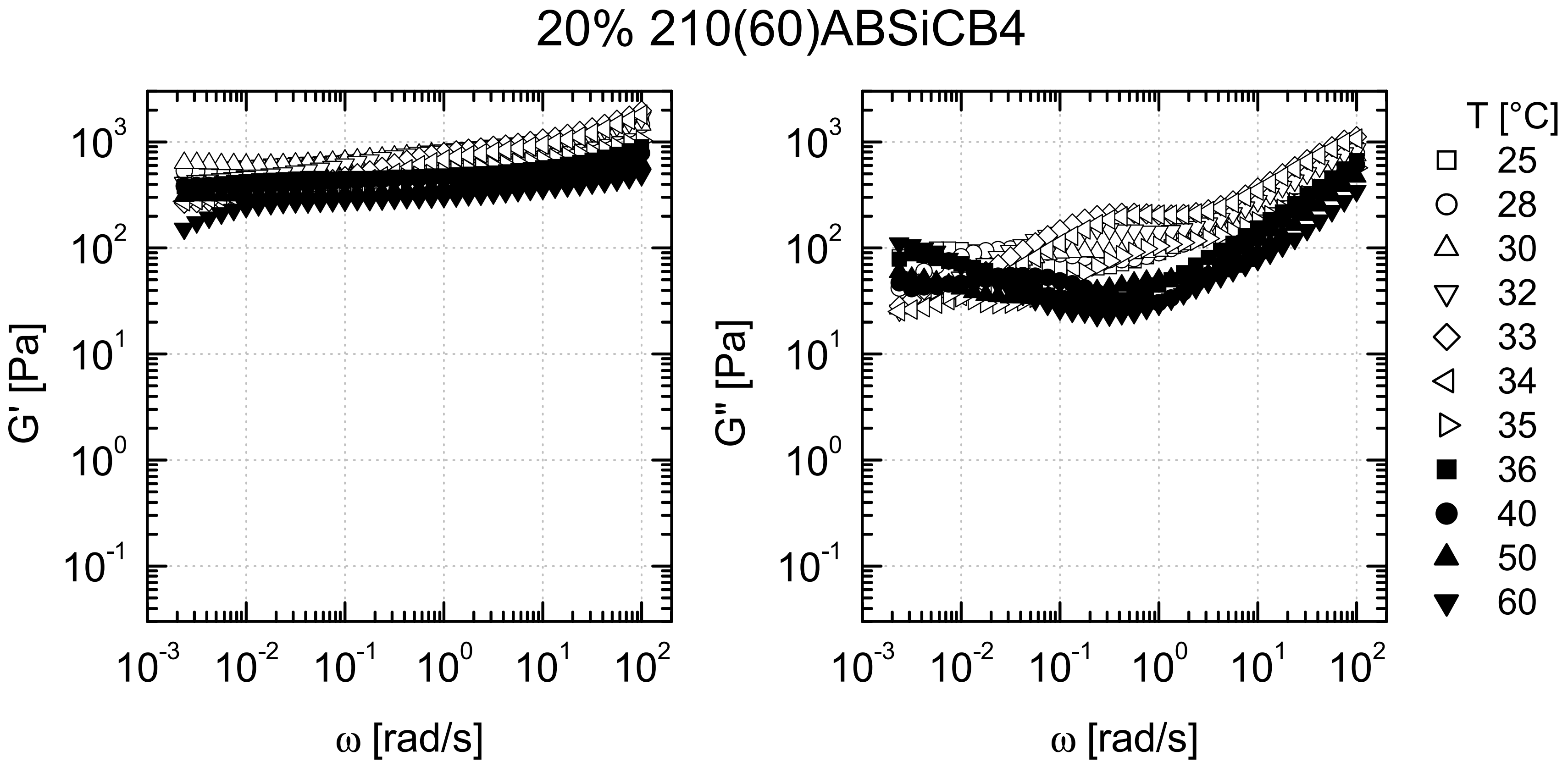

Figure E.18 Frequency (*ω*) dependence of the storage (*G*′) and loss (*G*″) modulus of 20 wt % 210(60)ABSiCB4 in 5CB as a function of temperature (*T*) in the nematic phase (open symbols) and the isotropic phase (closed symbols).

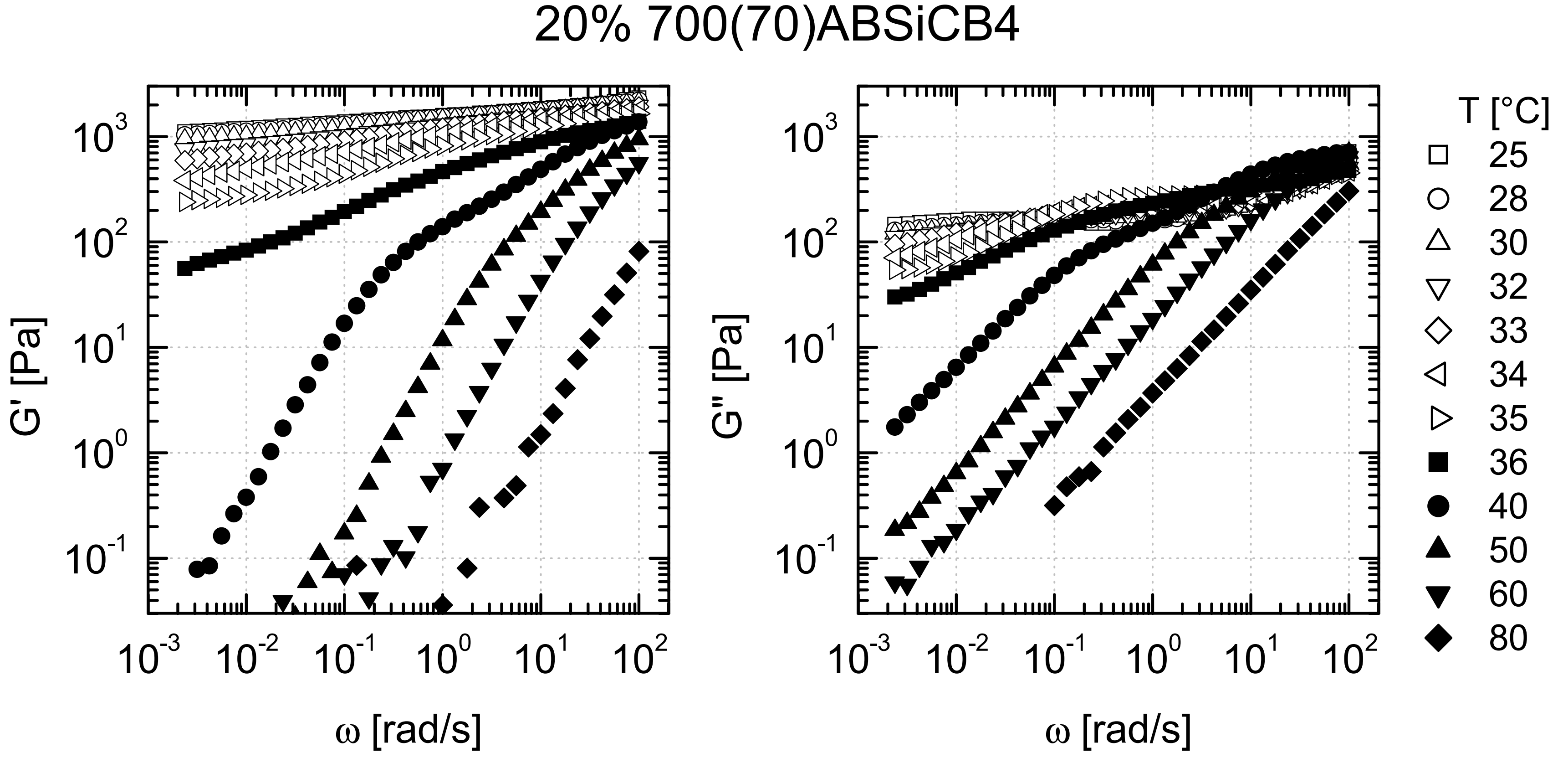

Figure E.19 Frequency (ω) dependence of the storage (G') and loss (G'') modulus of 20 wt % 700(70)ABSiCB4 in 5CB as a function of temperature (T) in the nematic phase (open symbols) and the isotropic phase (closed symbols).

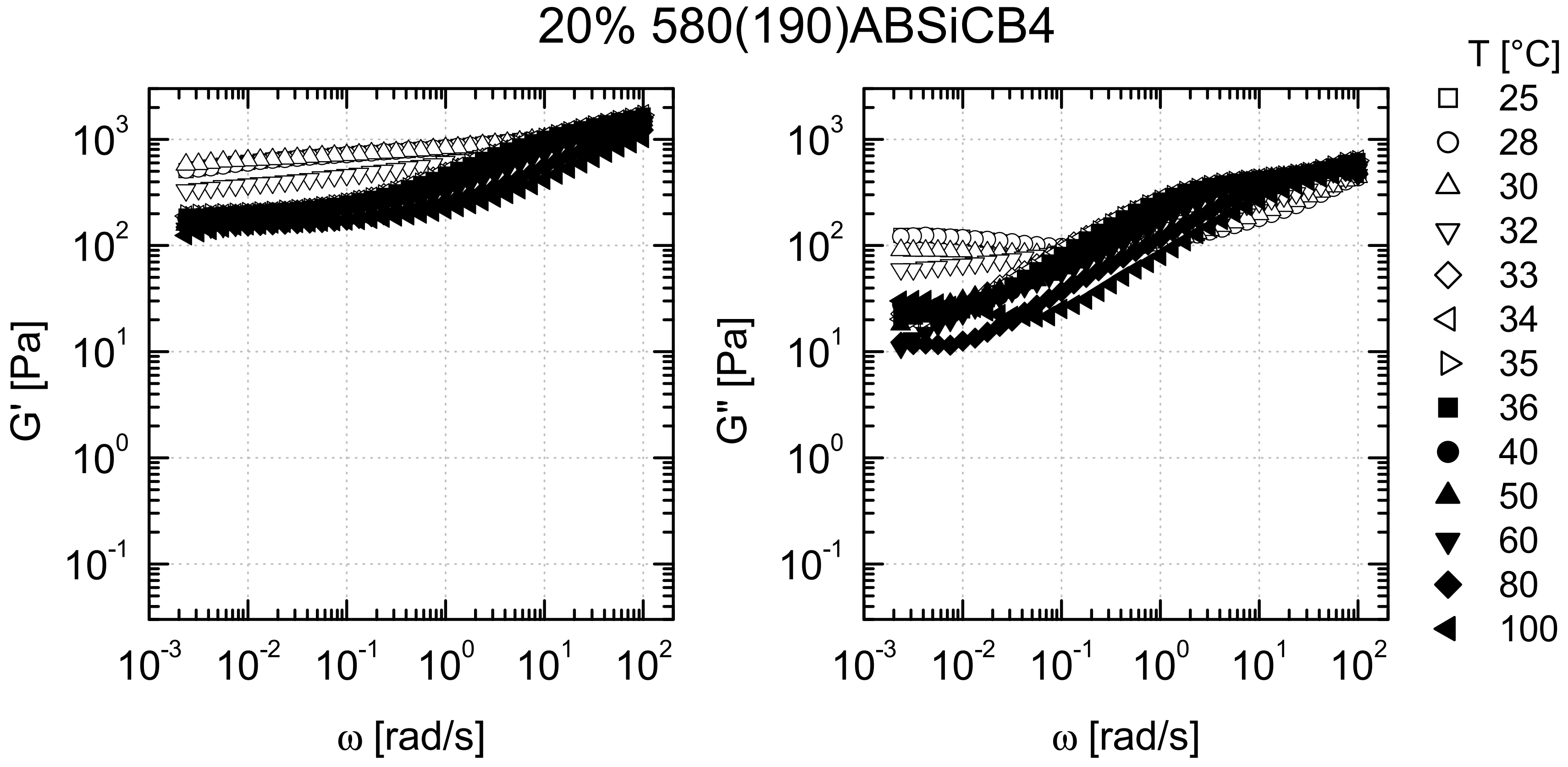

Figure E.20 Frequency (ω) dependence of the storage (G') and loss (G'') modulus of 20 wt % 580(190)ABSiCB4 in 5CB as a function of temperature (T) in the nematic phase (open symbols) and the isotropic phase (closed symbols).

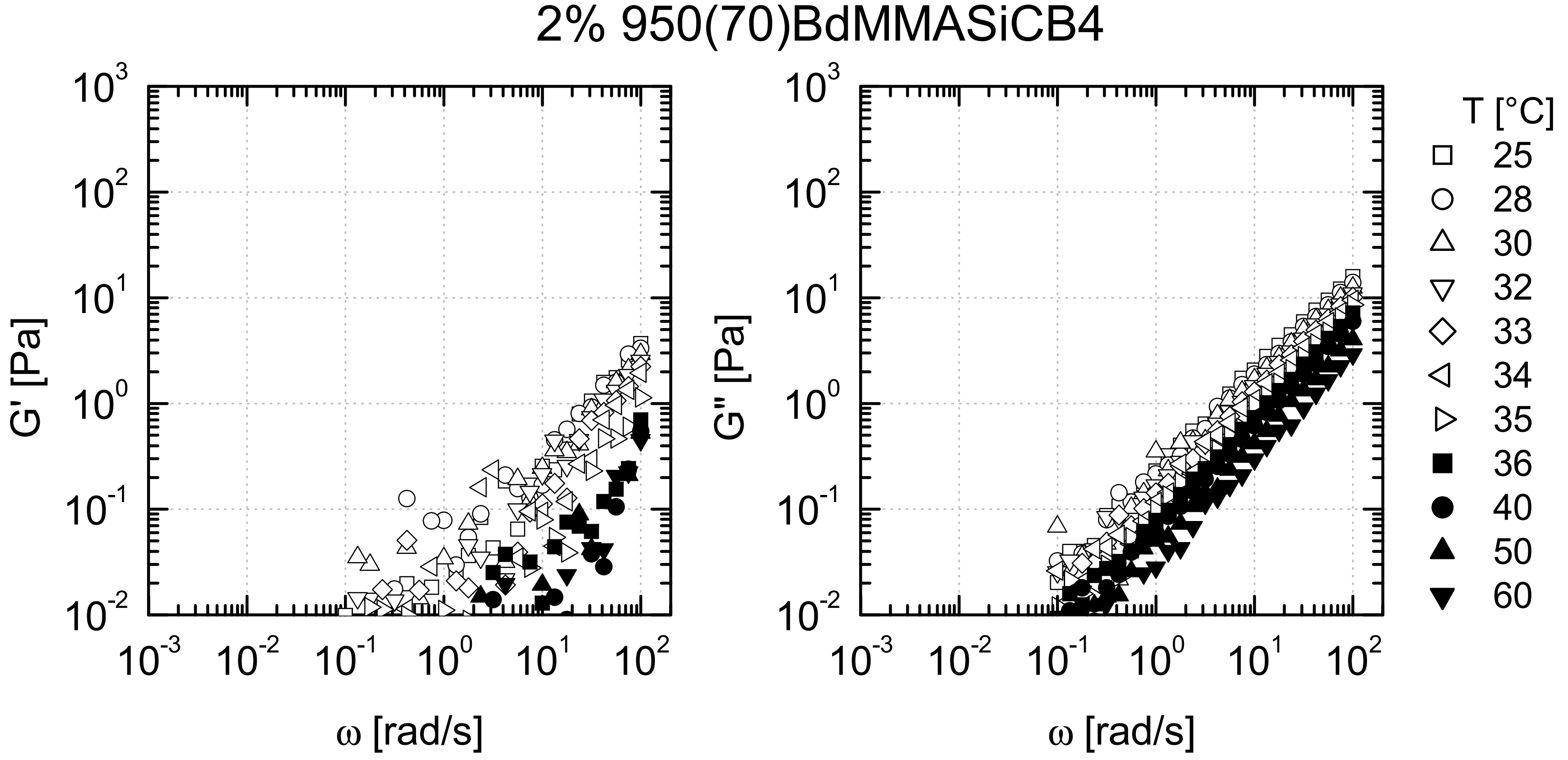

Figure E.21 Frequency (ω) dependence of the storage (G') and loss (G'') modulus of 2 wt % 950BdMMASiCB4 in 5CB as a function of temperature (T) in the nematic phase (open symbols) and the isotropic phase (closed symbols).

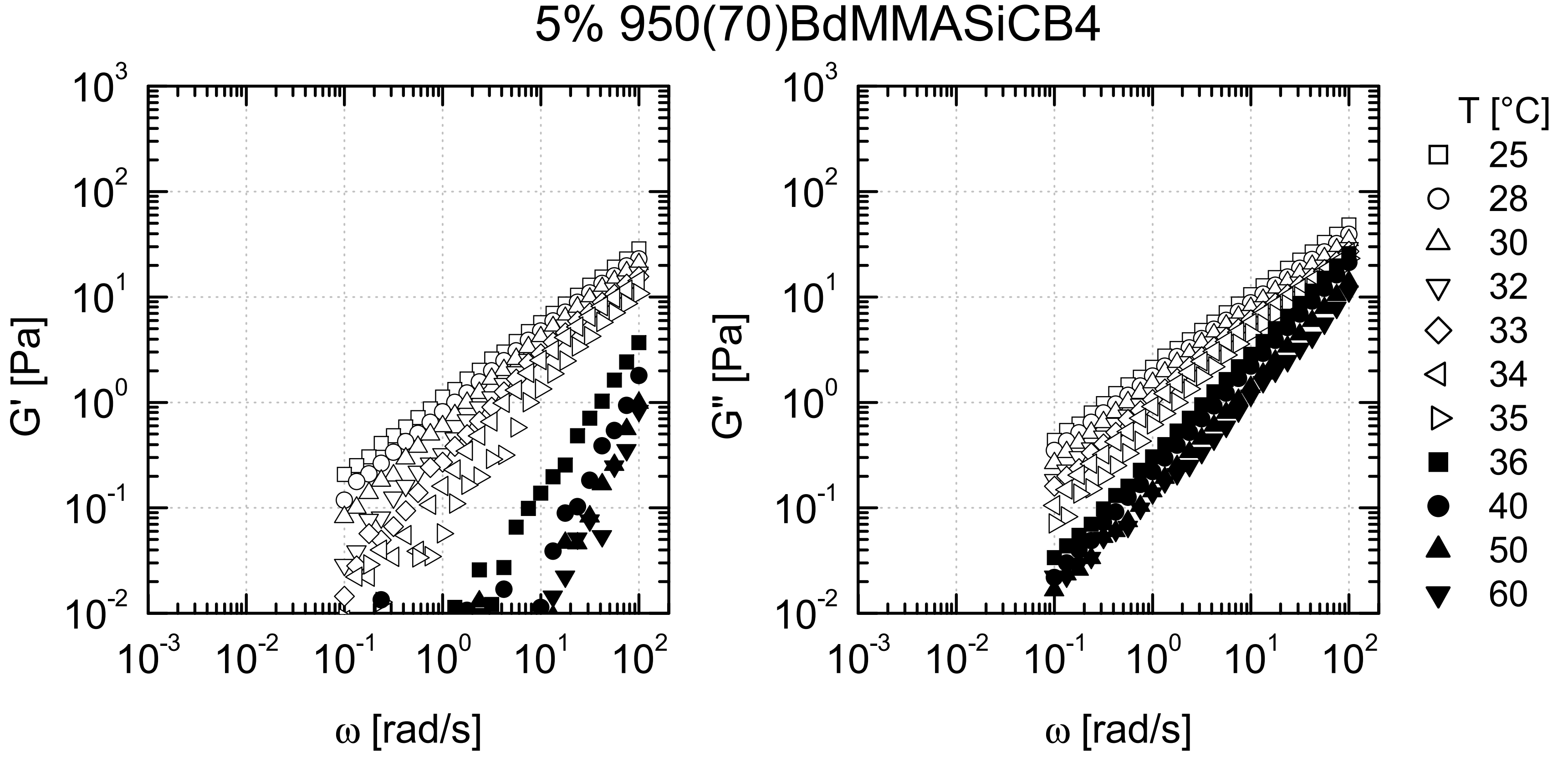

Figure E.22 Frequency (ω) dependence of the storage (G') and loss (G'') modulus of 5 wt % 950BdMMASiCB4 in 5CB as a function of temperature (T) in the nematic phase (open symbols) and the isotropic phase (closed symbols).

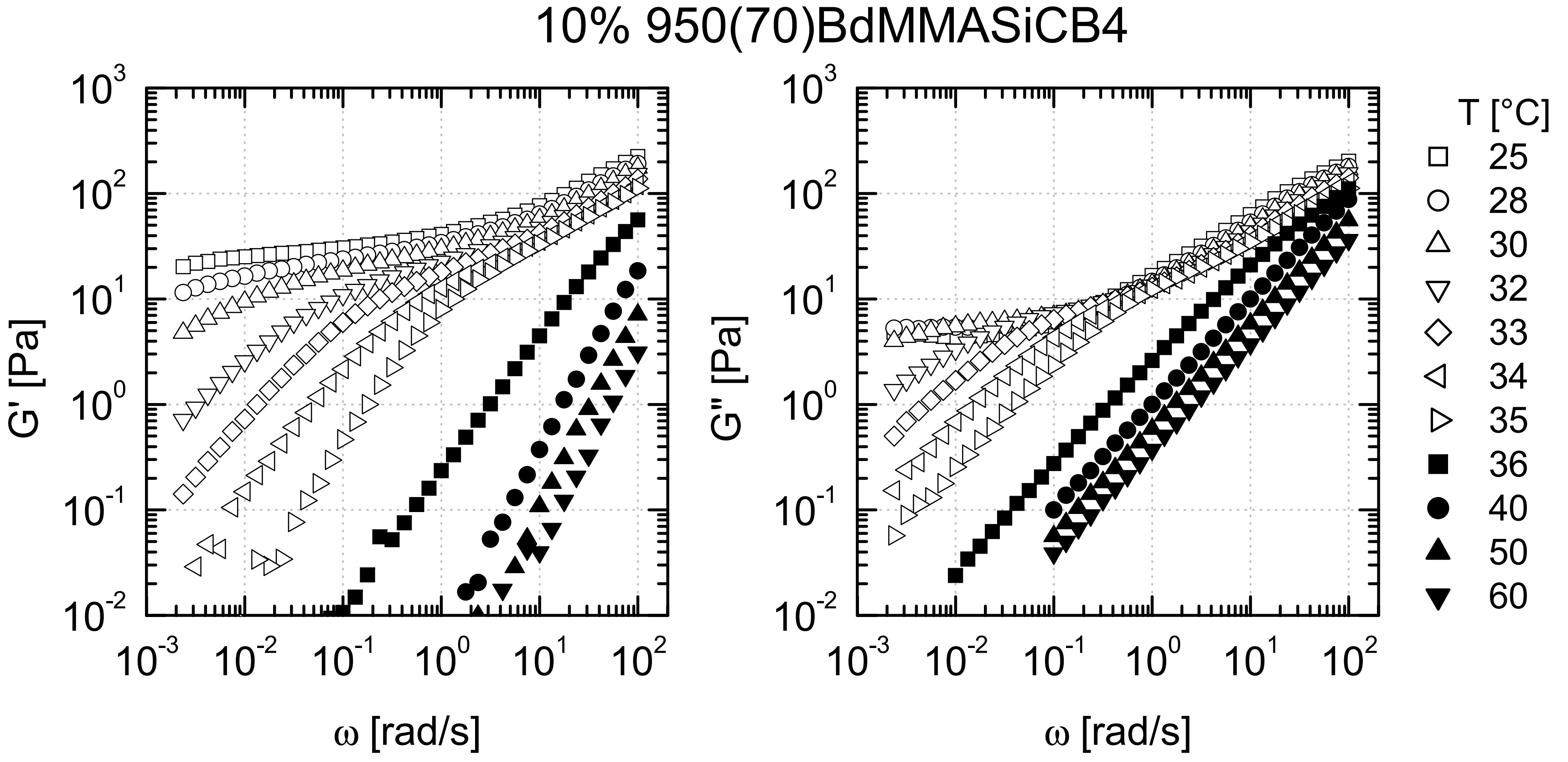

Figure E.23 Frequency (ω) dependence of the storage (G') and loss (G'') modulus of 10 wt % 950BdMMASiCB4 in 5CB as a function of temperature (T) in the nematic phase (open symbols) and the isotropic phase (closed symbols).

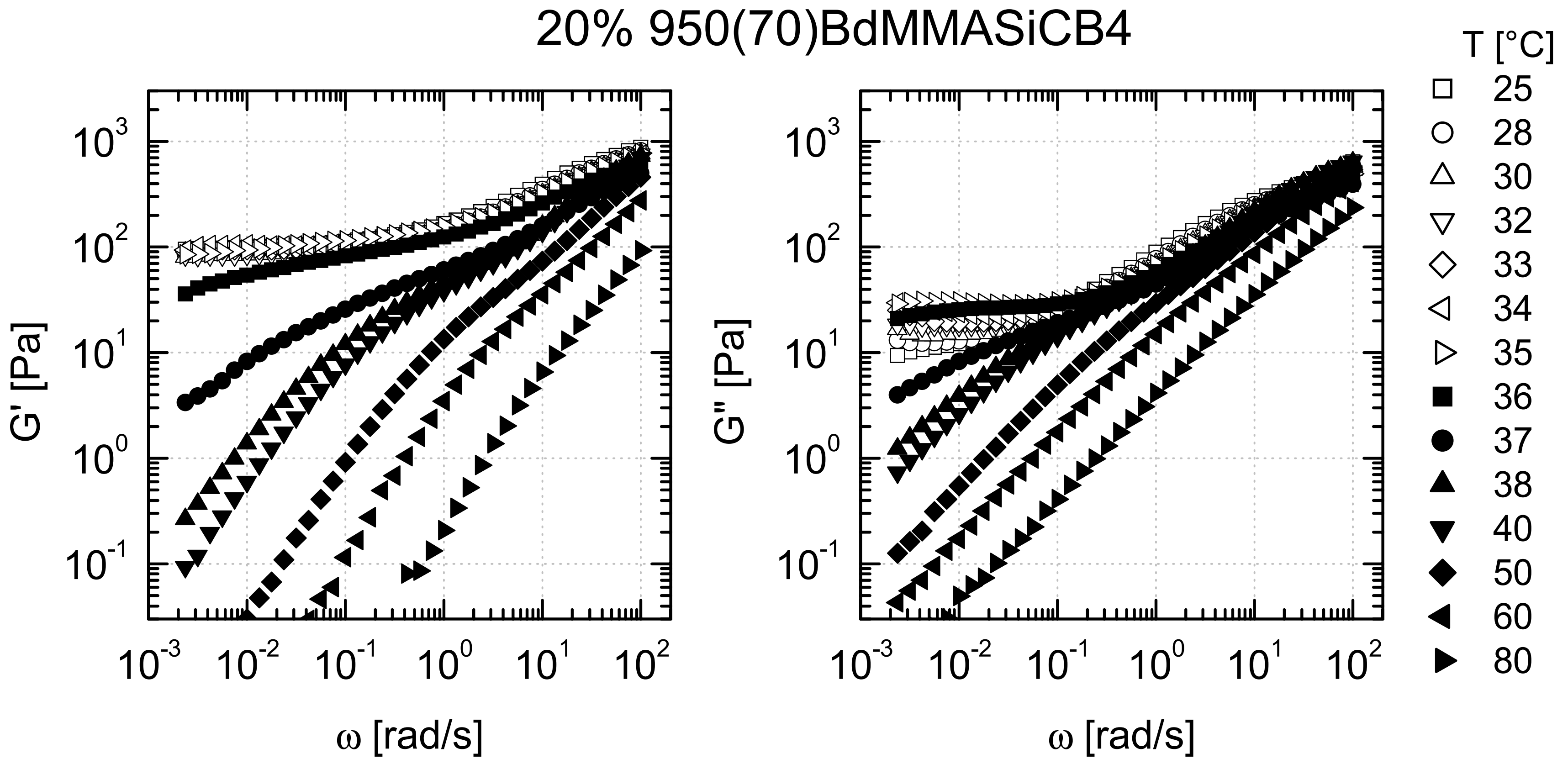

Figure E.24 Frequency (*ω*) dependence of the storage (*G′*) and loss (*G″*) modulus of 20 wt % 950BdMMASiCB4 in 5CB as a function of temperature (*T*) in the nematic phase (open symbols) and the isotropic phase (closed symbols).

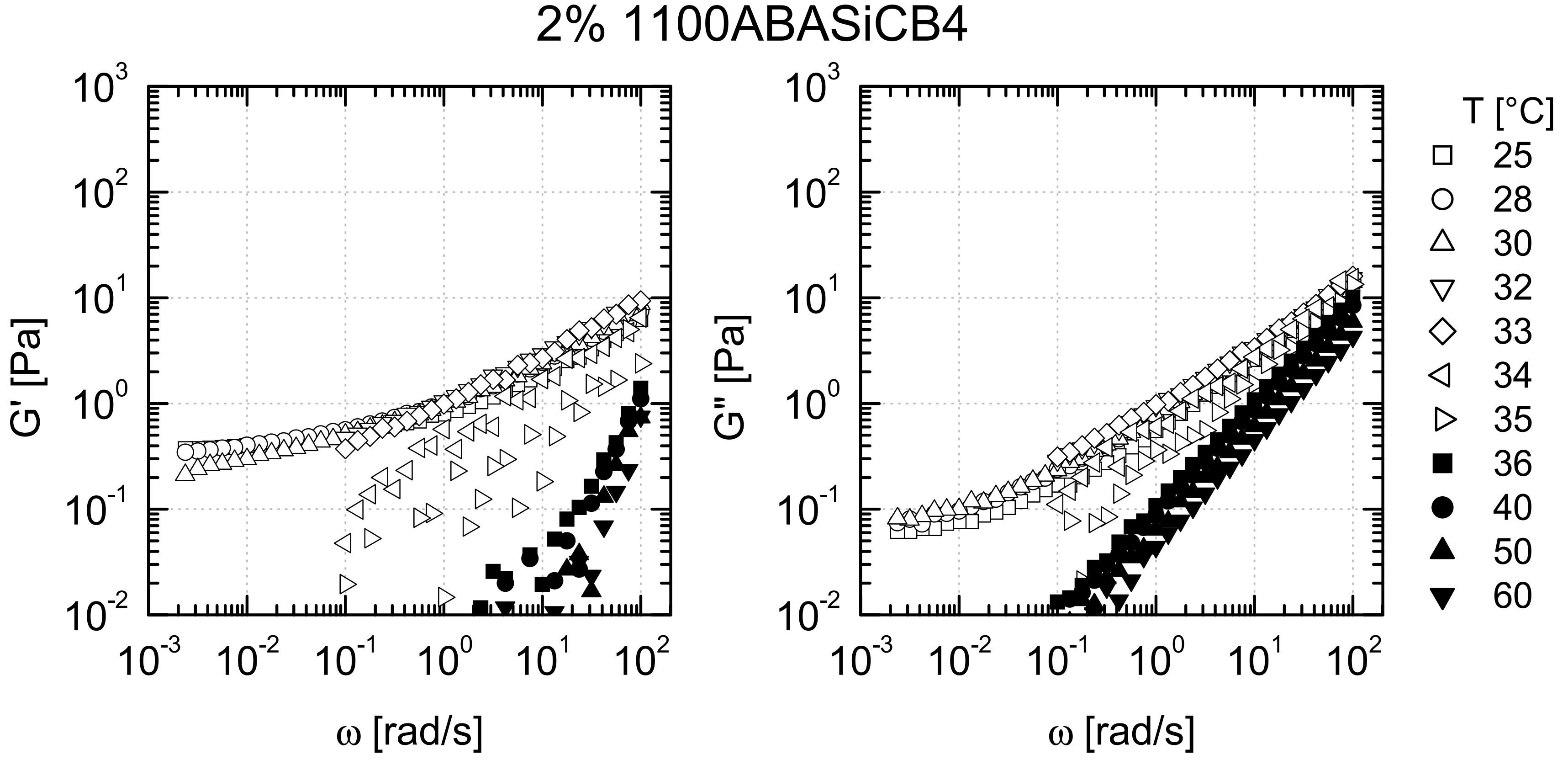

Figure E.25 Frequency (ω) dependence of the storage (G') and loss (G'') modulus of 2 wt % 1100ABASiCB4 in 5CB as a function of temperature (T) in the nematic phase (open symbols) and the isotropic phase (closed symbols).

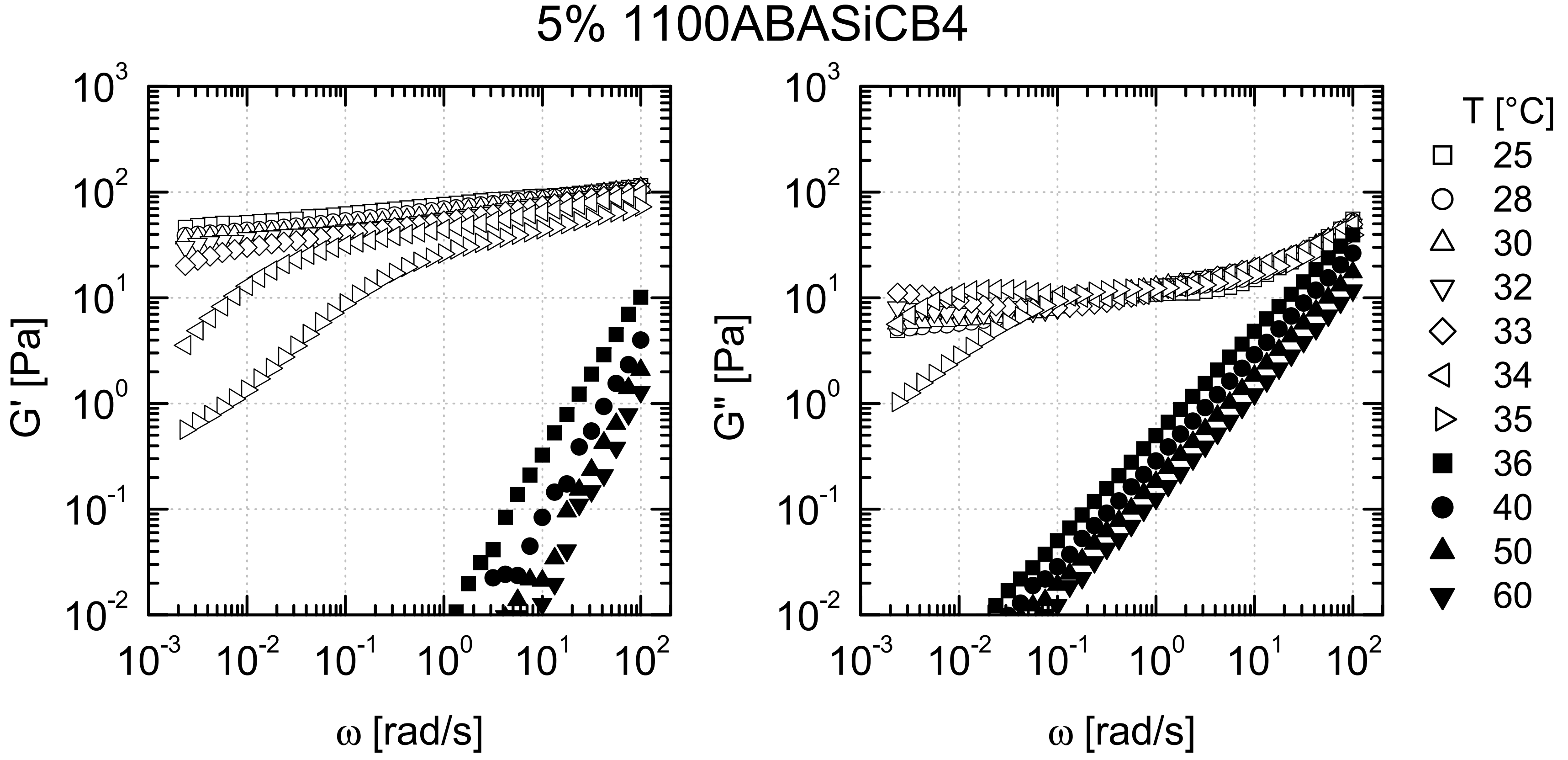

Figure E.26 Frequency (*ω*) dependence of the storage (*G*′) and loss (*G*″) modulus of 5 wt % 1100ABASiCB4 in 5CB as a function of temperature (*T*) in the nematic phase (open symbols) and the isotropic phase (closed symbols).

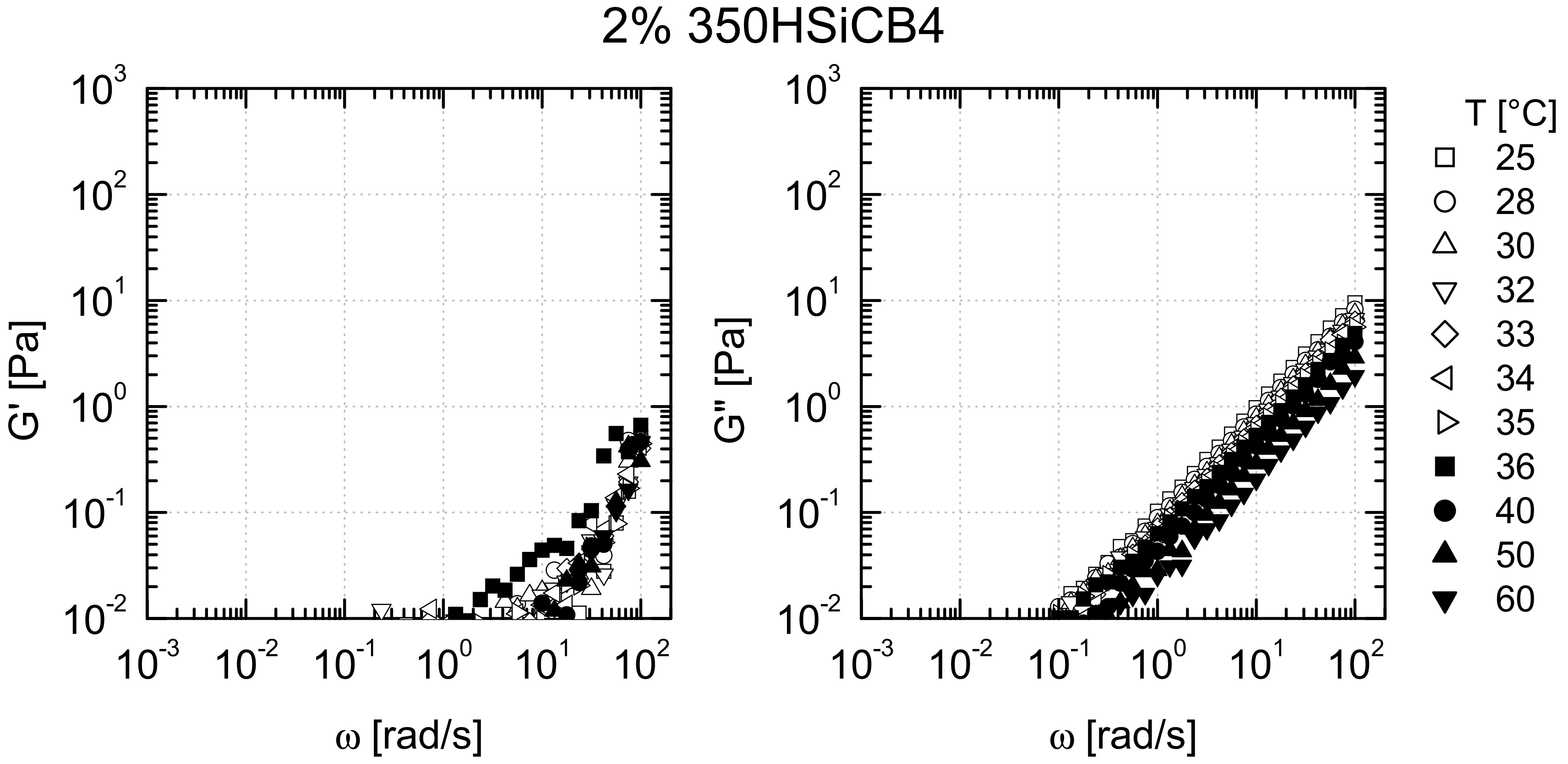

Figure E.27 Frequency (ω) dependence of the storage (G') and loss (G'') modulus of 2 wt % 350HSiCB4 in 5CB as a function of temperature (T) in the nematic phase (open symbols) and the isotropic phase (closed symbols).

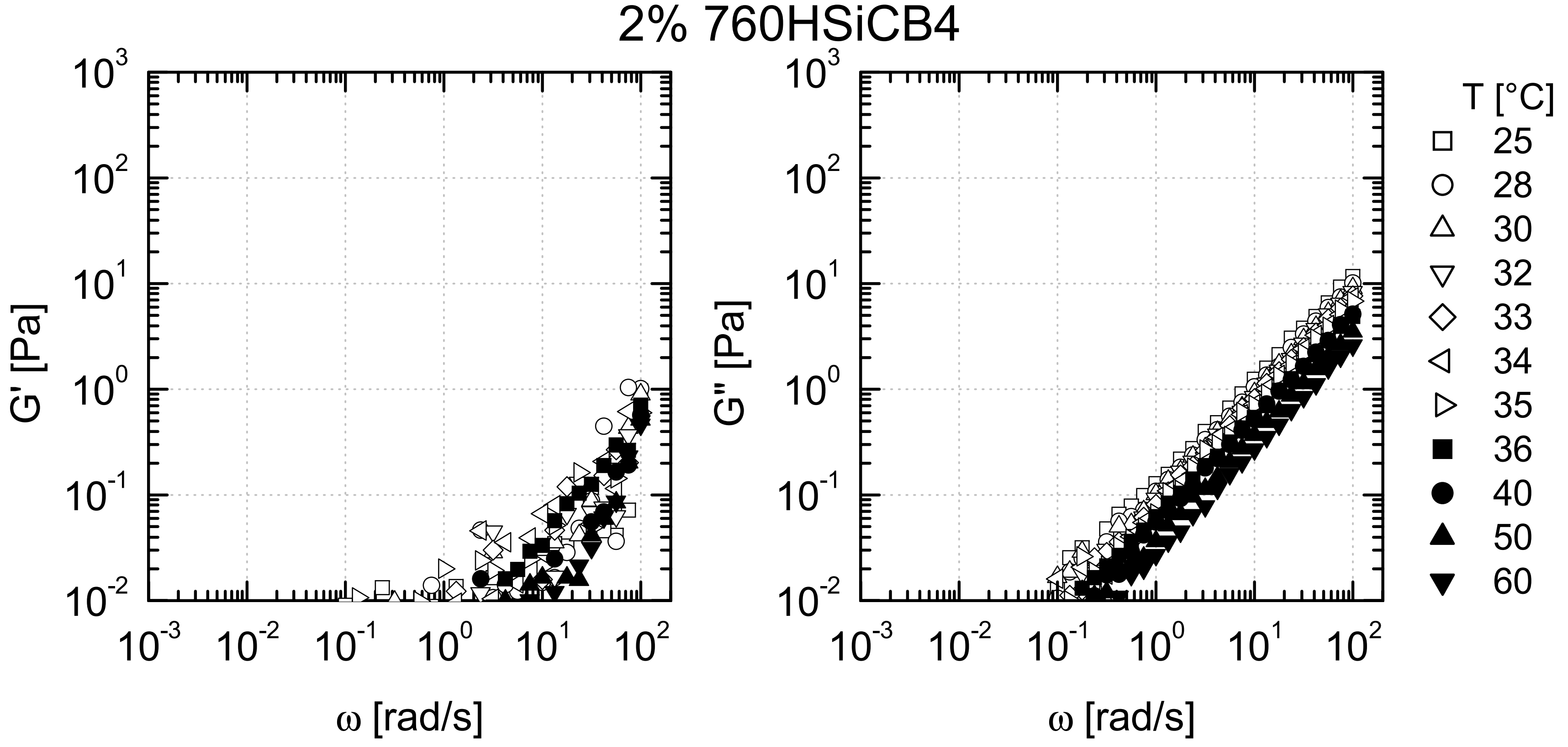

Figure E.28 Frequency (ω) dependence of the storage (G') and loss (G'') modulus of 2 wt % 760HSiCB4 in 5CB as a function of temperature (T) in the nematic phase (open symbols) and the isotropic phase (closed symbols).

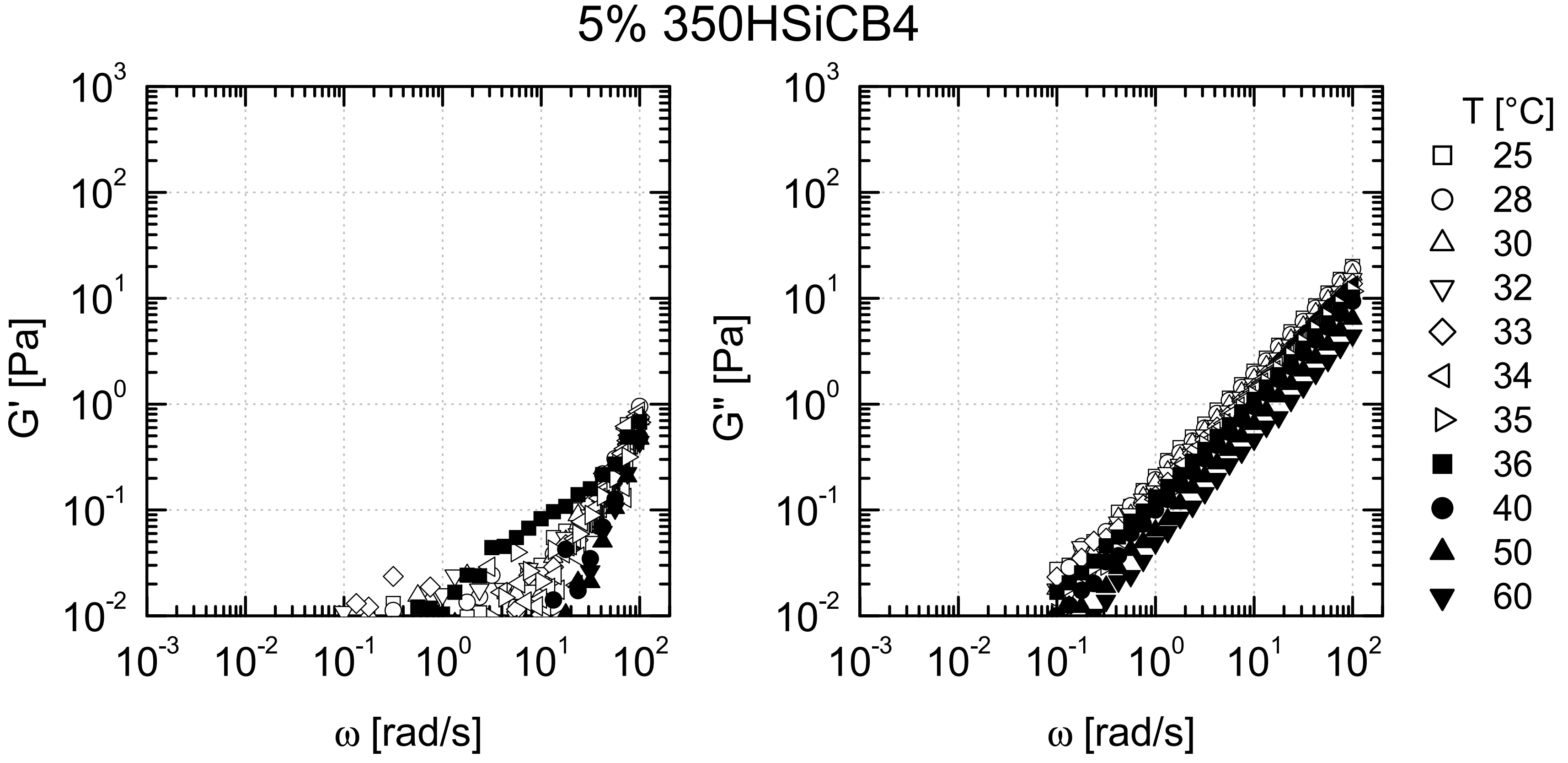

Figure E.29 Frequency (ω) dependence of the storage (G') and loss (G'') modulus of 5 wt % 350HSiCB4 in 5CB as a function of temperature (T) in the nematic phase (open symbols) and the isotropic phase (closed symbols).

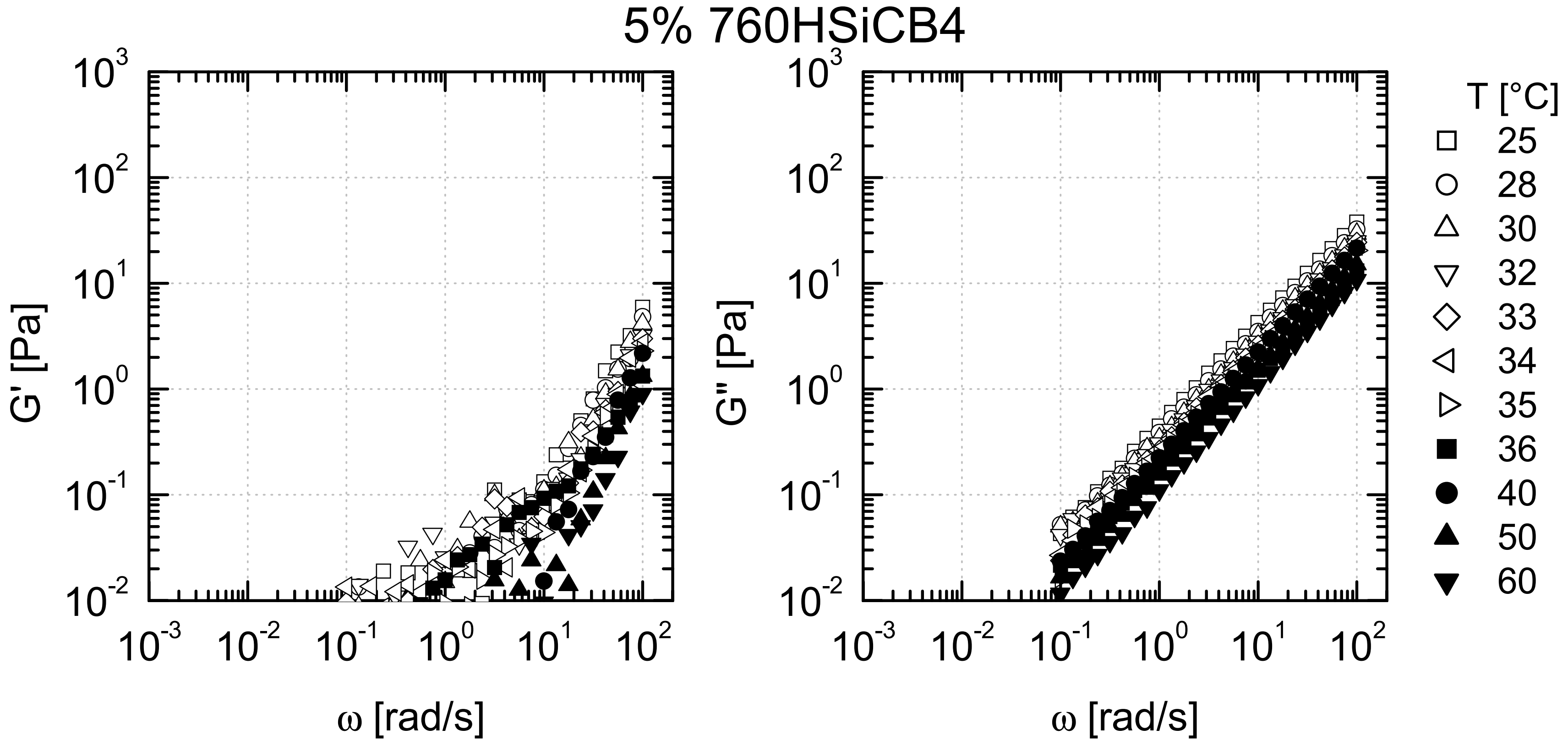

Figure E.30 Frequency (*ω*) dependence of the storage (*G*′) and loss (*G*″) modulus of 5 wt % 760HSiCB4 in 5CB as a function of temperature (*T*) in the nematic phase (open symbols) and the isotropic phase (closed symbols).

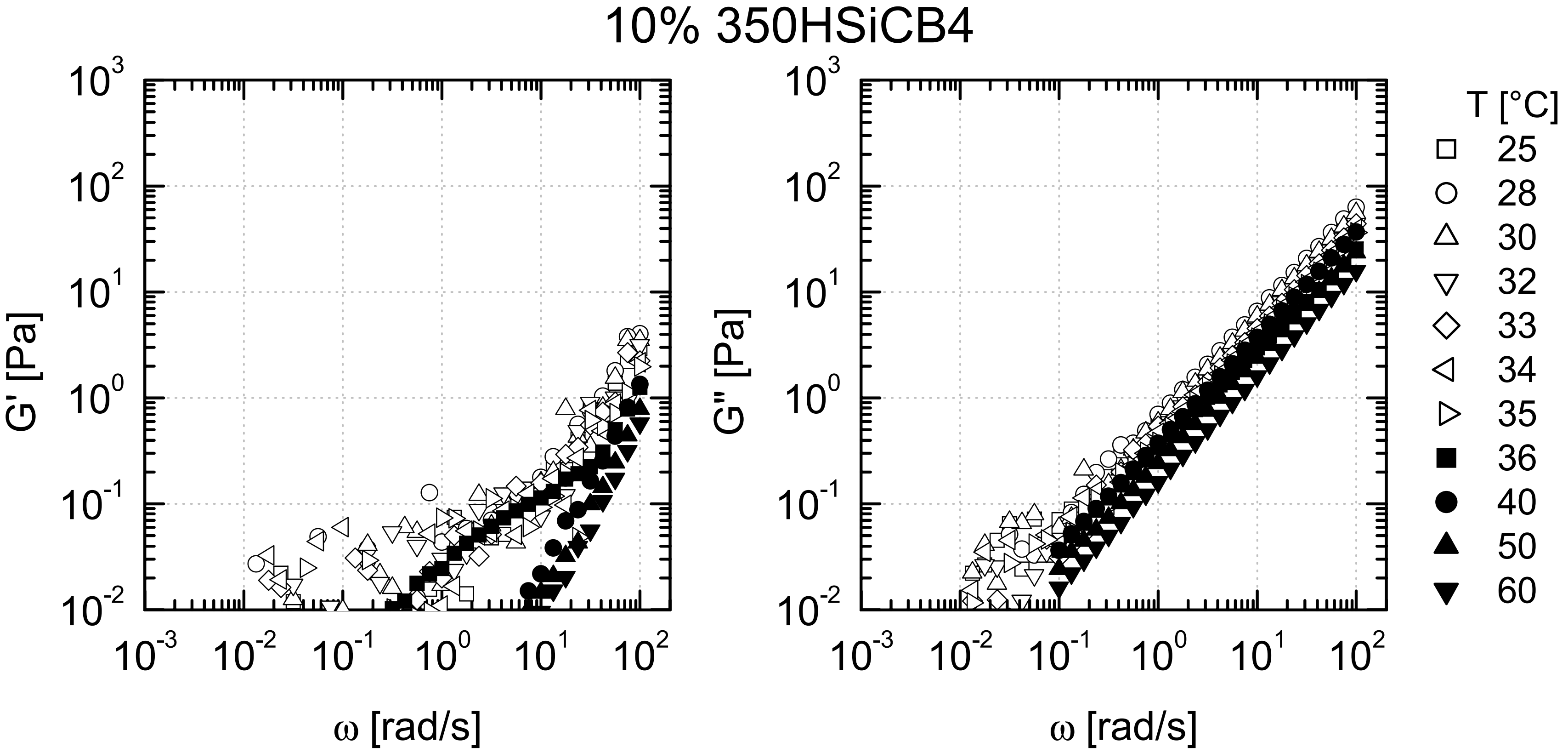

Figure E.31 Frequency (ω) dependence of the storage (G') and loss (G'') modulus of 10 wt % 350HSiCB4 in 5CB as a function of temperature (T) in the nematic phase (open symbols) and the isotropic phase (closed symbols).

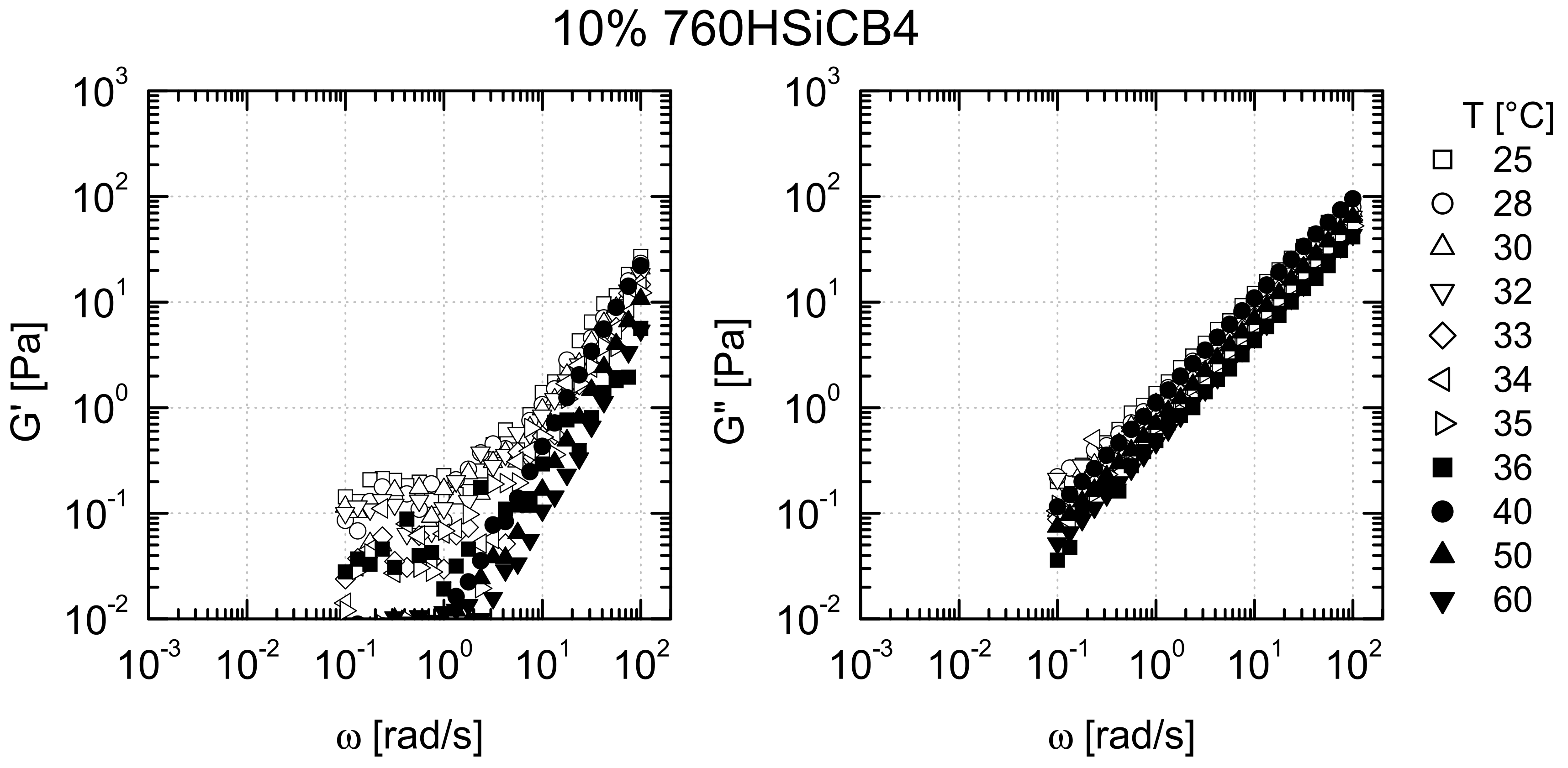

Figure E.32 Frequency (*ω*) dependence of the storage (*G*′) and loss (*G*″) modulus of 10 wt % 760HSiCB4 in 5CB as a function of temperature (*T*) in the nematic phase (open symbols) and the isotropic phase (closed symbols).

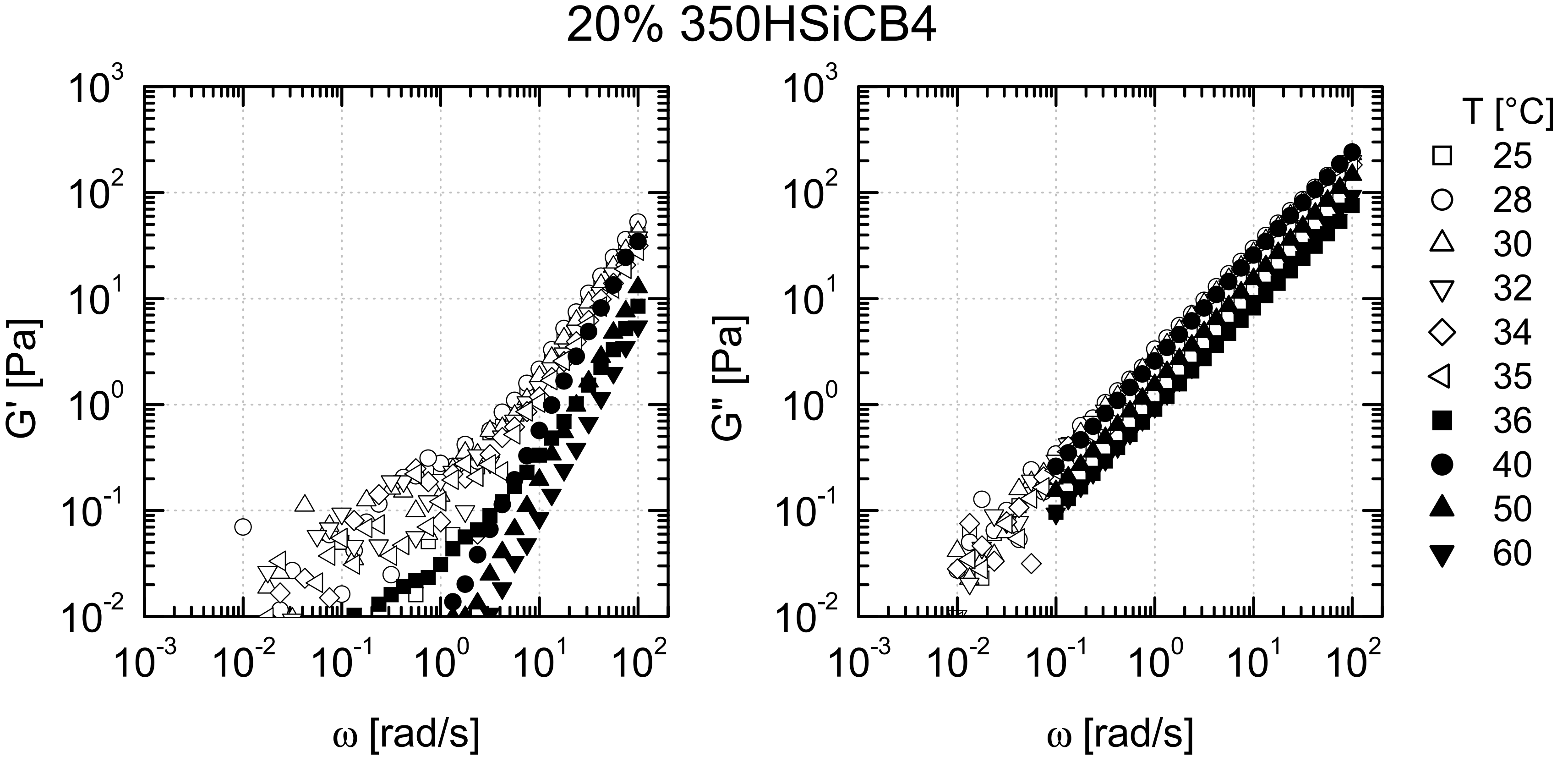

Figure E.33 Frequency (ω) dependence of the storage (G') and loss (G'') modulus of 20 wt % 350HSiCB4 in 5CB as a function of temperature (T) in the nematic phase (open symbols) and the isotropic phase (closed symbols).

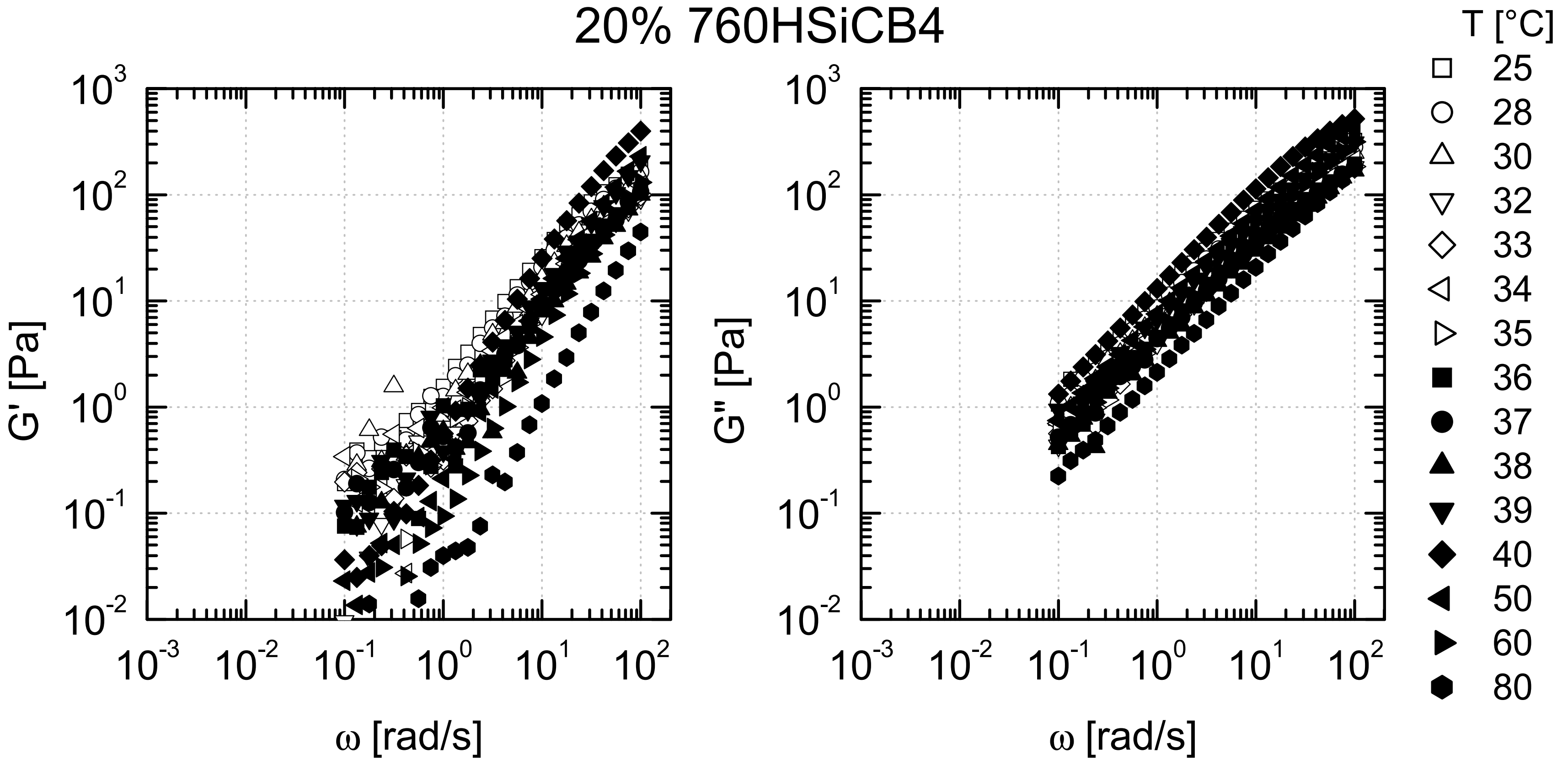

Figure E.34 Frequency (ω) dependence of the storage (G') and loss (G'') modulus of 20 wt % 760HSiCB4 in 5CB as a function of temperature (T) in the nematic phase (open symbols) and the isotropic phase (closed symbols).